Dissertation

submitted to the

Combined Faculties of the Natural Sciences and Mathematics
of the Ruperto-Carola University of Heidelberg, Germany

for the degree of

Doctor of Natural Sciences

Put forward by

Jonas Peter Wessely

born in: Heidelberg, Germany
Oral examination: 11th of July, 2025

Dynamical observables from spectral quantum field theory

Referees: Prof. Dr. Jan M. Pawlowski
Prof. Dr. Joerg Jaeckel

Dynamical observables from spectral quantum field theory

We present a framework for the direct, non-perturbative computation of real-time observables in quantum field theories using spectral functional methods. Building on spectral representations of correlators, particularly the Källén-Lehmann representation of the propagator, this approach enables the evaluation of functional diagrammatic relations, such as the Dyson-Schwinger equations and the functional renormalisation group, across the entire complex frequency domain. The primary focus of this work is on quantum chromodynamics (QCD), where we develop efficient methods for computing the propagator spectral functions of various elementary fields. These include the spectral function of a scalar field in three dimensions, the graviton in asymptotically safe quantum gravity, and, in particular, the light quark in QCD. To study the real-time properties of dynamical chiral symmetry breaking, we construct a causal quark-gluon interaction model. Building on the non-perturbative spectral functions of the propagators, we investigate the properties of bound states and show how the spectral approach can be applied to compute bound-state masses directly on the real frequency axis. Finally, we use spectral reconstruction techniques to compute the pion distribution amplitude directly on the light front.

Dynamische Observablen mit spektraler Quantenfeldtheorie

Wir präsentieren einen Zugang für die direkte und nicht-perturbative Berechnung dynamischer Observablen in Quantenfeldtheorien mithilfe spektraler funktionaler Methoden. Aufbauend auf spektralen Darstellungen von Korrelatoren, insbesondere der Källén-Lehmann-Darstellung des Propagators, ermöglicht dieser Ansatz die Auswertung funktionaler diagrammatischer Relationen, wie den Dyson-Schwinger-Gleichungen und der funktionalen Renormierungsgruppe, über den gesamten komplexen Frequenzbereich. Der Schwerpunkt dieser Arbeit liegt auf der Quantenchromodynamik (QCD), wobei wir Methoden zur effizienten Berechnung der Spektralfunktionen für Propagatoren verschiedener elementarer Felder entwickeln. Dazu zählen die Spektralfunktion eines skalaren Feldes in drei Dimensionen, die des Gravitons in asymptotisch sicherer Quantengravitation sowie insbesondere die Spektralfunktion des leichten Quarks in der QCD. Zur Untersuchung der Realzeit-Eigenschaften der spontanen chiralen Symmetriebrechung konstruieren wir ein kausales Quark-Gluon-Wechselwirkungsmodell. Aufbauend auf den nicht-perturbativen Spektralfunktionen der Propagatoren analysieren wir die Eigenschaften gebundener Zustände und zeigen, wie der spektrale Ansatz zur direkten Berechnung der Massen gebundener Zustände auf der reellen Frequenzachse angewendet werden kann. Abschließend präsentieren wir eine Berechnung der Pion Distribution Amplitude direkt auf der Light Front, ermöglicht durch spektrale Rekonstruktionsmethoden.

Publications

This thesis was solely written by the author. It is, however, result of a joint effort in a research collaboration. At the time of completion of this dissertation, these results have largely been published, are available as preprint or in preparation for publication. Figures and text taken from these articles are not marked explicitly. Instead, we indicate this at the beginning of the respective sections. The jointly authored publications are:

[1] J. Braun, Y. Chen, W. Fu, A. Geißel, J. Horak, C. Huang, F. Ihssen, J. M. Pawlowski, M. Reichert, F. Rennecke, Y. Tan, S. Töpfel, J. Wessely, N. Wink, *Renormalised spectral flows*, arXiv:2206.10232 [hep-th], SciPost Phys. Core 6, 061 (2023)

[2] J. M. Pawlowski, J. Wessely, *Bound states from the spectral Bethe-Salpeter equation*, arXiv:2310.16353 [hep-th], Phys. Rev. D 109, 096024 (2024)

[3] J. Horak, F. Ihssen, J. M. Pawlowski, J. Wessely, N. Wink, *Scalar spectral functions from the spectral functional renormalization group*, arXiv:2303.16719 [hep-th], Phys. Rev. D 110, 056009 (2024)

[4] J. M. Pawlowski, J. Wessely, *The causal structure of the quark propagator*, arXiv:2412.12033 [hep-ph], submitted to Eur. Phys. J. C

Additionally, we present results from the following manuscripts which are currently being prepared for publication:

[5] K. Kockler, J.M. Pawlowski, J. Wessely *Critical scaling for spectral functions*

[6] J. M. Pawlowski, M. Reichert, J. Wessely *Self-consistent graviton spectral functions*

[7] C. Huang, J.M. Pawlowski, J. Wessely, *Light-front PDAs from (spectral) functional methods*

Note on the author's contributions

In [3, 4, 6, 7], I performed all practical calculations of the respective works, contributed central ideas and took the leading role in writing the manuscripts.

Ref. [1] represents a joint publication of the fQCD collaboration [8], of which I co-authored in particular Sections IV, and V A.

Ref. [2] emerged from a projects with a Master student, whom I co-supervised during the thesis. All practical calculations were carried out by Andrés Gómez. I contributed central ideas before and during these project, provided technical supervision for the student and was sizably involved in writing the respective manuscripts.

Ref. [5] emerged from a project with a Bachelor student, whom I co-supervised during the thesis. All numerical calculations were carried out by Konrad Kockler. My contribution to this paper where the initial idea, the derivation the basic equations and the initial numerical code base. Furthermore, I wrote a substantial part of the manuscript.

In the cases where the practical calculations were not or not solely performed by myself, the collaborators involved in the computation are indicated at the beginning of the sections where the respective results are presented.

Contents

1. Introduction **1**

2. Quantum Chromodynamics **5**
- 2.1. Quarks and gluons 6
- 2.2. Correlation functions and observables 9
- 2.3. Gauge fixing, Renormalisation and Scattering 12
  - 2.3.1. Gauge fixed QCD 12
  - 2.3.2. The running coupling 14

3. Spectral functional methods **17**
- 3.1. Spectral representations and analytic continuations 18
  - 3.1.1. Propagator spectral functions 18
  - 3.1.2. Spectral sum rules and asymptotic behaviour 20
- 3.2. Functional equations 22
  - 3.2.1. Dyson-Schwinger equations 22
  - 3.2.2. The functional Renormalisation Group 23
- 3.3. From the Wetterich RG to the renormalised Callan-Symanzik equation . 25
  - 3.3.1. Infrared regularisation and symmetries 25
  - 3.3.2. RG-consistency and UV scaling 28
  - 3.3.3. Functional RG with flowing renormalisation 30
  - 3.3.4. Flowing renormalisation conditions 33
  - 3.3.5. Spectral renormalisation in gauge theories 35
- 3.4. Spectral functional equations 38

4. Applications in scalar theories and gravity **41**
- 4.1. Scalar spectral flows in three dimensions 42
  - 4.1.1. Spectral properties of the scalar theory 42
  - 4.1.2. Functional Callan-Symanzik equation 44
  - 4.1.3. Spectral on-shell renormalisation 47
  - 4.1.4. Flowing with the minimum 48
  - 4.1.5. Approximations and real-time flows 50
  - 4.1.6. Results 55
  - 4.1.7. Spectral flows close to the phase transition 58
  - 4.1.8. Conclusion 64
- 4.2. Boundstates from the spectral BSE 66
  - 4.2.1. Spectral DSEs and BSEs 67
  - 4.2.2. Results 74
  - 4.2.3. Conclusions 76
- 4.3. The graviton spectral function 77
  - 4.3.1. CS-flow in asymptotically safe gravity 78
  - 4.3.2. Renormalised spectral flow for the graviton propagator 79

4.3.3. Beyond the on-shell flow 83
4.3.4. Conclusion 83

5. Dynamical observables in Quantum Chromodynamics 85
5.1. The quark spectral function 86
5.1.1. The spectral quark gap equation 87
5.1.2. Spectral structure of quark and gluon propagators 87
5.1.3. A causal quark-gluon vertex 89
5.1.4. The causal structure of the quark propagator 93
5.1.5. The real pole of the quark propagator 94
5.1.6. Additional cc poles for large vertex strength 95
5.1.7. Phenomenological vertex fits 98
5.1.8. Conclusion 101
5.2. Mesonic parton distributions 102
5.2.1. The light-front wave function 103
5.2.2. Spectral PDA 104
5.2.3. Reconstructing the BSA 106
5.2.4. Light quark input 108
5.2.5. Pion distribution amplitudes 109
5.2.6. Conclusion 111

6. Summary & Conclusion 113

Appendices 117

A. Additional material 119
A.1. Additional material for the scalar spectral flows 120
A.1.1. Spectral diagrams 120
A.1.2. Renormalised flow of the two-point function on the physical minimum 121
A.1.3. Flow of ϕ_0 and critical exponents 123
A.1.4. Phase transition and critical scaling 124
A.1.5. Calculation of diagrams 126
A.1.6. Flow equation of the effective potential 127
A.1.7. Anomalous dimension η_ϕ 128
A.1.8. Scaling of $\rho_4(\lambda)$ 129
A.1.9. Computation of the LPA$'$ benchmark 131
A.1.10. Possible improvements and further work 132
A.2. Additional material for the spectral DSE-BSE system 133
A.2.1. Spectral DSE 133
A.2.2. Scaling limit 136
A.2.3. Modified skeleton expansion 136
A.2.4. Bethe-Salpeter equation 138
A.3. Additional material for the graviton spectral function 140
A.3.1. Analytic expressions of the diagrams 140
A.3.2. UV-limit of the spectral tail 141
A.4. Additional material for the quark gap equation 143
A.4.1. The spectral STI-vertex 143

A.4.2. Self-energy calculations 146
A.5. Spectral integrands for the pions DA and LFWF 148
A.6. Technical details and numerics 149
A.6.1. Scalar spectral flows 149
A.6.2. Scaling-Limit of scalar spectral flows 153
A.6.3. Scalar bound state 154
A.6.4. Spectral Gravity 156
A.6.5. Numerical implementation of the quark gap equation 158

Acknowledgments **159**

Bibliography **161**

1. Introduction

Our current understanding of nuclear matter, which makes up the largest part of the visible mass in the universe, is based on quantum chromodynamics (QCD). Although it is one of the most successful theories we have, there is a plethora of phenomenons that are not yet understood, ranging from the many phases of QCD at non-vanishing chemical potentials to the structure of hadrons and nuclei, for a recent review see [9]. Progress, both on the theoretical and experimental side, is thereby hampered by the phenomenon of confinement, which makes it impossible to measure direct properties of the fundamental degrees of freedom, namely the quarks and gluons. Instead, direct measurements are only possible for the physical degrees of freedom, which are hadrons and other bound states. This mismatch between the fundamental and physical degrees of freedom turns the connection of experimental observations to the fundamental features of the underlying theory into a difficult inverse problem.

The rôle of dynamic observables

A prominent example of this can be found in heavy ion collisions (HIC) at the LHC, RHIC, FAIR and others, where the collision of ultra-relativistic nuclei creates a hot and dense medium, usually referred to as quark gluon plasma (QGP) [10–14]. Albeit the violent and non-equilibrium nature of the collision, the QGP was found to thermalise quickly and to exhibit properties of a nearly perfect fluid, [15, 16]. At these high temperatures, quarks and gluons do not form bound states, but are said to be deconfined. Although many questions remain unanswered, the evolution of the QGP is remarkably well described by viscous hydrodynamics. As the system cools down, the quarks and gluons recombine into hadrons, which are then observed in the detector. Hence, the information we can extract about the QGP is convoluted through the hydrodynamic evolution. The large amount of uncertainties in the initial conditions, the details of the hadronisation process and the transport properties of the medium leaves the interpretation of the final state observables ambiguous.

Another important example is the structure of hadrons and nuclei, which where first probed in deep inelastic scattering (DIS) experiments [17–19] and will be studied in the upcoming Electron Ion Collider (EIC) experiments [20–23]. While the interaction of the constituents with incoming scattering partners at high energies is well described by perturbation theory, the actual structure of hadrons as bound states is dominated by non-perturbative effects. Most prominently, the dynamical breaking of chiral symmetry (DχSB) leads to the largest contribution to the mass of visible matter. To probe the hadron structure, one therefore relies on the separation of scales between the scattering at high energies and the non-perturbative IR-dominated processes in the hadron [24]. This results in the parton picture, where a scattering off the hadron is described by the sum of scattering amplitudes of the individual constituents, weighted by non-perturbative distribution functions which encode the momentum distribution of the contituents relative to the total momentum of the hadron [25].

In both cases, a large amount of measurable observables are inherently time- or lightlike,

like cross-sections in scattering experiments. Not only the scattering amplitudes of the constituents are real-time observables, also the distribution functions that describe the hadron structure fall in this class. They are defined on the light-front i.e., from matrix elements containing two partons at light-like separation. For a review, see [26]. Even to obtain information on static observables often requires knowledge on time-like observables. An example for the latter are the shear and bulk viscosities of the quark gluon plasma, or the diffusion coefficients of the quarks, which are directly related to the electric conductivity of the medium. To obtain information on the phase structure of QCD from HIC experiments, these observables are necessary input for the hydrodynamic models that describe the evolution of the QGP. We will refer to this class of observables as dynamic, in contrast to static observables, which are fully determined by space-like correlations.

How can we compute them?

On the theoretical side, the emergence of hadrons and confinement are non-perturbative phenomena, which govern the infrared dynamics of QCD. Traditionally, these strongly coupled systems are studied for space-like momenta using lattice QCD [27–32] or functional continuum methods like the Functional Renormalisation group (fRG) [33–36] or Dyson-Schwinger equations (DSE) and Bethe-Salpether equations (BSE) [37–40]. On the Euclidean frequency axis, both the lattice and functional methods have been very successful to compute static observables at finite temperature and in the vacuum. In the past decades, the progress of computational resources and systematic improvements of approximation schemes have led to a convergence of results from different methods. Unfortunately, the situation is very different for real-time correlation functions and dynamic observables.

While the lattice has the advantage of being in principle only limited by the computational resources and the numerical/statistical error, it requires a probability measure in the path-integral. This prohibits the direct computation of observables at finite baryon density, or of observables that rely on correlations at time-like or light-like momenta. In both cases, the path-integral measure is not positive-definite, leading to the infamous sign problem. Functional methods, on the other hand, are not limited to the Euclidean domain. If we accept that a Wick-rotation is always possible, the functional equations are indifferent whether we evaluate them at real (Minkowskian) or imaginary (Euclidean) frequencies. However, due to the singular structure of correlation functions on the real frequency axis, a straightforward numerical solution of the loop integrals at real external frequencies is often impossible.

There are several approaches to overcome this issue, which can be roughly divided into two classes. The first one is the reconstruction of correlation function from the Euclidean data, where the (inverse) Wick rotation is performed numerically, see [41–47]. It has the obvious advantage that it utilises data on the Euclidean axis, where the systematic errors are largely under control. However, due to the finite number of data points with finite precision, the reconstruction is an ill-conditioned problem and the choice of a method easily introduces biases and systematic errors, adding to the often large numerical uncertainties. Nevertheless, such reconstruction techniques have been employed very successfully in various situations. They are particularly useful for extrapolations of Euclidean data up to the first singularity in the complex plane, which makes them an invaluable tool for the extraction of bound-state masses from functional methods.

The second class is concerned with the direct computation of correlation functions in the complex plane. The singular structure of correlation functions can be avoided by deforming the integration contour of loop diagrams [48–50], or going to the Keldysh contour formulation of quantum field theory [51]. Alternatively, we can exploit the singularities by means of integral representations [52–54], which is the main approach we will follow throughout this thesis.

Spectral functional methods

The most prominent example of such an integral representation and the key tool of our work is the Källén-Lehmann (KL) representation [55, 56] of the propagator. In combination with functional, diagrammatic equations for the one particle irreducible (1PI) correlation functions, the use of integral representations allows for the direct and semi-analytic evaluation of loop integrals everywhere in the complex plane. In particular, for lower order correlation functions, this enables the development of efficient numerical solution strategies for direct real-time computations. Moreover, the direct relation of the KL-representation to the singularity structure of the theory offers insight into fundamental properties of the latter, such as causality and unitarity.

With this thesis, we aim to contribute to the understanding of non-perturbative and real-time quantum field theory and to work towards reliable approximations for phenomenological applications. To this end, we show how to compute spectral densities of elementary correlation functions self-consistently from non-perturbative diagrammatic equations like the DSE and the fRG. This allows us to discuss the causal structure of correlation functions, and to use them as input for the computation of observables like bound-state masses and properties. We will contextualise each of our projects at the beginning of the corresponding chapters and sections.

This thesis is structured as follows: in Chapter 2, we give a brief overview of QCD and discuss the basics of functional quantum field theory. Chapter 3 is dedicated to spectral functional methods. We discuss the KL-representation and real-time correlation functions, and introduce the Dyson-Schwinger equations and the Functional Renormalisation group. To make the latter compatible with the KL-representation, we introduce the renormalised Callan-Symanzik equation as the limit over finite Wetterich flows. In Chapter 4, we set up the computational framework and show how to compute spectral functions of elementary correlation functions. We start in Section 4.1 with the spectral flows in a scalar theory on both sides of a phase-transition. In Section 4.2, we use the spectral framework to solve the Bethe-Salpeter equation of a scalar bound state in the scaling limit for the first time directly on the real frequency axis. We also discuss the application to asymptotically safe quantum gravity, and show the first fully self-consistent graviton spectral function in Section 4.3. In Chapter 5, we turn to QCD and discuss the causal structure of the quark propagator in Section 5.1. We put special emphasize on the construction of a causal model for the quark gluon vertex, which is ready to use for phenomenological applications. The quark propagator is the key ingredient for the computation of bound-state properties, and we show in Section 5.2 how to utilize the quark spectral functions to compute hadron properties directly on the light-front, at the example of the pion distribution amplitude. We close the thesis in Chapter 6 with a summary and conclusion, where we discuss our results, the limitations, and prospects of our approach as well as future directions of research.

2. Quantum Chromodynamics

2.1. Quarks and gluons

This section is dedicated to a short theoretical overview on Quantum Chromodynamics (QCD), with a special emphasise on its key features. Our aim is to introduce the basic concepts, conventions and notation we will use and refer to troughout this thesis. The theory of strong interactions based on quarks as fundamental matter constituents was first proposed independently by Gellmann and Zweig in 1964 [57, 58]. They proposed fundamental SU(3)-triplets as fundamental particles, to explain the observed spectrum of mesons and baryons consisting of "up", "down" and "strange" quarks. The "charm" quark, to complete the second family of quarks, was suggested by Glashow and Bjorken in the same year [59] but its theoretical necessity was shown in 1970 with the discovery of the GIM mechanism [60]. The last two quarks, "bottom" and "top", were added by Kobayashi and Maskawa in 1973, [61].

To explain the existence of the Δ^{++} or Δ^{-} baryon, a new quantum number, later called "color", was introduced independently by Greenberg [62] and Han and Nambu [63]. These baryons consist in the quark model of three up or down quarks respectively, with all spins aligned. The overall anti-symmetry of the baryon wave function requires an additional quantum number. In 1973, the modern form of QCD as a local gauge theory for quark interactions was proposed and argued for by Fritzsch, Gell-Mann and Leutwyler [64], who used the framework of local gauge theories, developed by Yang and Mills in 1954 [65]. One of its striking features is asymptotic freedom, which was discovered by Gross, Wilczek and Politzer in the same year [66, 67]. This property implies that the strong coupling constant decreases if the theory is probed at higher energies, which allows not only for perturbative calculations at high energies but also renders QCD a valid theory for all energy scales. For a recent review on the theoretical and experimental aspects of QCD, see [9].

The classical QCD action is the sum of a gauged elementary matter part, and a Yang-Mills action that captures the dynamics of the gluon fields,

$$S_{\mathrm{QCD}}[\bar{q}, q, A] = S_{\mathrm{Matter}}[\bar{q}, q, A] + S_{\mathrm{YM}}[A]\,. \tag{2.1a}$$

For the matter action, we collect the different quark flavors in $q = (u, d, s, c, b, t)$ and denote the corresponding Dirac-conjugates by $\bar{q}$. The individual flavors are Dirac spinors in the fundamental representation of the gauge group SU(3). Suppressing all indices (color, flavor, spinor) and implicitly summing over all flavors, the matter action in Euclidean space-time reads

$$S_{\mathrm{Matter}}[\bar{q}, q, A] = \int_x \bar{q}\left(m_q + \not{D}\right) q\,, \qquad \int_x = \int d^4x\,, \tag{2.1b}$$

with the quark mass matrix $m_q = \mathrm{diag}(m_u, .., m_t)$. The renormalised values of the masses are summarised in Table 2.1. The interactions between the quarks are mediated by a gluon field A_μ, which lives in the adjoint representation of $SU(3)$. It couples to the quark through the covariant derivative $D_\mu = \partial_\mu - i g_s A_\mu$, where the strong coupling constant g_s controls the interaction. The Yang-Mills action, on the other hand, reads

$$S_{\mathrm{YM}}[A] = \int_x \frac{1}{4} F^a_{\mu\nu} F^a_{\mu\nu}\,, \quad \text{with} \quad F_{\mu\nu} = [D_\mu, D_\nu]\,, \tag{2.1c}$$

Throughout this work, we will use the slash notation for the contraction of a four-vector with the gamma matrices, $\not{D} = \gamma_\mu D_\mu$, where summation over repeated indices is tacitly

Flavor	Current quark mass	Electric charge
up	2.16 ± 0.07 MeV	2/3
down	4.70 ± 0.07 MeV	-1/3
strang	93.5 ± 0.8 MeV	-1/3
charm	1.2730 ± 0.0046 GeV	2/3
bottom	4.183 ± 0.007 GeV	-1/3
top	172.57 ± 0.29 GeV	2/3

Table 2.1.: Current quark masses from the Particle Data Group [68]. All but the top masses are obtained in the $\overline{\text{MS}}$-renormalisation scheme. The renormalisation point of the u-, d- and s-quark masses is $\mu = 2$ GeV, while the masses of the c-, and b-quarks are renormalised at their $\overline{\text{MS}}$-values, i.e. $\bar{m} = \bar{m}(\mu = \bar{m})$. For the top-quark, we cite the so called *Monte Carlo* mass. It is extracted from event-generator based reconstructions of measurements.

assumed. The Euclidean conventions are also used for the gamma matrices, $\{\gamma_\mu, \gamma_\nu\} = 2\delta_{\mu\nu}$.

The QCD action is locally invariant under the following (infinitesimal) gauge transformations,

$$q(x) \to (1 + \mathrm{i}\alpha)q(x)\,, \quad \bar{q}(x) \to \bar{q}(x)(1 - \mathrm{i}\alpha)\,, \tag{2.2}$$

$$A_\mu(x) \to A_\mu(x) - \frac{1}{g_s}\partial_\mu\alpha(x) - i\,[A_\mu(x), \alpha(x)]\;, \tag{2.3}$$

where $\alpha(x) = \alpha^a(x)t^a$ is an element of the algebra, which parametrises the gauge transformation $U(x) = \exp(\mathrm{i}\alpha)$. The generators t^a are the Gell-Mann matrices. Above and in the following we suppress color indices $\{a, b, c\}$, and only indicate them if necessary.

In the following paragraph, we give a short overview of the features of QCD and discuss their rôle in our work, before we delve into the theoretical groundwork in Section 2.3.

Asymptotic freedom. For short distances and accordingly large momentum transfer, the interaction between quarks (and gluons) becomes weak and approaches zero at the Gaussian fixed point in the UV-limit. This is a consequence of renormalisation, and is manifest in the negative beta function of QCD. While we will not directly compute the scale-dependent strong coupling in our work, its asymptotic decrease justifies perturbative calculations of correlation functions at high energies and momenta, and allows for reliable extrapolations in the UV, see e.g. Sections 3.1.2 and 5.1.7. Furthermore, asymptotic freedom explains the phenomenon of Bjorken scaling in deep inelastic scattering cross-sections, first predicted by Bjorken in [25] on the basis of the parton model and verified up to approximately 10% by the SLAC-MIT experiment [19]. It implies that the interactions between the constituents of the probed hadron can be ignored at high energies. We will give some more details on the running coupling in the following Section 2.3.

Confinement. The negative beta function also implies that the interaction strength increases at low energies and large distances, which gives rise to the phenomenon of confinement. This means that colored states are absent from the physical, measurable spectrum of the theory. Instead, quarks and gluons are confined to form color-neutral bound-states like hadrons or glue balls. The absence of asymptotic quarks or gluons manifests itself in the properties of their respective propagator spectral densities, see again Sections 3.1.2 and 5.1. The associated spectral functions are not positive semi-definite, and in general not normalisable. A proper resolution of confinement is still an open problem in Yang-Mills theory and QCD, and we do not attempt to solve it in this thesis. The phenomenon of confinement, however, is closely related to the dynamic generation of a mass gap for the gluons. The questions of the responsible mechanism and the associated complex structure of the gluon propagator are far from being settled, but at least for the former, suitable candidates such as the Schwinger mechanism, see e.g. [69–72], or the quartet mechanism, see e.g. [73] have been proposed. So far, no satisfying direct real-time computation of the gluon propagator has been achieved in QCD, and we will employ reconstructed spectral densities as input for our computations, see Section 5.1.2.

Dynamical chiral symmetry breaking. The second important infrared feature of QCD concerns the masses of quarks and hadrons. The current quark masses of the light flavors (up and down) are small compared to the masses of the lightest Baryons, which are of the order of $\propto 1$ GeV, see Table 2.1. This discrepancy is explained by the dynamical generation of quark masses through the spontaneous breaking of chiral symmetry (DχSB), which makes up for the largest amount of Baryon masses. Chiral symmetry is an axial $U(N_f)$, symmetry of the matter sector of the action in (2.1b), where N_f marks the number of quarks. The symmetry is explicitely explicitly broken by the quark masses. However, even in the limit of vanishing quark masses, chiral symmetry is broken spontaneously by the formation of a chiral condensate $\langle \bar{q}q \rangle \neq 0$ through the strong infrared dynamics. The associated formation of bound states, first and foremost the pions as massless Goldstone bosons of the broken symmetry, gives rise to the hadron structure of QCD. The non-vanishing expectation value then gives rise to quark masses through 4-quark interactions. For physical QCD, chiral symmetry is only an approximate symmetry, but the mechanism that drives the dynamics of DχSB is still present and dominates the low-energy properties of the theory and the structure of (light) hadrons. This identifies the pions as pseudo-Goldstone bosons with a non-vanishing mass $m_\pi \approx 135$ MeV for the neutral pions. In this thesis, we employ Iso-spin symmetric approximations and in general neglect QED effects, so that the three pions are degenerate. DχSB will be discussed in Section 5.1 in terms of the quark mass function. In Section 5.2, we will further discuss its implication for the hadron structure at the example of the pion distribution amplitude.

2.2. Correlation functions and observables

In this short interlude, we introduce the basic concepts and definitions of the functional approach to quantum field theory. We will mainly use the example of a scalar field theory, but the generalisation to arbitrary superfields is straight-forward. In quantum field theoretical descriptions of physical systems, the central objects that can be computed are correlation functions of the fields. They encode the quantum fluctuations of the field by means of a weighted average over all possible field configurations, described by the path integral. The expectation value of an operator $\mathcal{O}[\varphi]$, which is usually taken to be a polynomial in the quantum field φ, is given by

$$\langle \mathcal{O}[\varphi] \rangle = \frac{1}{\mathcal{N}} \int \mathcal{D}\varphi \, \mathcal{O}[\varphi] \, e^{iS[\varphi]} \, . \tag{2.4}$$

The weight of the path integral is given by the phase factor $e^{iS[\varphi]}$, where $S[\varphi]$ is the action of the theory in Minkowski spacetime. The normalisation factor $\mathcal{N}$ is chosen such that the expectation value of the identity operator is unity. Before we proceed, we need to address the question of the analytic continuation of the path integral to Euclidean spacetime. Although we are interested in real-time observables and correlation functions, we will formulate all functional relations of this work in the setting of Euclidean quantum field theory. Hence, we assume that it is always possible to perform the (inverse) Wick rotation from the Euclidean path integral to its real-time counterpart. The (inverse) Wick rotation interpolates between imaginary and real-time coordinates, $\tau \leftrightarrow \mathrm{i}t$, or equivalently $p_0 \leftrightarrow -\mathrm{i}\omega$ in the frequency domain. In the path integral, this amounts to $-S_E[\varphi] \leftrightarrow \mathrm{i}S[\phi]$, where the subscript $_E$ denotes the Euclidean action.

We start from the Euclidean path integral by introducing the partition function

$$Z[J] = \int \mathcal{D}\varphi \, e^{-S_E[\varphi] + J\cdot\varphi} \quad \text{with} \quad J\cdot\varphi = \int d^dx \, J(x)\varphi(x) \, , \tag{2.5}$$

which acts as a generating functional for the correlation functions of the fields φ. The expectation values of the field and higher moments can be obtained by functional derivatives with respect to the source J,

$$\langle \varphi(x_1)\dots\varphi(x_n) \rangle = \frac{1}{Z[J]} \frac{\delta^n Z[J]}{\delta J(x_1)\dots\delta J(x_n)}\bigg|_{J=0} \, . \tag{2.6}$$

In practice, we will never compute the partition function or the respective moments directly, as they carry redundant information. Instead, we will compute connected correlation functions, indicated by the subscript $_c$, and in particular their 1-particle irreducible (1PI) parts. The connected correlation functions are the cumulants of the theory, and are generated by the Schwinger functional:

$$W[J] = \log Z[J] \, , \quad \text{with} \quad \langle \varphi(x_1)\dots\varphi(x_n) \rangle_c = \frac{\delta^n W[J]}{\delta J(x_1)\dots\delta J(x_n)}\bigg|_{J=0} \, . \tag{2.7}$$

The first two cumulants, i.e., the mean field and the connected two-point function or propagator, are particularly important for functional computations and deserve their own notation. They read

$$\phi(x) = \langle \varphi(x) \rangle \quad \text{and} \quad G(x,y) = \langle \varphi(x)\varphi(y) \rangle_c \, . \tag{2.8}$$

Both depend implicitly on the source J, if it is not taken to zero. We will make the J dependence explicit with a subscript $_J$.

So far, we have not specified the fields φ or the action $S[\varphi]$. It is convenient to adopt a super-field notation, which collects all fields that could be present in a superfield ϕ_a. Then, the mean field carries a field index $_a$ and the propagator carries two field indices $_a$ and $_b$. All following derivations can be carried out within the super-field formalism, but we will stick to a scalar field theory for simplicity and merely quote the respective results for the general case if necessary.

All computations in this work are carried out in translationally invariant settings. This implies that the mean field is constant at vanishing source, and the two-point function depends only on the difference of the coordinates, $G(x, y) = G(x - y)$. The propagator then reads in momentum space

$$G(p, q) = G(p)\delta(p + q)(2\pi)^d \,, \quad \text{with} \quad G(x - y) = \int \frac{d^d p}{(2\pi)^d}\, e^{-ip(x-y)} G(p) \,. \tag{2.9}$$

The propagators of the QFT at hand and its analytic properties will play the central rôle of this thesis, and we will discuss them in detail in the next section Section 3.1.

The importance of propagators for functional approaches shows in the functional identity for the expectation value of a local operator $\mathcal{O}[\varphi]$ in the presence of a source. To derive it, we start with the expectation value of a monomial in the field,

$$\frac{1}{Z[J]} \frac{\delta^n Z[J]}{\delta J(x_1) \dots \delta J(x_n)} = \left(\phi(x_1) + \frac{\delta}{\delta J(x_1)} \right) \frac{1}{Z[J]} \frac{\delta^{n-1} Z[J]}{\delta J(x_2) \dots \delta J(x_n)} \,, \tag{2.10}$$

where we have used the product rule to pull out the derivative with respect to $J(x_1)$. By iteration, all derivatives can be pulled in front of the normalisation factor, which eventually cancels out to arrive at

$$\langle \varphi(x_1) \dots \varphi(x_n) \rangle_J = \left(\phi(x_1) + \frac{\delta}{\delta J(x_1)} \right) \dots \left(\phi(x_n) + \frac{\delta}{\delta J(x_n)} \right) . \tag{2.11}$$

For the last step, we use that local operators can be expanded in monomials in the fields and its derivatives, and that we can use the chain rule to convert the derivatives with respect to the source to derivatives with respect to the mean field. This leads to

$$\langle O[\varphi] \rangle_J = O\left[\phi + G \cdot \frac{\delta}{\delta \phi} \right] \,, \tag{2.12}$$

where both the mean field and the propagator depend on J implicitly. As a consequence of (2.12), we can express expectation values of operators, which contain only finite powers of the field, in terms of a finite amount of diagrams over full propagators and vertices. We will use (2.12) in Sections 3.2.1 and 3.2.2, to derive the functional equations we will use throughout this work.

To close this section, we introduce the 1PI effective action, which allows us to compute the successive field derivatives of the propagator that appear in (2.12). It is defined as the Legendre transform of the Schwinger functional with respect to the source,

$$\Gamma[\phi] = \sup_J \, J \cdot \phi - W[J] = J_{\text{sub}} \cdot \phi - W[J_{sub}] \,. \tag{2.13}$$

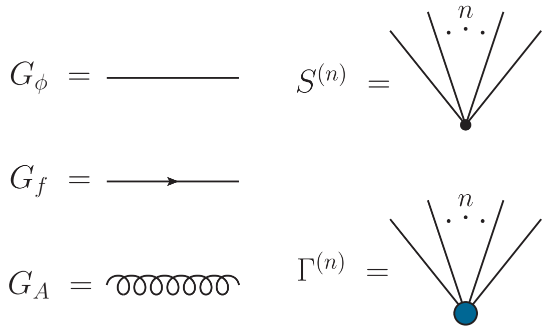

Figure 2.1.: Diagrammatic notation for the relevant fields in this thesis. Full propagators for scalars are denoted by solid lines, solid lines with arrows represent fermions and gluon propagators are represented by curled lines. 1PI n-point vertices are denoted by a vertex with n legs. Full vertices are big blue dots while classical vertices are small, black dots.

The 1PI effective action now depends only on the mean field ϕ, and, by construction, acts as an action for the quantum theory,

$$\frac{\delta\Gamma[\phi]}{\delta\phi(x)} = J(x)\,. \tag{2.14}$$

The source on the right-hand-side depends on the mean field implicitly. At vanishing source, we recover the full quantum equation of motion for the expectation value of the field.

We will refer to the successive functional derivatives of $\Gamma[\phi]$,

$$\frac{\delta^n\Gamma[\phi]}{\delta\phi(x_1)\dots\delta\phi(x_n)} = \Gamma^{(n)}(x_1\dots x_n)\,, \tag{2.15}$$

as full n-point vertices. For the diagrammatic notation see Figure 2.1. To finally work out general diagrammatic relations, we use that $\Gamma^{(2)}$ is nothing but the inverse propagator,

$$(\Gamma^{(2)}\cdot G)(x_1,x_2) = \int_x \frac{\delta^2\Gamma[\phi]}{\delta\phi(x_1)\,\delta\phi(x)}\frac{\delta^2 W[J]}{\delta J(x)\,\delta J(x_2)} = \int_x \frac{\delta J(x)}{\delta\phi(x_1)}\frac{\delta\phi(x_2)}{\delta J(x)} = \delta(x_1-x_2)\,. \tag{2.16}$$

This allows us to compute the field derivatives of the propagator, which appear in (2.12):

$$\frac{\delta G(x_1,x_2)}{\delta\phi(x_3)} = -\int_{y_1,y_2} G(x_1,y_1)\Gamma^{(3)}(y_1,x_3,y_2)G(y_2,x_2)\,. \tag{2.17}$$

With this, we have established the connection between the 1PI n-point vertices and connected correlators of the fields.

2.3. Gauge fixing, Renormalisation and Scattering

We will now return to (functional) QCD, and discuss its theoretical foundations. We will start with the gauge fixing procedure in Section 2.3.1. This allows us to introduce and discuss the covariant Landau gauge, which is typically employed in functional computations. In Section 2.3.2, we will give an overview on the renormalisation of QCD and in particular discuss the anomalous UV-running of the correlation functions we are interested in, namely quark, gluon, and ghost propagators and respective vertices.

To quantise the theory, we consider the Euclidean path integral of QCD,

$$Z_{\mathrm{QCD}} = \int \mathcal{D}\bar{q}\,\mathcal{D}q\mathcal{D}A\, e^{-S_{\mathrm{QCD}}[\bar{q},q,A]}\,. \tag{2.18}$$

Correlation functions are then defined by the insertion of the respective operator in the path integral, and the division by Z_{QCD}, for more details, see Section 2.2. There are different approaches to compute these correlation functions, but they can be roughly divided into two classes: continuum methods, like perturbation theory or functional methods, and the lattice approach. In the latter, spacetime is discretised on a lattice, and the path integral reduces to a finite- but high-dimensional integral that can be solved numerically. One of the main advantages of lattice QCD, or rather lattice gauge theories, is that it can be formulated in gauge-invariant link variables, where the integration over the group elements can be carried out without gauge fixing. Continuum methods, on the other hand, operate in the group algebra, and the corresponding path integral contains the integration over an infinite number of physically equivalent configurations. This prohibits a naive definition of the gluon propagator. To overcome this, one has to fix the gauge by choosing one representative per gauge orbit.

2.3.1. Gauge fixed QCD

The gauge fixing is solely concerned with the Yang-Mills part of the action, and we will follow the standard Fadeev-Popov procedure, which eventually leads to an additional gauge fixing term in the action, and the introduction of the Faddeev-Popov ghosts. The basic idea of this procedure is the introduction of a gauge-fixing constraint by inserting a 1 into the path integral, which allows to factor out and hence cancel the additional gauge-orbit integration when computing correlation functions via (2.6). As a last disclaimer: we will not discuss the intricacies and conceptual difficulties of non-perturbative gauge fixing, such as the problem of Gribov copies [74], as the associated question on the IR-closure of YM-theories is not relevant for most of our computations.

To fix the gauge, one can introduce the following representation of unity in the path integral,

$$1 = \int \mathcal{D}\alpha\, \delta\left(\mathcal{F}(A)\right) \det\left(\frac{\delta \mathcal{F}(A)}{\delta\alpha}\right)\,,$$

where $F(A) = 0$ realises the gauge fixing condition, and α parametrises a finite gauge transformation. For gauge fixing conditions linear in the gauge field, the Faddeev-Popov determinant does not depend on α. This, together with the gauge invariance of the measure and the action, entails that the integration over the group, $\int_{\mathcal{D}} \alpha$ can be factored out of the functional integral as a global normalisation. For observables, which are represented by gauge invariant, local operators, their insertion into the path integral does not change this property. Hence, the global normalisation drops out and the expectation value of an observable reads

$$\langle \mathcal{O} \rangle = \frac{\int \mathcal{D}\bar{q}\,\mathcal{D}q\mathcal{D}A\,\mathcal{O}[\bar{q},q,A]\,\delta\left(\mathcal{F}(A)\right)\det\left(\frac{\delta\mathcal{F}(A)}{\delta\alpha}\right)\,e^{-S_{\text{QCD}}[\bar{q},q,A]}}{\int \mathcal{D}\bar{q}\,\mathcal{D}q\mathcal{D}A\,\delta\left(\mathcal{F}(A)\right)\det\left(\frac{\delta\mathcal{F}(A)}{\delta\alpha}\right)\,e^{-S_{\text{QCD}}[\bar{q},q,A]}}\,.$$

For generalised ξ-gauges, we choose $\tilde{\mathcal{F}}(A) = \mathcal{F}(A) - C$ with a Gaussian average over C,

$$\delta\left(\mathcal{F}(A)\right) \to \int \mathcal{D}C\,\exp\left(-\frac{1}{2\xi}\int_x C^a C^a\right)\delta\left(\mathcal{F}(A) - C\right) = \exp\left(-\frac{1}{2\xi}\int_x \mathcal{F}(A)^a\mathcal{F}(A)^a\right)\,.$$

For $\xi = 0$, the Gaussian weight collapses to the original gauge fixing. To bring the Fadeev-Popov determinant into a form that is more amenable to computations, one introduces auxiliary Grassman fields in the adjoint representation of the group, the Faddeev-Popov ghosts c and $\bar{c}$. This allows to represent the determinant as a functional integral,

$$\det\left(\frac{\delta\mathcal{F}(A)}{\delta\alpha}\right) = \int \mathcal{D}c\,\mathcal{D}\bar{c}\,\exp\left(\int_x \bar{c}\,\frac{\delta\mathcal{F}(A)}{\delta\alpha}\,c\right)\,.$$

For the linear covariant gauge, $\mathcal{F}(A) = \partial_\mu A_\mu$, which is usually employed in functional QCD computations, the Fadeev-Popov operator is $\frac{\delta\mathcal{F}(A)}{\delta\alpha} = -\partial_\mu D_\mu$, up to global factors which are absorbed in the normalisation. The gauge fixed QCD action now reads

$$S_{\text{QCD}}[\bar{q},q,\bar{c},c,A] = S_{\text{Matter}}[\bar{q},q,A] + S_{\text{YM}}[A] + S_{\text{GF}}[A] + S_{\text{FP}}[A,c,\bar{c}]\,, \tag{2.19}$$

with

$$S_{\text{GF}}[A] = \int_x \frac{1}{2\xi}\left(\partial_\mu A_\mu\right)^2 \quad \text{and} \quad S_{\text{FP}}[A,c,\bar{c}] = -\int_x \bar{c}\left(\partial_\mu D_\mu\right)c\,.$$

The generating functional of gauged fixed QCD takes the form

$$Z_{\text{QCD}}[\eta_q,\bar{\eta}_q,\eta_q,\bar{\eta}_q,J_A] = \int \mathcal{D}\bar{q}\,\mathcal{D}q\bar{c}\,\mathcal{D}c\mathcal{D}A\,e^{-S_{\text{QCD}}[\bar{q},q,\bar{c},c,A]+\int_x(\bar{q}\cdot\eta_q - \bar{\eta}_q\cdot q + \bar{c}\cdot\eta_c - \bar{\eta}_c\cdot c + J_A\cdot A)}\,. \tag{2.20}$$

This allows to read off the classical inverse propagators from the quadratic parts of the action. Their inversion leads to the classical propagators,

$$G^{\mu\nu}_{A,cl}(p,q) = (2\pi)^4\delta(p+q)\Pi_\xi(p)\frac{1}{p^2}\,, \quad \text{with} \quad \Pi^{\mu\nu}_\xi(p) = \delta^{\mu\nu} - (1-\xi)\frac{p^\mu p^\nu}{p^2}\,,$$

$$G_{c,cl}(p,q) = (2\pi)^4\delta(p+q)\frac{1}{p^2}\,, \quad G_{q,cl}(p,q) = (2\pi)^4\delta(p+q)\frac{1}{\mathrm{i}\not{p} + m_q}\,. \tag{2.21}$$

The form of the gluon propagator entails that the specific choice of $\xi = 0$, the Landau gauge, leads to a fully transverse gluon propagator, $\Pi_{\xi=0} = \Pi$. Crucially, this property persists in the full quantum theory. It is ensured by the non-perturbative Slavnov-Taylor identity for the gluon propagator, viz.

$$p_\mu\left\langle A_\mu(p)A_\nu(q)\right\rangle = \xi\,\delta^{ab}\,\frac{p_\nu}{p^2}(2\pi)^4\delta(p+q)\,. \tag{2.22}$$

In Landau gauge, the transversality of the gluon propagator leads to a decoupling of the transverse and longitudinal parts of the system, which makes it a convenient choice for systematic truncations and numerical computations. Indeed, most of the non-perturbative, functional computations are performed in the Landau gauge, and we will adopt this choice in our work as well. For a more detailed discussion of the propagators beyond the classical level, we refer to Section 5.1.2.

2.3.2. The running coupling

(Gauge-fixed) QCD contains a number of UV-relevant parameters, which are subject to renormalisation. These include wave-function renormalisations of all fields Z_ϕ, associated with the respective kinetic operators, the strong coupling constant g_s and the quark masses m_q. Gauge invariance, or rather the invariance of the gauge-fixed action under BRST transformations, dictates that the renormalisation of the vertices is fully determined by the wave-function renormalisations of the fields and the renormalisation constant of the strong coupling. Schematically, this is expressed by

$$Z_g = \frac{Z_{\phi_{i_1}..\phi_{i_n}}}{Z^{\frac{1}{2}}_{\phi_{i_1}}..Z^{\frac{1}{2}}_{\phi_{i_n}}}\,, \tag{2.23}$$

where the $Z_{\phi_{i_1}..\phi_{i_n}}$ are the renormalisation constants of the vertices in the classial action, i.e.. $Z_{\bar{q}qA}, Z_{\bar{c}cA}, Z_{A^3}, Z_{A^4}$ and the wave function renormalisations of fields relate the bare and renormalised fields by $\phi_{i,0} = \sqrt{Z_{\phi_i}}\phi_{\text{i,ren}}$. For the parameter we have analogously $(g_0, \xi_0, m_{q,0}) = (Z_g g, Z_\xi \xi, Z_{m_q} m_q)$. For a more detailed discussion, see also [75, 76].

The renormalisation constants are eventually fixed at a certain renormalisation point μ. The independence of the theory on the latter is encoded in the Callan-Symanzik (CS) equation, which simply states that the dependence of correlation functions on the renormalisation scale vanishes, in the case of an observable $\mathcal{O}$, this leads to

$$\mu\frac{d}{d\mu}\mathcal{O} = \left(\mu\partial_m u + \beta_g\partial_g + \gamma_{m_q}\partial_{m_q}\right)\mathcal{O} = 0\,. \tag{2.24a}$$

Here, we have defined the beta function, and anomalous mass dimension

$$\beta_g = \mu\frac{dg}{d\mu} = -\mu\frac{dZ_g}{d\mu} \quad \text{and} \quad \gamma_{m_q} = \frac{dm_q}{d\mu}. \tag{2.24b}$$

In (2.24a), we already used that observables, as for example cross-sections or scattering amplitudes, do not depend on global rescaling of the fields. General correlation functions also carry the dependence on the wave function renormalisations of the fields, and the associated CS-equation contains the respective anomalous dimensions γ_{ϕ_i}. See also Section 3.3.2 for a thorough discussion. If we consider asymptotically large energy scales that exceed the highest mass scale of the theory - in full QCD this is the top-quark mass - we can even neglect the quark masses and simply set $\gamma_{m_q} = 0$ in (2.24a). Then, the CS equation states that a shift in the renormalisation scale can be compensated by an appropriate change in the coupling constant. With (2.23), there are several ways to compute the beta function from the μ dependence of one of the vertices in combination with the respective wave function renormalisations of the attached legs. We simply quote the one-loop result here for arbitrary number of colors and flavors,

$$\beta_g^{\text{one-loop}} = -\frac{g^3}{16\pi^2}\beta_0, \quad \text{with} \quad \beta_0 = \left(\frac{11}{3}N_c - \frac{2}{3}N_f\right)\,. \tag{2.25}$$

We can integrate the beta function to obtain the running coupling. In terms of the strong coupling constant $\alpha_s = g^2/4\pi$, the solution reads

$$\alpha_s(\mu) = \frac{\alpha_s(\mu_0)}{1 + \frac{\beta_0}{4\pi}\alpha_s(\mu_0)\log(\frac{\mu^2}{\mu_0^2})} \,. \tag{2.26}$$

It is important to note that experiments cannot measure a dependence on some arbitrary renormalisation scale. What is measurable, is the momentum dependence of couplings which are associated with certain processes, e.g. $\bar{q}q \to \bar{q}q$ scattering, mediated by a gluon. Its Matrix element can be used to define a momentum dependent running coupling,

$$\alpha_s(p^2) = \frac{g_s(p^2)^2}{4\pi} \approx p^2 M_{\bar{q}q\to\bar{q}q}(p^2) \,, \tag{2.27}$$

where p^2 is the momentum transfer carried by the gluon. At large energies, the right-hand side of (2.27) satisfies the CS equation (2.24a) and can only depend on dimensionless parameters $\alpha_s(p^2) = \alpha_s(p^2/\mu^2, \alpha_{s,ren}(\mu))$. This also entails

$$\alpha_s(p^2) = \alpha_s(1, \alpha_{s,ren}(\mu^2 = p^2)) \,,$$

if we choose to match the renormalisation scale and the momentum transfer. Hence, the momentum dependence of the physical running coupling (2.27) is nothing but the μ-dependence of the running coupling (2.26),

$$\alpha_s(p^2) = \frac{\alpha_s(\mu^2)}{1 + \frac{\beta_0}{4\pi}\alpha_s(\mu^2)\log(\frac{p^2}{\mu^2})} = \frac{4\pi}{\beta_0}\frac{1}{\log(\frac{p^2}{\Lambda_{\mathrm{QCD}}})} \,. \tag{2.28}$$

The second equation in (2.28) makes the independence on μ manifest. The necessary scale is provided by the physical and RG-invariant Λ_{QCD}. In perturbation theory, this scale sets the location of the IR Landau pole. In general, it is the scale where the running coupling becomes non-perturbative and triggers DχSB and the dynamical generation of a gluon mass gap.

We close this section with a brief discussion on the anomalous running of the quark, ghost, and gluon propagators in the Landau gauge at one loop. A convenient parametrisation of the inverse propagators reads

$$\Gamma^{(\bar{q}q)}(p) = Z_q(p^2)\left(\mathrm{i}\not{p} + M_q(p^2)\right), \quad \Gamma^{(c\bar{c})}(p) = p^2 Z_c(p^2), \quad \Gamma^{(AA)}_{\mu\nu}(p) = \Pi_{\mu\nu}(p)p^2 Z_A(p^2) \,. \tag{2.29}$$

The momentum dependence of the dressings in the UV is determined by the respective anomalous dimensions,

$$Z_A(p^2) \to Z_A^{\mathrm{UV}}\log(\hat{p}^2)^{\gamma_A} \,, \quad Z_c(p^2) \to Z_c^{\mathrm{UV}}\log(\hat{p}^2)^{\gamma_c} \,, \quad M_q(p^2) \to m_q\left(\frac{\log\left(\hat{\mu}^2\right)}{\log\left(\hat{p}^2\right)}\right)^{\gamma_{m_q}} , \tag{2.30}$$

where the $\hat{p}$ and $\hat{\mu}$ are measured in units of Λ_{QCD}. Note that in Landau gauge, the wave function renormalisation of the quark field vanishes at one loop, see also Appendix A.4.2, and the ghost-gluon vertex stays unrenormalised, even beyond one loop, $Z_{\bar{c}cA} = 1$. The anomalous dimensions are given by

$$\gamma_A = \frac{1}{\beta_0}\left(\frac{13N_c}{6} - \frac{4N_f}{6}\right), \quad \gamma_c = \frac{1-\gamma_A}{2}, \quad \gamma_{m_q} = \frac{3C_F}{\beta_0}, \tag{2.31}$$

where $C_F = (N_c^2 - 1)/(2N_c)$ is the Casimir operator of the fundamental representation of $SU(N_c)$. Together with (2.23), the non-renormalisation of the ghost-gluon vertex and the quark wave function also entails that the large momentum behaviour of the quark-gluon vertex is proportional to the ghost dressing function. This is as well a consequence of the Slavnov-Taylor identity for the quark-gluon vertex, see Appendix A.4.1, and we will use it to construct a causal vertex model for the quark-gluon vertex in Section 5.1.

3. Spectral functional methods

In this chapter, we explain the spectral functional framework that we use to compute real-time correlation functions and dynamic observables. The central ingredient for our discussion are spectral representations for elementary correlation functions and composites. We will introduce them in Section 3.1, where we review the connection of Euclidean correlators with their real-time counterparts. We proceed in Section 3.2 by deriving the functional relations that we use throughout this work to compute expectation values of operators. This includes the Dyson-Schwinger equations (DSE) and the standard Wetterich type functional Renormalisation Group (fRG). For the latter, the presence of the regulator function alters the propagator of the theory and can invalidate the Källén-Lehmann representation. The only known regulator that ensures both, causality and Lorentz invariance is the Callan-Symanzik (CS) regulator, given by a momentum independent mass term. While the ad-hoc implementation of the CS-regulator preserves the causal structure of the propagator and Lorentz invariance, it would sacrifice a priori UV-finiteness of the flow equation. In Section 3.3, we show how to consistently derive the manifestly finite, renormalised Callan-Symanzik equation (3.48) as the limit over UV-finite flow equations. The remainder of this limit is the counter term action. It can be exploited to fix flowing renormalisation conditions, what facilitates computations. Finally, we discuss the spectral form and renormalisation of functional diagrammatic relations in Section 3.4.

3.1. Spectral representations and analytic continuations

This section is in parts based on [1].

In this section, we review the relevant aspects of spectral representations of correlation functions, with a special focus on the spectral representation of propagators. We discuss the necessary conditions for the existence of a Källén-Lehmann representation [55, 56] and its form both in vacuum and at finite temperature and density. In Section 3.1.2, we proceed with the relation to the canonical commutation relations, which impose sum-rules on the spectral functions.

3.1.1. Propagator spectral functions

As we have seen in the previous section, the propagator plays the central rôle for the computation of expectation values. It encodes the quantum fluctuations of the field, and often carries the most relevant information about the physical states of the theory. In this section, we will not restrict ourselves to the propagator of a fundamental scalar field theory, but consider the general case of a two-point function, often referred to as Green's function, of a composite (bosonic) operator $\Phi[\phi]$. There are various ways to choose a Green's function, which are all equivalent in equilibrium and only depend on the integration contour of the time variable in the complex plane. For a thorough discussion, see e.g., [77].

In our case, it suffices to discuss the relation between the Euclidean propagator, as defined in (2.9), and the advanced and retarded propagators. We define the latter with respect to real-time coordinates, and denote the respective space-time or momentum variable with capital letters. With $X^0 = t$ and $P_0 = \omega$, the advanced and retarded Green's functions read

$$\begin{aligned} G^R_\Phi(P) &= \mathrm{i}\int_X e^{\mathrm{i}PX}\langle\, [\Phi(X),\Phi^\dagger(0)]\,\theta(-t)\,\rangle_c\,, \\ G^A_\Phi(P) &= \mathrm{i}\int_X e^{\mathrm{i}PX}\langle\, -[\Phi(X),\Phi^\dagger(0)]\,\theta(t)\,\rangle_c\,. \end{aligned} \tag{3.1}$$

The step function $\theta(\pm t)$ leads to exponential suppression of the integrals for $\mathrm{Im}\,\omega \gtrless 0$, which allows to close the contour in the upper or lower half-plane, and leads to analyticity of the Green's functions in the respective frequency domains. Both correlators are related by a mirror symmetry along the real frequency axis, $G^*_R(\omega^*,\vec{p}) = G_A(\omega,\vec{p})$. A propagator is causal, if all discontinuities, as for example poles and cuts, are located on the at $\mathrm{Im}\,\omega = 0$. These discontinuities turn out to be the spectral function ρ_Φ. It is defined as

$$\rho_\Phi(P) = \int_X e^{\mathrm{i}PX}\langle\, [\Phi(X),\Phi^\dagger(0)]\,\rangle_c\,. \tag{3.2}$$

We proceed by discussing the relations between the different propagators and the spectral function. By inserting the Fourier decomposition of the step function,

$$\theta(t) = \frac{1}{2\pi}\int_{-\infty}^{\infty}\frac{d\omega}{\omega - \mathrm{i}0^+}e^{-\mathrm{i}\omega t}\,, \tag{3.3}$$

where $f(0^+) = \lim_{\epsilon \searrow 0} f(\mathrm{i}\epsilon)$. Assuming that the spectral function decays sufficiently fast for large frequencies, we immediately find a spectral representation for the advanced and retarded propagators,

$$G_\Phi^{A/R}(P) = \int_{-\infty}^{\infty} \frac{d\lambda}{2\pi} \frac{\rho_\Phi(\lambda, \vec{p})}{\lambda - \omega \pm \mathrm{i}0^+}\,, \quad \text{with} \quad \rho_\Phi(\omega, \vec{p}) = 2\mathrm{Im}\, G_\Phi^R(\omega, \vec{p})\,. \tag{3.4}$$

If the decay behaviour is not sufficiently fast, one can either assume a UV cutoff or consider a subtraction scheme to make the spectral integral finite. For similar representations, see the (subtracted) Kramers-Kronig relations (A.138) and (A.140).

The non-trivial Källén-Lehmann spectral representation further relates the Euclidean propagator to the spectral function, and hence to the retarded and advanced Green's functions. For it to exist, the propagator must satisfy the causality condition, which restricts all non-analyticities of the function to lie on the real frequency axis. Then, one can perform the (inverse) wick rotation to connect the Euclidean propagator to its real-time pendant. The Källén-Lehmann representation then reads

$$G(p_0, \vec{p}) = \int_{-\infty}^{\infty} \frac{d\lambda}{2\pi} \frac{\rho_\Phi(\lambda, \vec{p})}{\lambda - \mathrm{i}p_0}\,. \tag{3.5}$$

In the finite temperature case, the Euclidean propagator is only defined on the discrete Matsubara frequencies.This amounts to the replacement $p_0 \to p_n = 2\pi T n$ for bosonic operators. For fermionic operators, the spectral function is defined via the anti-commutator of the operators instead of the commutator, courtesy to the anti-commuting nature of the fields. Then, all relations carry over with the appropriate sign changes under commutation. The fermionic Matsubara frequencies are $\tilde{p}_n = \pi T(2n + 1)$.

The Källén-Lehmann representation also makes the relation between the Euclidean and the real-time propagators explicit:

$$G_\Phi^{A/R}(\omega, \vec{p}) = G_\Phi(p_0 \to -\mathrm{i}\omega^\mp, \vec{p})\,, \tag{3.6}$$

where $\omega^\mp = \omega \mp \mathrm{i}0^+$ denotes the advanced and retarded limit respectively.

To close this subsection, we discuss the situation in Lorentz invariant settings, where the spectral representations simplify significantly and focus on the different fundamental fields. By definition, the spectral function carries the same index structure as the propagator of the associated operator. Hence, one can associate one spectral function to each linearly independent tensor structure that has a non-vanishing overlap with the respective propagator. For a single scalar field, the manifestly Lorentz invariant spectral representation (of the Euclidean propagator) reads

$$G(p) = \int_0^{\infty} \frac{d\lambda\, \lambda}{\pi} \frac{\rho(\lambda)}{\lambda^2 + p^2}\,. \tag{3.7}$$

To arrive at this form, we went to the rest frame $\vec{p} = 0$ and dropped the explicit dependence on the spatial momentum $\rho(\lambda) = \rho(\lambda, \vec{p} = 0)$. After multiplying and dividing by the complex conjugate of the denominator, we can use the anti-symmetry of the spectral function, $\rho(-\lambda) = -\rho(\lambda)$ to see that only the term proportional to λ survives under the symmetric integration. The symmetry relations between positive and negative frequencies are violated at finite densities. The location of the fermi surface at non-vanishing frequencies leads to an asymetry of positive and negative frequencies in loop diagrams, which directly translates to the corresponding spectral functions.

Under the assumptions of locality and causality, spectral representations also exist for higher n-point functions, see e.g., [77, 78]. The spectral functions of the propagators takes a special rôle, as they encode the spectrum of the theory. If the fundamental field is associated with an asymptotic state that can be attributed to states in the physical Hilbert space, the spectral representation can be derived by inserting a complete set of energy eigenstates between the field operators. The resulting spectral function is then nothing but the (squared) projection onto the respective energy eigenstate. It is then normalised to one and positive definite. In gauge theories, the situation is more complicated, as the fundamental fields and the respective propagators are not gauge-invariant. For more details on the weight of the spectral function see Section 3.1.2.

For Dirac fermions in Lorentz invariant settings, the propagator has two linearly independent tensor structures, $\not{p}$ and $\mathbb{1}$. The associated spectral representation reads

$$G_f(p) = -\mathrm{i}\not{p}\, G_f^d(p) + G_f^s(p) = \int_{-\infty}^{\infty} \frac{d\lambda}{2\pi} \frac{\rho_f(\lambda)}{\mathrm{i}\not{p} + \lambda}\,, \tag{3.8}$$

where the spectral functions of the scalar and Dirac part of the quark propagator $\rho_f^{(s/d)}$ are given by the antisymmetric and symmetric parts of the quark spectral function ρ_f, respectively. They are defined via the imaginary part of the retarded propagator on the real frequency axis as

$$\begin{aligned} \rho_f^{(d)}(\omega) &= 2\omega\, \mathrm{Im}\, G_f^d(p_0 \to -\mathrm{i}\omega_+)\,, \\ \rho_f^{(s)}(\omega) &= 2\, \mathrm{Im}\, G_f^s(p_0 \to -\mathrm{i}\omega_+)\,. \end{aligned} \tag{3.9}$$

At finite temperature or density, such a compact form is no longer possible, as both break Lorentz symmetry. Instead, as for the propagator, the dirac spectral function is split into a spatial a temporal part

$$G_f(p_0, \vec{p}) = \int_{-\infty}^{\infty} \frac{d\lambda}{2\pi} \frac{\gamma_0 p_0\, \rho_f^0(\lambda, \vec{p}) + \vec{\gamma}\cdot\vec{p}\, \rho_f^v(\lambda, \vec{p}) + \lambda \rho_f^s(\lambda, \vec{p})}{\lambda - \mathrm{i}p_0}\,, \tag{3.10}$$

where chose a form such, that all spectral functions have mass dimension -2. The spectral representations can also be generalised to propagators of higher spin fields, where one simply has to consider an independent spectral function for each tensor structure of the chosen decomposition. We defer further discussions on this to Section 4.3 for the graviton, and to Section 5.1 for the gluon spectral function.

3.1.2. Spectral sum rules and asymptotic behaviour

For the two-point function of asymptotic states, the spectral function is positive semidefinite and normalised to unity, if the states are normalised. In general, this is not the case, since (3.4) and (3.5) are mere statements about the causal propagation of the associated operator.

The KL spectral representation (3.7) links the infrared asymptote for $\lambda \to 0$ and its ultraviolet asymptote for $\lambda \to \infty$ to the IR and UV behaviour of the Euclidean propagator. This also fixes its normalisation. These properties are discussed and verified in detail in

[43, 79–81]. The UV or IR asymptotic behaviour of the dimensionless Euclidean propagator can be parametrised as

$$\hat{G}_\phi(p^2 \to \mathrm{UV/IR}) = \frac{Z_\phi}{\hat{p}^2} \frac{\hat{p}^\eta}{(\log \hat{p}^2)^\gamma} \,, \tag{3.11}$$

with the dimensionless momentum squared $\hat{p}^2 = p^2/m_{\mathrm{gap}}^2$ and some reference scale m_{gap}. In the UV limit one has the parameters $Z_{\phi,\mathrm{UV}}$, η_{UV}, γ_{UV}, and in the IR $Z_{\phi,\mathrm{IR}}$, η_{IR}, γ_{IR}.

This general asymptotic form of the propagator includes a power behaviour arising from the anomalous dimension η besides the canonical power -2, as well as a logarithmic dependence, see e.g., [43, 79, 80] for details. For some non-local theories, the propagator shows an exponential decay behaviour [79], which is not taken into account here. With (3.11) and the definition of the spectral function (3.4), the UV asymptote of the spectral function for nonvanishing η_{UV} or γ_{UV} reads

$$\lim_{\hat{\omega}\to\infty} \hat{\rho}(\hat{\omega}) = \frac{Z_{\phi,\mathrm{UV}}}{\hat{\omega}^2} \frac{2\hat{\omega}^{\eta_{\mathrm{UV}}}}{(\log \hat{\omega}^2)^{\gamma_{\mathrm{UV}}}} \left(\sin\left[\frac{\pi}{2}\eta_{\mathrm{UV}}\right] - \cos\left[\frac{\pi}{2}\eta_{\mathrm{UV}}\right] \frac{\pi\gamma_{\mathrm{UV}}}{\log \hat{\omega}^2} \right) , \tag{3.12}$$

For $\eta_{\mathrm{UV}} = 0$, $\gamma_{\mathrm{UV}} = 0$ we have $\lim_{\hat{\omega}\to\infty} \hat{p}^2 \log(\hat{p}^2) \hat{\rho}(\hat{\omega}) \to 0$, what entails a normalisable spectral function with

$$\int_0^\infty d\lambda \, \lambda \, \rho_\phi(\lambda) = Z_{\phi,\mathrm{UV}} \,. \tag{3.13a}$$

This is usually refered to as spectral sum rule and is in one-to-one correspondence with the commutation relations $[\phi(t,\vec{x}), \partial_t \phi(t,\vec{y})] = Z_{\phi,\mathrm{UV}} \delta(\vec{x}-\vec{y})$. The standard normalisation is obtained for $Z_{\phi,\mathrm{UV}} = 1$, which entails canonical commutation relations.

In turn, for $\eta_{\mathrm{UV}} < 0$ or $\gamma_{\mathrm{UV}} > 0$ the UV-tail of the spectral function is negative, and the respective field does not describe an asymptotic state. Moreover, the spectral function is normalised to zero,

$$\int_0^\infty d\lambda \, \lambda \, \rho_\phi(\lambda) = 0 \,. \tag{3.13b}$$

In QCD this is the well-known Oehme-Zimmermann super convergence property [82, 83] for the gluon in the covariant Landau gauge, see also [43]. In asymptotically safe gravity it holds true as well for the background graviton, for a reconstruction see [84].

For $\eta_{\mathrm{UV}} > 0$ or $\gamma_{\mathrm{UV}} < 0$ the UV tail of the spectral function is positive, but the spectral function is not normalisable,

$$\lim_{\Lambda\to\infty} \int_0^\Lambda d\lambda \, \lambda \, \rho_\phi(\lambda) \to \infty \,, \tag{3.13c}$$

in the absence of IR singularities. Equation (3.13c) holds true for the spectral function of the fluctuation graviton in covariant gauges, see [84] for a reconstruction, and [81] for a direct computation. Note that also in this case, the field does not generate an asymptotic state by applying it to the vacuum, $\phi|0\rangle$. However, this is not to be expected in a non-Abelian gauge theory or quantum gravity. However, the anomalous dimension can possibly be removed by an on-shell renormalisation. In Section 4.3, we will show results for the fluctuating Graviton spectral function in an on-shell renormalisation scheme, which has a normalisable spectral function.

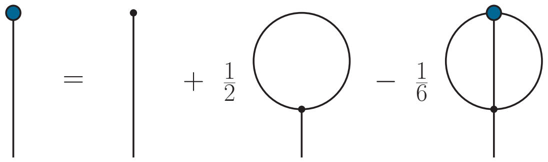

Figure 3.1.: Master DSE for a scalar ϕ^4 theory. Each diagram contains exactly one classical vertex, the rest is fully dressed. For the general notation, see Figure 2.1.

3.2. Functional equations

In this section, we derive the functional equations used throughout this work, namely the Dyson-Schwinger equations (DSE) and the functional Renormalisation Group (fRG). Both equations are in principle exact functional identities, which relate full correlation functions of the theory. In practice and with only very few exceptions they cannot be solved without approximations, as the derived functional equation for a given n-point function depend on higher order correlation functions. To close the system of equations, one needs to truncate the tower of equations. Both the DSE and the fRG, if treated as non-perturbative systems of equations, resummate quantum corrections diagrammatically. As the respective resummation schemes differ in presence of approximations, the comparison of results from both equations provide a non-trivial cross-check and possibilities for a systematic error estimate. In this thesis, we employ the DSE of a scalar field in three dimensions to compute scalar bound state masses in Section 4.2, and we solve the quark propagator DSE in Section 5.1. In particular for the latter, the DSE has the advantage of a very simple, one-loop exact form, and only depends on the gluon propagator and the quark gluon vertex. We use the fRG as well for the computation of scalar spectral functions on both sides of the phase transition in Section 4.1 and for the graviton propagator in Section 4.3.

3.2.1. Dyson-Schwinger equations

The Dyson-Schwinger equations are a set of exact functional equations, which relate full vertices and propagators of a quantum field theory. To derive them, one assumes a well-defined measure of the path integral, which is symmetric under arbitrary shifts of the fields. Then, the total derivative with respect to a given field vanishes,

$$0 = \int \mathcal{D}\varphi \, \frac{\delta}{\delta\varphi(x)} e^{-S_E[\varphi]+J\cdot\phi} = \left\langle -\frac{\delta S_E[\varphi]}{\delta\varphi(x)} + J(x) \right\rangle_J .$$

With the quantum equation of motion (2.14), the source is nothing but the functional derivative of $\Gamma[\phi]$ with respect to the mean field, and we arrive at the DSE for the 1PI effective action,

$$\frac{\delta\Gamma[\phi]}{\delta\phi(x)} = \left\langle \frac{\delta S_E[\varphi]}{\delta\varphi(x)} \right\rangle_J = \frac{\delta S_E[\varphi]}{\delta\varphi(x)} \left[\varphi = \phi + G \cdot \frac{\delta}{\delta\phi} \right] . \tag{3.14}$$

By successive functional derivatives of (3.14), one generates an infinite tower of equations for full n-point vertices. For the example of a scalar ϕ^4 theory, the diagrammatic representation of (3.14) is shown in Figure 3.1. It is a two-loop exact equation, and contains a full 3-point function as its highest non-trivial ingredient. Hence, the DSEs for higher n-point functions will always depend on the full $(n+2)$-point function and for most practical applications, one has to employ a truncation to close the system of integral equations. For a detailed discussion on DSEs in QCD and QED see, e.g., [85], and [54] for a spectral DSE framework in a scalar theory.

While the DSE has been employed successfully in various research areas, notably in Hadron physics, it has practical difficulties. In many cases, it is only two-loop exact and accordingly involves a larger number of diagrams with different topologies. Furthermore, it is non-trivial to derive a manifestly finite formulation of a DSE, and the classical vertex that is present in each diagram necessitates a non-trivial cancellation in the system of equation to ensure invariance under general field redefinitions. In particular for the latter reason, the DSE is often used in a skeleton expansion, where all vertices are fully dressed. We will come back to this in Section 4.2.

3.2.2. The functional Renormalisation Group

A functional relation which is not only 1-loop exact, but also manifestly finite and RG-invariant is the functional renormalisation group (fRG). The derivation follows the concept of the Wilsonian RG [86, 87], where quantum fluctuations are integrated out momentum shell by momentum shell. On the level of the 1PI effective action, this idea is implemented by a masslike regulator function, that cuts off momentum modes above a certain cutoff scale k. The change of correlation functions with respect to the variation of the cutoff scale is then governed by the Wetterich equation [88].

To derive the Wetterich equation, we introduce the regulator as an infrared modification of the classical dispersion.

$$e^{W_k[J]} = \int \mathcal{D}\varphi \, e^{-S[\varphi]-\Delta S_k[\varphi]+J\cdot\varphi} \,, \tag{3.15}$$

with the regulator term

$$\Delta S_k[\varphi] = \frac{1}{2}\int \frac{d^d p}{(2\pi)^d} \varphi(-p) R_k(p^2) \varphi(p) \,. \tag{3.16}$$

The regulator serves thereby as an infrared cutoff and can be parametrised with

$$R_k^\phi(p) = Z_\phi \, k^2 \, r^\phi(x) \,, \qquad x = \frac{p^2}{k^2} \quad \text{or} \quad x = \frac{\vec{p}^{\,2}}{k^2} \,, \tag{3.17}$$

where Z_ϕ is the (cutoff dependent) wave function renormalisation of the field at hand. The optimal choice of the shape function r_ϕ depends on the problem at hand, but it is usually taken to be greater than zero for $p^2/k^2 \to 0$ and vanishes for $p^2/k^2 \to \infty$. For more details on the choice of the shape function see the discussion in Section 3.3.1.

To derive the flow of the effective action with respect to the cutoff scale k, we simply take a (logarithmic) k-derivative of the scale dependent Schwinger functional $W_k[J]$,

$$\partial_t W_k[J] = \frac{1}{Z[J]} \int \mathcal{D}\varphi \, \partial_t \Delta S_k[\varphi] \, e^{-S[\varphi]-\Delta S_k[\varphi]+J\cdot\varphi} = -\langle \partial_t \Delta S_k[\varphi] \rangle_J \,, \tag{3.18}$$

with the (negative) RG-time $t = \log(k/k_{ref})$. Hence, the flow of the effective action (2.13) evaluated at a fixed mean field ϕ reads

$$\partial_t \Gamma[\phi] = -(\partial_t W_k)[J_\phi] = \frac{1}{2}\int_p G_k[\phi](p)\partial_t R_k(p) + \Delta S_k[\phi]\,, \tag{3.19}$$

where the t-derivative of the first term in (2.13) cancels the term arrising from the chain rule, and we have used the operator identity (2.12) in the second step.

It is often useful to define the average effective action, denoted by Γ_k via a modified Legendre transform,

$$\Gamma_k[\phi] = J_\phi \cdot \phi - W_k[J_\phi] - \Delta S_k[\phi]\,. \tag{3.20}$$

The subtraction of the counter term removes the trivial running of the regulator term in the flow. The derivation for multiple fields is straightforward within the superfield formalism, which introduces the superfield as a vector of fields $\Phi = (\phi, \psi, \bar{\psi}, A_\mu, ...)$. The regulator term is then a bilinear form in the superfield, and the regulator function is represented by a matrix which is diagonal for bosonic fields and symplectic for fermionic fields. The Wetterich equation then takes the compact form

$$\partial_t \Gamma_k[\Phi] = \frac{1}{2}\mathrm{STr}\, G[\Phi]_{ab}\, \partial_t R_k^{ba}\,, \tag{3.21}$$

where the supertrace is the trace over all internal and space-time/momentum indices of the superfield.

3.3. From the Wetterich RG to the renormalised Callan-Symanzik equation

This section is based on [1].

In this section, we focus on one of the conceptual developments that are crucial for the real-time formulation of the fRG in this work. The main idea is to derive a renormalised flow equation for the effective action with a Callan-Symanzik cutoff, i.e., a simple mass without a momentum dependence via a limit of finite Wetterich-type flow equations. We start by discussing the causal structure of the propagator in presence of the regulator in Section 3.3.1. In Sections 3.3.2 and 3.3.3, we derive the renormalised CS equation from the generalised flow equation. We close the section with the discussion of flowing renormalisation conditions at the example of a scalar theory in Section 3.3.4 and the special case of gauge theories in Section 3.3.5.

3.3.1. Infrared regularisation and symmetries

In the following we discuss some properties of the functional flow equation (3.21) with respect to the choice of regulator. The discussion holds for a generic quantum field theory. We concentrate on the simple example of a real scalar field $\Phi = \phi$ with the classical action

$$S_\phi[\phi] = \int d^{\mathrm{d}}x \left[\frac{1}{2}\phi\left(-\partial^2 + m_\phi^2\right)\phi + \frac{\lambda_\phi}{4!}\phi^4\right] . \tag{3.22}$$

The addition of the regulator term (3.16) alters the dispersion relation,

$$p^2 + m_\phi^2 \to p^2 + m_\phi^2 + R_k^\phi(p) . \tag{3.23}$$

The regulator is parametrised as $R_k^\phi(p) = Z_\phi k^2 r(x)$, where the *shape function* $r(x)$ depends on either full or spatial momenta squared, $x = p^2$ or $x = \vec{p}^{\,2}$, measured in the cutoff scale k^2, see also (3.17). It implements both, the vanishing momentum limit associated with an infrared (IR) mass as well as the ultraviolet (UV) decay,

$$\lim_{x\to 0} r(x) = 1 , \qquad \lim_{x\to\infty} x^{d/2} r(x) \to 0 , \tag{3.24}$$

see e.g. [89] for a respective discussion. The first property implements IR regularisation through an, in general momentum-dependent, mass term that effectively suppresses quantum fluctuations of field modes with momenta $p^2 \lesssim k^2$. The second property leads to a suppression of modes with $p^2 \gtrsim k^2$ in the momentum-loop integrals, rendering the flow (3.21) and all its field derivatives, which yield the flow of (1PI) correlation functions, UV finite. A specific example for a smooth shape function is

$$r^\phi_{exp}(x) = e^{-x} . \tag{3.25}$$

In addition to the conditions in (3.24), which guarantee the finiteness of fRG flows, we might want to impose additional, physically motivated conditions onto the regulators. For relativistic theories it is desirable that the regulators do not spoil Lorentz/Poincaré invariance. Furthermore, for studies of real-time properties, i.e. in Minkowski space, causality should also not be violated. The latter is directly related to the existence of a spectral representation for the propagator of ϕ.

To maintain Lorentz invariance, the regulator must be a function of the four-momentum squared, $R_k^\phi(p^2)$. However, as discussed, e.g., in [90], such regulators might spoil causality through unphysical poles in the complex frequency plane. Typically, such regulators either do not admit a spectral representation or generate fictitious mass poles that only disappear in the vanishing cutoff limit, for a discussion of the latter see [90–92]. As an example, consider a classical Euclidean propagator

$$G_{\phi,k}(p) = \frac{1}{p^2 + m_\phi^2 + R_k^\phi(p)}\,, \tag{3.26}$$

with a regulator shape function, c.f. (3.17),

$$r_{\text{rat}}^\phi = \sum_{n=n_{\text{min}}}^{n_{\text{max}}} c_n \left(\frac{k^2}{k^2+p^2}\right)^n\,. \tag{3.27}$$

Already for such a simple propagator, the existence of a spectral representations of the regularised propagator is highly dependent on the coefficients c_n, and in general not the case, see [43, 90] for more details. For general propagators, regulators of the type (3.27) typically generate at least n_{max} poles in the propagator, whose positions in the complex plane usually spoil the spectral representation. Another choice would be a variation of the exponential regulator (3.25), see [91, 92] for more details. Regulators of this type lead to series of poles in the propagator as well as an essential singularity at infinity.

A further common choice are regulators that only depend on the spatial momenta, $R_k^\phi(\vec{p}^{\,2})$. Clearly, these regulators do not lead to additional poles in the complex frequency plane, but merely modify the dispersion of the fields. Thus, they admit a spectral representations at the cost of violating Lorentz invariance. If the system is in a medium, explicit Lorentz symmetry breaking might seem innocuous, as it is broken anyway. While this has been confirmed in specific examples [92, 93], it is *a priori* unclear in general. Especially when considering limiting cases of a phase diagram such as $T \to 0$, the question becomes much more intricate than the comparisons in the aforementioned works. Hence, effectively we either violate (or at least complicate) causality, or we violate Lorentz invariance. All known examples of regulators rely on the regularisation conditions in (3.24). However, by relaxing at least one of these conditions, there is a natural choice for a regulator which preserves both causality and Lorentz invariance,

$$R_{k,\text{CS}}^\phi = Z_\phi\, k^2\,, \qquad r_{\text{CS}}(x) = 1\,, \tag{3.28}$$

which we refer to as the CS regulator. It implements IR regularisation through an explicit mass $\Delta m_\phi^2 = Z_\phi\, k^2$. In this case the flow equation (3.21) has been derived in [94]. To our knowledge, it is indeed the first occurrence of such a closed (and one loop) exact functional equation for the effective action. The functional CS flow has been picked up and discussed later in [95–100] as a special choice of the general flow equation (3.21) .

The insertion of the CS regulator in (3.21) leads us to the (inhomogeneous) functional CS equation. However, it violates the second condition (3.24). The CS regulator only lowers the UV degree of divergence by two, for example, quadratically divergent diagrams such as the tadpole diagram in the two point function of the ϕ^4 theory in $d = 4$ leads to logarithmically divergent tadpole diagrams in the CS equation. In short, at each k

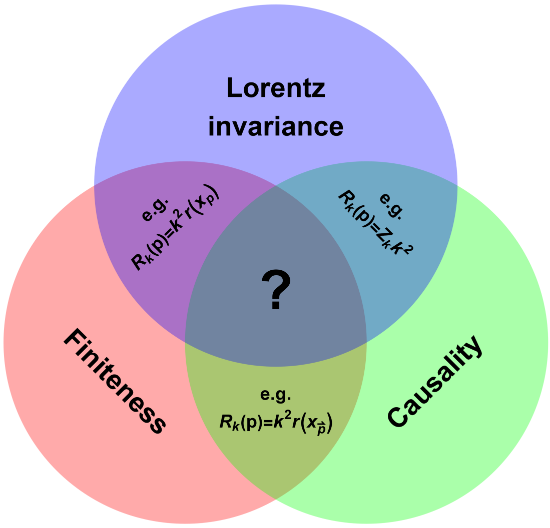

Figure 3.2.: Sketch of the competing requirements for regulators: finiteness of the flow, Lorentz invariance and causality of regulators. Examples for regulators with two of the properties are given. A fully systematic construction of regulators with all three properties in the flow is lacking to date.

in the flow, all loop momenta contribute. To render the flow finite, an additional UV regularisation is required in general.

The different properties of the regularisation are summarised in Figure 3.2. Restricting the discussion to vacuum for simplicity, the three different property of interest are

1. **Lorentz invariance:** The regulator is a function of p^2 and respects Lorentz symmetry.

2. **Causality:** The *regularised* propagator admits a spectral representation, c.f. (3.5). Expressed in Euclidean momenta, the right half-plane for analytically continued momenta is holomorphic.

3. **Finiteness:** All diagrams arising from (3.21) and its functional derivatives are finite.

In the overlap regions of Figure 3.2 we provide examples for regulators with the respective two properties.

No example is given in the overlap regime in the middle with all three properties: at present, no regulator keeping all three properties in Figure 3.2 simultaneously is known: indeed, the structure of the full propagator,

$$G_k(p) = \frac{1}{\Gamma_k^{(2)}(p) + R_k(p)}\,, \tag{3.29}$$

which is the inverse of the sum of the regulator and the (yet to be determined) two point function $\Gamma_k^{(2)}$, entails that a systematic construction of such a regulator for all cutoff scales k necessarily requires the use of the complex structure of $\Gamma_k^{(2)}$ in the regulator. This leaves us with a combination of requirements: the existence of the spectral representation of the propagator (3.29) with the regulator limits (3.24) for an unknown two-point function $\Gamma_k^{(2)}$. This combination is rather obstructive, and if a systematic construction is possible at all, it evidently requires using constraints on the complex structure of the two point function at hand.

As an illustration, let us assume we have a Lorentz invariant regulator with the properties (3.24). We observe that the regulator needs to be a decaying function as $p \to \infty$, by assumption, while $\Gamma^{(2)}(p)$ needs to be a growing function for $p \to \infty$, being the inverse of the propagator. This implies finite Lorentz invariant flow equations (properties 1 & 3). Now we show that then causality (property 2) is at stake:

A simple consideration of the Cauchy–Riemann equations suggest different signs of their imaginary parts in the top-right quadrant of $p \in \mathbb{C}$. However, the regulator needs to have a positive real part, at least for small Euclidean momenta, to provide the IR regularisation. In a partially simplified picture, this leads to lines in the complex plane where the real part of the regulator is zero. Similarly, the real part of the two-point function has lines with vanishing real part, related to the dispersion relation. The different limiting cases detailed above make it almost impossible to avoid zeros in the top right quadrant of the complex momentum plane, and consequently lead to a violation of causality in the regularised propagator. Partly, this reasoning can also be found in [101]. The argument presented here is a very pictorial, simplified version. While it is easy to construct explicit counterexamples, so far even in tailor made applications, such as spectral functions of a simple scalar theory, no regulator has been provided that escapes this problem, leave aside a generic systematic construction scheme. A full discussion of this issues is postponed to future work.

This leaves us with the situation that we may consider regulators in the three overlap regions, put differently, regulators, that lack one of the properties 1-3. In this context we emphasise a peculiarity of the overlap regime without finiteness including the CS regulator: the structural similarity of the Wetterich equation (3.21) with regulators obeying (3.24) and the flow with the CS regulator (3.28) is misleading. While the former equation implements a Wilson-type momentum-shell integration in a fixed underlying quantum field theory, the CS flow constitutes a flow in the space of theories. To be specific, the need for additional UV regularisation at different cutoff scales k implies that we have different theories which necessarily require a different renormalisation. Hence, the flow must be re-renormalised; only specifying the initial effective action $\Gamma_{k_{init}}$ does not lead to a finite renormalised solution of the flow equation. As we will show in the next section, this can be achieved instead by the introduction of explicit counter terms to the flow, supplemented with renormalisation conditions which are fixed at a, in general k-dependent, renormalisation scale μ.

3.3.2. RG-consistency and UV scaling

For standard infrared regulators with shape functions $r(x)$ that obey (3.24), the flow equation is manifestly finite as loop momenta are effectively restricted to $p^2 \lesssim k^2$. Then, choosing a specific $r(x)$ amounts to specifying a UV regularisation scheme for fRG flows. The effective action Γ_k of a general theory is then obtained by integrating (3.21) from some initial cutoff scale k_{init} to $k \leq k_{init}$, The renormalisation conditions are implicitly fixed through the initial effective action $\Gamma_{k_{init}}$. The theory at a given cutoff scale k should not depend on the initial cutoff scale k_{init}, which is called *RG-consistency*, see [89, 102, 103],

$$k_{\text{init}} \frac{d\Gamma_k}{dk_{\text{init}}} = 0 \,. \tag{3.30}$$

The initial effective action implicitly fixes the renormalisation conditions. RG-consistency entails renormalisation group invariance, and specifically the independence of the theory on these conditions.

As a first step towards the desired finite flow equations, also for regulators such as the CS one, we discuss how the UV scaling can be absorbed within a general RG rescaling. Then, the UV limit of the effective action is the finite renormalised UV action and not the diverging bare action. For more details we refer the reader to [89] and in particular [104].

It has been shown in Chapter VIII B of [89], that the RG invariance of the theory is maintained in the scale-dependent theory in the presence of the regulator term for regulators of the form of (3.17). Such regulators are called *RG-adapted* as they satisfy the RG equation

$$\left(\mu\partial_\mu + 2\gamma_\Phi^{(\mu)}\right) R_k^\Phi = 0 \,, \tag{3.31}$$

where we denote the β-functions $\beta^{(\mu)}$ and anomalous dimensions $\gamma_{\Phi_j}^{(\mu)}$ of the theory at hand as

$$\gamma_\Phi^{(\mu)} \Phi = \mu \frac{d\Phi}{d\mu} \,, \qquad \beta_\lambda^{(\mu)} = \mu \frac{d\lambda}{d\mu} \,. \tag{3.32}$$

The coupling vector $\lambda = (\lambda_1, ..., \lambda_m)$ contains all relevant parameters of the theory, including the mass parameters. The full RG invariance of the theory in the presence of the cutoff is then given by

$$\left(\mu\partial_\mu + \beta_{\lambda_i}^{(\mu)} \partial_{\lambda_i} + \int \gamma_{\Phi_j}^{(\mu)} \Phi_j \frac{\delta}{\delta \Phi_j}\right) \Gamma_k[\Phi] = 0 \,, \tag{3.33}$$

and has the same form as the RG equation at $k = 0$. From this, we obtain the general flow equation that comprises the change of a cutoff scale, here k, as well as an accompanying general RG transformation. Using (3.21), an additional total k-derivative of (3.33) yields the flow equation with reparametrisation at each flow step, see (4.25) in Chapter IV of [89],

$$\left(s\partial_s + \beta_{\lambda_i}^{(s)} \partial_{\lambda_i} + \int_x \gamma_{\Phi_j}^{(s)} \Phi_j \frac{\delta}{\delta \Phi_j}\right) \Gamma_k[\Phi] = \frac{1}{2} \mathrm{Tr}\, G_k[\Phi] \left(\partial_s + 2\gamma_\Phi^{(s)}\right) R_k^\Phi \,, \tag{3.34}$$

where we consider $k(s)$ and $\mu(s)$ with

$$s\partial_s = \mu\partial_\mu + \partial_t \,. \tag{3.35}$$

The β-functions $\beta^{(s)}$ and anomalous dimensions $\gamma^{(s)}$ then encode the full s-scaling of a combined cutoff (k-) and RG (μ-) flow, including a reparametrisation of the theory,

$$\gamma_\Phi^{(s)} \Phi = s \frac{d\Phi}{ds} \,, \qquad \beta_\lambda^{(s)} = s \frac{d\lambda}{ds} \,. \tag{3.36}$$

For RG-adapted regulators with (3.31) the renormalisation group scaling with μ drops out of the right hand side of (3.34).

The central result of [1] shows, that the additional μ-flow can be absorbed into a well-defined flow of a non-perturbative counter term action for the k-flow in a manifestly finite way. The flow of the counter term action serves a two-fold purpose: Firstly, it allows to change consistently the renormalisation conditions with the k-flow for general IR flows. We call this flowing renormalisation. Secondly, it also leads to manifestly finite flows for the CS regulator with a flowing counter term action for general non-perturbative truncation schemes. The number of parameters in these counter term matches that of relevant parameters in the theory.

3.3.3. Functional RG with flowing renormalisation

We now use the general flow equation with an infrared regulator and an ultraviolet one for deriving a flow equations which also incorporates an explicit UV renormalisation in a manifestly finite approach in terms of a generalised BPHZ scheme with the subtraction of a flowing counter term action. In contradistinction to multiplicative schemes this leads to finite loop diagrams by subtraction. Such a construction has the benefit of a simple and robust numerical implementation.

This general setup also allows us to monitor and change the renormalisation conditions within the infrared flow. This generalises the standard fRG setup, in which the (UV) renormalisation and the respective renormalisation conditions are implicit in the choice of the finite initial action, see the discussion around (3.30).

The access to the UV behaviour of the theory is obtained by introducing a regulator $R_{k,\Lambda}(p)$, where an UV cutoff $\Lambda = \Lambda(k)$ enters as a free parameter/function. The regulator $R^{\Phi}_{k,\Lambda}$ is chosen such that it effectively restricts loop momenta to $p^2 \lesssim \Lambda(k)^2$ in the loops of the flow equation, see the examples (3.39c) below. We may also use the regulator for a full UV regularisation of the theory and not only the flow equation, see e.g. (3.39d) below.

Changing the UV scale $\Lambda = \Lambda(k)$ alongside with the infrared flow allows us to introduce a *flowing* (UV) renormalisation in the latter. For these regulators the flow (3.21) can be written as

$$\left(\partial_t\big|_\Lambda + \mathcal{D}_k\,\partial_{t_\Lambda}\right)\Gamma_{k,\Lambda} = \frac{1}{2}\mathrm{Tr}\, G^{\Phi}_{k,\Lambda}\left(\partial_t\big|_\Lambda R^{\Phi}_{k,\Lambda} + \mathcal{D}_k\,\partial_{t_\Lambda} R^{\Phi}_{k,\Lambda}\right)\,, \tag{3.37}$$

where $t_\Lambda = \log(\Lambda/k_{\mathrm{ref}})$, with a reference scale k_{ref}. The factor $\mathcal{D}_k$ is a relative measure of RG steps in the $k-$ and the Λ-direction,

$$\mathcal{D}_k = \partial_t \log\Lambda(k)\,. \tag{3.38}$$

The flow (3.37) is a finite functional flow which allows us to successively integrate out momentum shells. For $\partial_{t_\Lambda} R^{\phi}_{k,\Lambda} = 0$ we arrive at the standard (infrared) flow in (3.21). This naive limit can only be taken for infrared momentum cutoffs that decay sufficiently fast in the ultraviolet. Most importantly, we can identify the terms $\propto \mathcal{D}_k$ in (3.37) as UV-cutoff flows that can be used for a flowing renormalisation scheme.

This derivation holds true for general infrared regulators. In the following we use as an important example regulators $R^{\phi}_{k,\Lambda}$, that converge towards the CS regulator with the shape function (3.28) for $\Lambda \to \infty$. In this case the flowing renormalisation can now be used to derive the finite fRG flow (3.37) for the CS regulator. For this derivation it is convenient to consider regulators $R^{\phi}_{k,\Lambda}$ with

$$R^{\phi}_{k,\Lambda}(p) = Z_{\phi}\, k^2\, r(x_{\Lambda})\,, \qquad x_{\Lambda} = \frac{\vec{p}^{\,2}}{\Lambda^2}\,, \tag{3.39a}$$

where we have considered a spatial momentum regulator in order to retain causality in a simple manner, as discussed in the previous section. Again, we emphasise that this choice is only taken for the sake of the spectral flows discussed later, it is not a necessary one. For $\Lambda \to \infty$ we require

$$\lim_{\Lambda\to\infty} R^{\phi}_{k,\Lambda} = Z_{\phi}\, k^2\,, \tag{3.39b}$$

which leaves us with the CS flow as limit of well-defined UV-finite flows. Explicit examples for shape functions that satisfy the CS-limit (3.39b) are given by

$$r_{\exp}(x_{\Lambda}) = e^{-x_{\Lambda}} \text{ and } \quad r_{\text{CS}}(x_{\Lambda}) = \theta(1 - x_{\Lambda})\,. \tag{3.39c}$$

Both damp or cut off the UV-modes in the loop of the flow equation via the regulator derivative in the numerator of the flow. We may augment the IR regulator with a UV regulator, leading to UV and IR finite loops with

$$r_{\text{sharp}}(x_{\Lambda}) = \frac{1}{\theta(1 - x_{\Lambda})}\,. \tag{3.39d}$$

This regulator leads to momentum loops, e.g. in perturbation theory or a system of Dyson-Schwinger equations, that do not receive any contribution from spatial loop momenta $\vec{p}^{\,2} > \Lambda^2$. Naturally, this property also holds true for the respective flow equations.

To understand the CS limit, we have to explicitly determine the part of the flow that comes from changing the UV cutoff Λ. For $\Lambda \to \infty$ the second part of the flow,

$$\frac{1}{2}\text{Tr}\, G^{\phi}_{k,\Lambda}\, \mathcal{D}_k\, \partial_{t_{\Lambda}} R^{\phi}_{k,\Lambda}\,, \tag{3.40}$$

takes a simple form: First of all, up to sharply peaked contributions for large momenta, see the examples in (3.39), the t_{Λ}-derivative of the regulator vanishes in the CS limit (3.39b) with

$$\lim_{\Lambda\to\infty} \partial_{t_{\Lambda}} R^{\phi}_{k,\Lambda} = 0\,. \tag{3.41}$$

Note that (3.41) simply entails removing the Λ-part of the flow in the limit $\Lambda \to \infty$, so it holds true beyond the CS example. Thus, in this limit the contribution of the Λ-flow, (3.40), to the full flow, (3.37), vanishes unless this zero is compensated by a divergence in the Λ-flow.

On the more technical level we define diagrams with UV *irrelevant* power counting in the flow equation: these are the diagrams $\text{Diag}^{(n)}_i\big(\partial_{t_{\Lambda}} R^{\phi}_{k,\Lambda}\big)$ in the flow of n-point functions $\Gamma^{(n)}_k$ which remains finite if the substitution $\partial_{t_{\Lambda}} R^{\phi} \to 1$ is done. Here, the superscript ${}^{(n)}$ indicates a diagram of the flow of $\Gamma^{(n)}_k$, while the subscript ${}_i$ labels the different diagrams in this flow. We write

$$\lim_{\Lambda\to\infty} \left|\text{Diag}^{(n)}_i\big(\partial_{t_{\Lambda}} R^{\phi}_{k,\Lambda} \to \Lambda^2\big)\right| < \infty\,. \tag{3.42}$$

Diagrams with (3.42) either contain a sufficiently large number of propagators or sufficiently rapidly decaying vertices to render the integration over loop momenta finite. In the CS limit, the contribution of UV-irrelevant diagrams to the flow vanishes like Λ^{-n} with some $n > 0$.

In turn, the power counting marginal and relevant parts of the Λ-flow (3.40) will survive in this limit and indeed diverge with powers and logarithms of Λ. Importantly, these terms are also local *if* the vertices are: they only depend on powers of momenta. Note also that the Λ-flow has the same UV power counting as standard diagrams, as the regulator behaves like an inverse propagator for $\Lambda \to \infty$. This can be seen from the example regulators (3.39), whose t_Λ-derivative yields

$$\begin{aligned} \partial_{t_\Lambda} r_{\exp}(x_\Lambda) &= 2x_\Lambda e^{-x_\Lambda}\,, \\ \partial_{t_\Lambda} r_{\text{CS}}(x_\Lambda) &= 2x_\Lambda \delta(1-x_\Lambda)\,. \end{aligned} \tag{3.43}$$

Hence, the Λ-flows for n-point functions diverge with the same power of Λ as standard loop diagrams, e.g., in perturbation theory. The above analysis reveals an intricacy of the UV power counting that is elucidated [1], Appendix A, at the example of the ϕ^4-theory in $d = 4$. In short, the standard UV power counting only holds true if the truncation at hand respects the UV power counting of the theory. A prominent important counter example is the derivative expansion in a ϕ^4-theory. Already its lowest order (0th order derivative expansion or local potential approximation (LPA)) includes a full effective potential $V_{\text{eff}}(\phi^2)$, and hence all order (point-like) interactions $\lambda_n/(n!)\phi^{2n}$ with $n \in \mathbb{N}$. Due to its momentum-independence these couplings persist unchanged at arbitrarily large momentum $p \to \infty$. Accordingly, they seemingly introduce infinitely many fundamental couplings λ_n, which would render the theory UV-sick. Note that this intricacy also is present for other functional approaches, the Dyson-Schwinger equation for the effective potential in LPA has been discussed in [105], Appendix F.

Finally, the prefactors of the UV-relevant terms in the t flow may be different from that in the t_Λ flow, as the respective scale derivatives of the regulator have a different momentum-dependence if taken for a fixed shape function. This is remedied by using shape functions with

$$r_\Lambda = r(x_\Lambda) + \Delta r_\Lambda(x_\Lambda)\,, \tag{3.44}$$

and the correction $\Delta r_\Lambda(x_\Lambda)$ is taken such that the relative prefactors of all UV relevant terms of the t_Λ-flow equals the relative prefactors of the relevant terms in the t-flow.

In summary, this leads us to the definition of the counter term action,

$$\partial_t S_{\text{ct}}[\phi] := -\frac{1}{2}\text{Tr}\, G^{\phi}_{k,\Lambda}\, \mathcal{D}_k\, \partial_{t_\Lambda} R^{\phi}_{k,\Lambda}\,, \tag{3.45}$$

which removes all terms with positive powers Λ^n as well as logarithms $\log \Lambda/k_{\text{ref}}$ from (3.37) and renders the infinite UV cutoff limit finite,

$$\lim_{\Lambda\to\infty} \big|\partial_t \Gamma_{k,\Lambda}[\phi]\big| < \infty\,. \tag{3.46}$$

The counter term action (3.45) depends on a finite set of renormalisation parameters required for the finite limit (3.46). The size of this set is equivalent to the number of UV relevant and marginal directions. Moreover, in the limit $\Lambda \to \infty$ the counter term action takes a local form for approximations with local vertices that reduce to the classical ones for large momenta.

Finally, we arrive at the novel flow equation with flowing renormalisation

$$\partial_t \Gamma_k[\phi] = \frac{1}{2} \mathrm{Tr}\, G_\phi[\phi]\, \partial_t R^\phi - \partial_t S_{\mathrm{ct}}[\phi]\,, \tag{3.47}$$

with the flow of the counter term action (3.45) accounting for the flow of the renormalisation conditions as well as the finiteness for infrared cutoffs such as the CS regulator. This general equation constitutes a main result of our work. It can be augmented with general reparametrisations of the theory, leading to a generalisation of (3.34): we simply have to subtract $\partial_t S_{\mathrm{ct}}[\phi]$ defined in (3.45) on the right hand side of (3.34). Note, that heuristically such a procedure is suggestive but in general a naive removal of divergent terms does not provide a consistent renormalisation. The results of [1] show, that (3.47) is correct. The derivation also offers a systematic practical way to compute the counter term and it was shown that within commonly used truncation schemes this goes beyond using standard counter terms.

3.3.4. Flowing renormalisation conditions

Enacting the CS-limit (3.39b) for a suitable regulator and denoting the anomalous dimension as $\eta = -\partial_t Z_\phi / Z_\phi$, the general equation (3.47) reduces to

$$\partial_t \Gamma_k[\phi] = \frac{1}{2}(2 - \eta_\phi) \mathrm{Tr}\, G_\phi[\phi]\, Z_\phi k^2 - \partial_t S_{\mathrm{ct}}[\phi]\,. \tag{3.48}$$

As for the general equation (3.47) the novelty of (3.48) is not its finiteness per se. Indeed, already the original functional CS equation as derived in [94] can be shown to be finite order by order in perturbation theory. However, (3.48) is manifestly finite in *general* perturbative and non-perturbative truncation schemes with a manifestly finite effective action. Moreover, the present setup allows for a direct computation of the flow of the counter term action, only dependent on a set of renormalisation parameters which are in one-to-one correspondence to the coefficients of the UV marginal and relevant operators. Finally, the finite CS flow can be applied to perturbatively and non-perturbatively renormalisable theories, and for a first application in quantum gravity we refer to [81].

The general flow (3.47) and its finite CS limit (3.48) seemingly imply that we are left with the task of computing the non-trivial scaling factor $\mathcal{D}_k$ as well as the Λ-trajectory (3.44) at each RG-step. This would exact a heavy price for the finiteness (3.46). It is therefore noteworthy that we do not have to compute $\partial_t S_{\mathrm{ct}}[\phi]$ from the flow, as it can completely fixed by the choice of renormalisation conditions. The subtraction $\partial_t S_{\mathrm{ct}}[\phi]$ has to be simply chosen such that the flow of these conditions vanish. This choice is practically implemented by subtracting the t-flow of the correlation functions $\Gamma_k^{(n)}(p^2 = \mu^2)$, that is the renormalisation condition from the full t-flow. This renders the functional t-flow finite (if one also subtracts the zero point function) and guarantees the RG conditions to hold.

We illustrate this within a simple example for the finite CS flow. Again we use a real scalar field theory with the renormalised effective action $\Gamma_{k,\Lambda}$ with a given UV cutoff Λ. The renormalisation entails that the effective action $\Gamma_{k,\Lambda}$ stays finite in the limit $\Lambda \to \infty$. Moreover, it may satisfy the following on-shell renormalisation conditions at the flowing scale $\mu = \mu(k)$,

$$\begin{aligned}\lim_{\Lambda\to\infty} \Gamma^{(2)}_{k,\Lambda}[\bar\phi](p)\Big|_{p^2=-\mu^2} &= -\,k^2\,,\\ \lim_{\Lambda\to\infty} \partial_{p^2}\Gamma^{(2)}_{k,\Lambda}[\bar\phi](p)\Big|_{p^2=-\mu^2} &= 1\,,\\ \lim_{\Lambda\to\infty} \Gamma^{(4)}_{k,\Lambda}[\bar\phi](p)\Big|_{p^2=-\mu^2} &= \lambda_\phi\,,\end{aligned} \tag{3.49}$$

where p^2 is evaluated at a timelike Minkowski momentum. Here, $\bar\phi$ is a background field, which is typically given by the solution of its (quantum) equation of motion (EoM), $\bar\phi = \phi_{\text{EoM}}$.

The first condition is an on-shell mass renormalisation: the effective action in the presence of an IR regulator is defined as a modified Legendre transform excluding the regulator term. Hence, for the physical CS regulator we have to consider the full Euclidean two-point function with the CS mass term $Z_\phi k^2$, that is $\Gamma^{(2)}_k(p^2) + Z_\phi k^2$. Thus, (3.49) simply implies $\Gamma^{(2)}_k(-\mu^2) + k^2 = 0$, so the renormalisation scale determines the k-dependent pole mass, $\mu = m_k$. By setting $\mu = k$, we can enforce this pole mass to be given by the mass introduced by the CS regulator. Thus, for a given physical mass the RG flow from the initial UV scale k_{init} is terminated at $k_{\text{fin}} = m_{\text{phys}} = m_{k_{\text{fin}}}$. Put differently, with this RG condition we flow through the space of scalar theories with the physical pole mass k^2.

The second condition in (3.49) fixes the wave function renormalisation at μ, $Z_\phi(-\mu^2) = 1$ on-shell. We remark, that this leads to a spectral function $\rho_{\phi,k}$ that is not normalised to unity if ϕ is a physical field (defining an asymptotic state), see Section 3.1.2.

The last condition in (3.49) fixes the quartic interaction vertex. We have not specified the momentum configuration here, but natural choices are the symmetric point and specific momentum channels such as the s-channel.

Below, we shall consider more general on-shell as well as off-shell renormalisation conditions adapted to specific theories or classes of theories. We emphasise that every RG-condition serves our purpose, but on-shell RG conditions are in most cases a specifically convenient physical choice, only accessible for real-time formulations. Moreover, they facilitate the numerical implementation of spectral CS-flows, as we shall see in Sections 4.1 and 4.3.

We also remark that adjusting specific renormalisation conditions in the standard fRG setting is a fine-tuning problem: One has to adjust the initial effective action at the initial cutoff scale k_{init} such, that the effective action at k_{fin} satisfies the renormalisation conditions. However, adjusting specific renormalisation conditions is not required in the fRG approach but the same finite tuning task extends to adjusting the physics parameters at the initial scale. Both tasks are solved or at least facilitated in the presence of flowing renormalisation, and (3.49) exemplifies this general pattern. With (3.49) both the adjustment of the renormalisation conditions and the adjustment of the physics parameters is done directly.

We emphasise that the implementation of the above full flowing renormalisation is not required within the formulation. Indeed, in the example of the ϕ^4 theory in $d = 4$, the only divergence in the flow equation is related to the mass renormalisation: The CS flow lowers the standard UV degree of divergence by two and the field-dependent part of the flow is logarithmically divergent. Thus, the flow of the counter term action $\partial_t S_{\text{ct}}$ only needs to include one term to ensure finiteness. Note, that using a "minimal" counter term with k-independent parameters, i.e. one that only regularisers the divergent contributions, the present approach reduces to the standard infrared flow: the renormalisation group conditions at $k = 0$ are implicitly set at $k = k_{\text{init}}$ and the physics parameters and RG conditions flow into their final values, which have to be fine-tuned for given physics and RG conditions.

3.3.5. Spectral renormalisation in gauge theories

The scope of the spectral Callan-Symanzik flow equations also extends to the particularly interesting case of gauge theories. Especially the non-perturbative infrared regime of QCD has been been studied intensively within the fRG approach [33, 106–114]. In this section we discuss the application of the spectral renormalisation group to gauge theories at the example of Yang-Mills theory, for respective works with the spectral DSE see [80, 115]. The classical gauge-fixed Yang-Mills action including the ghost term reads

$$S_{\text{YM}} = \int_x \left[\frac{1}{4} F^a_{\mu\nu} F^a_{\mu\nu} - \bar{c}^a \partial_\mu D^{ab}_\mu c^b + \frac{1}{2\xi} (\partial_\mu A^a_\mu)^2 \right] , \tag{3.50}$$

Generally, setting up spectral flow equations for gauge theories works analogously as for scalar theories, discussed in Section 3.3.4. The flow equations are derived in the usual manner, and spectral representations are used for the propagators of all fields, i.e. ghost and gluon propagator.

3.3.5.1. Ghost propagator

Formally, the ghost propagator is expected to obey the KL-representation [116, 117], if the corresponding propagator is causal. A recent direct calculation of the ghost spectral function with the spectral Dyson-Schwinger equation in [80] has confirmed this expectation. This computation has utilised a spectral representation for the gluon, which is discussed in Section 3.3.5.2. Moreover, recent reconstructions [44, 118] show no signs of a violation of this property. It is found that the ghost spectral function exhibits a single particle peak at vanishing frequency with residue $1/Z_c$, whose value may depend on the non-perturbative infrared closure of the Landau gauge. Specifically, the scaling solution is obtained for the limit $Z_c \to 0$, see [43, 80]. In this case, the particle pole in the origin is no longer present. Instead, in the origin there is the branch point of the non-integer power scaling law branch cut of the scaling solution. Note that in this case, the ordinary KL representation can no longer be applied, since the corresponding spectral function would show an IR divergence. For the current discussion, we will stick to the case of a massless particle pole in the IR.

Independent of the IR behaviour addition, a continuous scattering tail shows up in the spectral function via the logarithmic branch cut. This leads us to the general form of the ghost spectral function,

$$\rho_c(\omega) = \frac{\pi}{Z_c} \frac{\delta(\omega)}{\omega} + \tilde{\rho}_c(\omega) \,, \tag{3.51}$$

where $\tilde{\rho}_c$ denotes the continuous tail of the spectral function. It has been shown in [80] that the ghost spectral function obeys an analogue of the Oehme-Zimmermann superconvergence property of the gluon [82, 83]. Expressed in terms of the spectral representation of the dressing, it reads

$$\int \frac{d\lambda}{\pi} \lambda \, \tilde{\rho}_c(\lambda) = -\frac{1}{Z_c} \,. \tag{3.52}$$

Equation (3.52) entails that the total spectral weight of the ghost vanishes. A generic discussion can be found in [79, 80].

Since the ghost spectral function (3.51) shows a (massless) particle pole, as for scalar theories, on-shell renormalisation conditions like (3.49) can be applied. This fixes the pole position of the scale-dependent ghost spectral function to $p^2 = -k^2$. In analogy to (3.51), the flowing ghost spectral function reads

$$\rho_{c,k}(\omega) = \frac{\pi}{Z_{c,k}} \frac{\delta(\omega - k) + \delta(\omega + k)}{\omega} + \tilde{\rho}_{c,k}(\omega) \,, \tag{3.53}$$

where $\tilde{\rho}_{c,k}(\omega)$ has support for $|\omega| > 2k$. In the limit of vanishing cutoff, pole position and scattering onset move into the origin, and (3.51) is recovered.

3.3.5.2. Gluon propagator

The above discussion of the ghost spectral function and its existence was done under the assumption of a spectral representation of the gluon. In contrast to the ghost spectral function, there is an ongoing debate in the community whether or not this assumption is justified. In local QFTs only the existence of a spectral representation for asymptotic states is guaranteed. It has been argued that in Landau gauge this also applies to the gluon propagator [119–121]. While high precision spectral reconstructions are not in contradiction to this assumption and do work for the gluon propagator [43, 45, 122, 123], extensions with complex conjugate poles are also commonly entertained in reconstructions, see e.g. [44, 124–132]. A recent computation has shown, that the situation is indeed exceedingly intricate: its resolution may only be possible by also resolving the problem of a consistent non-perturbative gauge fixing [115]. The self-consistent implementation of the latter for propagators *and* vertices is subject to a non-perturbative infrared realisation of the respective Slavnov-Taylor identities. For a detailed discussion of the complex structure of Yang-Mills theory see [43, 115]. Specifically in [115] is has been shown that a solution of the Yang-Mills system with a spectral ghost and a non-spectral gluon would require non-trivial relations between the complex structures of vertices and propagators. In turn, while less conclusive, in [115] we have also found numerical indications, that a self-consistent solution system with spectral representations for both ghost and gluon propagators, if existent, may also require self-consistent or rather STI-consistent solutions for non-trivial vertices.

In the present work we add nothing new to the resolution of this intricate problem, but simply consider the flow of the gluon spectral function under the assumption of its existence. Likewise, we assume a spectral representation for the ghost, with a pole at $\omega^2 = k^2$, c.f. (3.53). The branch point of the ghost loop contribution to the gluon propagator's branch cut lies at $\omega^2 = (2k)^2$. Due to the massless nature of the ghost, the position of the branch point in the gluon propagator thus necessarily is in the origin for vanishing cutoff scale, $k = 0$. However, due to the lack of a gluon particle peak, a direct identification of a flowing mass scale k as in the scalar theory, see Section 4.1, is not possible for the gluon. Consequently, there is no unique way to stop the flow at some $k_{\mathrm{IR}} = m_{\mathrm{phys}}$, where the physical limit of the theory is recovered. Furthermore, the lack of unique gluon mass scale entails that we cannot use on-shell renormalisation here. Eventually, we wish to recover the IR behaviour of the gluon propagator known from other non-perturbative studies, e.g. via functional approaches [111, 133, 134]. In consequence, we can define the IR scale only implicitly, and k_{IR} depends directly on the initial conditions employed. This poses the question of how to consistently couple the gluonic flow to that of the ghost. A consistent, coupled flow is required to simultaneously reach the explicitly resp. implicitly defined IR scales $k_{\mathrm{IR}}^{(\mathrm{ghost})} = 0$ and $k_{\mathrm{IR}}^{(\mathrm{gluon})}$. This can be implemented by flowing both equations with a common scale k down to 0, where the IR limit of the ghost propagator is reached. We then proceed to further lower k solely in the gluon propagator flow equation down to the point where we reach $k_{\mathrm{IR}}^{(\mathrm{gluon})}$ defined by, e.g. scaling as IR behaviour, c.f. [111, 134]. Note that this procedure needs to be supplemented with an appropriate choice of initial conditions guaranteeing $k_{\mathrm{IR}}^{(\mathrm{gluon})} \leq 0$. This clarifies that the described procedure of flowing with two seemingly different scales simply amounts to an implicit choice of initial conditions and does not lead to an inconsistency between the different flow equations. In such a procedure, adjusting the initial conditions is similar to common fRG calculations. We therefore expect a similar fine-tuning problem for the Yang-Mills system as for example encountered in [111].

The proper choice of initial conditions comes in case of the gluon propagator with another technical complication. It is well-known that in massive Yang-Mills theory, the gluon propagator exhibits complex-conjugate poles. It has been demonstrated in [115] that these can also violate the spectral representation of the ghost propagator, in turn inducing a cascade of non-analyticities in both propagators. Since the Callan-Symanzik cutoff effectively constitutes a mass term, the construction of an initial condition respecting the spectral representation poses a crucial challenge. On the other hand, using modified spectral representations that explicitly take into account complex singularities [115], one is able to track the evolution of the complex poles through the flow. This allows to make a statement about their existence in the full correlation function at k_{IR}. It has been studied e.g. in [101] how regulator-induced poles vanish in the $k \to 0$ limit in a quantum mechanical system.

3.4. Spectral functional equations

This section is in parts based on [1, 3].

In this section, we want to briefly recapitulate the important properties of spectral renormalisation. It has been set up in [54] for general functional approaches, and has been exemplified within the Dyson-Schwinger equation (DSE) for the scalar theory. The respective loop equations contain up to two-loop diagrams with non-perturbative propagators and vertex functions. In the case of the spectral fRG we only have to consider the renormalisation of one-loop diagrams, which facilitates the task. One of the lines carries the cutoff insertion, and the momentum routing is typically chosen such, that it only depends on the loop momentum q. In terms of the frequency dependence, the line with the cutoff insertion simply leads to two classical propagators with the spectral masses λ_1^2 and λ_2^2, both carrying the loop frequency q_0. The CS or spatial regulator does not depend on the loop frequency, but only on $x = \vec{q}^{\,2}/k^2$. To facilitate numerical computations in $d > 1$, it is advantageous to use a spectral representation of the full regulator line or more precisely the propagator squared,

$$G_\phi(q)\partial_t R^\phi(x) G_\phi(q) = \partial_t R_\phi(x) \int_{-\infty}^{\infty} \frac{\mathrm{d}\lambda}{2\pi} \frac{\lambda\, \rho^{(n)}_{G^2}(\lambda, \vec{q})}{(\lambda^2 + q_0^2)^n}\,, \tag{3.54}$$

where $n = 1$ coincides with the usual spectral representation. It can be advantageous to use $n = 2$, to account for the correct canonical momentum scaling, see e.g., Section 4.3.2 and in particular (4.98) for a implementation with $n = 2$.

We may either use (3.54) or the product of the two spectral functions for the propagators on the right hand side of (3.54). In both cases, general flow or DSE diagrams Diag($\mathbf{p}$) of vertex functions and inverse propagators with the external momenta $\mathbf{p} = (p_1, ..., p_n)$ have the representation

$$\mathrm{Diag}(\mathbf{p}) = \int \frac{d^d q}{(2\pi)^d} \mathrm{Vert}(\mathbf{l}, \mathbf{p}) \prod_{i=1}^{N_{\max}} \int_{-\infty}^{\infty} \frac{d\lambda_i}{2\pi} \frac{\lambda_i \rho_i(\lambda_i, \vec{l}_i)}{\lambda_i^2 + (l_i)_0^2}\,, \tag{3.55}$$

where $\mathbf{l} = (q, q + p_1, ...,)$ is the vector of all momenta entering the propagators and vertices of the loop diagram at hand, and $N_{\max}$ is the number of spectral functions. The factor Vert($\mathbf{l}, \mathbf{p}$) stands for the momentum dependences of vertex and regulator factors and possible projections and is a rational function in the momenta $\mathbf{l}$ and $\mathbf{p}$. Note, that it is also possible to include spectral representations of vertices, and in particular of products of vertices and propagators. In particular the latter facilitates the computation of the loop integrals which include non-trivial vertices significantly.

For example, for constant vertex functions N_{Max} is simply the number of internal lines, including that of the regulator line (3.54) for the spectral fRG.

In Lorentz invariant situations, all spectral functions $\rho_i(\lambda, \vec{q})$ can be reduced to $\rho_i(\lambda) = \rho_i(\lambda, 0)$ within spectral representations such as (3.5) and (3.54),

$$\int_{-\infty}^{\infty} \frac{d\lambda}{2\pi} \frac{\lambda \rho_i(\lambda, \vec{q})}{\lambda^2 + q_0^2} = \int_{-\infty}^{\infty} \frac{d\lambda}{2\pi} \frac{\lambda \rho(\lambda, 0)}{\lambda^2 + q^2}\,. \tag{3.56}$$

Then, the momentum integral in (3.55) has the standard form of a one loop perturbative integral, and can be computed with dimensional regularisation with $d \to d-2\epsilon$ and $\epsilon \to 0$. We are led to

$$\mathrm{Diag}(\mathbf{p}) = \prod_{i=1}^{N_{\max}} \int_{-\infty}^{\infty} \frac{d\lambda_i}{2\pi} \lambda_i \rho_i(\lambda_i)\, F_{\mathrm{diag}}(\boldsymbol{\lambda}, \mathbf{p}; \epsilon)\,, \tag{3.57}$$

with

$$F_{\mathrm{diag}}(\boldsymbol{\lambda}, \mathbf{p}; \epsilon) = \int \frac{d^d q}{(2\pi)^d} \mathrm{Vert}(\mathbf{l}, \mathbf{p}) \prod_{i=1}^{N_{\max}} \frac{1}{\lambda_i^2 + (l_i)^2}\,, \tag{3.58}$$

where the bold symbols denote the collection of all spectral masses λ_i and momenta p_i. Equation (3.58) has the form of a perturbative momentum integral, with different masses on each line. For power-counting divergent momentum integrals, F_{diag} contains $1/\epsilon$-terms in even dimensions $d = 2n$ with $n \in \mathbb{N}$. It is tempting to apply the minimal subtraction idea of only subtracting these divergent pieces. This would amount to simply dropping the $1/\epsilon$-terms in F_{diag}. However, as thoroughly discussed in [54], the remaining spectral integrations have the same ultraviolet degree of divergence and may not be finite. Note that these divergences are sub-divergences and are absent at one loop perturbation theory where the spectral functions are Dirac δ-functions. This leaves us with two choices:

(i) *Spectral dimensional renormalisation:* if we want to maintain all symmetry-features of dimensional regularisation, we also have to perform the UV part of the spectral integrations analytically. This can be done using splits

$$\rho(\lambda, \vec{q}) = \rho_{\mathrm{IR}}(\lambda, \vec{q}) + \rho_{\mathrm{UV,an}}(\lambda, \vec{q})\,. \tag{3.59}$$

where the 'IR' part decays sufficiently fast for large spectral values, and $\rho_{\mathrm{UV,an}}$ carries the UV-tail of the spectral function and its form is chosen such that it facilitates the analytic computation of the UV-part of the spectral integrations. Finally, we are left with $1/\epsilon$ terms from both the momentum and spectral integrals, which can be subtracted by an appropriate counter term.

(ii) *Spectral* BPHZ-*renormalisation:* We implement the RG-conditions at an RG-scale μ in terms of subtractions at the level of the integrand in (3.58). This amounts to subtracting a Taylor expansion in $\mathbf{p}$ of F_{diag}. For the sake of simplicity we restrict ourselves to a case with one external momentum and a quadratic divergence, e.g. the flow of the two-point function $\Gamma^{(2)}(p)$ in a scalar theory in $d = 4$ dimensions. Then, $\mathbf{p} = p$ and the BPHZ-subtraction reads schematically,

$$\begin{aligned}\mathrm{Diag}_{\mathrm{ren}}(\mathbf{p}) = \prod_{i=1}^{N_{\max}} \int_{-\infty}^{\infty} \frac{d\lambda_i}{2\pi} \lambda_i \rho_i(\lambda_i, 0) \Bigg[& F_{\mathrm{diag}}(\boldsymbol{\lambda}, p; \epsilon) - F_{\mathrm{diag}}(\boldsymbol{\lambda}, \mu; \epsilon) \\ & - (p^2 - \mu^2)\, \frac{\partial F_{\mathrm{diag}}(\boldsymbol{\lambda}, p; \epsilon)}{\partial p^2}\bigg|_{p^2=\mu^2} \Bigg]\,.\end{aligned} \tag{3.60}$$

In (3.60) we can take the limit $\epsilon \to 0$ before performing the spectral integrations which are manifestly finite. The showcase (3.60) straightforwardly extends to the flow of general correlation functions with the standard BPHZ-procedure. Evidently, the subtraction terms constitute a specific choice of $\partial_t S_{\mathrm{cl}}$ in (3.48).

The spectral dimensional or BPHZ-renormalisation is implemented by a respective choice of a counter term. In DSEs, this counter term is part of the classical action, which carries the difference of bare and renormalised quantities. In the spectral CS equation, the counter term is implemented by the counter term action on the level of the flow, see (3.48).

Evidently, the spectral BPHZ-renormalisation is technically less challenging, and is the renormalisation method of choice in most cases. However, we emphasise that the limit $\epsilon \to 0$ and the integration do not commute, and hence the spectral BPHZ-renormalisation and the spectral dimensional renormalisation may not agree in terms of symmetries. This may be specifically important for gauge theories.

The spectral structure of the diagrams allows for a simple discussion of the emergent scattering thresholds that can be easily tracked within spectral functional approaches. An illustrative example is given by the contribution of the vacuum polarisation diagram to the spectral function of a single scalar field: It features a branch cut that opens at the sum of the spectral masses of the two propagators. The spectral function entering the diagram consists of a mass pole at m_{pole} and a sum of scattering continua ρ_N starting at Nm_{pole} with $N \geq 2$. It follows straightforwardly from the analytic structure of that diagram that substituting scattering contributions ρ_N and ρ_M for the two internal lines directly yields a contribution to ρ_{N+M}. This demonstrates how any scattering structure, once seeded, gives rise to higher scattering contributions.

4. Applications in scalar theories and gravity

To illustrate the power of the spectral framework, we will use the following sections to present a series of applications to different theories in non-perturbative settings. We begin with the scalar theory in three dimensions and present results from three publications [2, 3, 5]. The focus of the first part, Section 4.1, lies on the spectral flow equations in both the broken and symmetric phases, where we highlight both the strengths and challenges of the flowing renormalisation approach. In Section 4.2, we shift gears and introduce a spectral DSE–BSE setup to compute bound-state masses in the scalar theory near the phase transition. We conclude this Chapter in Section 4.3 with a discussion of the graviton spectral function, where flowing renormalisation is employed to achieve a fully self-consistent computation.

4.1. Scalar spectral flows in three dimensions

This Section is based on [3, 5].

In this Section, we accompany the conceptual progress made in [1], see Section 3.3, with a non-perturbative application to spectral functions in the three dimensional ϕ^4-theory. This allows to directly compare our results with those obtained in [54] within the spectral DSE approach. Both functional approaches implement different resummation schemes for the correlators of the given theory through infinite towers of one-loop (fRG) or two-loop (DSE) exact diagrammatic relations. Within an fRG implementation, the successive momentum-shell integration of loop momenta $p^2 \approx k^2$ with the infrared cutoff scale k, already provides an average momentum dependence within simple approximations. Due to their intricate spectral representation, this is particularly beneficial for including non-trivial vertices into the flow, e.g., via momentum-independent but cutoff-dependent approximations.

This work is organised as follows: In Section 4.1.1 we set up the spectral functional renormalisation group for a scalar theory. After discussing the different phases of the theory in Section 4.1.5, we present our results in Section 4.1.6. This includes a detailed comparison to those obtained with the spectral DSE in [54]. We discuss the scaling limit of the theory in Section 4.1.7, where we approach the phase transition of the scalar ϕ^4-theory from the symmetric side, and extract the anomalous dimension η from the power law behaviour of the spectral function. We summarise our findings in Section 4.1.8.

4.1.1. Spectral properties of the scalar theory

In the spectral fRG approach put-forward in [1, 81], the quantum effective action of the theory at hand is obtained by starting with a theory with an asymptotically large classical pole mass $m_\phi \to \infty$, and then lowering the mass successively until the physical point is reached. The respective classical action is given by

$$S[\phi] = \int \mathrm{d}^3x \left\{ \frac{1}{2}\phi\Big(-\partial^2 + Z_\phi\, \mu\Big)\phi + \frac{\lambda_\phi}{4!}\phi^4 \right\}, \tag{4.1}$$

with positive or negative μ. The wave function Z_ϕ has been introduced for convenience, anticipating the emergence of a wave function. For asymptotically large pole masses we have $Z_\phi \to 1$, see Figure 4.3b. Then, (4.1) reduces to (3.22) (with $\mu = \pm m_\phi^2$), and the pole mass is given by

$$m_\phi^2 = \mu - 3\mu\, \theta(-\mu)\,, \tag{4.2}$$

capturing both the symmetric and broken phase. This setup captures both, theories deep in the symmetric phase with $\mu \to +\infty$ and theories deep in the broken phase with $\mu \to -\infty$.

The central idea of spectral functional approaches is to use the spectral representation for all propagators and vertices in the non-perturbative loop diagrams. Then, the momentum integrals can be performed analytically, and the remaining numerical task boils down to the solution of real spectral integrals. In this Section, we revise the important relations for this application of the spectral fRG to a scalar field. For the general discussions of spectral functions and spectral functional equations see Section 3.1 and Section 3.4 respectively.

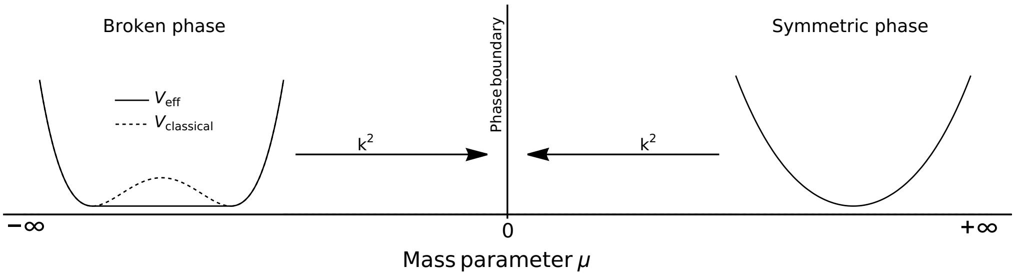

Figure 4.1.: Schematic phase diagram with respect to the mass-parameter μ. The phase boundary is located at $\mu = 0$. The flow is initiated in the deep UV, i.e. $|\mu| = k^2 \to \infty$ with the respective (classical) initial effective potential.

4.1.1.1. Spectral properties of the two-point and four-point function

The spectral representation of the propagator of a given field ϕ is at the core of the spectral functional approach.

$$G(p) = \int_{0_-}^{\infty} \frac{\mathrm{d}\lambda}{\pi} \frac{\lambda \rho\left(\lambda, \vec{p}\right)}{\lambda^2 + p2} \,, \qquad \rho(\omega) = 2\, \mathrm{Im}\, G\left(p^2 = -(\omega + \mathrm{i}0^+)^2\right) \,, \tag{4.3}$$

where 0_- ensures that massless poles are taken into account properly. In the absence of higher order resonances, the spectral function of the ϕ^4-theory is given by

$$\rho(\omega) = \frac{2\pi}{Z_\phi} \delta(\omega^2 - m_{\rm pole}^2) + \theta(\omega^2 - m_{\rm scat}^2) \tilde{\rho}(\omega) \,. \tag{4.4}$$

The mass $m_{\rm pole}$ in (4.4) is the pole mass of the full quantum theory. The scattering continuum $\tilde{\rho}(\omega)$ sets in at $\lambda^2 = m_{\rm scat}^2$. In the case of a non-vanishing background field, the theory admits $1 \to 2$ scattering (broken phase), and we have $m_{\rm scat} = 2 m_{\rm pole}$. Higher thresholds of $1 \to N$ scattering processes lead to further discontinuities in the scattering tail and are typically strongly suppressed. In the absence of $1 \to 2$ scatterings (symmetric phase), the first allowed scattering is $1 \to 3$ and the scattering threshold is $m_{\rm scat} = 3 m_{\rm pole}$, the respective spectral function is depicted in Figure 4.7b and discussed there.

If the spectral representation (4.3) holds, all non-analyticities of the propagator lie on the real frequency axis. These non-analyticities are given by either poles or cuts. Poles originate from asymptotic states that overlap with the propagator of the field ϕ, while cuts represent scattering states. For the propagator of a physical field that describes an asymptotic state, the spectral function is positive. Furthermore, the canonical commutation relations imply a normalisation via the sum rule (3.13a) with $Z_{\rm UV} = 1$.

Vertices also admit spectral representations, which get increasingly complicated for higher order correlation functions due to their increase in arguments. In the present case, we restrict ourselves to an s-channel approximation of the full one-particle irreducible (1PI) four-point function or vertex. This leaves us with a single momentum argument and an accordingly simple spectral representation. The four-point function is given by the fourth field derivative of the effective action $\Gamma[\phi]$, whose $n^{\rm th}$ field derivatives $\Gamma^{(n)}[\phi]$ are the 1PI n-point functions. We use a spectral representation for this s-channel vertex [54],

$$\Gamma^{(4)}(p_0, \vec{p}) = \lambda_\phi + \int_\lambda \frac{\rho_4(\lambda, \vec{p})}{\lambda^2 + p_0^2} \,, \qquad \rho_4(\omega, \vec{p}) = 2\, \mathrm{Im}\, \Gamma^{(4)}(p_0 = -(\omega + \mathrm{i}0^+), \vec{p}) \,, \tag{4.5}$$

where λ_ϕ is the classical vertex in (4.1) and $\int_\lambda = \int_{0_-}^\infty \frac{\mathrm{d}\lambda}{\pi}\lambda$.

Analogue to the spectral function of the propagator, ρ_4 is defined by the discontinuities of the four-point function, see (4.5). Also for the four-point function, the spatial momentum dependence of spectral function $\rho_4(\omega,\vec{p})$ follows from the one at vanishing spatial momentum, $\rho_4(\omega) = \rho_4(\omega,0)$ via a Lorentz boost.

4.1.1.2. Structural properties of diagrams

In the spectral functional approach, spectral representations are utilised to rewrite diagrams in terms of momentum loop integrals over classical propagators with spectral masses and residual spectral integrals; for a general discussion see Section 3.4. Here, we apply this approach in the context of the functional renormalisation group. The spectral fRG leads to perturbative one-loop momentum integrals in diagrams, which can be solved analytically. The non-perturbative information of the diagrams such as pole masses and thresholds is stored in the remaining spectral integrals. For purpose of this application, it is sufficient to consider a single external momentum argument, which is either that of the propagator or the s-channel momentum of the four-point function. In the present case, we only have to consider diagrams with one in-flowing or out-flowing external momentum $\pm p$, and we encounter diagrams of the general form

$$D[p] = g\int_q \prod_{j=1}^N G(l_j)\,, \qquad \int_q = \int \frac{\mathrm{d}^d q}{(2\pi)^d}\,. \tag{4.6}$$

The $l_i = q, q\pm p$ are the momenta of the N internal propagators or vertex representations and we collected all constant prefactors in g. By inserting the spectral representation (4.3) for each propagator, the momentum integrals acquire a standard perturbative form, where the masses are the respective spectral parameters squared, λ_i^2. Finally, the spectral parameters are integrated over, weighted by the respective spectral function,

$$D[p] = g\prod_{j=1}^N \int_{\lambda_j} \rho(\lambda_j) I(\lambda_1,..,\lambda_N,p)\,, \qquad I(\lambda_1,..,\lambda_N,p) = \int_q \prod_{j=1}^N \frac{1}{\lambda_j^2 + l_j^2}\,. \tag{4.7}$$

The momentum integral in (4.7) is readily solved and the resulting analytic expression holds true for $p \in \mathbb{C}$. This gives us access to the spectral function (4.3) via the limit $p \to -\mathrm{i}(\omega + \mathrm{i}0^+)$. We remark that in the present spectral fRG approach to the (1+2)-dimensional scalar theory, all integrals are finite, and we can safely change the order of integration even prior to renormalisation. For more detalis and the general case, see Section 3.4.

4.1.2. Functional Callan-Symanzik equation

The infinitesimal change of the full quantum effective action $\Gamma[\phi]$ under a change of the mass μ is governed by the manifestly finite, non-perturbative *renormalised* Callan-Symanzik equation, see [1, 81] and Section 3.3. It reads

$$\mu\partial_\mu\Gamma[\phi] = \frac{1}{2}\left(1-\frac{\eta_\phi}{2}\right) Z_\phi \mu \,\mathrm{Tr}\left[G[\phi] + \phi^2\right] - \frac{1}{2}\,\mu\partial_\mu S_{\mathrm{ct}}[\phi]\,, \tag{4.8a}$$

with the anomalous dimension

$$\eta_\phi = -2\frac{\mu\partial_\mu Z_\phi}{Z_\phi}\,. \tag{4.8b}$$

The first term on the right-hand side of (4.8a) is the standard one-loop exact contribution to the flow of the effective action that arises from the variation of the mass in the classical action. It was first derived by Symanzik in [94] in the framework of renormalised perturbation theory, where the UV-divergences cancel order by order in the perturbative parameter. In non-perturbative flow equations this is not sufficient. Let us briefly recapitulate the findings of Section 3.3. Starting from non-perturbative finite flow equations with a UV-regulating cut-off, one can analyse a combined RG-step of the IR- and UV-regularisation scale, where the change of the latter evidently induces a second term in the flow equation that governs the flow of correlation functions with the UV-cutoff. This term can be used to impose explicit renormalisation conditions, which are usually set implicitly by the initial condition of the IR flow. Most importantly, as demonstrated in [1], it removes the UV-divergent terms of the diagrams associated to the flow of the mass parameter and renders the CS-limit *finite*, where the UV-regularisation scale is taken to infinity. In the process, it leads to the term $\mu\partial_\mu S_{\text{ct}}[\phi]$ in the second line of (4.8a). It is constituted by the *finite* parts of the UV-cutoff flow that do not vanish. Such a finite term arises for each UV-relevant direction and implements the corresponding renormalisation condition. We will refer to them as counter-term flows. The derivation of (4.8a) entails it's finiteness. Importantly, the counter term flow contains no tree-level contributions to the respective correlation functions. This entails that classical values of the correlation functions are solely given by the respective choice of tree-level values specified in the classical action (4.1), and in particular cannot be further changed by specification of renormalisation conditions. In consequence, the latter can only be used to renormalise the flow contributions, but not the initial conditions of the flow. This excludes, for example that the counter term flow rearranges the theory from the symmetric into the broken phase or vice versa by $\mu\partial_\mu S_{\text{ct}} \propto \pm\text{const.}\,\mu\int\phi^2$. However, the counter term can contain similar terms proportional to $\lambda_\phi/m_{\text{pole}} = \lambda_{\text{eff}}$.

In the momentum basis, the trace in (4.8a) corresponds to a momentum integral. Note that the effective action $\Gamma[\phi]$ in (4.8) includes the full mass term $1/2\int_x \mu\,\phi^2$ in contradistinction to the effective action used in standard fRG momentum-shell flows. There, the momentum dependent regulator part of the mass term is subtracted, and the physical theory is reached when it vanishes. In the present setup, the μ-dependent effective action is that of a physical theory with mass parameter μ, and the flow is one in (physical) theory space. In contrast to usual momentum shell flows, this physical flow is both manifestly Lorentz invariant and sustains causality of physical correlation functions throughout the flow, allowing for the use of the Källén-Lehmann spectral representation (3.7).

In particular, the counter term flow allows for *flowing renormalisation conditions*, and we shall use it to adjust a *flowing on-shell renormalisation*, based on the spectral on-shell renormalisation put forward in [54]. Then, the pole mass m_{pole} is identified with m_ϕ in (4.2) in both phases, $m_{\text{pole}}^2 = \mu - 3\mu\,\theta(-\mu)$. In this physical RG scheme, the phase transition between the symmetric and broken phase happens for $m_\phi^2 = 0$. Hence, we approach the phase transition both from the broken and the symmetric phase in the limit $\mu \to 0$, and the flows are taking place in the one or the other phase, see Figure 4.1. Thereby, our setup avoids flows through the strongly interacting phase transition regime, which are usually present in momentum cutoff flows. This minimises the systematic error stemming from the

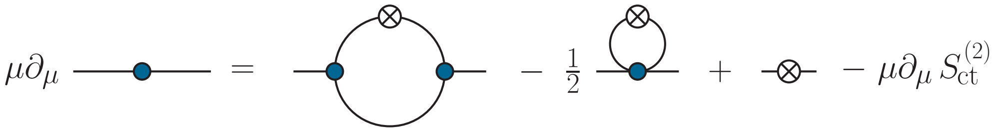

Figure 4.2.: Renormalised CS equation for the inverse propagator. The notation is given in Figure 2.1. The crossed circle is the regulator insertion, $\mu\partial_\mu R = (1-\eta_\phi/2)Z_\phi\mu$

strong dynamics in the vicinity of a phase transition, where the flows are highly sensitive to truncation artefacts. However, it is in principle possible to flow through the phase transition, what can be advantageous if it is difficult to identify a proper starting point in one phase, at which the theory is particularly simple. An example for this situation can be found in quantum mechanics, where the theory for $\mu \to -\infty$ does not approach the classical limit but the instanton dominated regime. We consider the flow of the inverse propagator within the spectral representation. The flow is given by

$$\mu\partial_\mu\Gamma^{(2)}(p^2) = \left(1-\frac{\eta_\phi}{2}\right) Z_\phi\mu \left[D_{\text{pol}}(p^2) - \frac{1}{2}D_{\text{tad}}(p^2)\right] + \left(1-\frac{\eta_\phi}{2}\right) Z_\phi\mu - \frac{1}{2}\,\mu\partial_\mu S_{\text{ct}}^{(2)}, \tag{4.9}$$

where D_{tad} and D_{pol} refer to the tadpole and polarisation diagram, see Figure 4.2. Their general form, in terms of the spectral representation for the propagator and four-point function, is discussed in Appendix A.1.1. Moreover, all quantities in (4.9) depend on the chosen background ϕ. For general spacetime dependent backgrounds $\phi(x)$ this would lead to $\Gamma^{(2)}[\phi](p,q)$. In the explicit computations we consider the background ϕ_0, which is the constant solution of the equation of motion

$$\left.\frac{\delta\Gamma[\phi]}{\delta\phi}\right|_{\phi=\phi_0} = 0\,. \tag{4.10}$$

In the symmetric phase, we have $\phi_0 = 0$, while $\phi_0 \neq 0$ signals the broken phase. The two phases are separated by a second order phase transition in the Ising universality class in three dimensions. From now on we drop the field argument ϕ_0. It is implicitly understood that all correlation functions are evaluated at $\phi = \phi_0$.

In a final step, we substitute μ with $\pm k^2$, to keep the relations to standard fRG flows with momentum cutoffs simple, where k is commonly used. This facilitates the comparison and benchmarking of the real-time results obtained with the spectral fRG. For example, the three dimensional ϕ^4-theory has been studied abundantly within the Euclidean fRG, including systematic studies of the convergence of approximation schemes, for a recent review see [114]. These results carry over straightforwardly to the present approach, and the Euclidean correlation functions obtained from the spectral functions can be directly compared. This substitution leads us to

$$k^2 = |\mu|\,, \qquad \partial_t = k\,\partial_k = 2\mu\partial_\mu\ , \tag{4.11}$$

where the (negative) RG-time $t = \log(k/k_{\text{ref}})$ is measured relatively to a suitable reference scale or mass.

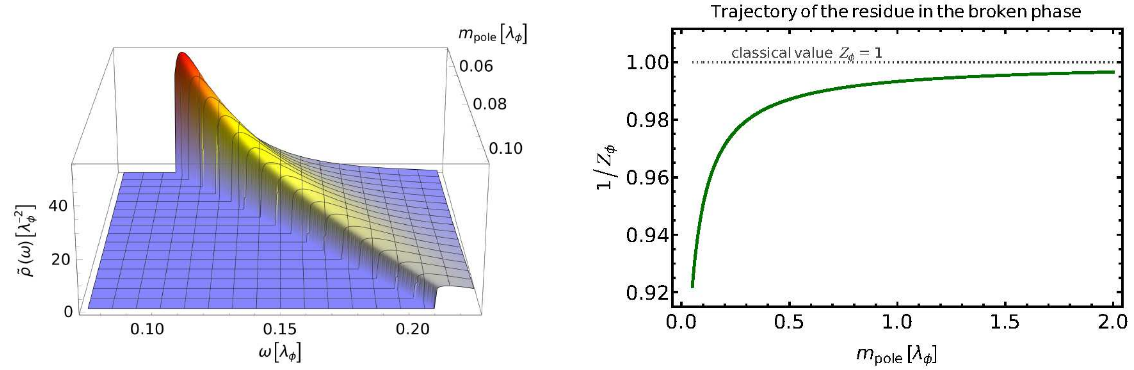

(a) Scattering tail $\tilde\rho_k$ for vanishing spatial momentum $\vec{p} = 0$ as a function of the spectral value ω and the pole mass $m_{\rm pole}$ for $1/20 \leq m_{\rm pole}/\lambda_\phi \leq 1/10$.

(b) Amplitude $1/Z_\phi$ of the pole contribution of the spectral function (4.14) as a function of the pole mass $m_{\rm pole}$ for $1/20 \leq m_{\rm pole}/\lambda_\phi \leq 1/2$. The classical value for Z_ϕ is indicated in grey.

Figure 4.3.: Spectral function ρ, (4.14), for different pole masses $m_{\rm pole}/\lambda_\phi$, measured in the fixed coupling λ_ϕ.

4.1.3. Spectral on-shell renormalisation

We proceed with discussing the on-shell spectral renormalisation, using the direct access to Minkowskian momenta. In (1+2)-dimensions, both diagrams in the CS flow of the inverse propagator (4.9) are manifestly finite and do not need regularisation. The flow of the counter term action $\mu\partial_\mu S_{\rm ct}$ only guarantees the implementation of the chosen renormalisation conditions. The (1+2)-dimensional ϕ^4-theory is super-renormalisable, and has only one UV-relevant direction. This leaves us with one renormalisation condition for the mass. Now we use on-shell renormalisation to keep the full pole mass on the classical input mass (4.2) with $m^2_{\rm pole} = k^2$ in the symmetric phase, and $m^2_{\rm pole} = 2k^2$ in the broken phase. This leads us to

(i) symmetric phase:

$$\Gamma^{(2)}[\phi_0]\Big|_{p^2=-k^2} = 0\,, \tag{4.12}$$

(ii) broken phase:

$$\Gamma^{(2)}[\phi_0]\Big|_{p^2=-2k^2} = 0\,. \tag{4.13}$$

In the symmetric phase, the first allowed scattering process is the 1 → 3 scattering, and the onset of the scattering continuum is located at three times the pole mass. In turn, in the broken phase with 1 → 2 scattering, the onset of the scattering continuum of the spectral function is located at twice the pole mass. Thus, the spectral function reads

$$\rho(\lambda) = \frac{2\pi}{Z_\phi}\delta(\lambda^2 - m^2_{\rm pole}) + \theta(\lambda^2 - m^2_{\rm scat})\tilde\rho(\lambda)\,, \tag{4.14}$$

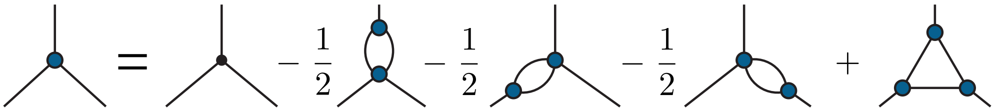

Figure 4.4.: Truncated DSE for the three-point function in the skeleton expansion.

with $m_{\text{scat}} = 3m_{\text{pole}}$ (symmetric phase) and $m_{\text{scat}} = 2m_{\text{pole}}$ (broken phase). In Figure 4.3, we show the scale evolution of the spectral function ρ in the broken phase: in Figure 4.3a we depict the scattering tail $\tilde{\rho}$, and in Figure 4.3b we depict the amplitude of the pole contribution. All quantities are measured relative to the coupling λ_ϕ.

The spectral tail is rising towards smaller pole masses for a fixed classical coupling, and in turn the amplitude $1/Z_\phi$ of the pole contribution is decreasing. In combination, the sum rule

$$1 = \frac{1}{Z_\phi} + \int_{m_{\text{scat}}^2}^{\infty} \frac{d\lambda^2}{2\pi} \tilde{\rho}(\lambda)\,, \tag{4.15}$$

i.e., (3.13a), with $Z_{\text{UV}} = 1$, holds during the evolution. The growing importance of the scattering processes can be understood from the fact that the dynamics of the theory only depend on the dimensionless ratio λ_ϕ/m_ϕ with $m_\phi \propto k$. Hence, the effective coupling grows strong for smaller pole masses and on the other hand the dynamics of the theory are vanishing for asymptotically large pole masses.

In contrast to the Callan-Symanzik or mass regulator used in the present work, commonly used regulators in Euclidean flows decay for momenta larger than the IR cutoff k. This provides manifestly finite flows without the need of further renormalisation. Moreover, for Euclidean momenta, the respective flows of lower order correlation functions decay faster than for a CS regulator. In Minkowski space, however, the CS or mass regulator has the welcoming property that the one-loop flow of $\rho(\omega)$ contains only classical correlation functions and is maximally local. While this is trivial in the symmetric phase where the one-loop flow only shifts the pole mass and does not generate a scattering continuum, it is non-trivial in the broken phase. There, the flow of the scattering continuum is given by a single delta function at the onset of the scattering spectrum, which originates from $\partial_t \operatorname{Im} \Gamma^{(2)} \propto \delta(\omega^2 - 4m_{\text{pole}}^2)$. Since the mass pole constitutes the dominant part of the propagator, the flow of the spectral function at spectral values larger than the flowing onset $2m_{\text{pole}}$, which is solely induced by the scattering tail, is sub-leading.

4.1.4. Flowing with the minimum

In general, the flow equation (4.8a) can be evaluated for arbitrary values of the external field ϕ, which requires the inclusion of the full effective potential. However, this goes beyond the scope of this work, and we simply evaluate the flow on the solution ϕ_0 of the equation of motion (4.10). This is a commonly used truncation as it gives access to the physical correlation functions.

In the present fRG approach with the spectral CS regulator, the flow takes place in theory space and the effective action is physical for all values of k. In the broken phase, the minimum of the full effective potential depends on k, and the total mass flow of

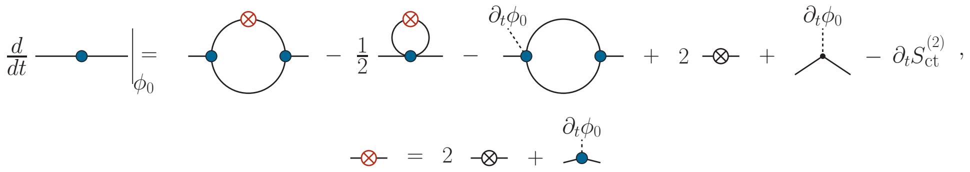

Figure 4.5.: Diagrammatic representation of the flow of the two-point function on the flowing minimum in the broken phase. The red crossed circle comprises the scale derivative of the mass parameter and the three-point function, where the additional factor of 2 comes from the change from μ to k. The dashed lines indicate the contraction with $\partial_t\phi_0$.

the two-point function is given by the flow diagrams originating from the CS equation, $\partial_t\Gamma^{(2)}[\phi_0](p)$ and a term proportional to the mass flow of ϕ_0,

$$\frac{d}{dt}\Gamma^{(2)}[\phi_0](p) = \partial_t\Gamma^{(2)}[\phi_0](p) + \Big(\partial_t\phi_0\, \Gamma^{(3)}[\phi_0]\Big)\,(p)\,. \tag{4.16}$$

The novel ingredient in the present setup originates in the tree-level k-dependence of $\phi_0 \approx \sqrt{6k^2/\lambda_\phi} + \mathcal{O}(\lambda_\phi k)$, where the second term comprises the loop corrections. This tree-level dependence is usually absent in the flow of the minimum in standard momentum-shell flows. There, $\partial_t\phi_0$ only comprises the effects of the momentum shell integration and hence is inherently one-loop and beyond. The tree-level k-dependence of ϕ_0 in the present case triggers a tree-level k-dependence of $\partial_t\phi_0\Gamma^{(3)}(p)$ and the tree-level flow of the physical two-point function considered here reads

$$\frac{d}{dt}\,\Gamma^{(2)}\Big|_{\text{tree-level}} = -2k^2 + \partial_t\phi_0 S^{(3)}[\phi_0] = 4k^2\,, \tag{4.17}$$

where the classical three-point function is given by $S^{(3)}[\phi] = \lambda_\phi\phi$. Note that only the combination of both terms leads to the expected positive flow of the physical mass, while the flow of the mass parameter $-k^2$ has a negative sign.

To obtain the full momentum structure of the second term in of (4.16), we first note that the additional leg of the three-point function is always augmented with an incoming momentum of zero, as it is contracted with the scale derivative of a constant field. The full momentum dependence can then be incorporated via the DSE of the three-point function, see Figure 4.4, which allows for an exact diagrammatic flow of the two-point function on the physical minimum. In the presence of approximations, a fully self-consistent treatment would require us to use the integrated flow of $\Gamma^{(3)}[\phi_0](p,0)$. However, also the flow of $\Gamma^{(3)}[\phi_0]$ includes a similar additional term as in (4.17), which is proportional to the four-point function. To avoid solving the flow of the three- and four-point function, we resort to the DSE to include the leading momentum dependence of the (contracted) three-point function. To ensure the correct RG-scaling of the flow equation, we further employ the skeleton expansion in the DSE, where every vertex is dressed. Approximating $\Gamma^{(n>4)} \approx 0$ and dropping the remaining two-loop diagrams, we arrive at the simple diagrammatic structure of the three-point function depicted in Figure 4.4.

Additionally, using the DSE for $\Gamma^{(3)}$ in (4.16) demonstrates the structure of the flow as a total derivative. To make this explicit, we choose the vertical leg in Figure 4.4 to be contracted with $\partial_t\phi_0$. Then, the three-point functions connected to this leg carry only internal momenta, and we approximate them as constant. With that, the first fish- and the triangle diagram in Figure 4.4 are proportional to the tadpole and polarisation diagram respectively, and the second term on the RHS of the flow (4.16) reads

$$\left(\partial_t\phi_0\,\Gamma^{(3)}[\phi_0]\right)(p) = \partial_t\phi_0\left(S^{(3)}[\phi_0] - \frac{1}{2}\Gamma^{(3)}[\phi_0]\,D_{\text{tad}}(p) - D_{\text{fish}}(p) + \Gamma^{(3)}[\phi_0]\,D_{\text{pol}}(p)\right)\,. \tag{4.18}$$

Note that the explicit three-point functions on the right-hand side are now momentum independent. For the full expressions of the spectral diagrams we refer to Appendix A.1.1. We discuss our approximations for the remaining vertices in Section 4.1.5.

Substituting (4.9) and (4.18) into (4.16), we eventually arrive at the full flow equation of the two-point function. Its diagrammatic representation is depicted in Figure 4.5. It is illuminating to consider the one-loop structure of the flow, where the nature of the flow being a total derivative can be read off Figure 4.5. Then, the red crossed circle comprises the total derivative of the internal propagators in the (one-loop) polarisation and tadpole diagram, while the fish-diagram accounts for the running of the three-point vertices. The full equation reads

$$\begin{aligned}\frac{d}{dt}\Gamma^{(2)}[\phi_0](p) =\; &(\partial_t\phi_0)\,S^{(3)}[\phi_0] - (2-\eta_\phi)\,Z_\phi k^2\\ &+\dot{\mathcal{R}}\left[-\frac{1}{2}D_{\text{tad}} + D_{\text{pol}}\right] - \partial_t\phi_0 D_{\text{fish}} - \partial_t S_{\text{ct}}[\phi_0]\,,\end{aligned} \tag{4.19a}$$

where

$$\dot{\mathcal{R}} = \left(\partial_t\phi_0\Gamma^{(3)}[\phi_0] - (2-\eta_\phi)\,Z_\phi k^2\right)\,, \tag{4.19b}$$

is represented as red crossed circle in Figure 4.5. Note the appearance of a relative minus sign in front of the mass derivative contribution (second term) to (4.19b) due to $\mu = -k^2$ in the broken phase. The first line in (4.19a) carries the trivial, tree-level running of inverse propagator. It consists of the running of the mass parameter and the classical part of the three-point function, connected to the flow of the minimum. Its mean-field value cannot be altered by the renormalisation condition and is, analogue to the respective term in $\dot{\mathcal{R}}$, crucial to recover the correct sign of the flow, see (4.17). A detailed evaluation of (4.19a) can be found in Appendix A.1.2.

4.1.5. Approximations and real-time flows

In the following Section, we discuss the approximations used for the higher correlation functions, which lead to non-trivial spectral flow-equations in both phases. This enables us to write down the renormalised flow equations for the two-point function and evaluate them on the real frequency axes.

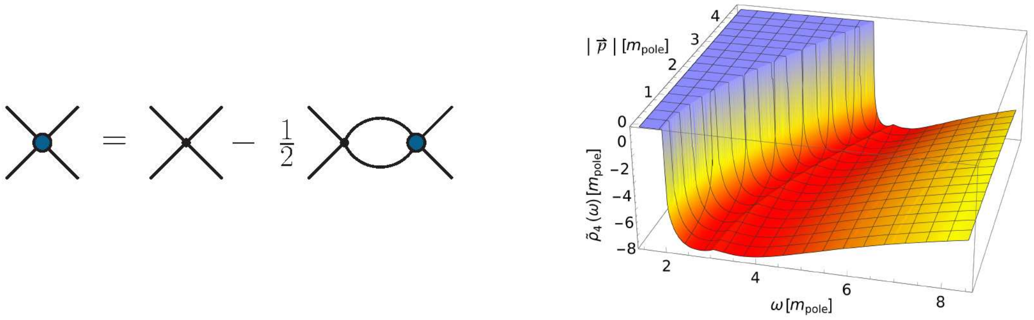

(a) Bubble resummed four-point function.

(b) Spectrum of the resummed four-vertex.

Figure 4.6.: Diagrammatic representation and spectral function of the four-vertex in a bubble resummed, s-channel approximation. It features Lorentz invariance and the spectral function exhibits a sharp onset at the two-particle threshold. and has a visible three-particle onset at $3m_{\rm pole}$ in the broken phase

In the ϕ^4-theory, correlation functions of an odd number of fields, $\Gamma^{(2n+1)}[\phi]$, are proportional to the mean field ϕ. In the present approximation we only consider three- and four-point functions, setting all the higher correlation functions to zero:

$$\Gamma^{(n>4)} \approx 0\,. \tag{4.20}$$

Then, the three-point function is proportional to a product of the four-point function and ϕ_0. This closes our approximation.

For constant vertices, the tadpole diagram only provides a constant contribution to the flow of the two-point function. This contribution is absorbed completely in the on-shell renormalisation condition (4.13) and (4.12), for the broken and symmetric phase respectively. In the symmetric phase of the theory with $\phi_0 = 0$, the tadpole is the only contribution to the flow of the two-point function. Hence, the scattering tail originates only from the non-trivial momentum dependence of the four-point function. In a first but important step towards the full momentum dependence of $\Gamma^{(4)}(p_1, ..., p_4)$ we use an s-channel resummation of the full four-point function, see Figure 4.6a,

$$\Gamma^{(4)}(p^2) = \frac{\lambda_\phi}{1 + \frac{\lambda_\phi}{2}\int_q G(p+q)G(q)}\,. \tag{4.21}$$

In (4.21), $p^2 = s = (p_1 + p_2)^2$ is the s-channel momentum, and we choose vanishing t and u channels to perform the resummation: $(p_3 - p_1)^2 = (p_1 - p_4)^2 = 0$. This approximation admits the simple spectral representation of the four-point function (4.5), see also [54].

Figure 4.6b shows the spectrum of the four-point function in the s-channel approximation discussed above. It shows the 2 → 2 scattering onset at twice the pole mass $m_{\rm pole}$ of the field ϕ. The next threshold from the 2 → 3 scattering is also visible, but the result also contains the strongly suppressed threshold of higher order scattering processes. A more detailed discussion of our results is given in Section 4.1.6.

We emphasise that (4.21) only holds true in the symmetric phase. In contrast, in the broken phase the flow or BSE for the four-point function contains additional diagrams with two or four three-point vertices. Their combined contributions are readily estimated and are suppressed by a factor 1/8. Hence, they are dropped in the following computation. Accordingly, we use (4.21) in both phases.

Note also that the four-point function exhibits a bound state pole below $2m_{\text{pole}}$ close to the phase transition. This is discussed for example in [2, 135] in terms of a Bethe-Salpeter equation, see also Section 4.2, and indeed seen in lattice and fRG calculations, see [136–138]. The present s-channel resummation for the four-vertex does not include the resonant channel. A full bound state analysis and the systematic inclusion of other channels will be considered elsewhere.

It is left to specify the three-point function $\Gamma^{(3)}(p_1, p_2, p_3)$ in (4.19a). In contrast to the pivotal importance of the momentum dependence of the four-point function that of the three-point function is averaged out in the vacuum polarisation and the fish diagram. For the sake of simplicity, we therefore approximate the full vertex by its value at vanishing momenta, $p_i = 0$ for $i = 1, 2, 3$. There, the three-point function is given by the third derivative of the effective potential on the equations of motion, $V_{\text{eff}}^{(3)}(\phi_0)$. The effective potential $V_{\text{eff}}(\phi)$ is the quantum analogue of the classical potential, and is nothing but the effective action $\Gamma[\phi]$, evaluated for constant fields ϕ_c,

$$V_{\text{eff}}(\phi_c) = \frac{1}{\mathcal{V}}\Gamma[\phi_c]\,, \qquad \mathcal{V} = \int d^3x\,. \tag{4.22}$$

Due to the Z_2-symmetry of the ϕ^4-theory under $\phi \to -\phi$, the effective potential is symmetric, $V_{\text{eff}}(-\phi) = V_{\text{eff}}(\phi)$. Moreover, it admits an expansion about the solution to the equation of motion, $\phi^2 = \phi_0^2$, which is valid for $\phi^2 \geq \phi_0^2$. The latter constraint on the modulus of $(\phi^2 - \phi_0^2)$ originates from the fact that the classical effective potential is the double Legendre transform of the classical potential. In the case of a non-convex potential it is simply the convex hull. Schematically, this is depicted in Figure 4.1.

The effective potential satisfies its own flow equation, and for the sake of completeness we briefly discuss its derivation and explicit form in Appendix A.1.6, more details can be found in [1]. The present computation can be augmented by the full flow of the effective potential, effectively leading to a cutoff dependence of the coupling λ_ϕ in (4.21) and similar changes. While this provides further quantitative precision to the computation, it goes beyond the scope of the present work and will be presented elsewhere. Here we shall consider the expansion up to $(\phi^2 - \phi_0^2)^2$, dropping higher order terms in accordance with (4.20), and discuss the symmetric and broken phase separately in Section 4.1.5.2 and Section 4.1.5.1 below.

4.1.5.1. Symmetric phase

In the symmetric phase with $\phi_0 = 0$ in (4.10), we use a Taylor expansion about $\phi^2 = 0$ for the effective potential,

$$V_{\text{eff}}(\phi) = \sum_{n=1}^{\infty} \frac{\lambda_n}{2n!}\phi^{2n}\,. \tag{4.23}$$

The first two couplings, λ_1 and λ_2 are related to the correlation functions $\Gamma^{(2)}$ and $\Gamma^{(4)}$ considered here. Hence, the coupling λ_1 agrees with the curvature mass squared in the symmetric phase, where the curvature mass is defined as

$$m_{\text{curv}}^2 = V_{\text{eff}}^{(2)}(\phi_0) = \Gamma^{(2)}[\phi_0](p = 0)\,, \tag{4.24}$$

in both phases. Moreover, the coupling λ_2 is nothing but the full four-point function, evaluated at vanishing momentum. In summary we have

$$\lambda_1 = m^2_{\text{curv}}\,, \qquad \lambda_2 = \Gamma^{(4)}(p=0)\,. \tag{4.25}$$

For the initial UV pole mass $m_{\text{pole}} = \Lambda$, the curvature mass and the pole mass agree, $\lambda_1 = \Lambda^2$, and the initial coupling is the classical one, $\lambda_2 = \lambda_\phi$. Hence, the initial effective potential $V_{\text{UV}}(\phi)$ at $k = \Lambda$ reads

$$V_{\text{UV}}(\phi) = \frac{1}{2}\Lambda^2\phi^2 + \frac{1}{4!}\lambda_\phi\,\phi^4\,. \tag{4.26}$$

With the above approximations, all higher correlation functions are fixed and the flow equation of the two-point function on the real frequency axes reads

$$\partial_t\Gamma^{(2)}(\omega_+) = -\frac{Z_\phi\,(2-\eta_\phi)\,k^2}{2} D^{\text{dyn}}_{\text{tad}}(\omega_+) + 2Z_\phi k^2 - \partial_t\hat{S}^{(2)}_{\text{ct}}\,, \tag{4.27}$$

where the retarded limit is given by $\omega_+ = -\mathrm{i}(w + \mathrm{i}0^+)$ and is explicitly carried out in Appendix A.1.5. $\hat{S}^{(2)}_{\text{ct}}$ is given schematically by

$$\hat{S}^{(2)}_{\text{ct}} = \text{diagramms}\left(p^2 = -k^2\right)\,. \tag{4.28}$$

We denoted the counter term action with a tilde since we already dropped constant terms in the flow of order $\lambda_\phi k$. Hence, only the dynamic part of the tadpole $D^{\text{dyn}}_{\text{tad}}$ contributes. It arises from the scattering tail of $\Gamma^{(4)}(p)$ and carries the spectral structure of the polarisation diagram, see (A.4). In particular, the deviation of the constant term in Figure 4.2 from its classical value, $2k^2$, is of order $(\lambda_\phi k)$ and is therefore absorbed in the renormalisation constant. With that, (4.27) is consistent with the flowing on-shell renormalisation condition (4.12).

4.1.5.2. Broken phase

In the broken phase with $\phi_0 \neq 0$ we use a Taylor expansion about $\phi^2 = \phi_0^2$ for the effective potential,

$$V_{\text{eff}}(\phi) = \sum_{n=2}^{\infty} \frac{\lambda_n}{2n!}\left(\phi^2 - \phi_0^2\right)^n\,. \tag{4.29}$$

At vanishing momentum and constant fields, the correlation functions derived from the effective action $\Gamma[\phi_0]$ coincide with the moments of the effective potential. We consider n-point functions for $n \leq 4$ with

$$\begin{aligned}
\Gamma^{(2)}[\phi_0]\,(p=0) &= \frac{1}{3}\lambda_2\phi_0^2\,,\\
\Gamma^{(3)}[\phi_0]\,(p=0) &= \lambda_2\,\phi_0 + \frac{\lambda_3}{15}\,\phi_0^3\,,\\
\Gamma^{(4)}[\phi_0]\,(p=0) &= \lambda_2 + \frac{2}{5}\lambda_3\,\phi_0^2 + \frac{1}{105}\lambda_4\,\phi_0^4\,,
\end{aligned} \tag{4.30}$$

In contrast to the symmetric phase discussed in Section 4.1.5.1, also higher order terms with couplings λ_n contribute due to $\phi_0 \neq 0$. For this reason we have indicated the

ϕ_0-dependence of $\Gamma^{(n)}$ in (4.30). As discussed below (4.10), we generically drop the ϕ_0-dependence for the sake of readability, it is implicitly assumed that all expressions are evaluated at ϕ_0.

As a consequence of (4.20), all expansion coefficients λ_n with $n \geq 3$ vanish. The three and four-point couplings are then given by

$$\Gamma^{(3)}(0) = \Gamma^{(4)}(0)\phi_0 \,, \qquad \lambda_2 = \Gamma^{(4)}(0) \,. \tag{4.31}$$

With (4.24) we can express the minimum of the effective potential in terms of the curvature mass and λ_2, yielding

$$\phi_0^2 = \frac{3m^2_{\text{curv}}}{\Gamma^{(4)}(0)} \,, \tag{4.32}$$

Using (4.32), the three-point function is expressed in terms of the full two- and four-point functions at vanishing momentum,

$$\Gamma^{(3)}(0) = \sqrt{3\,\Gamma^{(4)}(0)}\, m_{\text{curv}} \,. \tag{4.33}$$

Evidently, in the classical limit with $Z_\phi = 1$ and $\tilde{\rho}_k = 0$, the curvature mass agrees with the pole mass. This limit is approached for asymptotically large pole masses, where the effective coupling $\lambda_\phi / m_{\text{pole}}$ tends towards zero. Hence, the ultraviolet effective potential $V_{\text{UV}}(\phi)$ with $k = \Lambda \to \infty$ is augmented with a classical dispersion with $\mu = -\Lambda^2$ and the initial (classical) coupling $\lambda_2 = \lambda_\phi$,

$$V_{\text{UV}}(\phi) = \frac{1}{4!}\lambda_\phi \left(\phi^2 - \phi_0^2\right)^2 \,, \qquad \phi_0^2 = \frac{6\Lambda^2}{\lambda_\phi} \,, \tag{4.34}$$

for $\phi^2 \geq \phi_0^2$. The initial curvature and pole mass are given by

$$m^2_{\text{pole}} = m^2_{\text{curv}} = 2\Lambda^2 \,. \tag{4.35}$$

With these approximations, the real-time flow of the two-point function in the broken phase, derived in Appendix A.1.2, reads

$$\partial_t \Gamma^{(2)}(\omega_+^2) = \dot{\mathcal{R}} \left(D_{\text{pol}}(\omega_+^2) - \frac{1}{2} D^{\text{dyn}}_{\text{tad}}(\omega_+^2) \right) + A\, D_{\text{fish}}(\omega_+^2) + 4 Z_\phi k^2 - \partial_t \hat{S}^{(2)}_{\text{ct}} \,. \tag{4.36}$$

The prefactors are given in (A.10) and $\hat{S}^{(2)}_{\text{ct}}$ is given by

$$\hat{S}^{(2)}_{\text{ct}} = \text{diagramms}\left(p^2 = -2k^2\right) \,. \tag{4.37}$$

Additionally to the polarisation topology, we note that flow equation in the broken phase differs from that in the symmetric phase. The constant part of (4.36) carries an additional factor of 2. This resembles the additional factor 2 of the squared pole-mass in the broken phase compared to its symmetric phase counterpart. Also the prefactor of the tadpole diagram deviates from the symmetric case, since it includes the implicit k-dependence of the internal lines via the flowing physical minimum.

4.1.5.3. Resumé

In both phases, we have a positive curvature mass $m_{\text{curv}} > 0$ on the equation of motion ϕ_0. Its value is related to the pole mass $m_{\text{pole}} = k$ in the symmetric, and $m_{\text{pole}} = 2k$ in the broken phase. The difference between the flows is the existence of vertices $\Gamma^{(2n+1)}$ in the broken phase. They are proportional to sums of powers of ϕ_0, see (4.30), and hence vanish in the symmetric phase. Specifically, the flow of the two-point function in the broken phase contains the diagrammatic topology of a vacuum polarisation, see Figure 4.5.

This leads us to the following structure: the CS flows are initiated deep in the symmetric and deep in the broken phase for large pole masses and a given classical coupling λ_ϕ, see (4.26) and (4.34) respectively. For the broken phase this entails that also the field expectation value at the initial scale is large as it scales with Λ, see (4.32) and (4.34). Then, the pole mass is successively lowered and for $k = 0$ one reaches the phase transition point from both sides. In particular, the flows do not leave the broken or symmetric phase. This is in seeming contradiction to the standard fRG picture in a scalar theory, where flows in the broken phase may end up in the symmetric phase, and those in the symmetric phase end up deeper in the symmetric phase. This apparent contradiction is resolved by the fact that ϕ_0 in the standard fRG is defined from the subtracted EoM. There, the trivial cutoff flow, which is $\propto k^2\phi^2$, is subtracted from the effective potential, and one recovers physics only in the limit $k \to 0$.

4.1.6. Results

In this Section, we present results for the non-perturbative spectral functions of the scalar propagator in the symmetric and broken phase. The discussion of the numerical implementation is deferred to Appendix A.6.1. The results allow for an investigation of the scattering processes in both phases. The present results are in remarkable quantitative agreement with that obtained with the spectral DSE in [54]. This agreement of the spectral functions from these two different functional approaches hold true for a large range of effective couplings λ_ϕ/m_ϕ, see Figure 4.7a, see also Table 4.1. In this coupling regime this agreement provides a non-trivial reliability check for both functional approaches, thus decreasing the respective systematic error.

$\lambda_\phi/m_{\text{pole}}$	$1/Z_\phi$ (fRG)	$1/Z_\phi$ (DSE)	$1/Z_\phi(\phi_0 = 0)$
5	0.971	0.969	0.9998
10	0.950	0.945	0.9995
20	0.921	0.907	0.9986

Table 4.1.: Amplitudes $1/Z_\phi$ of the pole contribution for given effective couplings, corresponding to the scattering tails displayed in Figure 4.7a and Figure 4.7b.

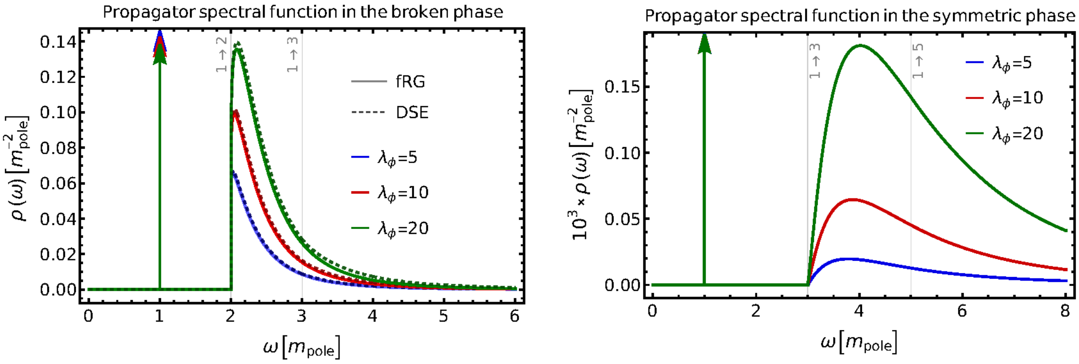

(a) Spectral function of the propagator. The $1 \rightarrow 2$ and $1 \rightarrow 3$ particle scattering onsets are indicated in grey.

(b) Spectral functions in the symmetric phase. $1 \rightarrow 3$ and $1 \rightarrow 5$ onsets are indicated in grey.

Figure 4.7.: Spectral functions in the symmetric phase (left) and in the broken phase. The allowed $1 \rightarrow n$ onsets are indicated by vertical gray lines.

4.1.6.1. Symmetric phase

In the symmetric phase with $\phi_0 = 0$ we are left with the tadpole diagram in the flow of the two-point function (4.9). The resummation (4.21) introduces a non-trivial momentum dependence to the four-point function and, in consequence, also to the tadpole diagram. This allows to calculate the propagator spectral function in the symmetric phase, i.e., at vanishing field value, where the polarisation diagram is absent. For the respective flow equation on the real frequency axes see (4.27). The resulting spectral function is shown in Figure 4.7b. In the symmetric phase, the scattering continuum starts at $3m_{\rm pole}$. As mentioned above, the dynamic tadpole contribution (A.4) carries the momentum structure of the polarisation diagram, resembling the s-channel structure of the four-vertex. Still, the onset of its imaginary part is at thrice the pole mass, since the bubble resummed vertex represents a series of $2 \rightarrow 2$ scatterings which leads to a generic two-particle onset of ρ_4. The quantum corrections to the symmetric phase propagator are small compared to the broken phase. The amplitude on the mass pole is close to one compared to the respective values in the broken phase, see Table 4.1. This is expected, since the first dynamic contribution is of two-loop order and corresponds to the sunset topology.

4.1.6.2. Broken phase

In the broken phase the condensate is non-vanishing, $\phi_0 \neq 0$. To compute the spectral function, the flow equation is evaluated on the real frequency axes see (4.36).

The N-particle onset positions of the spectral scattering tail are governed by the imaginary part of (4.36). For the polarisation diagrams, where only propagators come into play, the flow exhibits an onset at the sum of the two mass-poles. In contrast, the contribution of the tadpole leads to an onset at thrice the pole-mass, as the four-point spectral function only consists of a scattering continuum starting at $2m_{\rm pole}$, cf. Figure 4.8. A more detailed discussion of the scattering onsets in general is found in Appendix A.1.5 and specifically for the tadpole in Section 4.1.6.1.

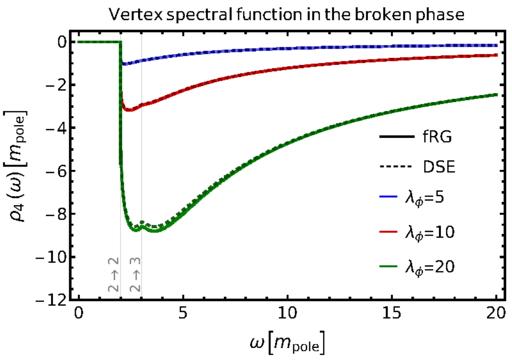

Figure 4.8.: Spectral function of the four-point function. The 2 → 2 and 2 → 3 particle scattering onsets are indicated in grey.

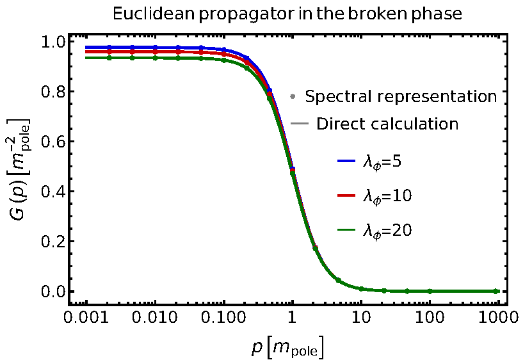

Figure 4.9.: Euclidean propagator in the broken phase from the direct computations and spectral representations

In Figure 4.7a the spectral function from the current fRG approach is compared to spectral DSE results from [54]. Every quantity is measured relative to the respective pole mass to facilitate comparison with the DSE results. This allows to compare the relative magnitude of the scattering continua for different coupling strengths. For effective couplings $\lambda_\phi/m_{\text{pole}} \lesssim 20$, the spectral weight of the scattering continuum is sub-leading, as can be inferred from the combination of Figure 4.3b and the sum rule (4.15). The amplitudes of the pole contributions are listed in Table 4.1.

We find a remarkable agreement of both methods in the tested coupling range. For effective couplings $\lambda_\phi/m_{\text{pole}} \approx 20$, the deviations start growing, specifically at the thresholds. Deviations between both methods arise due to differences in the resummation structure of the two functional equations in the current truncation. The convergence of functional techniques for a large range of couplings is non-trivial and strengthens our confidence in spectral functional approaches.

In general, the tail of the propagator spectral function is enhanced for stronger couplings, while the residue of the mass pole decreases as the scattering states become more accessible due to the rising dimensionless interaction strength. The three- and higher N-particle onsets are graphically not visible in the full spectral functions of Figure 4.7a, but present in the data. In the limit of large couplings we expect the three-particle onset to become more pronounced as the tadpole contribution becomes large.

The four-point spectral function shown in Figure 4.8 consists of only a negative scattering tail corresponding to a 2 → 2 scattering process. For higher couplings, the three-particle onset becomes visible. The different suppression of higher N-particle thresholds in the propagator- and four-point spectrum are explained by dimensional analysis. While for the propagator spectral function, higher N-particle onsets are suppressed by their squared energy threshold, the four-point spectral function decays only with λ^{-1}, leading to a suppression linear in their respective energy thresholds. In both cases, four-particle or higher onsets are strongly suppressed, since they come with at least one additional loop each.

Figure 4.9 shows the Euclidean propagators corresponding to the spectral functions of Figure 4.7a. As a cross-check, we compare the Euclidean propagator calculated from the spectral representation to the propagator directly obtained from the integrated Euclidean flow. We find the spectral representation to hold.

4.1.7. Spectral flows close to the phase transition

This subsection is based on [5]. *All practical calculations have been carried out by Konrad Kockler in the context of his Bachelor thesis, which I co-supervised. This includes the additional material for this Section in Appendices A.1.7 to A.1.10 and A.6.2.*

As discussed below (4.10), this theory exhibits a second order phase transition of the Ising-universality class, given by the Wilson-Fisher fixed point of the renormalisation group. It has two independent critical scaling exponent, that are carried by the propagator $G(p)$ of the theory.

$$G(p^2) \propto \frac{1}{(p^2)^{1-\eta/2}}\,, \tag{4.38}$$

characterised by a single critical exponent $\eta \approx 0.036$. To probe this scaling region for real frequencies, we approach it from the symmetric side, see also the discussions in Sections 4.1.5.1 and 4.1.6.1. In the following, we present results for the spectral functions near the phase transition and extract the scaling exponent η from our computations in three different ways: utilizing the spectral tail of the propagator, the wave function renormalisation on the pole, and the scaling behaviour of the four-point spectrum. We compare our results for the critical exponent to that obtained via a fixed point analysis in LPA' and discuss the necessary improvements to obtain a quantitative description of the scaling regime in the future. In the scaling limit, the scaling form of the propagator (4.38) carries over to the single particle spectral function,

$$\rho(\lambda) \propto \lambda^{-2+\eta}\,. \tag{4.39a}$$

In the absence of approximations, the exponent in (4.39a) is the critical exponent $\eta \approx 0.036$ of the three-dimensional Ising model. The s-channel spectral function ρ_4 in (4.5) of the four-point scattering vertex shows the scaling

$$\rho_4(\lambda) \propto \lambda^{1-2\eta}\,. \tag{4.39b}$$

The scaling (4.39b) follows readily from (4.5) and (4.21), and specifically from the scaling behaviour of the fish diagram, for more details see Appendix A.1.8.

We remark that (4.39) cannot hold true for $\eta > 0$ in the UV: the renormalised CS flows with on-shell renormalisation exhibits a sub-leading momentum scaling of the flow $\Gamma^{(2)}(p)$ for large momenta and hence for large spectral values. Accordingly, the momentum dependence of the classical input prevails at large momenta. Note also that (4.39a) for all spectral values violates the sum rule (3.52). Indeed, it can be shown, see e.g. [43, 79], that this sum rule is violated for $\eta > 0$ if (4.39a) holds true for $\lambda \to \infty$. A trivial momentum dependence in the UV with $1/p^2$, which is encoded in the spectral sum rule, is in one-to-one correspondence with canonical commutation relations and hence with unitarity and probability conservation. For $\eta > 0$ we find $\int_\lambda \rho(\lambda) = \infty$.

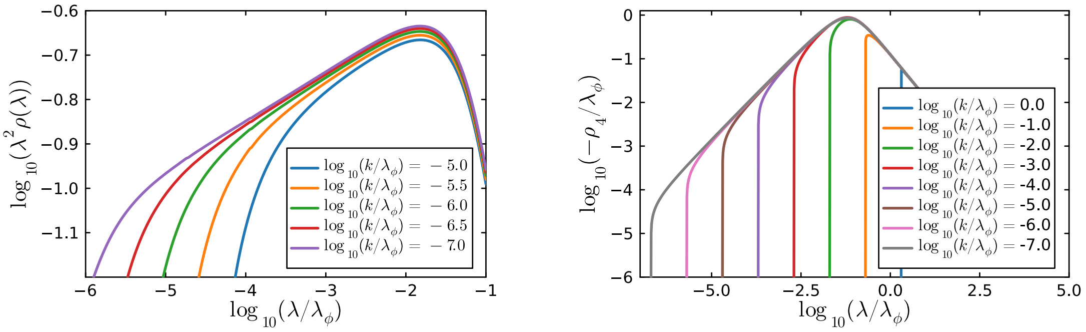

(a) Propagator spectral function in the scaling regime. The trivial dimensional scaling is removed by a multiplication with λ^2. The spectral parameter is measured in units of the bare coupling λ_ϕ.

(b) Scaling behaviour of the vertex spectral function: Both the trivial UV and the non-trivial IR scaling regimes as well as the onsets at $m_{\text{scat}} = 2m_{\text{pole}}$ are visible.

Figure 4.10.: Propagator and vertex spectral function in the scaling regime: The different curves correspond to spectral functions at different pole masses $m_{\text{pole}} = k$, varied over two and seven orders of magnitude respectively. We measure the spectral parameter in units of the classical coupling λ_ϕ.

4.1.7.1. Spectral scaling

We proceed by a discussion of the spectral functions $\rho(\lambda)$ and $\rho_4(\lambda)$ as well as the respective critical exponents defined by the methods (1,2). Our numerical results for the spectral functions are shown in the doubly logarithmic plots in Figure 4.10. The emergence of an increasing scaling window in the spectral regime $\lambda/\lambda_\phi \lesssim 10^{-2}$ with power law decays (4.39) for successively smaller pole masses is clearly visible. The respective critical exponents can be extracted from Figure 4.11a and Figure 4.11b, where we show the sliding scaling exponents $\eta_i(\lambda)$ with $i = \rho, \rho_4$. These sliding scaling exponents are defined by logarithmic spectral derivatives of the logarithms $\log\rho, \log(-\rho_4)$. We also subtract the canonical scalings, to wit,

$$\eta_\rho(\lambda) := 2 + \frac{\lambda}{\rho(\lambda)}\frac{\partial\rho}{\partial\lambda}\,, \tag{4.40a}$$

and

$$\eta_{\rho_4}(\lambda) := 1 - \frac{\lambda}{\rho_4(\lambda)}\frac{\partial\rho_4}{\partial\lambda}\,. \tag{4.40b}$$

For the scaling spectral functions (4.39), the sliding scaling exponents $\eta_i(\lambda)$ reduces to the critical exponent η and $2\,\eta$ respectively. We define the critical exponent η_i by the plateau value of $\eta_i(\lambda)$ in Figure 4.11. Both plateaus extend successively into the infrared in the scaling limit with $\lambda_\phi/m_\phi \to \infty$.

The upper boundary of the plateaus stays constant: as already discussed below (4.39), the s-channel resummation for the four-point function in the current approximation leads to decaying momentum dependence of the flow of the two-point function. This is related to the UV-behaviour of the four-point function, that approaches the classical coupling λ_ϕ

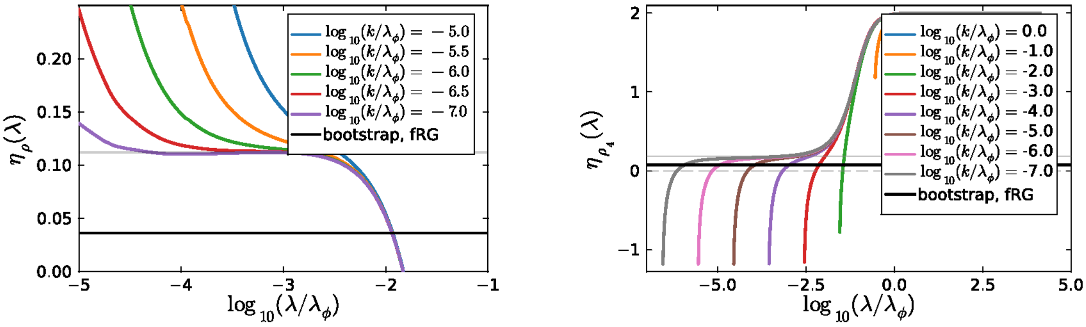

(a) Scaling exponent $\eta_\rho(\lambda)$, (4.40a), as a function of λ.

(b) Scaling exponent $\eta_{\rho_4}(\lambda)$, (4.40b), as a function of λ.

Figure 4.11.: Sliding scaling exponents $\eta_{\rho_i}(\lambda)$ with $i = \rho, \rho_4$ as functions of λ/λ_ϕ. The scaling regime emerges for $\lambda/\lambda_\phi \lesssim 10^{-2}$. We also depict the quantitative reference results by the thick black line: conformal bootstrap, $\eta = 0.03631(3)$, [139], and fRG, $\eta = 0.0361(3)$ from [140].

at high momenta due to the decay of the loop term in (4.21). This behaviour ensures the sum rule. Note also, that the intrinsic scale, at which the four-point function looses scaling, depends on the initial condition, i.e., the initial classical coupling λ_ϕ. For a detailed discussion, see Appendix A.1.8. This freezing of the flow explains the position of the upper boundary. The elimination of the intrinsic scale requires the feedback of non-trivial momentum dependencies of the four-point function as well as a more sophisticated initial condition, for a discussion see Appendix A.1.10.

In conclusion, we extract the critical exponents from the frequency regime, in which the single particle and s-channel vertex spectral functions approach a scaling form. The critical exponents η_i are readily extracted from the plateau values of $\eta_i(p)$, (4.40) for $\lambda/\lambda_\phi \lesssim 10^{-2}$, depicted in Figure 4.11. These plateaus extend towards $\lambda \to 0$ for $m_\phi/\lambda_\phi \to 0$. This leads us to

$$\eta_\rho = 0.111(1)\,, \tag{4.41a}$$

and

$$\frac{\eta_{\rho_4}}{2} = 0.093(5)\,. \tag{4.41b}$$

The disagreement of the respective values for η point at the fact, that our computation has not reached the full scaling limit yet. The loop contributions to the flow equation of the inverse propagator (4.27) and the loop diagram in the denominator of (4.21) still receive considerably large contributions from the *non-scaling* part of the propagator. See also the wave function renormalisation on the pole in Figure 4.12, which still carries approximately half of the spectral weight at $k = 10^{-6}$. We can see in 4.11b, that η_ρ is lowered towards smaller pole masses, while η_{ρ_4} grows in the scaling limit. This entails, that the results in (4.41a) and (4.41b) constitute upper and lower limits for the true η of our computation respectively:

$$0.093(5) \leq \eta \leq 0.111(1)\,. \tag{4.42}$$

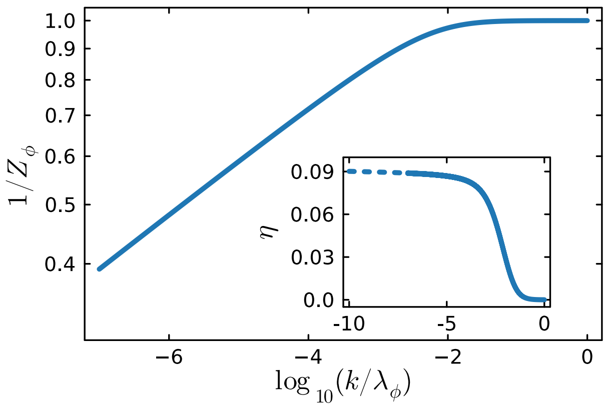

Figure 4.12.: Flow of the spectral weight $1/Z_\phi$ of the pole contribution as a function of the pole mass $m_{\text{pole}} = k$. For large pole masses with $k/\lambda_\phi \to \infty$, Z_ϕ approaches unity, which reflects its UV-irrelevance. For $k/\lambda_\phi \to 0$, the tail successively carries more of the spectral weight, and the pole contribution vanishes with a power law. The inset shows the anomalous dimension η_ϕ, (4.43), as a function of the pole mass. For $k \to 0$ it approaches the critical exponent η.

We close this Section with a discussion of the results (4.41) in view of the critical exponent $\eta \approx 0.036$ in the three-dimensional Ising model with the reference results: conformal bootstrap, $\eta = 0.03631(3)$, [139], and fRG, $\eta = 0.0361(3)$ from [140]. A large part of the deviation can be traced back to the ϕ^4 approximation of the effective potential. This will be illustrated in a comparison of the critical exponents in LPA′ in Section 4.1.7.3. This deficiency is readily resolved by implementing a full effective potential along the lines of [141]. For a discussion, see Appendix A.1.10. The current results are compatible with spectral DSE results in a comparable truncation in the broken phase, see [2], and fRG results on the Keldysh contour, see [142].

4.1.7.2. Cutoff scaling

With (4.41a) and (4.41b) we have obtained η from the spectral scaling discussed in Section 4.1.7.1. The third method consists of using the k-scaling of the wave function on the pole as a proxy for the momentum and spectral scaling. The result for $Z_{\phi,k} = Z_{\phi,k}(p^2 = -k^2)$ as a function of the pole mass $m_{\text{pole}} = k$ is depicted in Figure 4.12. For large pole masses, $k \to \infty$, the wave function Z_ϕ approaches unity: it is a UV-irrelevant coupling, and accordingly its flow dies out. Moreover, the theory approaches the classical one, and the full spectral weight is carried by the pole, while the scattering tail vanishes throughout.

The scaling regime is approached for $k/\lambda_\phi \lesssim 10^{-2}$, which is rather similar to the scaling regime in the spectral functions ρ, ρ_4 with $\lambda/\lambda_\phi \lesssim 10^{-2}$, see Figure 4.10. For $k/\lambda_\phi \to 0$, the theory is increasingly dominated by scattering processes, and the spectral weight $1/Z_\phi$ of the pole contribution is successively suppressed and vanishes for $k = 0$. As the spectral weight of the scattering tale s increasingly dominated by the scaling part, the wave function Z_ϕ on the pole has to scale with $k^{-\eta}$. Similar to (4.40a) and (4.40b) we define

$$\eta_{\phi,k} = -\frac{\partial_t Z_{\phi,k}}{Z_{\phi,k}} \,. \tag{4.43}$$

We remark that $\eta_{\phi,k}$ differs from the standard anomalous dimension used in fRG studies: the latter are typically defined as total t-derivatives at a fixed momentum,

$$\eta_{\phi,k}(p) = -\frac{\partial_t Z_{\phi,k}(p)}{Z_{\phi,k}(p)} \,, \tag{4.44}$$

often evaluated at $p = 0$. In turn, (4.43) is given by $\eta_{\phi,k} = \eta_{\phi,k}(p) - p\partial_p Z_{\phi,k}(p)$, evaluated at $p^2 = -k^2$.

The anomalous dimension $\eta_{\phi,k}$ is depicted in the inlay Figure 4.12 as a function of the pole mass $m_{\text{pole}} = k$. Figure 4.12 also shows Z_{ϕ_k}, and the scaling limit is visible in both quantities. We read off the critical exponent η as the limit $\lim_{k\to 0} \eta_{\phi,k}$ with

$$\eta = \eta_{\phi,k\to 0} = 0.095(9) \,. \tag{4.45}$$

Equation (4.45) agrees well with the critical exponent obtained from the spectral functions, (4.41a) and (4.41b), all of which provide a value $\eta \approx 0.1$. In order to appreciate its accuracy, it should be contrasted with similar approximations in the derivative expansions, which is done in the next Section.

4.1.7.3. Benchmarks and extensions

We close Section 4.1.7 with a discussion of the systematics of the present approximation, its embedding in existing results, and of systematic improvements. In the present work we aimed at the computation of fully momentum-dependent real-time correlation functions with an emphasis on the approach to and the scaling in the scaling regime around a second order phase transition. The respective critical exponent η is one of the outcomes of this analysis, but it was not the primary target. Still, we will embed the present results and the underlying approximation in the landscape of dedicated fRG computations of critical exponents. Typically, these computations are done within a fixed point analysis of the fRG which allows for the most direct access to critical physics but does not cover the interface to the non-universal regime. These results have mostly been achieved within the derivative expansion, for an overview see the review [114]. In terms of comparability of fixed point the current approximation with momentum- but field-independent dressings fits to the LPA$'$ (effective potential and cutoff dependent wave function) that lies in between the 0th and first order of the derivative expansion.

In contradistinction to LPA$'$ we have considered full momentum-dependent propagators and vertices but only considered the effective potential up to the order ϕ^4. Moreover, we approached the scaling regime from the symmetric regime while the fixed point analysis reveals a finite dimensionless expectation value of the field with the fixed point value $\bar\rho^* \neq 0$ and $\bar\rho = Z_\phi \phi^2/(2k)$, see (A.55) in Appendix A.1.9. This entails that scaling properties converge faster in the broken regime. Furthermore, we have already mentioned before that a comparison between LPA$'$ and the present approximation scheme, or rather the specific order of this scheme used here, has been done for a Yukawa model in [141], concentrating on non-universal physics. There it was found that pole masses and further

	Correlation function	η
Spectral flow	propagator	0.111(1)
	four-point function	0.093(5)
	flow of Z_ϕ	0.095(9)
Fixed point analysis	LPA$'$, $n=2$	0.1600
	LPA$'$	0.0802

Table 4.2.: Critical exponent η from different correlation functions in the present work. The results define upper and lower boundaries on the true scaling η in our computation. We also list benchmarks from LPA$'$ with the CS-regulator. Here, $V_{\text{eff}}^{(n)} = \partial_\rho^n V_{\text{eff}}$, see (4.53) and below. The last entry sets a point of reference, obtained with the standard fixed point analysis, see Appendix A.1.9.

observables agreed very well on the percent level, if fully momentum dependent computations and LPA$'$ computations with full effective potentials are compared. We expect that this agreement worsens in the scaling regime with its algebraic (non-local) momentum decays. In any case, LPA$'$ can be embedded in the present approximation as a lower order approximation. Accordingly, its results should be seen as a lower bound for the quantitative precision of the current scheme. Finally, the momentum dependent computation of this work uses the on-shell renormalisation scheme instead of the standard one: With on-shell renormalisation all quantities are measured directly in the physical correlation length $\xi \propto 1/k$ with the pole mass $m_{\text{pole}} = k$ in contradistinction to $\xi \propto k^{-\eta}$ in the standard fRG renormalisation scheme. This scheme, the MOM^2-scheme has similarities to a MOM-scheme commonly used in perturbation theory and Dyson-Schwinger equations, but also carries some differences, see [39]. In any case, we expect different convergence pattern for both schemes.

Bearing these differences and similarities in mind, we compare the present results to LPA$'$ results of a fixed point analysis within a Taylor expansion of the full effective potential. The respective computations in LPA$'$ within the standard RG scheme for different regulators can be found in the literature, see the review [114]. We start the discussion with the comparison of the present truncation with $V_{\text{eff}}^{(n>2)} \equiv 0$ to a standard Euclidean fixed point analysis in LPA$'$ with standard and on-shell renormalisation in the same order of the Taylor expansion. For the computation, see Appendix A.1.9. We are led to the critical exponent $\eta_{(n=2)} = 0.1600$. This has to be compared with $\eta \approx 0.1$ from (4.41a), (4.41b) and (4.45), see Table 4.2. Evidently, the inclusion of full momentum or spectral dependences yields significantly better results, even though the fixed point analysis is bound to have the better convergence due to expanding about the fixed point value of the field with $\bar{\rho}^* > 0$. A further difference to the standard fixed point analysis is the on-shell renormalisation scheme (4.12). We close this comparison of the current results with the standard fixed point analysis. Our result for the critical exponent of the fixed point analysis in LPA$'$ with the CS-regulator is: $\eta_{(LPA')} = 0.0802$. The comparison with our entails that higher orders scatterings in the fixed point potential are crucial for the extraction of critical exponents. This large improvement upon including the momentum dependence is expected for the CS-regulator from functional optimisation theory, see [89, 102, 143–145]: the CS-regulator is not optimised in terms of a convergence of an expansion in momentum dependences as it collects contributions in the full (loop) momentum regime. Accordingly, we expect better approximations of the full momentum dependence to lead to sizeable improvements. In turn, regulators that are optimised for approximation schemes relying on expansions in momentum dependences, such as the derivative expansion, lead to a more raid convergence. This is evident within a comparison to LPA and LPA$'$ results with the flat or Litim regulator, [143–145], that is the optimised one for LPA but not beyond [89]. With the same approximation to the effective potential as in the spectral flows, we obtain $\eta = 0.0546$, and with a full effective potential, we obtain $\eta = 0.0443$.

4.1.8. Conclusion

In this section, we demonstrated how to compute single-particle spectral functions of a scalar ϕ^4-theory within the spectral functional renormalisation group (fRG) approach proposed in [1]. This method leads to renormalised spectral flows with flowing renormalisation conditions and enables fully self-consistent computations of non-perturbative spectral functions. We derived full flow equations for the inverse propagator in both the symmetric and broken regimes of the theory; for a detailed discussion, see Sections 4.1.4 and 4.1.5.

Our setup is manifestly Lorentz invariant and preserves the causal properties of the theory throughout the flow. Every point on the Callan-Symanzik RG trajectory corresponds to a physical theory with mass scale k. Trajectories in the symmetric and broken regimes each originate from an infinitely heavy theory in their respective phases and meet at the phase boundary in the strongly interacting, massless limit of the theory; see Section 4.1.2 and Figure 4.1. Thus, our setup avoids flows through the strongly interacting phase transition region, which are typically present in momentum cutoff flows. This minimises systematic errors arising from strong dynamics near the phase transition, where flows are highly sensitive to truncation artefacts. Moreover, the implementation of a flowing renormalisation condition removes the need for fine-tuned initial conditions and allows for monotonous mass flows.

The explicit results in the broken phase show impressive agreement with those obtained in [54] within the spectral DSE approach; see Section 4.1.6.2. This affirms the reliability of the spectral functional approach for the non-perturbative computation of fundamental Minkowski-space correlation functions.

In Section 4.1.7, we presented the results of [5], where we used the spectral CS-flows to approach the phase transition from the symmetric side. The resulting spectral functions, shown in Figure 4.10a, develop an infrared scaling form. The scaling behaviour in the UV is limited by an intrinsic scale arising from the s-channel resummation of the four-point function, reflecting the constant UV-limit due to the neglect of u- and t-channel contributions. This limitation can be overcome by coupling the flow to the full effective potential, which is also necessary for a quantitative analysis of critical exponents. While the inclusion of a full potential is conceptually straightforward, it requires substantial numerical effort and is thus left for future work.

We computed the critical exponent of the propagator in the scaling regime using different methods. The results yield a band $0.093(5) \leq \eta \leq 0.111(1)$ due to non-critical remnants in the propagator. We expect this band to narrow further for even smaller pole masses; see the discussion below (4.41). Although the extracted anomalous dimensional still deviate from the true critical value, the inclusion of full momentum dependencies significantly improves the result compared to the LPA' approximation in a comparable truncation. We emphasise that the present spectral fRG approach is not designed for precise computations of scaling exponents. Rather, the main achievement of this work is to demonstrate the power and numerical feasibility of the fully self-consistent spectral Callan-Symanzik approach for the computation of real-time correlation functions near criticality.

In contrast to DSEs, the fRG approach captures average momentum dependencies of vertices via their scale dependence. This allows the inclusion of non-trivial vertex dynamics without requiring intricate spectral representations of higher-order correlation functions. Furthermore, the current spectral fRG framework can be straightforwardly extended to include the flow of the full effective potential, and we hope to report on respective results in the near future.

4.2. Boundstates from the spectral BSE

This subsection is based on [2]*. All practical calculations have been carried out by Andrés Gómez in the context of his Master thesis, which I co-supervised. This includes the additional material for this Section in Appendices A.2 and A.6.3.*

The study of bound states with functional methods requires the resummation of a large set of diagrams in a non-perturbative manner. The standard tool for computing such properties in continuum formulations of quantum field theory (QFT) is the Bethe-Salpeter equation (BSE) [146, 147]. Direct extraction of the physical spectrum in terms of the corresponding poles and cuts requires to solve the BSE and, in consequence, knowing the input correlation functions in the timelike domain. This entails additional computational complexity in comparison to calculations in the spacelike domain.

This intricacy has been treated within different approaches. Important examples are direct calculations in the complex momentum plane below the onset of singularities [40, 148–151], Cauchy integration [152–157] and contour deformation techniques [48–50, 91, 92, 158–168], or the Nakanishi method [52, 169–173]. Other works employ reconstructions from Euclidean space data, for example with Padé approximants or the Schlessinger-point method [44, 48, 138, 168, 174–181], or ML-inspired reconstructions [43, 45, 46, 182–185, 185–189]. These methods have been successful in extracting physical spectra, but do not fully recover the analytic structure of correlation functions.

In this work, we introduce the spectral BSE approach, allowing for an efficient solution in the timelike domain by making use of spectral representations for the input correlation functions. Their corresponding spectral functions are accessible via the recently developed spectral functional approach [54], which has found application to QCD in the context of DSEs [45, 80, 115, 190, 191], and was extended to the functional renormalisation group in [1], with applications to scalar theories [3] and gravity [81]. This enables the direct computation of physical masses of bound states and resonances from the corresponding spectral BSE, while also opening the door to investigating the analytic structure of Bethe-Salpether wave functions [40, 148, 149, 170, 172, 192–199].

The spectral BSE is set up at the example of a scalar ϕ^4 theory in three spacetime dimensions. The theory exhibits a second order phase transition and belongs to the Ising model universality class. In the vicinity of the phase transition, the emergence of a two-particle bound state with mass $M \sim 1.8m$, where m is the mass gap of the theory, has been observed in several works [135, 138, 200–203]. The aim of the present study is to approach this bound state from the symmetry-broken phase by considering the infinite coupling limit $\lambda \to \infty$.

Our work is outlined as follows. In Section 4.2.1 we set up the spectral BSE-DSE system for the scalar ϕ^4 theory and discuss the suitable truncations for the infinite coupling limit. We present our numerical results for the correlation functions and the bound state position in Section 4.2.2, and conclude in Section 4.2.3. Details on the spectral DSE, the BSE and the numerical implementation can be found in the appendices.

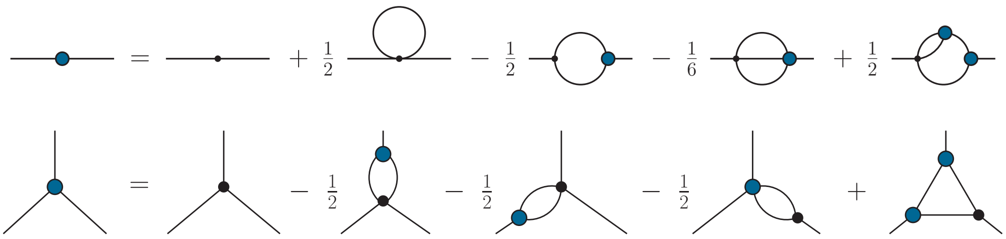

Figure 4.13.: Dyson-Schwinger equations for the two- and three-point functions; the latter contains further two-loop terms which are not shown. The full propagator is represented by a simple line, classical vertices are represented by small black dots and full vertices by large blue dots, see also Figure 2.1.

4.2.1. Spectral DSEs and BSEs

In this Section, we discuss the spectral BSE-DSE system used in this work. We briefly recollect the spectral DSE approach in Section 3.2.1, and discuss the employed expansion of our effective potential in Section 4.2.1.2. Section 4.2.1.3 is dedicated to a detailed discussion of our systematics relevant for the systematic error control. Finally, in Section 4.2.1.4 we discuss the BSE implementation in the present spectral approach.

4.2.1.1. Dyson-Schwinger equations

The classical action of the scalar ϕ^4 theory in $d = 3$ dimensions reads

$$S[\varphi] = \int \mathrm{d}^3x \left\{ \frac{1}{2}\varphi\left(-\partial^2 + m_0^2\right)\varphi + \frac{\lambda_\phi}{4!}\varphi^4 \right\} , \tag{4.46}$$

where λ_ϕ is the bare four-point coupling, and m_0 is the bare mass of the scalar field. Because the coupling constant λ_ϕ carries a dimension of mass, all quantities can only depend on the dimensionless ratio λ_ϕ/m_0. In the following, we switch to dimensionless parameters by considering all dimensionful parameters in units of the pole mass m.

The quantum analogue of the classical action (4.46) is the quantum effective action $\Gamma[\phi]$, see e.g. [204]. This is formalised through the master Dyson-Schwinger equation

$$\frac{\delta\Gamma[\phi]}{\delta\phi} = \left\langle \frac{\delta S[\varphi]}{\delta\varphi} \right\rangle , \tag{4.47}$$

stating that the quantum equation of motion of the scalar field φ is obtained by varying the quantum effective action w.r.t. the mean field $\phi = \langle\varphi\rangle$. Functional relations for all one-particle irreducible (1PI) correlation functions,

$$\Gamma^{(n)}[\phi](p_1, \ldots, p_n) = \frac{\delta^n\Gamma[\phi]}{\delta\phi(p_1)\ldots\delta\phi(p_n)} , \tag{4.48}$$

are obtained from (4.47) by the respective ϕ-derivatives. Generally, the DSE for $\Gamma^{(n)}$ depends on $\Gamma^{(n+2)}$, leading to an infinite tower of coupled equations. A closed system of DSEs is achieved by truncating this tower, e.g., by approximating correlation functions by their classical counterpart from some order n on, $\Gamma^{(m>n)} \approx S^{(m)}$.

The central object in any functional application is the full propagator G which can be obtained from the DSE for its inverse $\Gamma^{(2)}$. The corresponding diagrammatic representation of the latter is shown in the top panel of Figure 4.13, containing a tadpole, polarisation, squint and sunset diagram. Apart from the classical vertices, these diagrams also involve the full three- and four-point vertices (marked by blue blobs). The corresponding DSE for the three-point function is depicted in the bottom panel of Figure 4.13.

We employ the spectral DSE framework developed in [54]. Accordingly, we make use of the Källén-Lehmann representation for the full propagator,

$$G(p) = \int_0^\infty \frac{\mathrm{d}\lambda}{\pi} \frac{\lambda\,\rho(\lambda)}{p^2+\lambda^2}\,, \quad \text{with} \quad \rho(\lambda) = 2\,\mathrm{Im}\,G\big(-\mathrm{i}(\lambda+\mathrm{i}0^+)\big)\,, \tag{4.49}$$

in the diagrams of the gap equation. Within a suitable truncation, the DSE can then be solved directly for timelike momenta due to the resulting perturbative form of the momentum loop integrals. This yields direct access to the spectral function and we dropped the spatial momentum due to Lorentz covariance.

The spectral function ρ represents the distribution of the physical states in the full quantum theory, and is parametrised as a sum of poles and a continuum tail, see also (4.14).

In an s-channel approximation $p^2 = s$ and $t = u = 0$, a similar spectral representation can be devised for the four-point function, see also (4.50)

$$\Gamma^{(4)}(p) = \lambda_\phi + \int_0^\infty \frac{d\lambda}{\pi} \frac{\lambda\,\rho_4(\lambda)}{p^2+\lambda^2}\,. \tag{4.50}$$

The ϕ^4 theory in three dimensions is super-renormalisable. The only two superficially divergent diagrams in the propagator DSE are the tadpole and sunset diagrams in Figure 4.13, carrying a linear resp. logarithmic divergence. We employ the spectral renormalisation scheme devised in [54]. By choosing an on-shell renormalisation condition, the physical scales of our theory are fixed by the pole position of the propagator; see Appendix A.2.1 for details.

4.2.1.2. Effective potential

Instead of resolving the full field dependence of the correlation functions, it is convenient to work on the physical solution to the quantum equation of motion (EoM)

$$\frac{\delta\Gamma[\phi]}{\delta\phi(x)} = 0\,. \tag{4.51}$$

The symmetry-broken regime of the scalar theory is signalled by a non-vanishing and constant vacuum expectation value $\phi_0 = \langle\varphi\rangle$, giving rise to a non-vanishing three-point interaction already at the classical level. For this reason, we solve the Dyson-Schwinger equations in the background of the non-vanishing condensate ϕ_0. The classical vertices $S^{(n)}[\phi_0]$ in the Dyson-Schwinger equations are given by

$$S^{(3)}[\phi_0] = \lambda_\phi\,\phi_0\,, \qquad S^{(4)}[\phi_0] = \lambda_\phi\,. \tag{4.52}$$

To determine ϕ_0 in the broken phase dynamically, we expand the effective potential around the solution of the equation of motion,

$$V_{\text{eff}}[\phi] = \sum_{n=2}^{\infty} \frac{v_n}{(2n)!}(\phi^2-\phi_0^2)^n\,. \tag{4.53}$$

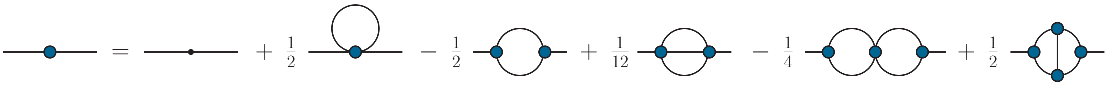

Figure 4.14.: The skeleton expansion for the propagator employed in this work. The full propagator is represented by a simple line, classical vertices are represented by small black dots and full vertices by large blue dots, see also Figure 2.1.

The n-point vertices at vanishing momenta, which we abbreviate by Γ_n, are then obtained from

$$\Gamma_n = \Gamma^{(n)}[\phi_0](\boldsymbol{p}_n = 0) = \left.\frac{\partial^n V_{\text{eff}}[\phi]}{(\partial\phi)^n}\right|_{\phi=\phi_0} , \tag{4.54}$$

with $\boldsymbol{p}_n = (p_1, ..., p_n)$. We assume that higher orders in the mean field ϕ_0 are subleading and truncate the series at second order, thus parametrising $V_{\text{eff}}[\phi]$ by its second and third moments v_2 and v_3. Accordingly, the two-, three- and four-point vertices at zero momentum are given by

$$\begin{aligned}\Gamma_2 &= \frac{1}{3} v_2\, \phi_0^2 \,, \\ \Gamma_3 &= v_2\, \phi_0 + \frac{1}{15} v_3\, \phi_0^3 \,, \\ \Gamma_4 &= v_2 + \frac{2}{5} v_3\, \phi_0^2 \,. \end{aligned} \tag{4.55}$$

By inverting (4.55), one obtains ϕ_0, v_2 and v_3 from the zero-momentum correlations functions as

$$\phi_0 = \frac{3\Gamma_3 - \sqrt{9\Gamma_3^2 - 15\Gamma_2\Gamma_4}}{\Gamma_4} , \tag{4.56}$$

and

$$v_2 = \frac{6\Gamma_3 - \Gamma_4\phi_0}{5\phi_0} , \quad v_3 = \frac{3(\Gamma_4\phi_0 - \Gamma_3)}{\phi_0^3} . \tag{4.57}$$

The minus sign in front of the square root in (4.56) is determined by the limit $\lambda_\phi/m \longrightarrow 0$, where the full vertices approach their classical values.

4.2.1.3. Systematics and truncations

Without approximations, the DSE of the inverse two point function carries the full non-perturbative structure of the propagator. In practice, truncations are necessary to deal with the higher correlation functions, which correspond to a certain resummation structure. We are particularly interested in the scaling limit $\lambda_\phi/m \longrightarrow \infty$, where the two-, three- and four-point functions should follow the scaling relations

$$\Gamma^{(2)} \sim p^{2-\eta} , \quad \Gamma^{(3)} \sim p^{3(1-\eta)/2} , \quad \Gamma^{(4)} \sim p^{1-2\eta} . \tag{4.58}$$

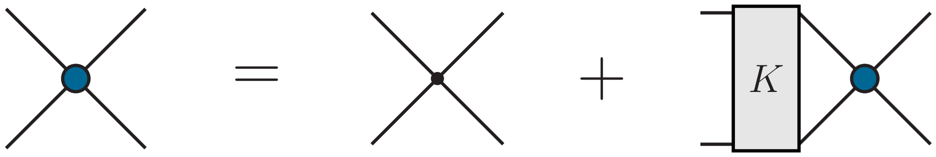

Figure 4.15.: Inhomogeneous BSE for the four-point vertex. The BSE kernel is denoted with a grey box, for the full propagators and vertices see Figure 2.1.

The anomalous dimension η is known to be $\eta \approx 0.0360$ for the Ising universality class in three dimensions [205–207]. This imposes tight constraints on the approximation scheme. To ensure the correct scaling behaviour of the diagrams, we employ a skeleton expansion of the propagator DSE. To that end, we convert the classical three- and four-point vertices into full ones. This procedure introduces additional diagrams which have to be subtracted to remain consistent at a given loop-order. For simplicity, we truncate the expansion of the DSE at two-loop order, leading to the DSE in the skeleton expansion depicted in Figure 4.14. Note the changed prefactor of the sunset diagram, stemming from the additional contributions to the tadpole diagram with a full four-point function. The squint diagram is fully absorbed in the now fully dressed polarisation diagram. The latter also produces the double polarisation and the kite, which have to be subtracted. Both of them will be ignored in the present work since the kite corresponds to higher-order terms in ϕ_0 and the double polarisation does not add qualitatively to the analytic structure of the propagator DSE.

To close our approximation, we need to specify the higher order correlation functions. We generally perform a zero momentum vertex approximation for all dressed vertices. Nevertheless, since we have argued that the tadpole produces also the sunset topology, we have to include the relevant momentum structure of the four-point function in this diagram. For simplicity, we start from an inhomogeneous BSE, which is shown in Figure 4.15 and reads

$$\Gamma^{(4)}(q_1,q_2,p) = \lambda_\phi + \int_k K(q_1,k,p)\, G(k_+)\, G(k_-)\, \Gamma^{(4)}(k,q_2,p)\,. \tag{4.59}$$

Here, p is the total momentum, q_1 and q_2 are relative momenta, K is the two-particle interaction kernel, G is the full propagator with $k_\pm = k \pm p/2$, and $\int_k = \int d^3k/(2\pi)^3$. If we retain only the classical vertex in the kernel, $K(q_1,k,p) = -\lambda_\phi/2$, the equation amounts to a bubble resummation in the s-channel approximation,

$$\Gamma^{(4)}(p) = \frac{\lambda_\phi}{1+\lambda_\phi\,\Pi_{\text{fish}}(p)}\,. \tag{4.60}$$

Equation (4.60) is also readily derived from the DSE of the four-point function in the s-channel approximation with $\phi = 0$, also dropping the two-loop terms in the DSE.

The structure of the ‘fish diagram’ in (4.60) is the same as that of the polarisation diagram and reads

$$\Pi_{\text{fish}}(p) = \frac{1}{2}\int_k G(k_+)\, G(k_-)\,, \tag{4.61}$$

it corresponds to the spectral integral (A.61) with $g_{\text{fish}} = 1/2$ in Appendix A.2.1. In the limit $\lambda_\phi/m \to 0$, i.e., for a classical propagator $G(k) = 1/(k^2+m^2)$, the integral reduces to

$$\Pi_{\text{fish}}(p) \to \frac{\arctan\sqrt{x}}{16\pi m\sqrt{x}}\,, \qquad \Pi_{\text{fish}}(0) \to \frac{1}{16\pi m}\,, \tag{4.62}$$

with $x = p^2/(4m^2)$. The spectral function of the resummed s-channel four-point function is extracted by inverting (4.50) in analogy to the propagator spectral function (A.60). In this manner, the tadpole with a dressed four-point vertex can be computed in the form of a polarisation diagram with the insertion of this spectral function.

For the three-point vertex we consider its DSE up to one-loop terms as shown in Figure 4.13. For simplicity we restrict ourselves to vertices at zero momentum, i.e., we assume

$$\Gamma^{(3)}(p_1,p_2,p_3) \approx \Gamma_3\,, \qquad \Gamma^{(4)}(p) \approx \Gamma_4\,. \tag{4.63}$$

With the classical three-point function $S^{(3)}[\phi_0] = \lambda_\phi\phi_0$, the DSE reduces to the algebraic equation

$$\Gamma_3 = \phi_0\lambda_\phi - 2\lambda_\phi\Gamma_3\Pi_{\text{fish}}(0) - \phi_0\lambda_\phi\Gamma_4\Pi_{\text{fish}}(0)\phi_0\lambda_\phi\Gamma_3^2\,\Pi_{\text{tr}}(0)\,. \tag{4.64}$$

Hereby, the triangle diagram

$$\Pi_{\text{tr}}(p) = \int_k G(k)\,G(k_+)\,G(k_-) \tag{4.65}$$

corresponds to the spectral integral (A.61) in Appendix A.2.1 with a prefactor $g_{\text{tr}} = 1$. For a classical propagator it reduces to

$$\Pi_{\text{tr}}(p) \to \frac{1}{8\pi m^3}\frac{1}{x^{3/2}}\arctan\left[\frac{x^{3/2}}{4+3x}\right]\,, \tag{4.66}$$

with $x = p^2/(4m^2)$ and $\Pi_{\text{tr}}(0) \to 1/(32\pi m^3)$. One can further eliminate ϕ_0 by combining (4.56) and (4.64), which results in a quartic equation for Γ_3 and yields

$$(\Gamma_3)^2 = \frac{5\Gamma_4}{6\lambda_\phi}\frac{6a + b\left(\sqrt{c^2+\frac{12}{5}a} - c\right)}{\Pi_{\text{tr}}(0)\,(2b-5a)}\,, \tag{4.67}$$

with the coefficients

$$a = \ \lambda_\phi\Gamma_2\Pi_{\text{tr}}(0)\,, \quad b = 1 + 2\lambda_\phi\Pi_{\text{fish}}(0)\,, \quad c = 1 - \frac{2}{5}\lambda_\phi\Pi_{\text{fish}}(0)\,. \tag{4.68}$$

This closes our approximation for the DSE system. For the respective results, see Section 4.2.2 and especially Figure 4.17.

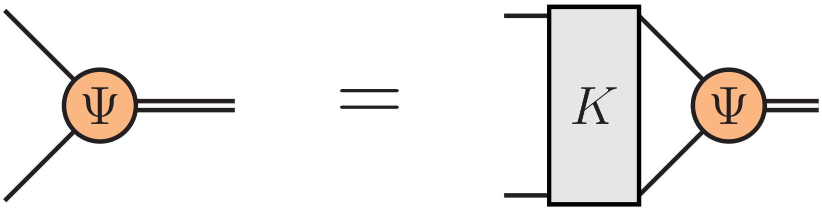

Figure 4.16.: Homogeneous Bethe-Salpeter equation, derived from the inhomogeneous one in Figure 4.15. The BSE kernel is denoted with a grey box, the BSE wave function with a orange circle and the lines are full propagators.

4.2.1.4. Bethe-Salpeter equation

For the calculation of scalar two-particle bound states, we consider the homogeneous BSE shown in Figure 4.16,

$$\Psi(q,P) = \int_k K(q,k,P)\, G(k_+)\, G(k_-)\, \Psi(k,P)\,. \tag{4.69}$$

Its structure is analogous to that in Figure 4.15 except for the inhomogeneous term: $\Psi(q,P)$ is the Bethe-Salpeter amplitude, K is the two-particle irreducible kernel, and $G(k_\pm)$ with $k_\pm = k \pm P/2$ are the dressed propagators. The total momentum is on-shell, i.e., $P^2 = -M^2$, where M is the mass of the bound state.

Even though the homogeneous and inhomogeneous equations share the same structure, we note that in our setup they are not directly connected. We employed (4.59) as an ingredient to generate a minimal four-point vertex that is consistent with scaling, whereas the kernel of the homogeneous BSE is related to the self-energy through a functional derivative with respect to the propagator. A possible alternative would be to consider a 4PI system [208–210], which automatically generates a consistent truncation for the two-, three- and four-point vertices together with the BSE kernel, but this is beyond the scope of the present work. Here we restrict ourselves to the contributions originating from the one-loop terms in the self-energy, which are the tadpole and polarisation diagrams. The former generates a scalar four-point vertex and the latter t- and u-channel exchanges in the BSE kernel. Thus, up to two-loop terms the kernel takes the form

$$K(q,k,P) = \frac{G(q-k)+G(q+k)}{2}\,\Gamma_3^2 - \frac{\Gamma_4}{2}\,, \tag{4.70}$$

where Γ_3 and Γ_4 are the three- and four-point vertices at zero momentum. Note also that the inhomogeneous BSE (4.59) does not support bound states since its kernel $-\lambda_\phi/2$ carries a negative sign, whereas the additional t- and u-channel exchanges in the homogeneous BSE change the sign of the kernel to be positive.

Each dressed propagator can then be computed by means of its spectral representation (4.49) via the assignment of a unique spectral mass. Thus, aside from the spectral integrals over λ_1 and λ_2 which are performed numerically, the two internal propagators in the BSE take the form

$$\frac{1}{k_+^2+\lambda_1^2}\,\frac{1}{k_-^2+\lambda_2^2} = \frac{1}{Q_1^4 - Q_2^4}\,, \tag{4.71}$$

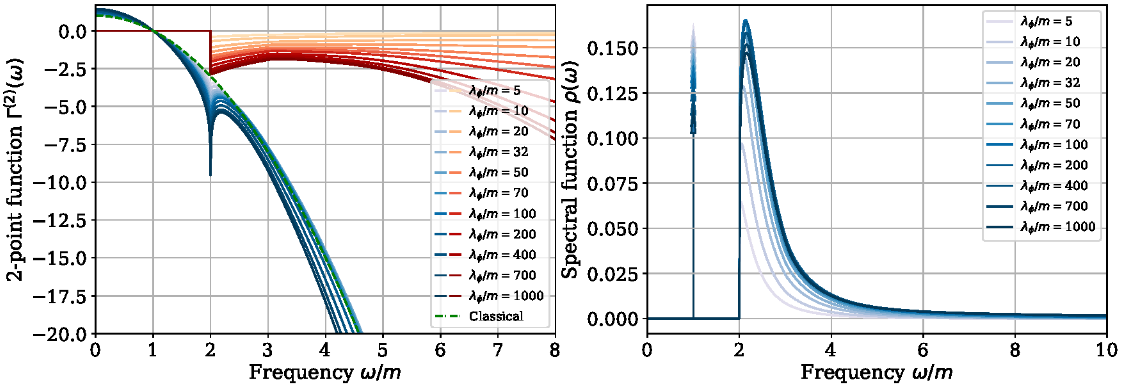

Figure 4.17.: *Left:* Real (blue) and imaginary (red) part of the two-point function obtained in the skeleton expansion, plotted for real frequencies and different values of λ_ϕ/m. *Right:* Spectral function $\rho(\omega)$. All quantities given in mass units.

and the sum of the t- and u-channel contributions in the kernel is

$$\frac{1}{(q-k)^2+\lambda_3^2}+\frac{1}{(q+k)^2+\lambda_3^2}=\frac{2\,Q_3^2}{Q_3^4-4\,(q\cdot k)^2}\,, \tag{4.72}$$

with

$$\begin{aligned} Q_1^2 &= k^2+P^2/4+(\lambda_1^2+\lambda_2^2)/2\,,\\ Q_2^2 &= k\cdot P+(\lambda_1^2-\lambda_2^2)/2\,,\\ Q_3^2 &= q^2+k^2+\lambda_3^2\,. \end{aligned} \tag{4.73}$$

Apart from the spectral representation, we solve the BSE using standard methods, see e.g. [40, 211]. By expressing the amplitude $\Psi(q,P)$ in terms of spherical coordinates and discretising the momentum grid (see Appendices A.2.4 and A.6.3 for details), the BSE turns into an eigenvalue equation for a kernel matrix $\mathcal{M}$,

$$\mathcal{M}\,\Psi_i=\eta_i\Psi_i\,, \tag{4.74}$$

whose eigenvalues η_i correspond to the ground and excited states and their eigenvectors Ψ_i encode the respective Bethe-Salpeter amplitudes. Apart from the dependence on the parameter λ_ϕ/m, the eigenvalues depend on the bound state mass ratio M/m through the total momentum P. We then numerically find the value of M/m for which the relation

$$\eta_i\left(\frac{M_i}{m},\frac{\lambda_\phi}{m}\right)=1\,, \tag{4.75}$$

holds. This is the on-shell solution for a given state. The largest eigenvalue corresponds to the ground state, which is the focus of this work.

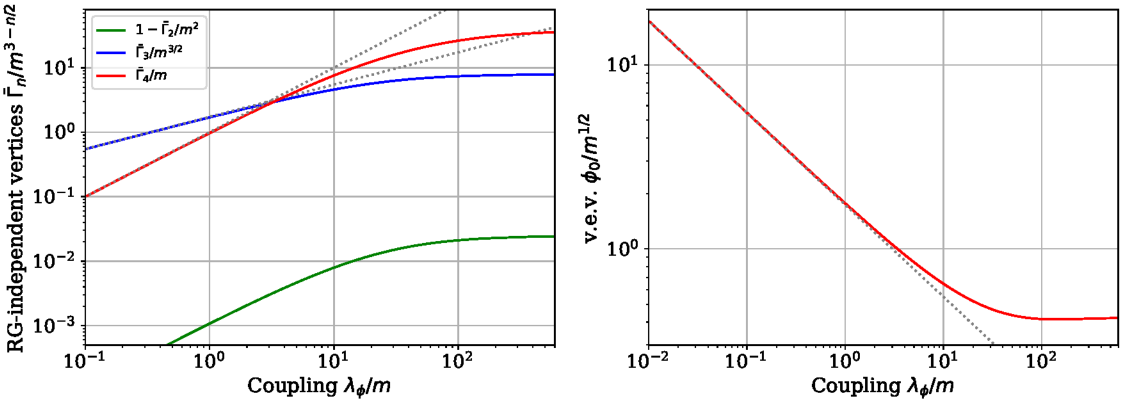

Figure 4.18.: Zero momentum RG-invariant vertices $\bar{\Gamma}_n/m^{3-n/2}$ with $\bar{\Gamma}_n$ in (4.76), and of the vacuum expectation value $\phi_0/m^{1/2}$ as functions of the coupling λ_ϕ/m. The dotted gray lines are the tree-level values from (4.77). All quantities saturate for large couplings.

4.2.2. Results

Following the discussion of our setup in the previous Section, we now present our results. The left panel of Figure 4.17 shows the fully dressed inverse propagator for real frequencies ω. It exhibits an imaginary part, starting at the threshold $\omega = 2m$, which marks the onset of two-particle production.

The right panel of Figure 4.17 shows respective spectral function $\rho(\omega)$ It is visible how the peak of the spectral tail increases with the coupling, which implies an increasing dominance of the scattering states. The peak saturates at around $\lambda_\phi/m \sim 100$ in favor of a broader UV tail.

The set of RG-independent zero-momentum vertices $\bar{\Gamma}_2$, $\bar{\Gamma}_3$ and $\bar{\Gamma}_4$ are presented in Figure 4.18 as functions of the coupling λ_ϕ/m. These are given by

$$\bar{\Gamma}_n \equiv \Gamma_n/Z_\phi^{n/2}\,, \tag{4.76}$$

where $Z_\phi = 1/Z$ is the wave function renormalisation given at the pole mass as the inverse of the residue. This divides out the RG-running of the external legs, which otherwise leads to a power-law divergence, for further discussions see Appendix A.2.2.

In the limit $\lambda_\phi/m \to 0$, quantum corrections become negligible and the vertices reduce to their tree-level values

$$\frac{\Gamma_2}{m^2} \to 1\,, \quad \frac{\Gamma_3}{m^{3/2}} \to \sqrt{\frac{3\lambda_\phi}{m}}\,, \quad \frac{\Gamma_4}{m} \to \frac{\lambda_\phi}{m}\,. \tag{4.77}$$

In turn, for asymptotically large couplings $\lambda_\phi/m \to \infty$ we expect a scaling behavior as in this limit we approach the phase transition with $m/\lambda_\phi \to 0$. One can clearly see the deviation from the tree-level behavior for increasing values of the coupling. With the curvature mass $m^2_{\mathrm{cur}} = \bar{\Gamma}_2$, the ratio m^2_{cur}/m^2 deviates from unity, as is also visible in Figure 4.17 at vanishing momentum. The RG-independent three- and four-point vertices saturate in the large coupling limit. The right panel of Figure 4.18 shows the evolution of the (dimensionless) vacuum condensate $\phi_0/m^{1/2}$, which starts from its classical result $\sqrt{3m/\lambda_\phi}$ and eventually saturates as well at a non-trivial value.

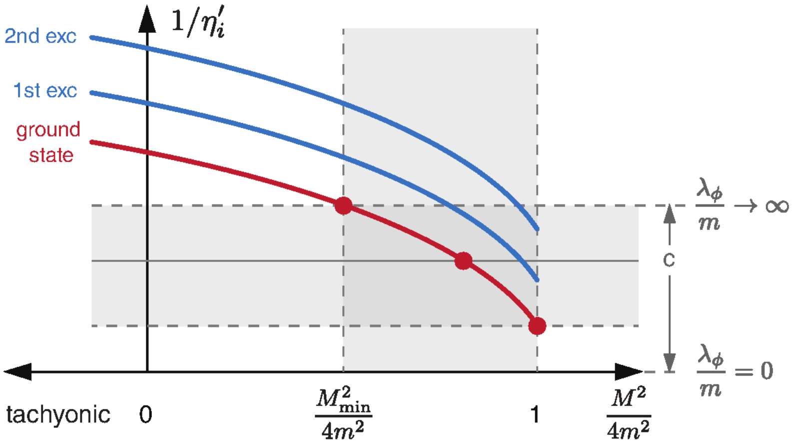

Figure 4.19.: Sketch of the eigenvalue spectrum for a Bethe-Salpeter equation of the form (4.78). The masses of the ground and excited states are determined from the condition $1/\eta_i' = c$. If c saturates for $\lambda_\phi/m \to \infty$, the bound state mass has a lower bound M_{min}.

In summary we find that the dressed RG-invariant vertices calculated from their DSEs eventually saturate, in contrast to their respective tree-level counterparts. This has important consequences for the properties of bound states obtained from the BSE, as it leads to a physical bound-state mass in the scaling limit. To see this, suppose we drop the term $-\Gamma_4/2$ from the BSE kernel (4.70) and solve the BSE with classical (free) propagators only. This yields the massive Wick-Cutkosky model [52, 212, 213] which has been frequently studied in the literature, see e.g. [48, 169–172, 214]. If we pull out the dimensionless factor $c = \Gamma_3^2/m^3$ from the kernel, the BSE (4.74) takes the form

$$c\,\mathcal{M}'\,\Psi_i = c\,\eta_i'\,\Psi_i\,. \tag{4.78}$$

The dimensionless remainder $\mathcal{M}'$ does not depend on λ_ϕ/m and neither do its eigenvalues η_i'. Thus, if we plot the eigenvalue spectrum over the bound state mass, as sketched in Figure 4.19, the on-shell solution can be read off from the intersection $1/\eta_i' = c$. The 'coupling' c in front of the BSE kernel is now a free parameter that can be tuned arbitrarily; e.g., for the tree-level vertex in (4.77) it rises linearly with λ_ϕ/m. In particular, if c is large enough the intersection $1/\eta_i' = c$ occurs at spacelike values $P^2 = -M^2 > 0$, so that with increasing coupling one generates tachyonic solutions.

Such a behavior does not happen if the RG-invariant vertices saturate with λ_ϕ/m, as they do in our system: If the coupling does not exceed a certain maximum value, then the mass of the bound state is bounded from below and the system cannot become tachyonic. If in addition the propagators are dressed, as in our case, then the BSE eigenvalues η_i' themselves also depend on λ_ϕ/m. Finally, if we put the four-point vertex back into the kernel there is no longer an overall coupling that can be pulled out since all propagators and vertices appearing in the BSE kernel are determined from their DSEs.

The resulting evolution of the bound state mass ratio M/m with λ_ϕ/m is shown in Figure 4.20. At $\lambda_\phi/m \approx 5$ the bound state mass is at the threshold $M = 2m$. For smaller couplings one might expect either a virtual state like in the massive Wick-Cutkosky

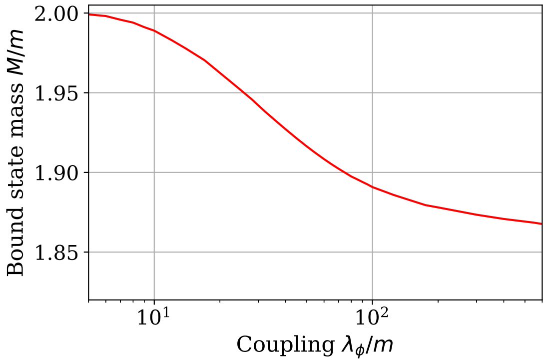

Figure 4.20.: Evolution of the bound state mass M/m as a function of λ_ϕ/m calculated from the BSE, with propagators and vertices determined from their DSEs.

model [48] or a resonance on the second Riemann sheet. For larger values of λ_ϕ/m, the bound state mass decreases and eventually saturates. Numerical instabilities prohibited us to go beyond $\lambda_\phi/m \gtrsim 10^3$. However, as the bound-state mass already starts to saturate at this scale, an extrapolation allows us to estimate the mass ratio in the scaling limit:

$$\frac{M}{m} \approx 1.85 \quad \text{for} \quad \frac{\lambda_\phi}{m} \to \infty\,. \tag{4.79}$$

This is close to the upper range of lattice values $M/m = 1.82(2)$ [135, 138, 200–203]. The deviation is of the order of our numerical error of about 1%, cf. Appendix A.6.3. We note again that this result is only possible through a consistent solution for the n-point functions, which underlines the need for systematic truncations with functional methods.

4.2.3. Conclusions

In this work we studied scalar ϕ^4 theory in three spacetime dimensions. We determined the mass of the lowest-lying scalar bound state from its Bethe-Salpeter equation, whose value in the scaling limit $\lambda_\phi/m \to \infty$ is predicted to be $M/m \approx 1.80\ldots1.84$ from lattice studies [135, 138, 200–203]. We argued that such a saturation cannot even be achieved qualitatively if the Bethe-Salpeter equation only features tree-level propagators and interactions. Instead, it requires a consistent truncation of the Dyson-Schwinger equations where not only the propagators but also the vertices acquire a non-perturbative dressing.

To this end, we constructed truncations for the two-, three- and four-point functions where such an internal consistency is explicitly built in. To solve the system numerically, we employed the spectral DSE approach which allows us to access the timelike behavior of the correlation functions directly. Up to an anomalous dimension, we find that the three- and four-point vertices saturate in the large coupling limit $\lambda_\phi/m \to \infty$, and so does the resulting mass of the bound state. Our result $M/m \approx 1.85$ in that limit lies within 1% of the lattice prediction.

In conclusion, the combination of spectral Dyson-Schwinger and Bethe-Salpeter equations is a powerful tool that also allows one to access the resonance spectrum above physical thresholds, or the evolution and melting of bound states with temperature. We hope to report on respective results in the near future.

4.3. The graviton spectral function

This Section is based on [1, 6].

In this Section, we discuss the spectral function of the fluctuating graviton of asymptotically safe quantum gravity in an on-shell renormalisation scheme. We will not go into the details of asymptotically safe quantum gravity, but merely discuss the necessary equations and refer to the literature for further details. We will also use this example, to discuss some technical developments compared to computations of the previous Sections. The present approach including the use of the spectral BPHZ-renormalisation has already been applied in [81] to the graviton spectral function. We extend this work by feeding back the non-trivial frequency dependence of the propagator and the use of on-shell renormalisation conditions.

The search for a quantum theory of gravity that is compatible with the Standart-Model of particle physics has inspired many generations of physicists to go beyond the framework of quantum field theories to avoid the problem of perturbative non-renormalisability. Beyond perturbation theory, this problem might not be there in the first place. The asymptotic safety scenario [215, 216] utilises that the UV-theory can be defined at an interacting, rather than a gaussian fixed point.

The classical action of gravity is the Einstein Hilbert (EH) action,

$$S_{\mathrm{EH}}[g_{\mu\nu}] = \frac{1}{16\pi G_{\mathrm{N}}} \int \mathrm{d}^4 x \, |\det g_{\mu\nu}|^{\frac{1}{2}} \Big(\mathcal{R} - 2\Lambda\Big), \tag{4.80}$$

with Newton's coupling G_{N}, the curvature scalar $\mathcal{R}$ and the cosmological constant Λ. The dynamical quantum field is the metric $g_{\mu\nu}$. The EH action is then augmented with a gauge-fixing term given by

$$S_{\mathrm{gf}}[\bar{g}, h] = \frac{1}{2\alpha} \int \mathrm{d}^4 x \sqrt{\bar{g}} \, \bar{g}^{\mu\nu} F_\mu F_\nu \,, \tag{4.81}$$

with the gauge-fixing condition F_μ

$$F_\mu[\bar{g}, h] = \bar{\nabla}^\nu h_{\mu\nu} - \frac{1+\beta}{4} \bar{\nabla}_\mu h^\nu{}_\nu \,. \tag{4.82}$$

The respective ghost action reads

$$S_{\mathrm{gh}}[\bar{g}, \phi] = \int \mathrm{d}^4 x \sqrt{\bar{g}} \, \bar{c}^\mu M_{\mu\nu} c^\nu \,, \tag{4.83}$$

with the Faddeev-Popov operator

$$M_{\mu\nu} = \bar{\nabla}^\rho (g_{\mu\nu} \nabla_\rho + g_{\rho\nu} \nabla_\mu) - \frac{1+\beta}{2} \bar{g}^{\sigma\rho} \bar{\nabla}_\mu g_{\nu\sigma} \nabla_\rho \,. \tag{4.84}$$

Throughout this work, we use the harmonic gauge $\alpha = \beta = 1$, analog to what has been done in [81]. The gauge-fixing sector enforces the introduction of a background metric $\bar{g}_{\mu\nu}$ as the full metric would introduce unwanted interaction terms to the gauge fixing. For the discussion of spectral flows we use the flat Minkowski metric as a background, $\bar{g}_{\mu\nu} = \eta_{\mu\nu}$. Amongst other reasons this choice is taken as spectral representations in the presence of non-trivial backgrounds pose additional conceptual intricacies. Furthermore, we use a linear split of the full metric,

$$g_{\mu\nu} = \eta_{\mu\nu} + \sqrt{16\pi G_{\mathrm{N}}} \, h_{\mu\nu} \,, \tag{4.85}$$

where the fluctuation field $h_{\mu\nu}$ carries the full dynamics of quantum gravity. For more details on this fluctuation approach to gravity see [217].

In [81], the spectral flow of the graviton propagator has been computed with the spectral CS equation. First of all, this has provided a non-trivial proof for the existence of the graviton spectral representation within the approximation discussed there. This is specifically remarkable, given the ongoing discussion concerning the existence of a spectral representation for the gluon, see Section 3.3.5. Furthermore, in [81] explicit numerical results for the spectral function ρ_h have been obtained: the spectral function is strictly positive but not normalisable due to the large positive UV anomalous dimension $\eta_h \approx 1$, see the discussion in Section 3.1.2.

4.3.1. CS-flow in asymptotically safe gravity

Here, we show that the momentum structure of asymptotically safe propagators and vertices allows for a renormalised spectral CS flow with a finite number of counter terms: to begin with, the loops in quantum gravity have the same spectral representation displayed in (3.55). As in four-fermi models in four space-time dimensions, the theory is perturbatively non-renormalisable. Moreover, already classical vertices involve general powers of the graviton, $S_{\text{EH}}^{(n)} \neq 0$ for all $n \in \mathbb{N}$, and further ones are generated by loop corrections.

Since the seminal Euclidean fRG paper of Reuter [216] quite some further evidence has been accumulated for quantum gravity being asymptotically safe [215, 218], for recent fRG-reviews see e.g. [114, 217, 219]. This scenario is based on a non-trivial ultraviolet fixed point, the Reuter fixed point. In the fRG setting it implies

$$\lim_{k\to\infty} G_{\text{N},k} k^2 = g_{\text{N}}^* \,, \qquad G_{\text{N},k=0}(p \to \infty) \to \frac{g_{\text{N}}^*}{p^2} \,, \tag{4.86}$$

where g_{N}^* is the fixed point of the dimensionless Newton's coupling, and $G_{\text{N},k} = G_{\text{N},k}(p = 0)$. Typically, for fixed point investigations, the (unphysical) limit $k \to \infty$ with $p \ll k$ is used, as this limit is technically less challenging and the k-scaling and fixed point 'couplings' reflect the physical momentum scaling and fixed point coupling.

For our discussion of the spectral setting it is important to note that the asymptotically safe Newton's coupling *necessarily* decays with $1/p^2$ for large momenta with the respective FP equation,

$$\lim_{p^2\to\infty} \frac{\partial_{p^2} G_{\text{N},k=0}(p)}{p^2} = 0 \,, \tag{4.87}$$

which is reflected in $\lim_{k\to\infty} \partial_t g_{\text{N}} = 0$ with $g_{\text{N}} = k^2 G_{\text{N},k}$. These considerations entail that a convenient parametrisation of $h_{\mu\nu}$-vertices is given by

$$\Gamma_{h^n}^{(n)}(p_1, ..., p_n) = \prod_{i=1}^{n} Z_h^{1/2}(p_i) \bar{\Gamma}_{h^n}^{(n)}(p_1, ..., p_n) \,, \tag{4.88}$$

where the $Z_h^{1/2}$ factors take care of the RG-running of the legs and $\bar{\Gamma}_{h^n}^{(n)}$ shows the momentum running of a (vertex) coupling. Accordingly, these vertex dressings decays with powers of $\bar{p}$ at a symmetric point with $p_i^2 = \bar{p}^2$: in terms of vertex avatars of Newton's coupling, $G_{\text{N},n}$, the symmetric point dressing $\bar{\Gamma}_{h^n}^{(n)}(\bar{p})$ is proportional to $G_{\text{N},n}^{n/2-1}(\bar{p})$. In the asymptotically safe UV regime all these couplings have to decay with $1/\bar{p}^2$ and we are led to

$$\lim_{\bar{p}\to\infty} \bar{\Gamma}^{(n)}_{h^n}(\bar{p}) \propto \lim_{\bar{p}\to\infty} \bar{p}^2\, G_{\mathrm{N},n}^{n/2-1}(\bar{p}) \propto \bar{p}^2 \left(\frac{1}{\bar{p}^2}\right)^{\frac{n}{2}-1} . \tag{4.89}$$

Inserting this scaling back in the loop equations shows the consistency of this scaling: the UV momentum scaling of all diagrams is given by

$$\lim_{\bar{p}\to\infty} \partial_t \bar{\Gamma}^{(n)}_{h^n}(\bar{p}) \propto \bar{p}^2 \left(\frac{1}{\bar{p}^2}\right)^{\frac{n}{2}} , \tag{4.90}$$

which is exactly that of $\bar{\Gamma}^{(n)}/\bar{p}^2$. In standard perturbation theory, the running would be $\partial_t\bar{\Gamma}^{(n)} \propto \bar{p}^2\bar{\Gamma}^{(n)}$ related to the perturbative non-renormalisability of the theory. Here, one additional $1/\bar{p}^2$ scaling stems from the second propagator in the cutoff line $G_k\, \partial_t R_k\, G_k$ and reflects the reduction of the UV degree of divergence by two in the CS flow in comparison to standard loop diagrams. The other $1/\bar{p}^2$ scaling stems from the fixed-point scaling of Newton's coupling, which effectively shifts the theory to its critical dimension.

In summary we deduce that the only diagrams that require renormalisation via $\partial_t S_{\mathrm{ct}}$ are that of $\bar{\Gamma}^{(2)}$. In turn, the flows of $\bar{\Gamma}^{(n>2)}$ are finite but the renormalisation conditions in gravity for $\mu \to 0$ should lead to the Einstein-Hilbert action, which uniquely fixes the full $\partial_t S_{\mathrm{ct}}$ in the CS flow (3.48). In summary, a fully consistent spectral CS flow requires also the inclusion of momentum-dependent vertex functions. However, the above analysis also entails that constant vertex approximations can be entertained. In this case the *finite* subtractions $\partial_t S^{(n)}_{\mathrm{ct}}$ are elevated to the standard subtraction of counter terms with the constraint of leaving the IR limit of the Einstein-Hilbert action intact. In any case it leaves us with a finite number of relevant couplings given by those obtained with a spectral spatial momentum regulator.

4.3.2. Renormalised spectral flow for the graviton propagator

The computations of this work build on the spectral flows derived in [81] for the graviton propagator, and we proceed by summarising the relevant equations. The computation is focused on the transverse traceless mode of the fluctuating graviton, defined via the traceless, transverse projector

$$\Pi^{\mu\nu\rho\sigma}_{\mathrm{TT}}(p) = \Pi^{\mu(\rho}(p)\Pi^{\sigma)\nu}(p) - \frac{1}{3}\Pi^{\mu\nu}(p)\Pi^{\rho\sigma}(p)\,, \quad \text{with} \quad \Pi^{\mu\nu}(p) = \eta^{\mu\nu} - \frac{p^\mu p^\nu}{p^2}\,, \tag{4.91}$$

where the parenthesis in the superscript stand for symmetrisation with respect to the indices. The respective transverse-traceless part of the graviton propagator is given by

$$G^{\mu\nu\rho\sigma}_{hh,\mathrm{TT}}(p) = G_{hh}(p)\Pi^{\mu\nu\rho\sigma}_{\mathrm{TT}}(p)\,, \qquad \text{with} \qquad G_{hh}(p) = \frac{1}{\Gamma^{(hh)}_{\mathrm{TT}} + Z_h k^2}\,. \tag{4.92}$$

For the scalar propagator function $G_{hh}(p)$, we use the KL spectral representation to access its complex structure. The latter is depicted in Figure 4.21, where we show the real and imaginary parts of the propagator in the full complex plane. Note that we subtracted

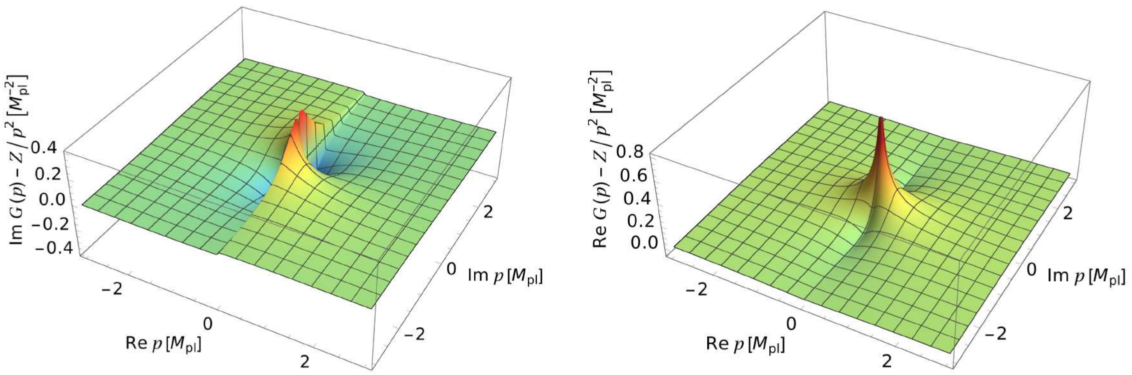

Figure 4.21.: Subleading part of the graviton propagator in the complex plane. It features a cut on the real axis, visible as a discontinuity in the imaginary part (left). The cut approaches a constant at the origin, where it flips sign. The resulting logarithmic divergence is shown in the real part (right).

the mass-pole at vanishing momentum which would otherwise dominate the non-trivial analytic structure.

$$G_{hh}(p^2) = \int_0^\infty \frac{\mathrm{d}\lambda}{\pi} \frac{\lambda\, \rho_h(\lambda)}{\lambda^2 + p^2} \,. \tag{4.93}$$

The spectral function is conveniently parametrised by

$$\rho_h(\lambda) = \frac{1}{Z_h}\Big[2\pi\delta(\lambda^2 - m_h^2) + \theta(\lambda^2 - 4m_h^2) f_h(\lambda)\Big], \tag{4.94}$$

where the global rescaling by $\frac{1}{Z_h}$ allows for a convenient implementation of the spectral flow via RG-invariant correlation functions $\bar{\Gamma}^{(n)}$, for their definition see (4.88). The flow of the RG-inariant 2-point function is given by

$$\partial_t \bar{\Gamma}^{(hh)}_{\mathrm{TT}} = \eta_h\, \bar{\Gamma}^{(hh)}_{\mathrm{TT}} + \frac{\partial_t \Gamma^{(hh)}_{\mathrm{TT}}}{Z_h} \,, \quad \text{with} \quad \eta_h = -\partial_t \log Z_h \,. \tag{4.95}$$

With the RG-adapted CS-Regulator $R_{CS} = Z_h k^2$, the division by Z_h removes it from the flow. What remains, are only factors of η. There are three diagrams contributing to the flow of the graviton two-point function, $\partial_t \Gamma^{(hh)}_{\mathrm{TT}} = \partial_t \Gamma^{(hh)}_{\mathrm{TT}}|_{\text{tadpole}} + \partial_t \Gamma^{(hh)}_{\mathrm{TT}}|_{\text{3-point}} + \partial_t \Gamma^{(hh)}_{\mathrm{TT}}|_{\text{ghost}}$. For their explicit expressions in terms of KL-representations, see Equation (A.83). As already pointed out in [81], the CS-flow of the two-point function carries a quadratic divergence, which is only removed by the counter term flow. There, the authors employed a renormalisation at vanishing momenta. To facilitate the numerical computation, we will use an on-shell renormalisation scheme, where the counter terms are fixed at the pole mass of the graviton, similar to the computations in the scalar theories in Sections 4.1 and 4.2. The renormalisation conditions read

$$\Gamma^{(2)}_{TT}(p^2 = -k^2) = 0 \,, \qquad \partial_{p^2} \Gamma^{(2)}_{TT}(p^2 = -k^2) = 1, \tag{4.96}$$

which allows extracting the (integrated) coefficients of the counter term action from the diagrams evaluated on the pole. This fixes $Z_h = 1$, what also implies $\eta_h = 0$, and

$m_h = k$ in (4.94). For the ghost propagator we used the classical approximation with $Z_c = 1$ and $m_c = k$. For the common parametrisation of the inverse graviton propagator $\Gamma^{(2)}_{TT}(p) = Z_h(p)(k^2(1+\mu)+p^2)$ this translates to $\mu = 0$ and $Z(p^2 = -k^2) = 1$.

To solve the flow, it turns out to be very convenient to convert it to an integral equation and focus on the imaginary part of the diagrams. This amounts to solve the CS-Symanzik equation iteratively for the scale and frequency dependent spectral function $\rho_h(\lambda) = \rho_h(k, \lambda)$. The imaginary part of the RG-invariant graviton two-point function is then simply given by

$$\operatorname{Im}\Gamma^{(hh)}_{TT}(k,\omega) = \int_k^{\omega/2} \frac{dk'}{k'} \int_{\lambda_1,\lambda_2} \rho^{(2)}_h(k',\lambda_1)\rho_h(k',\lambda_2)\operatorname{Im}D(k',\omega,\lambda_1,\lambda_2)\,, \tag{4.97}$$

where $D(k,\omega,\lambda_1,\lambda_2)$ is the sum of ghost and graviton polarisation, see (A.84) and (A.85), and we use a generalised spectral representation for the regulator line, which carries the propagator squared:

$$G^2_h(p) = \int_\lambda \frac{\rho^{(2)}_h(\lambda)}{(p^2+\lambda^2)^2}\,, \qquad \partial_{\omega^2}\rho^{(2)}_h(\omega) = \operatorname{Im} G^2_h(p \to -\mathrm{i}\omega^+)\,. \tag{4.98}$$

While we could also use the usual representation, we use the squared kernel for convenience as it does not change the superficial degree of divergence of the momentum integral, see also A.6.4.1 for detail. Note that the k-integral in (4.97) for a given frequency ω only goes to $\omega/2$, as the imaginary part of the flow is proportional to $\theta(\omega - 2k)$.

To extract the spectral function from the left-hand side of (4.97), we use suitably subtracted Kramers-Kronig relations, see (A.138) instead of calculating the real part from the diagrams. This is not only substantially cheaper, as it is only a single (principal value) integral instad of a potentially two-dimensional spectral one, it also allows for a covenient implementation of the renormalisation conditions (4.96). The spectral tail is then simply given by

$$f_h(k,\omega) = \frac{-2\operatorname{Im}\Gamma^{(hh)}_{TT}(k,\omega)}{\operatorname{Im}\Gamma^{(hh)}_{TT}(k,\omega)^2 + \operatorname{Re}\Gamma^{(hh)}_{TT}(k,\omega)^2} \qquad \text{for} \quad \omega > 2k\,. \tag{4.99}$$

We solve the system via fixed point iteration, for details on the numerics, see Section A.6.4.2.

Similar to [81], we use a constant vertex approximation, where the only momentum structure of the vertices come from their classical tensor structures and a k-dependent Newton coupling. Its beta function in the harmonic gauge reads

$$\partial_t g = 2g - \frac{2499}{380\pi} g^2 \tag{4.100}$$

where we identified the mass parameters and the anomalous dimensions of the scalar and traceless transverse mode and used the on-shell condition. This integrates to a simple trajectory for the newton coupling

$$g(k) = \frac{g^* k^2}{k^2 + g^* M^2_{\mathrm{pl}}}\,, \tag{4.101}$$

with the fixed point coupling $g^* = 760\pi/2499 \approx 0.955\,.$

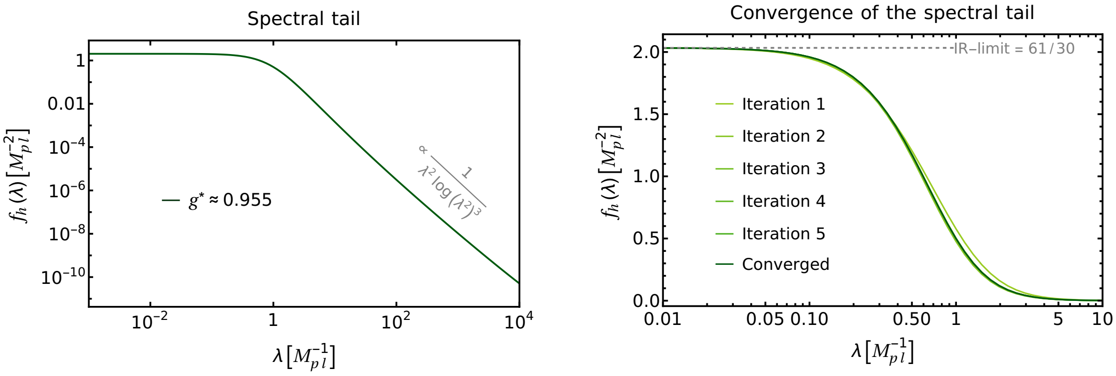

(a) Scattering continuum of the propagator spectral function. Its decay behaviour is indicated in gray and can be calculated analytically, see Appendix A.3.2

(b) Convergence of the iterative solution, the universal IR-value is indicated in gray.

Figure 4.22.: Tail of the propagator spectral function for the fixed point coupling $g^* \approx 0.955$, its exact value is given in the main text below (4.101). Everything is measured in units of the Planck mass M_{pl}.

The solution of this trajectory at $k = 0$ is depicted in Figure 4.22. In the IR, where the newton coupling becomes independent of UV fixed point and all propagators are dominated by their classical values, the quantum corrections to the propagator take a universal form, $G_h = p^{-2} - A_h \log(p^2) + \text{subleading}$, with $A_h = 61/(60\pi) \approx 0.32$. For the spectral function, this entails a constant onset at vanishing frequencies, and the prefactor translates to $61/30 \approx 2.033$. We find that the spectral tail indeed approaches this value without feedback of the spectral tails, if the spectral function is computed consistently via (4.99). The non-trivial denominator, which was effectively missing in [81], turns out to be crucial for a consistent treatment of the spectral flow. The change induced by the feedback of the scattering tail is rather small, as can be seen in Figure 4.22b. For the intermediate scales that we show, the additional logarithmic corrections lead to a faster decay of the spectral function. For asymptotic values, the decay of the tail follows a rather simple behaviour

$$f_h(\lambda \to \infty) = \frac{c_h^{\text{UV}}}{\lambda^2 \log(\lambda^2)^3} \tag{4.102}$$

where the feedback only influences the proportionality constant c_h. Ignoring the scattering tail, this fall-off behaviour can be computed analytically, see Appendix A.3.2. If we are to include the tail in this analysis, we have to notice that it decays around the Planck mass and, importantly, is normalisable in this scheme. Hence, in the UV, the contributions to the propagator from the scattering tail fall of as $1/p^2$, similar to that of the pole. A substantial part of the spectral weight is therefor stored in the spectral values/mass-scales around the Planck mass. For energies much larger than the latter, the associated contribution to the loop does not probe the details of the spectral tail but is dominated by the spectral weight accumulated at lower mass scales. This explains, why also the fully converged spectral tail follows (4.102) in the UV.

4.3.3. Beyond the on-shell flow

To go beyond the on-shell-scheme, we have to use a different renormalisation point. One very convenient possibility would be vanishing momentum, to ensure the correct limit in the IR. The difference to our approach reduces to a flowing Z_h, i.e., a non-vanishing η, with the boundary condition $Z_h(k=0)=1$, and a flowing mass parameter μ_h. To deal with the latter, it could be convenient to make the change of variables $k^2 \to m_h^2 = k^2(1+\mu)$. The flowing wave function renormalisation drops out of the flow equation for the RG-invariant inverse propagator (4.95). To deal with the first term in (4.95), we can turn it into an integral equation for $\mathrm{Im}\,\bar{\Gamma}$ and use an iterative procedure, where we compute the second term from the diagrams, and use $\mathrm{Im}\,\bar{\Gamma}=0$ as an initial guess. The full iterative structure of the procedure is then given by an outer loop, in which the first step is to update the flow that originates in the diagrams, i.e., $\partial_t \mathrm{Im}\,\Gamma$. It proceeds with an inner loop, where of $\mathrm{Im}\,\bar{\Gamma}$ is determined self-consistently, and ends with the extraction of the spectral function as desribed below (4.97).

4.3.4. Conclusion

We want to discuss the results obtained in this Section from two perspectives. First of all, we presented the first, fully self-consistent computation of the spectral function of the traceless transverse mode of the graviton propagator. However, we have employed a novel scheme, which differs qualitatively from the momentum dependent computations with standard Euclidean Wetterich flows, see e.g., [217]. The latter fact demands a more careful analysis, to elucidate the connection between these different schemes.

The on-shell renormalisation used in this work allowed for a very convenient numerical implementation of the spectral flow, due to its simplifications to the beta function and the easily tractable analytic structure. Note, however that the implementation of a different renormalisation point does not pose conceptual issues, see the discussion of Section 4.3.3. We showed how the consistent treatment of the real and imaginary part of the self energy is required to obtain the correct universal infrared behaviour of the propagator spectral function. The self-consistent feedback of the scattering tail lead only to small corrections, see Figure 4.22b, which only take a non-trivial form around the plank scale. While the IR-limit is not altered by the higher order contributions, they modify the UV-limit by a multiplicative constant, see also the discussion below (4.102).

The on-shell renormalisation leads to a normalisable spectral function, what corresponds to a vanishing anomalous dimension in the UV, i.e., a propagator that falls off as $1/p^2$, signalling the existence of canonical comutation relations for the graviton field. This is not supported by other momentum dependent computations in the fluctuation approach, where the anomalous dimension around the UV-fixed point has been found to be rather large, and the propagator to fall off as approximately $1/\sqrt{p^2}$ [217]. In the present approach, this cannot be accommodated for, and we deem it unlikely that a different choice of the renormalisation scale cures this mismatch easily. While the anomalous running of Z_k shown in [81] is easily reproduced, the mapping of the present scheme requires the inclusion of momentum dependent vertex function, which evidently play a mayor rôle in the momentum scaling of the flow close to the fixed point. We hope to report on respective results in the near future.

5. Dynamical observables in Quantum Chromodynamics

The study of dynamical processes in QCD — such as bound-state formation, transport properties of the quark-gluon plasma, and the calculation of form factors and scattering amplitudes — requires access to fully non-perturbative real-time correlation functions. A direct computation of these quantities is only feasible within functional approaches, such as Dyson-Schwinger equations (DSE) and the functional renormalisation group (FRG). In these frameworks, the diagrammatic relations are governed by the propagators of the elementary and emergent degrees of freedom. Moreover, in bound-state computations, for instance using Bethe-Salpeter equations (BSE) or Faddeev equations, the propagators — and specifically their causal structure — play a pivotal rôle and must be used self-consistently. For a comprehensive review, see [40].

As already outlined in the introduction, Chapter 1, the non-perturbative determination of dynamical observables is a formidable task and demands substantial numerical efforts. In QCD, the complexity is further increased by the gauge degrees of freedom, which include negative norm states. This is reflected in the spectral structure of gauge-variant correlation functions, and it remains unclear whether the Källén-Lehmann (KL) representation exists for elementary correlation functions or whether it is violated by the presence of additional complex poles or cuts. While such acausal structures are forbidden in physical observables, they may appear in the elementary correlation functions of a gauged theory and cancel out in the final measurable quantities.

The spectral functional approaches described in the previous chapter, Chapter 3, provide a framework for the direct computation of real-time correlators and their associated spectral functions. Their practical implementation relies on the existence of the KL representation for momentum-dependent correlation functions. We will therefore assume its validity and discuss potential consequences if this assumption were to be violated.

In this chapter, we begin by discussing the causal structure of the quark and determine its propagator spectral function using a novel causal vertex construction, see Section 5.1. Subsequently, in Section 5.2, we use the obtained spectral functions to compute the pion distribution amplitude directly on the light front.

5.1. The quark spectral function

This section is in parts based on [4].

This section focuses on the elementary spectral functions that are particularly relevant for the determination of dynamical observables in QCD. Special emphasis is placed on the quark propagator. In contrast, for the gluon propagator, we will only highlight the key aspects, as we rely on numerical reconstructions of the gluon spectral functions rather than direct computations.

In the first part, we discuss the causal structure of the quark propagator, with a focus on its qualitative changes depending on the interaction strength of the classical tensor structure in the quark-gluon vertex. In particular, we show that beyond a critical interaction strength, the quark propagator develops an additional pair of complex conjugate (cc) poles, qualitatively altering its causal structure. The interaction strength of the full QCD vertex remains safely below this critical threshold. Moreover, assuming a spectral representation for the combination of the gluon propagator and the quark-gluon vertex, the quark propagator does not develop any cc poles. In contrast, commonly used vertex models typically exceed the critical interaction strength, leading to additional cc poles. These poles are a robust feature in such models and can be traced directly to the over-enhancement and shape of the Euclidean dressing of the classical tensor structure, which defines the quark-gluon avatar of the strong coupling. In conclusion, the over-enhancement of the vertex, often necessary in the absence of further tensor structures (see, e.g., [33, 39, 220–222]), may trigger acausal structures in the system. Conversely, in computations with the full quark-gluon vertex, the interaction strength of the classical tensor structure remains below the critical value, and part of the total strength of spontaneous chiral symmetry breaking is carried by non-classical tensor structures. This combination suggests a mechanism by which the appearance of additional cc poles and related causality violations may be avoided.

Our analysis is based on the spectral Dyson-Schwinger equation (DSE) [54] for the inverse quark propagator. We solve the gap equation using input from a spectral gluon propagator [45, 185] and a quark-gluon vertex constructed from its Slavnov-Taylor identity (STI). Notably, this vertex construction avoids introducing unphysical poles or cuts in the complex plane. It is modeled to reproduce the peak position of a physical quark-gluon coupling in the infrared, and we systematically track qualitative changes in the causal structure of the quark propagator as a function of the vertex strength, i.e., the height of the peak.

In Section 5.1.1, we introduce the spectral Dyson-Schwinger equation for the inverse quark propagator and discuss the causal structure of the input correlation functions. In Section 5.1.4, we then analyze the emerging complex structure of the solutions to the gap equation. We evaluate under which conditions the quark propagator admits a Källén-Lehmann representation and how additional complex conjugate poles emerge as the strength of the quark-gluon vertex is enhanced. Finally, in Section 5.1.8, we argue that our results suggest the existence of a Källén-Lehmann representation for the quark propagator in full QCD and discuss the implications for phenomenological applications.

5.1.1. The spectral quark gap equation

The framework of spectral Dyson-Schwinger equations allows for a self-consistent numerical computation of the quark self-energy in the full complex frequency plane. It has been developed in [54] and put to use in [80, 115, 191] for Yang-Mills theories. For further applications and extensions of the framework to the functional renormalisation group (fRG) see [1–3, 81]. Complementary approaches and earlier real-time computations in a variety of fields with the fRG can be found in [90–92, 101, 142, 223–236]. For further real-time computations in QCD or QED utilising (generalised) spectral representations see e.g. [53, 190, 237–239], for related work using contour deformations see e.g. [151, 240, 241].

The full inverse quark propagator is uniquely parametrised by

$$\Gamma^{(q\bar{q})}(p) = Z_q(p)\left[\mathrm{i}\not{p} + M_q(p)\right] , \tag{5.1}$$

with the quark wave function $Z_q(p)$ and the quark mass function $M_q(p)$. The subscript $_q$ of the dressing functions refers to the light and strange quark flavors $_l$ and $_s$ respectively. The (inverse) propagator is diagonal in flavor space, and we focus on the light quarks with $(2+1)$ flavor input in this work. We use Euclidean conventions for gamma matrices and momenta, i.e. $\{\gamma_\mu, \gamma_\nu\} = 2\delta_{\mu\nu}$ and $p^2 = p_0^2 + \vec{p}^{\,2}$. Real frequencies will be denoted by ω to distinguish them from their Euclidean counterparts. The inverse propagator satisfies a one-loop exact Dyson-Schwinger equation

$$\Gamma^{(q\bar{q})}(p) = \mathrm{i}Z_2\not{p} + Z_m m_q + \Sigma_q(p). \tag{5.2}$$

The self energy $\Sigma_q(p)$ in (5.2) comprises the quantum fluctuations of the quark propagator, for a diagrammatic representation, see Figure 5.1. The renormalisation constants Z_2 and Z_m are the wave function and mass renormalisation constants that appear in the renormalised classical action. The self-energy has a diagrammatic representation in terms of full correlation functions and the classical quark-gluon vertex $\mathrm{i}g_s\gamma_\mu\mathbb{1}$ with the gauge coupling g_s, and $\mathbb{1}$ is the unity in flavor and color space. Then, the unrenormalised self energy takes the rather simple form

$$\Sigma_q(p) = g_s C_f Z_1(\mathrm{i}\gamma_\mu)\int_q G_A^{\mu\nu}(q)\, G_q(p+q)\Gamma_\nu(q,p)\,, \tag{5.3}$$

where we have omitted flavor and color indices as the gap equation is color and flavor diagonal and the loop integral is abbreviated as $\int_q = \int \frac{d^4q}{(2\pi)^4}$. Equation (5.3) depends on the full quark and gluon propagators $G_q(p+q)$ and $G_A^{\mu\nu}(q)$, as well as the full quark-gluon vertex $\Gamma_\nu(q,p)$. The Casimir of the fundamental representation $C_f[SU(3)] = 4/3$ and the vertex renormalisation constant Z_1 enters the gap equation as a prefactor.

5.1.2. Spectral structure of quark and gluon propagators

We solve the Dyson-Schwinger equation in the full complex frequency plane by utilising spectral representations of the full correlation functions involved. This allows for an analytic computation of the momentum integrals of a given loop including the renormalisation, and reduces the computation to a finite spectral one.

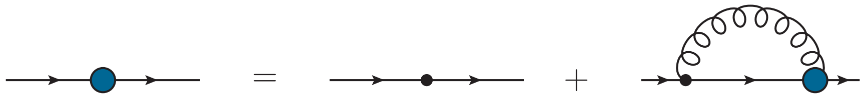

Figure 5.1.: Dyson-Schwinger equation for the inverse quark propagator. Big blue blobs denote full n-point functions, while classical n-point functions are represented by small dots with n legs attached. Full propagators are denoted by straight (quarks) and spiralling (gluons) lines.

The quark propagator $G_q(p)$ has a scalar and Dirac part with

$$G_q(p) = -\mathrm{i}\not{p}\, G_q^d(p) + G_q^s(p) = \frac{-\mathrm{i}\not{p} + M_q(p)}{Z_q(p)\big[p^2 + M_q^2(p)\big]}\,. \tag{5.4}$$

Both parts have a generalised Källén-Lehmann representation that also accommodates possible additional complex conjugate poles and cuts, induced by non-analyticities away from the real frequency axis. In the absence of the latter, the spectral representation of the quark propagator takes a very compact form [53]

$$G_q(p) = \int_{-\infty}^{\infty} \frac{d\lambda}{2\pi} \frac{\rho_q(\lambda)}{\mathrm{i}\not{p} + \lambda}\,, \tag{5.5}$$

where the spectral functions of the scalar and Dirac part of the quark propagator $\rho_q^{(s/d)}$ are given by the antisymmetric and symmetric parts of the quark spectral function ρ_q, respectively. They are defined via the imaginary part of the retarded propagator on the real frequency axis as

$$\begin{aligned} \rho_q^{(d)}(\omega) &= 2\omega\, \mathrm{Im}\, G_q^d(p_0 \to -\mathrm{i}\omega_+)\,, \\ \rho_q^{(s)}(\omega) &= 2\, \mathrm{Im}\, G_q^s(p_0 \to -\mathrm{i}\omega_+)\,, \end{aligned} \tag{5.6}$$

with real frequencies ω, and $\omega_+ = \omega + \mathrm{i}0^+$ denotes the retarded limit.

In general, the spectral functions feature delta functions or peaks with a given width and a continuous part that decays for large spectral values. The latter part arises from branch point singularities and continuous cuts and relates to a continuum of scattering states. The former part originates from isolated poles, related to (quasi) particle excitations with or without a decay width. In the following, we choose the Ansatz of a single pole and a scattering continuum for the quark spectral functions,

$$\rho_q^{(d/s)}(\lambda) = \pi R_q^{(d/s)} \delta\left(\lambda - m_{q,\mathrm{pole}}\right) + \tilde{\rho}_q^{(d/s)}(\lambda)\,, \tag{5.7}$$

which anticipates the following analytic structure of the quark self energy: firstly, a zero crossing of the real part of the inverse propagator at the pole mass $m_{q,\mathrm{pole}}$. Secondly a branch cut starting at $\lambda_{\mathrm{scat}} \geq m_{q,\mathrm{pole}}$, with the additional constraint that the imaginary part of the mass function approaches zero for $\omega \to m_{q,\mathrm{pole}}$. Note, that although the emergence of complex conjugate poles for certain parameter values violates the spectral representation (5.5), the spectral functions as defined in (5.6) from the cuts on the real axis, does not deviate from the pole-scattering split (5.7). The spectral representation

(5.5) entails the sum rules

$$\int_\lambda \rho_q^{(d)}(\lambda) = \lim_{p^2\to\infty} \frac{1}{Z_q(p)}\,, \qquad \int_\lambda \lambda\, \rho_q^{(s)}(\lambda) = 0\,, \tag{5.8}$$

with

$$\int_\lambda = \int_0^\infty \frac{d\lambda}{\pi}\,. \tag{5.9}$$

The sum rules (5.8) can be deduced from the asymptotic behaviour of the propagator, for details see [115]. Note, that the mass function $M_q(p)$ decays logarithmically for large momenta for finite current quark masses, while it decays polynomially with $1/p^2$ in the chiral limit. In both cases, the scalar sum rule in (5.8) holds true.

For the gluon propagator in (2+1)-flavor QCD, we use the spectral one obtained with a spectral reconstruction in [45, 185]. In these works, a Källén-Lehmann representation for the gluon propagator in the Landau gauge was assumed,

$$G_A^{\mu\nu}(q) = \Pi^{\mu\nu}(q) G_A(q) \quad \Pi^{\mu\nu}(q) = \delta^{\mu\nu} - \frac{q^\mu q^\nu}{q^2}\,, \tag{5.10}$$

with

$$G_A(q) = \int_\lambda \frac{\lambda \rho_A(\lambda)}{q^2+\lambda^2}\,, \qquad \int_\lambda \lambda \rho_A(\lambda) = 0\,. \tag{5.11}$$

The sum rule in (5.11) is the Oehme-Zimmermann super-convergence relation [82, 83, 242] in the Landau gauge.

For the generality of the analysis of the causal structure of the quark propagator done below, see Section 5.1.4 it is important to also discuss the impact of potential cc poles in the gluon propagator, as they have been observed in multiple reconstructions, see eg., [44, 243, 244]. In the present truncation for the quark-gluon vertex, they lead to complex conjugate cuts in the quark self energy. However, as the real part of potential complex poles in the gluon propagator would take a value related to the gluon mass scale, their inclusion would not alter the behaviour of the quark spectral function near the threshold. In conclusion, the structural results of this work do not depend on the existence or absence of cc poles in the spectral representation of the gluon.

5.1.3. A causal quark-gluon vertex

The quark-gluon vertex is the pivotal ingredient in the gap equation and hence for the dynamics of chiral symmetry breaking. It has been thoroughly studied in the literature, see e.g. [33, 39, 220–222, 245]. It can be decomposed into twelve Dirac structures,

$$\Gamma_\mu(p,q) = \sum_{i=1}^{12} \lambda^{(i)}(p,q)\, \mathcal{T}_\mu^{(i)}(p,q)\,, \tag{5.12}$$

of which four can be chosen purely longitudinal and hence do not enter the gap equation in the Landau gauge, for basis choices and more details we refer to [33, 35, 39, 220, 245]. While we only use the classical tensor structure in the explicit computation, our analysis

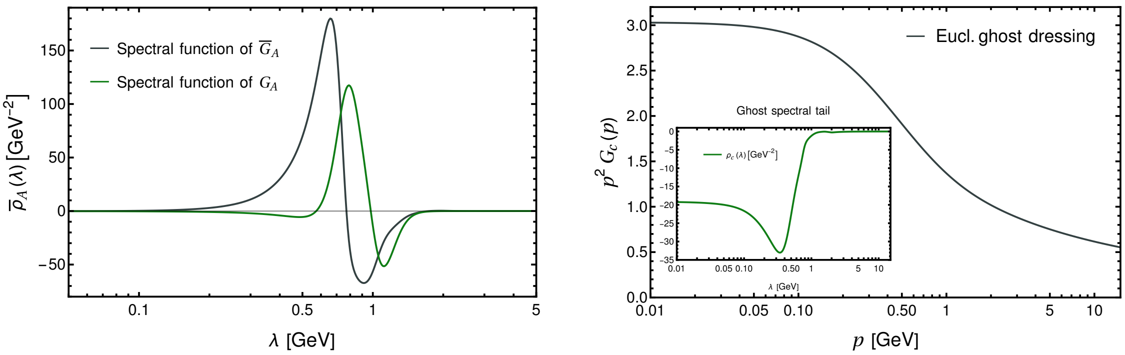

(a) Spectral function of $\bar{G}(p) = G_A(p)/Z_c(p)$ and $G_A(p)$ respectively. The ghost dressing shifts the peaked structures of the gluon spectral function to the infrared.

(b) Euclidean ghost dressing. The corresponding spectral tail is shown in the inset.

Figure 5.2.: Input for the spectral gap equation from the reconstructed glue sector.

uses the basis in [35]. We count all momenta as incoming, and p and q are the incoming gluon and antiquark momenta, respectively. The dominant transverse structures are given by

$$\mathcal{T}^{(1)}_\mu(p,q) = \mathrm{i}\,\gamma_\mu\,, \qquad \mathcal{T}^{(4)}_\mu(p,q) = \mathrm{i}\,\sigma_{\mu\nu}p_\nu\,,$$

$$\mathcal{T}^{(7)}_\mu(p,q) = \frac{1}{3}\Big[\sigma_{\alpha\beta}\gamma_\mu + \sigma_{\beta\mu}\gamma_\alpha + \sigma_{\mu\alpha}\gamma_\beta\Big]\,k^+_\alpha k^-_\beta\,, \tag{5.13}$$

where $\sigma^{\mu\nu} = \mathrm{i}/2[\gamma^\mu, \gamma^\nu]$ and $k^\pm = (p \pm q)$.

While the classical tensor structure is the dominant one, $\mathcal{T}^{(4,7)}$ also have a major impact on the size of chiral symmetry breaking. Specifically, the chiral symmetry breaking tensor structure $\mathcal{T}^{(4)}$ plays a sizeable rôle in the generation of the constituent quark mass in the chirally broken regime. Its impact on the causal structure will be studied in a forthcoming work, but here we focus on the analytic structure induced by the overall strength of the classical Dirac structure. Apart from being the dominant effect and hence deserves to be studied first, respective vertices have been and are used in manifold applications in low energy QCD, and are common place in bound state studies: roughly speaking, in all these applications one drops $\mathcal{T}^{(4,7)}$ and emulates the missing fluctuations by increasing the infrared strength of the dressing $\lambda^{(1)}$ of the classical tensor structure.

Hence, we proceed likewise here by only using the first tensor structure, where we identify the corresponding form factor with the ghost dressing to capture the UV running and peak position of the quark-gluon vertex. This dressing can be inferred by the Slavnov-Taylor identity and resembles a simplified variant of the Ball-Chiu vertex [246]. The STIs can also be used to construct a fully gauge-consistent causal vertex, see Appendix A.4.1. For a comparison of STI vertices with the full ones, see e.g. [39]. The vertex is then given by

$$\Gamma_\mu(p,q) = \mathrm{i}\,\gamma_\mu\lambda_1(p^2)\,, \tag{5.14a}$$

with

$$\lambda_1(p^2) = \eta\, g_s(\mu_r)\frac{Z_q(\mu_r^2)}{Z_c(p^2)}\,. \tag{5.14b}$$

The form factor $\lambda_1(p^2)$ contains an additional factor $Z_q(\mu_r)$ with the renormalisation group scale μ_r for RG-consistency and a global strength factor η. Note, that the global strength factor η accommodates two qualitatively different contributions: firstly, it compensates for the additional terms in the STI that have been dropped for the sake of convenience and numerical simplicity in the construction (5.14b). Second, it compensates for dropping the fluctuation effects from the other vertex structures, and in particular $\mathcal{T}^{(4,7)}$. For other constructions of the quark-gluon vertex in the context of bound state studies and the Dyson-Schwinger equation, see [152, 247–257].

In the present work, we use the spectral representation of the ghost dressing function in (5.14b). It has been calculated directly in [80] and this computation reveals its spectral structure. This facilitates and constrains its spectral reconstruction from Euclidean precision data, as done in [45, 185]. Since the ghost propagator contains a massless pole, the spectral function has to contain a delta function at zero. The spectral representation of the ghost dressing function $1/Z_c(p^2) = p^2 G_c(p)$ reads

$$\frac{1}{Z_c(p^2)} = \frac{1}{Z_c(0)} + p^2 \int_0^\infty \frac{d\lambda}{\pi} \frac{\lambda\,\rho_c(\lambda)}{p^2+\lambda^2}\,. \tag{5.15}$$

While the residue of the massless pole is determined by the value of the ghost dressing function at zero, the spectral function $\rho_c(\lambda)$ can be quantitatively described by a rather simple functional form as discussed in [80]. The ghost dressing function and the corresponding spectral function are shown in Figure 5.2b. It enters the gap equation only as the product of the ghost dressing and the gluon propagator $\bar{G}_A(p) = G_A(p)/Z_c(p)$, with

$$\bar{G}_A(p) = \int\limits_0^\infty \frac{d\lambda}{\pi} \frac{\lambda\,\bar{\rho}_A(\lambda)}{q^2+\lambda^2}\,. \tag{5.16}$$

The spectral function $\bar{\rho}_A(p)$ is shown in Figure 5.2a in comparison to that of the gluon, $\rho_A(p)$. In the present work, we use the spectral reconstruction of the lattice-type decoupling solution from [185].

We also note in passing, that due to its well-understood spectral form one may simply use the fitting form of the ghost spectral function devised in [80]. This can be used to model the form factor of the classical tensor structure, although a cautious monitoring of the complex structure of the model is required for minimising the impact of unphysical approximation artefacts.

In summary, the STI construction in (5.14) allows us to reproduce the form of the quark-gluon coupling in the IR. This coupling is defined via the exchange process of a gluon between two quarks projected on the classical tensor structure of the vertex on the symmetric point,

$$\alpha_s(\bar{p}) = \frac{1}{4\pi} \frac{\big(\lambda^{(1)}(\bar{p})\big)^2}{Z_q(\bar{p})^2 Z_A(\bar{p})}\,, \qquad \bar{p}^2 = \frac{1}{3}\sum_{i=1}^{3} p_i^2\,. \tag{5.17}$$

We will use results for (5.17) from quantitative functional computations in [33, 35, 39] as a point of reference, as they have been computed in the renormalisation scheme also employed here: In our computation, both the gluon and ghost dressings are fixed by the inputs; see Figure 5.2a and Figure 5.2b. Accordingly, (5.17) only depends on the global

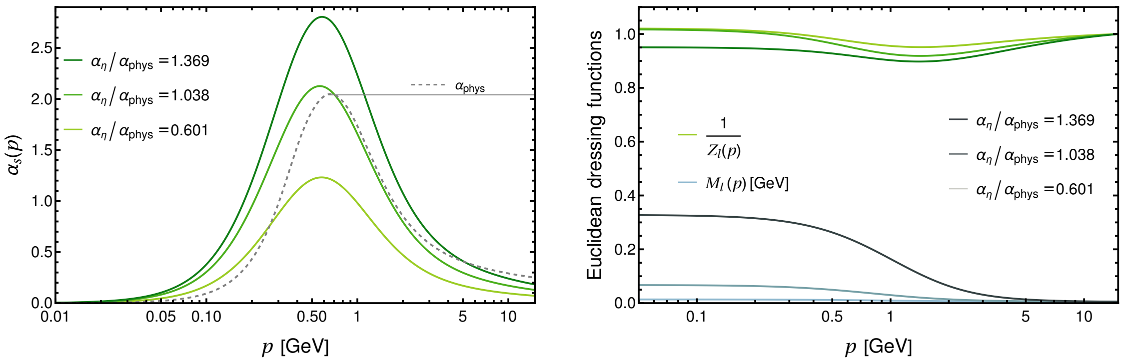

(a) Strong coupling α_s as a function of momentum and enhancement factor. The grey line indicates the peak value of the full quark-gluon coupling on the symmetric point for $(2+1)$ flavors from [35].

(b) Dressing of the light quark propagator $1/Z_l(p)$ and its mass function $M_l(p)$ for different enhancement factors. The mass function is renormalised to $m_l = 2.7$ MeV at the renormalisation scale.

Figure 5.3.: Couplings $\alpha_\eta(p)$ and light quark dressings $M_l(p), 1/Z_l(p)$ for different enhancement factors.

strength factor η introduced in (5.14b) and the η-dependent quark dressings. To compare against the physical coupling, we define the respective peak values as

$$\alpha_{\mathrm{phys}} = \max_{\bar{p}} \alpha_s(\bar{p})\,, \qquad \alpha_\eta = \max_{\bar{p}} \alpha_s^\eta(\bar{p})\,. \tag{5.18}$$

For the physical coupling, we use the result of the quantitative computation in [35]. The superscript η indicates the dependence of the coupling used in the present work on the global enhancement factor η. This dependence comes explicitly from the vertex dressing (5.14b) and implicitly from the quark dressing function, which we determine dynamically from the gap equation for a given value of η. We will use the ratio $\alpha_\eta/\alpha_{\mathrm{phys}}$ to quantify the enhancement of the coupling due to the global strength factor η. The couplings and the Euclidean quark dressing functions are given in Figure 5.3a and Figure 5.3b respectively. In Figure 5.3a we show the exchange coupling for various global strength factors $\eta \in \{0.553, 0.742, 0.883\}$ in comparison to the physical value. The corresponding rations of the peak are $\alpha_\eta/\alpha_{\mathrm{phys}} \in \{0.601, 1.038, 1.369\}$. We note that the approximate vertex (5.14) reproduces the qualitative features of the exchange couplings well, in particular the peak position: it is located at about $p_{\mathrm{glue}}^{\mathrm{peak}} \approx 0.6\,\mathrm{GeV}$, close to that of the full solution in [33, 35, 39]. The physical amount of chiral symmetry breaking requires a strong enhancement of the coupling with $\alpha_\eta/\alpha_{\mathrm{phys}} \approx 1.4$. However, part of this enhancement is also related to the details of the coupling. For the total amount of chiral symmetry breaking, it is rather the integrated coupling that is relevant. This includes in particular also the steepness of the coupling on both sides of the peak, which is not captured by our vertex construction.

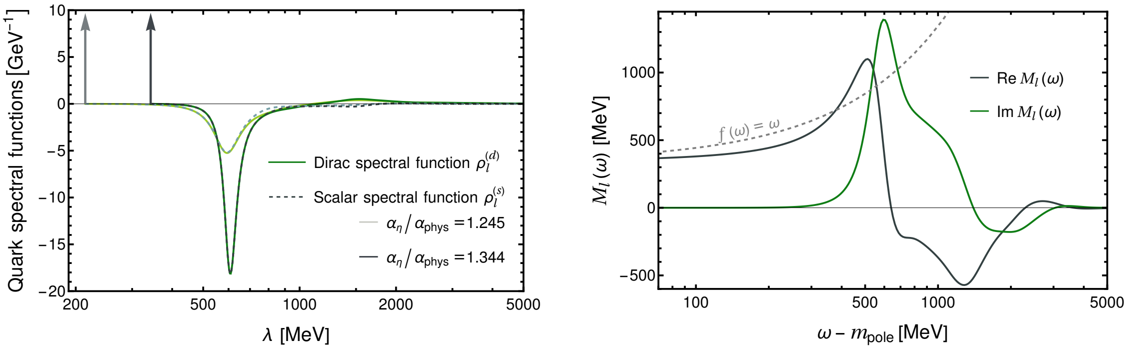

(a) Quark spectral functions for different enhancement factors, which correspond to qualitatively different complex structures. The arrows indicate real poles at the onset of the scattering continuum with $m_{\text{pole}} \in \{214, 342\}$ MeV.

(b) Real and imaginary parts of the mass function for $\alpha^\eta/\alpha_{\text{phys}} = 1.344$, see (5.14b) and (5.18). The x-axis shows $\omega - m_{\text{pole}}$. The real part crosses the line $f(w) = w$, indicated in grey, what signals cc poles.

Figure 5.4.: Spectral functions $\rho_l^{(d,s)}$ of the quark propagator (left), and its mass function M_l for real frequencies (right).

5.1.4. The causal structure of the quark propagator

The spectral gap equation is solved numerically with the input discussed in the last section. Inserting the quark-gluon vertex (5.14) in the gap equation (5.3) and using the spectral representations of the quark propagator (5.5) and that of the scattering kernel $G_A(p)/Z_c(p)$ in (5.16), we arrive at

$$\Sigma_q(p) = g_s^2\, C_f Z_1 \int\limits_{\lambda_q,\lambda_A} \lambda_A\, \bar\rho_A(\lambda_A)\rho_q(\lambda_q) I(\lambda_q, \lambda_A, p)\,, \tag{5.19}$$

with

$$I(\lambda_q, \lambda_A, p) = \int_q \frac{\gamma_\mu \Pi^{\mu\nu}(q)\left(-\mathrm{i}(\not p + \not q) + \lambda_q\right)\gamma_\nu}{\left(q^2+\lambda_A^2\right)\left((p+q)^2+\lambda_q^2\right)}\,. \tag{5.20}$$

The loop integral eq. (5.20) is computed in dimensional regularisation, and the whole self energy is renormalised within a BPHZ subtraction scheme,

$$\Sigma_q^{\text{ren}}(p) = \Sigma_q(p) - \Sigma_q(\mu_r)\,, \tag{5.21}$$

where the subtraction implicitly determines the renormalisation constants Z_2 and Z_m in eq. (5.2). This procedure not only removes the explicitly divergent terms of the loop integral eq. (5.20), but also the remaining divergences from the spectral integral. For details on the spectral renormalisation, see [54] and for the explicit implementation in the present work, see Appendix A.4.2.

The spectral function of the scattering kernel $\bar\rho_A(\lambda)$ is shown in Figure 5.2a. Since the vertex dressing does not diverge in the infrared, the combined spectral function still approaches zero at the onset of the scattering continuum fast enough and $\bar G_A$ remains finite at the origin. Moreover, the imaginary part of both, the Dirac and scalar part of

$I(\lambda_q, \lambda_A, p)$ in (5.20), contains only terms proportional to either $\sqrt{w-\lambda_q-\lambda_A}\,\Theta(w-\lambda_q-\lambda_A)$ or $(\omega-\lambda_q)^3\,\Theta(w-\lambda_q)$, see Appendix A.4.2 for details. Consequently, the imaginary part of the self energy vanishes at its onset with a power law. Hence, the self-consistent iteration converges towards a solution with a first zero crossing in $w - \mathrm{Re}\, M_l(w)$ that coincides with a vanishing imaginary part of the mass function. This leads to a real pole as the first singularity of the quark propagator in the complex plane, which is discussed in detail in the following Section 5.1.5. In Section 5.1.6 we complete the discussion of the causal structure of the quark propagator with that on the emergence of cc poles, in addition to the real one, for large coupling strength.

5.1.5. The real pole of the quark propagator

For the evaluation of the qualitative change of the causal structure, we scan the strength parameter η in the vertex (5.14) in the interval $[0.553, 0.883]$. This corresponds to a relative coupling strength $\alpha_\eta/\alpha_{\text{phys}}$ in the interval $[0.601, 1.36941]$. Technically, it is convenient to solve the spectral DSE first for the smallest value of η considered here and use the result iteratively as the input for the first iteration of the gap equation for the next bigger η-value.

We exemplify our results for the spectral functions in Figure 5.4a, where $\rho_l^{(s,d)}$ of the light quarks are shown (left panel) for two different values of the vertex strength $\eta = 0.829, 0.872$ with different causal structures. These η's correspond to relative coupling strengths $\alpha_\eta/\alpha_{\text{phys}} = 1.245, 1.344$. The real pole at $w = m_{\text{pole}}$ is indicated by a delta peak in the spectral functions in Figure 5.4a. The cut, induced by the gluon exchange, starts at the pole, but is vanishing there. The imaginary parts of mass function and wave function both approach zero at the onset, see Figure 5.4b for the mass function. We would like to emphasise that a real pole in the quark propagator does not correspond to a physical, asymptotic particle state that could be observed in the experiment. For larger values of the spectral parameter, the spectral functions are predominantly negative. This positivity violation is necessary for satisfying the spectral sum rules in (5.8). In the right panel, Figure 5.3b, we show the mass function $M_l(\omega)$ for the larger value $\alpha_\eta/\alpha_{\text{phys}} = 1.344$: the real part of the mass function crosses the line $f(\omega) = \omega$, indicating the emergence of additional pairs of cc poles, which will be discussed in Section 5.1.6.

The most prominent common feature of the spectral functions for all tested coupling strengths is the emergence of a real pole as the first singularity in the complex plane at the onset of the scattering continuum. Evidently, we cannot draw fully conclusive statements about the nature of the first singularity in the complex plane, as the vertex is not computed self-consistently. Instead, we use an STI-compatible vertex model. However, the mechanism that underlies the occurrence of the real pole is rather generic. It is simply based on two properties of the product of the gluon propagator and the vertex, which we expect to hold in full QCD in the Landau gauge. We shall discuss these properties by comparing our result with the results of direct real-time computations in the literature: in most cases, including the present work, the effective quark-gluon interaction is modelled by an effective gluon exchange that combines the gluon propagator and the vertex,

$$G_A(q)\Gamma_\mu(p,q) \propto \gamma_\mu \frac{\alpha_s^{\text{eff}}(q)}{q^2}\,. \tag{5.22}$$

The first property is the finiteness of (5.22) in the soft gluon limit. A singularity such as a pole, a branch-cut singularity, or a logarithmic divergence, signalled by a finite value of a cut at vanishing gluon momentum, possibly shifts the first singularity into the complex plane. Previous results that show a complex first singularity can be found in [240, 241, 258] for QCD-like models in four dimensions and [158] in QED$_3$. While the details of these vertex models differ, the combination of the gluon propagator and vertex diverges in the soft gluon limit. In [158, 240], the effective coupling α^s_{eff} stays finite in the soft gluon limit, effectively leading to the implementation of a massless gluon (or photon) propagator. The same holds true for [258], where the authors use a similar construction to that of the present work, only that the dressing function λ_1 is proportional to $1/Z_c(p)^2$. This leads to an α_s^{eff} that is proportional to the Taylor coupling, which acquires a finite value on the scaling solution. The confinement term in [241] even contains a delta function at the origin. In full computations, the product of the gluon propagator and the vertex stays finite in the soft gluon limit, see [33, 39, 220–222]. Note in this context, that this property is fulfilled in full calculations even if considering explicitly the dynamical generation of confinement by means of the Schwinger mechanism, see e.g. [69–72], or the quartet mechanism, see e.g. [73]. We discuss this at the example of the Schwinger mechanism. There, the confining mass gap of the gluon in the Landau gauge is related to the occurrence of a massless bound state in the longitudinal glue sector of the theory. While this massless bound state is mirrored in the longitudinal part of the quark-gluon vertex, the transverse quark-gluon vertex does not contain a pole at vanishing gluon momentum.

The second assumption that appears to be crucial for our analysis to hold, is the existence of a Källén-Lehmann representation for the product of the gluon propagator and the vertex. While the standard Rainbow-Ladder kernel [149] does not have a singularity in the origin, it also does not admit a spectral representation due to the finite width representation of $\delta(q)$. The latter implements the necessary infrared enhancement of the vertex but also carries an essential singularity at complex infinity. The nature of the first singularity in the complex plane for such models depends on the explicit parameters and has been studied in, e.g., [151] and [159], where the dependence of hadron masses on the position of the first pole is found to be mild in the latter.

Further studies that link the absence of a real pole to confinement, such as [259, 260], only deduce the possibility of cc poles from the positivity violation of the Schwinger function, which does not rule out a real pole, whereas the reconstructions in [261, 262] indicate the existence of a dominant singularity on the real axis. The scenario of a real pole was also found in [190] for a vertex model that resembles a massive gluon with the mass m_{glue}, i.e., where the cut of the quark self energy starts only at $m_{\text{pole}} + m_{\text{glue}}$, different to our construction. Moreover, the authors also report the emergence of additional cc poles for certain parameter choices, without giving a detailed analysis of the underlying mechanism.

5.1.6. Additional cc poles for large vertex strength

Having a real pole established as the first singularity of the quark propagator in our approximation, we proceed with the analysis of the remaining causal structure. The current approximation reproduces DχSB quantitatively, subject to an appropriate choice of the strength parameter η. The physical constituent quark mass is obtained for

$$M_l(0) \approx 350\,\text{MeV}, \quad \eta_{\text{const}} = 0.882 : \ \frac{\alpha_\eta}{\alpha_{\text{phys}}} \approx 1.39, \tag{5.23}$$

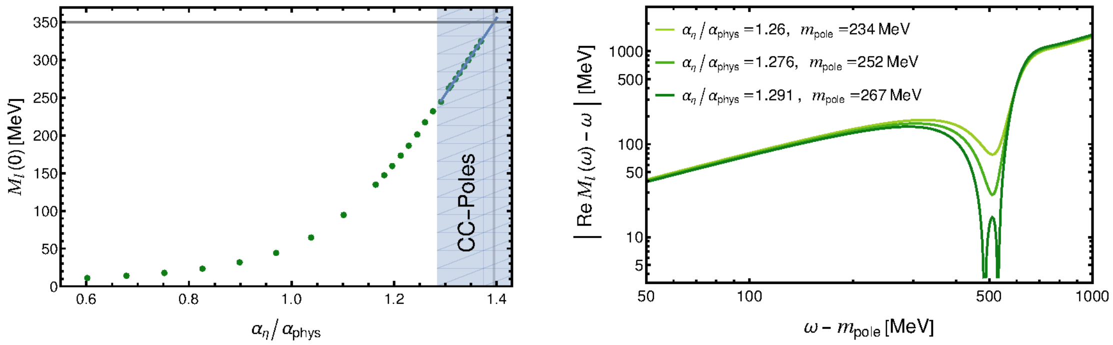

(a) Constituent quark mass over the enhancement factor. We find the emergence of cc poles for larger enhancement factors, that are indicated by the blue region. The grey lines indicate an estimate of the necessary enhancement to achieve a realistic amount of DχSB with $M(0) \approx 350$ MeV

(b) The absolute value of the Re $M(\omega) - w$ for different values of the coupling. For the largest value, the zero crossings show the emergence of cc poles. The critical value of the coupling is approximately $\alpha_{\eta^*}/\alpha_{\rm phys} \approx 1.283$

Figure 5.5.: Emergence of the complex conjugate poles for larger vertex strengths.

see Figure 5.5a. The ratio $\alpha_\eta/\alpha_{\rm phys}$ in (5.23) is the enhancement of the peak coupling for a given $\eta_{\rm const}$. This is a good measure for the overall enhancement of the vertex strength. We shall see that in this case the quark propagator has no Källén-Lehmann representation but contains at least two cc poles in addition to the real one.

In turn, using the vertex strength with the physical peak height of the coupling, the respective constituent quark mass is given by

$$M_l(0) \approx 60\,\text{MeV}, \qquad \eta_{\rm phys} = 0.741 : \quad \frac{\alpha_\eta}{\alpha_{\rm phys}} \approx 1, \tag{5.24}$$

see Figure 5.3. This compares well with the solution of the gap equation by using the full dressing $\lambda^{(1)}$ in [39] with $M_l(0) \approx 80\,$MeV, the difference can be attributed to the slightly different shape of the vertex functions, as the width and ultraviolet decay of $\lambda^{(1)}$ have a sizeable impact on the strength of chiral symmetry breaking. In any case, this illustrates impressively the importance of the other tensor structures, see e.g. [33, 39, 220–222], see also the review [40]. The full constituent quark mass is obtained with the physical vertex strength if also $\mathcal{T}^{(4,7)}$ are taken into account, a rather comprehensive analysis is given in [39].

In short, while the constituent quark mass is significantly smaller than the physical one for the physical vertex strength with $\eta_{\rm phys}$, the corresponding quark propagator has a Källén-Lehmann representation. This has to be contrasted with the results for $\eta_{\rm const}$ with the physical constituent quark mass, where we end up with cc poles.

We proceed by dissecting the emergence of these cc poles, including a preliminary assessment of the situation and possible causal structure of the quark propagator in full QCD, where we take into account the additional tensor structures of the quark-gluon vertex:

In Figure 5.5a, we show the constituent quark mass as a function of the strength factor η, or rather the respective ratio $\alpha_\eta/\alpha_{\rm phys}$. The respective (2+1)-flavor quark-gluon coupling is taken from [35]. Our computation shows the existence of a critical value of the vertex strength,

$$\eta^* \approx 0.846\,, \qquad \longleftrightarrow \qquad \frac{\alpha_{\eta^*}}{\alpha_{\text{phys}}} \approx 1.283\,. \tag{5.25}$$

For $\eta < \eta^*$, the quark propagator has a Källén-Lehmann representation, and the physical vertex strength is located in this regime. For $\eta > \eta^*$, we keep the real pole as the first singularity in the complex plane, but additional complex conjugated poles emerge. The enhancement of the vertex strength required to obtain the physical constituent quark mass $M_l(0) \approx 350\,\text{MeV}$ in the current approximation is given by $\alpha_\eta/\alpha_{\text{phys}} \approx 1.39$ and is deep in the regime with cc poles. It is indicated by the vertical straight grey line in Figure 5.5a.

It is left to assess the origin of the cc poles, which allows us to discuss its presence or absence in full QCD. The occurrence of the cc poles originates in the analytic structure of the mass function and is connected to the height and width of the effective coupling. The peak structure imprints itself on the imaginary parts of the mass function, see Figure 5.4b, and leads to a peaked structure with zero crossing in the real part. The cc poles emerge, when the peak of the real part crosses the line $f(\omega) = \omega$, i.e., when $\text{Re}\, M(\omega) - \omega = 0$, see Figure 5.5b. In comparison to the computation with a constant vertex dressing in [191], this novel feature is connected to the non-trivial momentum dependence of the quark-gluon vertex. This dynamical property shifts the peak of the effective coupling relevant for the solution of the gap equation to a more realistic value. The peak position in the full calculations are approximately 590 MeV for two flavors, see [33] and 670 MeV, [35] for (2+1) flavors. The boundary of the regime with cc poles certainly depends on the details of the vertex. However, it is dominantly sensitive to the position, width, and height of the quark-gluon coupling, as these properties influence the height and position of the peaked structure in the real part of the mass function significantly. Our results suggest, that for physical peak position of the coupling in two- or $(2+1)$-flavor QCD, cc poles are easily introduced by an enhancement of the vertex.

In summary, it is suggestive that the absence of cc poles seen for a physical vertex strength in the present approximation persists in full QCD: the inclusion of the other tensor structures may change the peak structure of the mass function, leading to the absence of cc poles. Indications for this scenario are present in the full vertex solutions, e.g., [33, 39]. There, the different momentum running of the dominant couplings $\lambda^{(4)}$ and $\lambda^{(7)}$ lead to different peak positions in the associated effective couplings. Hence, the inclusion of these contributions might simply lead to a broadened structure of the imaginary part of the mass function and allows for a larger constituent quark mass without the emergence of cc poles. Note, that while we consider the above scenario as the likely one, we can not make a definite statement about the causal structure with a full vertex prior to a direct computation. This matter will be resolved in a forthcoming work, where a computation with the physical quark-gluon vertex with the tensor structures $\mathcal{T}^{(1,4,7)}$ is performed.

We close this section with a discussion of the relevance of the findings above for existing bound state studies. To that end, we remark, that the additional cc poles seem to only have a mild influence on the Euclidean correlation functions. As can be seen in Figure 5.6, the Källén-Lehmann spectral representation holds true up to the permille level also for coupling strengths where the cc poles are present in the system. The two pairs of complex poles have residues of opposite signs, see Figure 5.5b, what leads to cancellations. This is particularly interesting for the applications to hadron physics. There, most numerical and

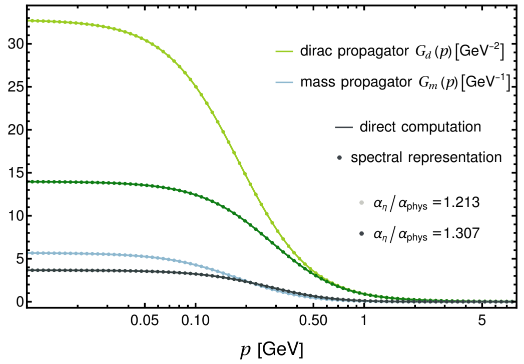

Figure 5.6.: Propagators in the Euclidean domain for different enhancement factors. The spectral representation is fulfilled up to the permille level for all coupling strengths, where the higher enhancement factor already has cc poles.

direct analytical continuation methods rely on simple causal structures, and the presence of cc poles could have serious consequences for the validity of expansion schemes or spectral representations. With such applications in mind, we would like to emphasise, that the cc poles are, if present, rather far away from the real frequency axis. Their location is tied to the peak-position of the imaginary part of the mass function. Moreover, the absolute distance of the cc poles to the origin is between $0.6 - 1$ GeV or even larger. This originates in the fact that their location in the quark mass function is approximately given by the sum of the quark pole mass and the peak position of the gluon dressing, $m_{\mathrm{pole}} + p_{\mathrm{glue}}^{\mathrm{peak}}$. For applications that do not probe this region in the complex frequency plane, as for example the computation of light hadron properties, the effects of these cc poles may even be negligible.

5.1.7. Phenomenological vertex fits

The results of the previous sections suggest, that we can use ghost-dressing inspired causal vertex models to solve the quark gap equation (5.2) in the full complex frequency plane. The reconstructed ghost dressing functions thereby lead to the couplings Figure 5.3a, and resemble the physical coupling only qualitatively. On the other hand, as was argued in [80], the ghost spectral function can be fitted rather well by a simple model. This opens the possibility to reconstruct a spectral function for the physical vertex from quantitative, state-of-the-art computations on the Euclidean axis, see e.g. [35, 36], and use it in the spectral gap equation. For the reconstruction, we will focus mainly on the intermediate momentum regime and the UV behaviour of the vertex-dressing, which is largely constraint by the gluon dynamics and the asymptotic UV-running. The IR vertex strength can be used to tune the correct amount of chiral symmetry breaking, as is often done in bound state studies, see e.g. [40] and references therein.

The strategy we follow will be to use the spectral reconstruction of the gluon propagator from [185] for all flavours, and only fit the flavour dependent dressing functions independently. To ensure the correct UV-behaviour of our correlation functions, the asymptotic running of the gluon dressing is pertinent. As the spectral reconstruction in [185] reconstructs the gluon propagator and hence focuses on the IR and intermediate momentum

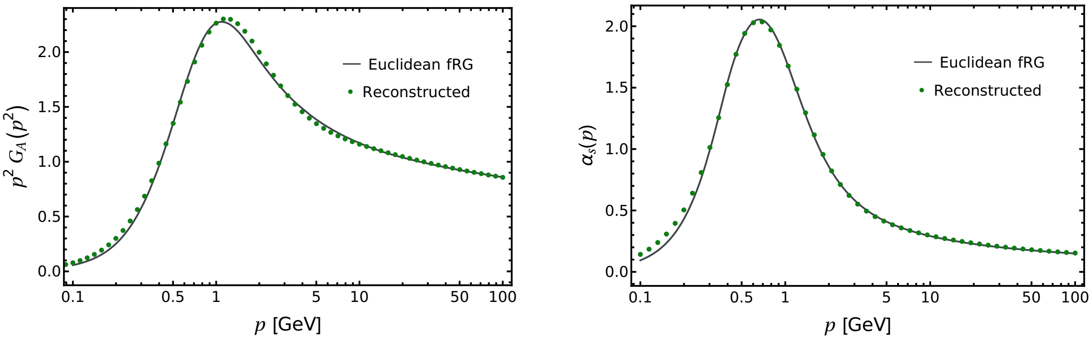

(a) Reconstructed inverse gluon dressing compared to the high accuracy data from the fRG. For the reconstruction ansatz see (5.27).

(b) Reconstructed light quark gluon coupling compared with the physical one. For the ansatz of the vertex dressing see (5.29) and (5.30)

Figure 5.7.: Euclidean (inverse) gluon dressing and light quark coupling. The green dots indicate our reconstructed results. The Euclidean data from [35] is indicated as solid line and was extrapolated above 20 GeV with the respective one-loop form.

regime, the resulting dressing function does not have a satisfactory UV-behaviour. The asymptotic form of the gluon propagator, and accordingly its spectral function read

$$\begin{aligned} G_A(p\to\infty) &\to \frac{Z_A^{UV}}{\hat{p}^2\log(1+\hat{p}^2)^{\gamma_A}} \\ \rho_A(\lambda\to\infty) &\to \rho_A^{\mathrm{UV}}(\lambda; Z_A^{UV},\gamma_A) = \frac{-\gamma_A Z_A^{UV}}{1+\hat{\lambda}^2\log(1+\hat{\lambda}^2)^{1+\gamma_A}}\,, \end{aligned} \tag{5.26}$$

with the anomalous dimension of the gluon propagator $\gamma_A = (13-4/3\,N_f)/(22-4/3\,N_f)$, and $N_f = 2+1$ for the data we use. The hats stand for dimensionless quantities, and Z_A^{UV} is a proportionality constant, which carries the dimension of the spectral function. See also the discussion around (2.30) and (3.12) for further reference. For the gluon propagator, or rather the associated (inverse) dressing $1/Z_A(p) = p^2 G_A(p)$, it is possible to smoothly connect it to its asymptotic form. In the previous sections, we have approached this issue by forcing a continuous, piecewise extrapolation of the spectral function to the UV, where we fixed the point of connection by enforcing the sum rule given in (5.11). The resulting gluon dressing falls off too quickly in the UV, as can be seen in the associated quark gluon coupling Figure 5.3. To remedy this problem, we choose a smooth extrapolation of the gluon spectral function in the UV with the following ansatz:

$$\rho_A(\lambda) = \rho_A^{\mathrm{rec}}(\lambda)\sigma(\lambda;\Lambda_{\mathrm{UV}},\nu_{\mathrm{UV}}) + \rho_A^{\mathrm{UV}}(\lambda; Z_A^{UV},\gamma_A)\sigma(\lambda;\Lambda_{\mathrm{UV}},-\nu_{\mathrm{UV}})\left(1+\frac{Z_2\sigma(\lambda;\Lambda_2,\nu_2)}{\lambda^2}\right)\,. \tag{5.27}$$

The function $\sigma(\lambda;\Lambda,\nu)$ is a smooth cutoff function that interpolates between the two terms in (5.27). It is defined as

$$\sigma(\lambda;\Lambda,\nu) = \frac{1}{1+\exp\left(\frac{\lambda-\Lambda}{\nu}\right)}\,. \tag{5.28}$$

For $Z_2 = 0$ and $\nu_{\mathrm{UV}} \to \infty$ this ansatz simply leads to the continuous, piecewise extrapolation described above. In fact, the subheading correction term proportional to Z_2 is necessary to reproduce the correct UV-running. It results in a small, positive bump in the spectral density at large intermediate momenta that compensates for a slight mismatch of the weight at lower scales. The bump is is most likely a reconstruction artefact which is necessary to ensure the super convergence relation Equation (5.11). The resulting inverse dressing is shown in Figure 5.7a. It compares well with the desired UV-behaviour for large momenta. The discrepancies around the peak are remnants from the modifications of the spectral tail. They are easily compensated by incorporating the deviation in the fit data of the coupling, and we proceed with the spectral reconstruction of the latter.

For the dressing function of the quark-gluon vertex, $\lambda^{(1)}(p)$, we use the fit function devised in [80] for the ghost spectral function, see Equation (5.15). The spectral representation of the quark-gluon vertex dressing then reads

$$\lambda^{(1)}_{\bar{q}qA}(p) = \lambda_1(0) + p^2 \int_0^\infty d\lambda \frac{\rho_{\bar{q}qA}(\lambda)}{\lambda^2 + p^2} \,. \tag{5.29}$$

The residue of the massless pole is determined by the value of the dressing in the IR. While the UV-behaviour is known from perturbation theory and the spectral function approaches a constant in the IR, one can expand the spectral function in terms of products of sigmoid and Breit-Wigner functions. Such an expansion captures the functional form of the ghost spectral function quantitatively, as has been shown in [80]. Our vertex spectral function is reconstructed with a slightly simplified Ansatz to facilitate the reconstruction:

$$\rho_{\bar{q}qA}(\lambda) = \kappa \left[\left(\hat{\rho}_0 + \sigma_{\mathrm{peak}}(\lambda) \hat{f}^{\mathrm{BW}}_{\mathrm{peak}}(\lambda) \right) \sigma_{\mathrm{IR}}(\lambda) + \sum_{i=1}^{N} f^{\mathrm{BW}}_i(\lambda) + \sigma_{\mathrm{UV}}(\lambda) \hat{\rho}^{\mathrm{UV}}_c \right] , \tag{5.30}$$

where the κ carries the dimension of the spectral function and the $\hat{\rho}_0$ is a dimensionless parameter that determines IR asymptotic of the spectral function. The sigmoid function and the Breit-Wigners are parametrised by

$$\sigma_i(y) = \frac{1}{1 + e^{-\nu_i (y - \Lambda_i)}} \,, \tag{5.31a}$$

and

$$f^{\mathrm{BW}}_i(\hat{y}) = \frac{c_i}{(\hat{y} - \hat{M}_i)^2 + \hat{\Gamma}_i} \,. \tag{5.31b}$$

The UV asymptotic is determined by the UV-running of the coupling (5.17), which approaches its perturbative form in the UV, see (2.28). Hence, the anomalous running of the coupling is fixed by $\gamma_{\bar{q}qA} = (1 - \gamma_A)/2$. The UV behaviour of the spectral function is then given by

$$\hat{\rho}^{\mathrm{UV}}_c(\hat{\lambda}) = \frac{Z^{\mathrm{UV}}_{\bar{q}qA}}{1 + \hat{\lambda}^2 \log(1 + \hat{\lambda}^2)^{\frac{1-\gamma_A}{2}}} \,. \tag{5.32}$$

The coupling data is taken from [35] and we extrapolate the data in the UV with the well known one-loop forms Equation (2.28). To obtain the actual fit-data up to global rescaling, we solve (5.17) for $\lambda^{(1)}(p)$, where we use the UV-extrapolated gluon dressing, which is associated with the reconstructed spectral function (5.27). We choose a logarithmic grid between 0.3 GeV and 1000 GeV, to ensure the correct running of the vertex for intermediate and large momentum scales. The result is shown in Figure 5.7b. The features of the quark gluon coupling are well reproduced. The UV-scaling and the peak of the quark gluon coupling are captured within a conservative error estimate of 1%. In the IR, the difference is explained by the IR closure of the respective data sets. While the Euclidean data of [35] corresponds to a computation on the scaling solution, the gluon spectral function in [185] was reconstructed on lattice data, which resolve a decoupling type solution. These couplings are the ideal starting point for phenomenological application with the spectral quark gap equation. Moreover, one can implement the necessary enhancement for the correct amount of DχSB in the IR and leave the UV tail of the coupling untouched, in contrast with the global enhancement in Section 5.1.3. This can be done by a suitable IR-enhancement of the Euclidean fit data. The respective necessary tuning and its impact on the causal structure for the light, strange and charm quark spectral functions is currently under investigation, and we will report on respective results in the near future.

5.1.8. Conclusion

In the present work, we have studied the causal structure of the quark propagator within the spectral DSE. In contrast to the previous work [191], we made a significant step towards its solution in full QCD: instead of a constant quark-gluon vertex we have used an STI-construction for the vertex, that includes a fully momentum-dependent dressing for the classical tensor structure, see Section 5.1.3. This allowed us to study the complex structure of the quark propagator by solving the spectral gap equation.

Specifically, we have shown in Section 5.1.4 that the quark propagator has a Källén-Lehmann representation for the physical vertex strength of the classical tensor structure, but fails to generate the correct strength of spontaneous chiral symmetry breaking. In turn, enhancing the quark-gluon coupling above the physical value with a factor 1.39 leads to the correct amount of chiral symmetry breaking. This procedure is the commonly used one for DSE and bound state studies, but introduces cc poles to the quark propagator in addition to the mass like poles that are associated with the first singularity in the complex plane. The nature of the latter cannot be answered conclusively without a direct computation with a fully frequency dependent vertex. However, we have discussed the relevant properties of common vertex approximations that decide about a real or complex pole scenario in Section 5.1.5. Independent of the nature of the first pole, our discussion in Section 5.1.6 reveals that the use of vertex models with an over-enhancement of the vertex generically lead to additional cc poles. Importantly, our results also entail that although current vertex models used in DSE and bound state applications lead to cc poles in the quark propagator, the contribution of the latter to the propagator is negligible. Hence, the quark effectively still has a Källén-Lehmann representation, and we have reconstructed the quark-gluon coupling in Section 5.1.7, which allows for phenomenological applications

A dissection of the mechanisms suggests that in full QCD, the additional relevant tensor structures in the quark-gluon vertex may lead to the full strength of chiral symmetry breaking without the additional cc poles. This assessment is based on the absence of these cc poles for the physical vertex strength of the classical tensor structure and the momentum dependence of these dressings, see e.g., [33]. The full computation including the additional tensor structures is the subject of ongoing work, and we hope to report on the respective results in the near future.

5.2. Mesonic parton distributions

This section shows preliminary results of [7].

In this section, we will utilise the spectral framework to compute the pion's distribution amplitude directly on the light front. As discussed in Section 4.2, the computation of bound state properties is itself inherently non-perturbative. We showed that the spectral approach allows the computation of bound state masses and the corresponding Bethe-Salpeter amplitude (BSA) directly on the real frequency axis. In QCD, additional non-perturbative dynamics like DχSB and confinement complicate the picture and leave plenty of questions about the structure of hadrons open. Euclidean, non-perturbative approaches have been very successful to give a rather comprehensive picture of the hadron spectrum in terms of masses, for a respective review see [40]. On the other hand, the computation of cross-sections requires knowledge about the structure of the hadrons even at high energies. The compositeness of the hadrons can be seen, for example, in deep inelastic scattering processes. There, the amplitudes can be described by the sum of perturbative interactions between the incoming particle and the constituents, weighted by their respective parton distribution functions (PDFs). The latter carry the non-perturbative information of the hadron structure and are dominated by low-energy physics. This structure of hadrons will also be the subject of a number of ongoing and upcoming experiments at the LHC and prominently the Electron-Ion Collider [20–23], which plan a three-dimensional spatial imaging of hadrons by measuring structure observables like angular momentum distributions and longitudinal or transverse momentum distributions. Adding to the PDFs, these structures are encoded in the respective generalized parton distributions (GPDs) and transverse momentum distributions (TMDs), see e.g., [263, 264].

The different distribution functions are commonly defined on the light front, meaning that the partons, i.e., the quarks and gluons, are probed at lightlike separation. The corresponding matrix elements in the momentum basis, require access to real frequencies, which prohibits the direct, non-perturbative computation from lattice QCD or Euclidean functional methods. Nonetheless, these approaches made huge progress in the past decade, making use of effective theory descriptions like large momentum effective theory (LaMET). The latter allows defining quasi-distribution functions which depend on a longitudinal momentum and can be calculated, to some extent, with the input of Euclidean correlation functions. In the infinite momentum limit, these quasi-distributions approach their light front counterparts, see [265, 266] and [267] for a review. For recent applications on the lattice see [268–270], for a discussion of the inverse problem connected to the LaMET method on the lattice see [271] and for a recent application with the fRG see [272]. A different approach relies on the computation of moments via non-perturbative, Euclidean methods. In principle, the knowledge of all moments allow for the reconstruction of the full PDAs or PDFs. Low order cumulants or moments have been calculated in lattice QCD with high precision, see e.g., [273, 274]. However, for higher order moments, the numerical error becomes large.

While these approaches have been shown to work reasonably well for intermediate Bjorken-x, they necessarily fail in the interesting limits of $x \to 1$ or $x \to 0$ due to their extrapolation errors. These regions are at the moment only poorly constraint from an experimental perspective, but upcoming experiments at the EIC promise to probe this region. This requires us to compute the hadron structure directly on the light front, what in turn requires real-time correlation functions. One route that has been recently proposed in [49] is based on contour-deformations. In contrast, although potentially complementary, we utilise the spectral framework for the quark gap equation, developed in [4], see also Section 5.1, to compute the quark propagator in the full complex frequency plane. For the Bethe-Salpeter amplitude of the Pion based we utilise a Nakanishi type integral representation, and reconstruct the associated weight function on state-of-the-art data from functional QCD [36]. For earlier fully reconstruction based results for the Pion distribution amplitude from Euclidean BSE-DSE data, see also [275].

This section is structured as follows. In Section 5.2.1, we discuss the definition of the pion distribution amplitude, where we put special emphasis on the light-front projection of the Bethe-Salpeter wave function (BSWF). In Section 5.2.2, we show how to include the complex structure of the quark propagator and discuss the reconstructed weight function of the Pion BSA and the corresponding PDA in Section 5.2.5. We find that the decay behaviour of the latter in direction of the relative quark momenta cannot be described by a factorised weight function with a single delta function, an ansatz that is often employed for phenomenological applications. To describe the data at least qualitatively, we add a second, similar term in the weight function. We then proceed to discuss the resulting PDA, where we find a strong dependence on the non-trivial features of the quark spectral function, which are connected to DχSB. We discuss the large systematic errors that come from the reconstruction ambiguities of the BSA and the corresponding weight function, and lay out a strategy toward reliable computations of the small and large x limits of the PDA. We conclude with a summary and outlook in Section 5.2.6.

5.2.1. The light-front wave function

In functional QCD, hadrons emerge as resonant multi-quark interactions. The lightest hadron is the pseudo Goldstone boson of DχSB, the pion, which is the first pseudo scalar resonance of a light quark-antiquark pair. The resonant momentum channel is the t-channel, $t = (p_1 + p_2)^2 = P^2$, where we count every momentum as incoming and $p_{1,3}$ and $p_{2,4}$ are antiquark and quark momenta respectively. If we choose $u = (p_1 + p_4)^2 = 0$, the four quark interaction is conveniently parametrised by the total t-channel momentum P and the relative momentum p, which is distributed symmetrically between quark-antiquark pair. Note that the definition of $p_\pm$ is not unique. One could pick $p_+ = p + (1 - \eta)P$ and accordingly $p_- = p - \eta P$ for a parameter $\eta \in [0, 1]$. This would amount to a different configuration of the non-resonant momentum channels. Close to the resonance, the respective four-quark interaction is dominated by the pion pole and we can write

$$\Gamma^{(\bar{q}q\bar{q}q)}_{\text{ps}}(-p_+, -p_-, p_+) \xrightarrow{P^2 \to -m_\pi^2} \frac{\Gamma_\pi(p, P)\Gamma^\dagger_\pi(p, P)}{P^2 + m_\pi^2}\,, \tag{5.33}$$

where $p_\pm = p \pm P$ and $\Gamma_\pi(p, P)$ is the Bethe-Salpeter amplitude of the pion and the subscript $_{\text{ps}}$ refers to the pseudo-scalar interaction. Note that the BSA is nothing but the Yukawa coupling between quarks and pions, a feature that is commonly exploited in fRG computations via dynamical hadronisation, for a recent discussion, see [35]. It satisfies a BSE, which can be used for its dynamical determination. A different approach was implemented in [36], where the BSA was computed as the residue of the pion pole in the full 1PI four quark interaction projected onto the pion channel. Then, the BSA reads

$$\Gamma_\pi(p,P) = i\gamma_5 h_\pi(p,P)\,.$$

Note that the full BSA also contains other tensor structures beyond the pure γ_5 structure, but we neglect them in a first approximation. Their inclusion in the present framework is however straight-forward, if suitable data becomes available. The respective scalar dressing functions, here only $h_\pi(p,P)$, fulfil a Nakanishi integral representation

$$h_\pi(p,P) = \int_0^\infty d\beta^2 \int_{-1}^1 dz \frac{\rho_\pi(\beta,z)}{\beta^2 + (p+\frac{z}{2}P)^2}\,, \tag{5.34}$$

which is valid for $-P^2 < (2m_{l,\text{pole}})^2$, where $(2m_{l,\text{pole}})$ is the threshold of the nonanalyticity that is associated with the (offshell) decay to its two constituents, starting at twice the constituents pole masses. For Kaons, being composed of a light and a strange quark, this threshold would be $m_{l,\text{pole}} + m_{s,\text{pole}}$, see also [52, 276]. For a non-symmetric definition of the relative momentum, one simply replaces $z \to z - \eta$ in (5.34).

The matrix element which defines the leading twist two Pion distribution amplitude (PDA) is given by the light-front projection of the Bethe-Salpeter wave function (BSWF), where the latter is the transition element between the vacuum and an on shell pion state. It is connected to the BSA via the attachment of external quark legs,

$$\chi_\pi(p,P) = G_q(p_+)\Gamma_\pi(p,P)G_q(p_-)\,. \tag{5.35}$$

The projection of (5.35) leads to definition of the valence light front wave function (LFWF) $\Psi(x,p_T)$ and the PDA

$$\begin{aligned}\phi(x) &= \mathcal{N}\,\text{Tr}_{CD} \int \frac{d^4p}{(2\pi)^4} \delta(p_+\cdot n - xP\cdot n)\,\gamma_5\,\gamma\cdot n\,\chi_\pi(p,P)\\ &= \frac{1}{16\pi^3}\int d^2p_\perp \psi(x,p_\perp)\,,\end{aligned} \tag{5.36}$$

where x is the longitudinal momentum fraction of the valence quark and Tr_{CD} denotes the color and Dirac trace. The total momentum is evaluated on-shell, i.e., $P^2 = -m_\pi^2$ and involves the light-like vector n with $n\cdot P = -m_\pi$. The subspace of transverse momenta is then defined by $n \cdot p_\perp = 0$. A convenient choice which we employ in our calculation is $n = (i,0,0,1)$. The normalisation $\mathcal{N}$ ensures that the PDA is dimensionless and normalised to 1. Note that (5.36) is independent of the definition of the relative momentum, i.e., η, what is easily seen by using the shift symmetry of the measure.

5.2.2. Spectral PDA

To compute (5.36) directly on the light front, we use the spectral representation of the quark propagator (5.5) and the integral representation (5.34) with $\eta = 1$. Carrying out the trace over the Dirac and color indices, we arrive at

$$\phi_\pi(x) = \tilde{\mathcal{N}} \int_{-\infty}^\infty d\lambda_1\, d\lambda_2\, d\beta^2 \int_{-1}^1 dz\, \rho_q(\lambda_1)\,\rho_q(\lambda_2)\,\rho_\pi(\beta,z)\, I_\phi(\lambda_1,\lambda_2,\beta,z;x)\,, \tag{5.37a}$$

where we absorbed global factors of the integral measure into the normalisation $\tilde{\mathcal{N}}$. After integrating out the longitudinal momentum with the delta function, the spectral integrand I_ϕ contains only the integration over the transverse momentum and (Euclidean) frequency,

$$\begin{aligned} I_\phi(\lambda_1,\lambda_2,\beta,z;x) &= \int d^2p_\perp \int_{-\infty}^{\infty} dp_0 \, \frac{\mathrm{i}\,(\lambda_1(x-1)-\lambda_2 x)}{4m_\pi^2 x(x-1)(2x-1+z)(q_0-r_q)(q_0-r_{\bar{q}})(q_0-r_\pi)} \\ &= \frac{1}{16\pi^3}\int d^2p_\perp I_\psi(\lambda_1,\lambda_2,\beta,z;x,p_\perp)\,, \end{aligned} \tag{5.37b}$$

where the poles $r_q, r_{\bar{q}}, r_\pi$ are purely imaginary, hence located on the real frequency axis:

$$\begin{aligned} r_q &= \mathrm{i}\,\frac{\lambda_1^2+p_\perp^2+m_\pi^2x^2}{2m_\pi x}\,, \quad r_{\bar{q}} = -\mathrm{i}\,\frac{\lambda_2^2+p_\perp^2+m_\pi^2(1-x^2)}{2m_\pi(1-x)}\,, \\ r_\pi &= \mathrm{i}\,\frac{m_\pi^2\left(4x^2-(z-1)^2\right)+4\left(q_\perp^2+\beta^2\right)}{4m_\pi(z-1+2x)}\,. \end{aligned} \tag{5.37c}$$

Note that the integrand in (5.37b) enjoys a symmetry under the simultaneous replacements $\lambda_1 \leftrightarrow \lambda_2$, $x \to (1-x)$ and $z \to -z$, which is simply a redefinition of the longitudinal momentum fraction. Furthermore, the denominator of the integrand in (5.37b) is only dependent on the $\lambda_{1,2}^2$, while the terms in the numerator are either symmetric or anti-symmetric in the respective spectral variables. Hence, the integration projects onto the even and odd parts of the quark spectral function, which are the Dirac and scalar spectral function $\rho_q^{(d)}$ and $\rho_q^{(s)}$ respectively, see also the discussion below (5.5).

The integration over the Euclidean frequency p_0 is easily carried out with the residue theorem. For $0 < x < 1$, the poles r_q and $r_{\bar{q}}$ are located in the upper and lower half plane respectively. The third pole r_π switches sign if $z = 1-2x$, without crossing the imaginary axis. Hence, the integration simply picks up the residues of either r_q or $r_{\bar{q}}$, depending on the location of r_π. We note in passing that the deformation of the contour does not affect the result in the region $0 < x < 1$. For $x > 1$ or $x < 0$, all poles are located in the same half plane and the usual iϵ prescription leads to a vanishing, hence non-analytic result. It was pointed out in [49] that one can choose a different contour that agrees with the usual iϵ prescription in the physical region $0 < x < 1$, but always picks up one pole and defines an analytic function everywhere, up to defining branch cuts. With this analysis, the PDA simply reads

$$\begin{aligned} \phi_\pi(x) = \tilde{\mathcal{N}} \int_{-\infty}^{\infty} d\lambda_1\, d\lambda_2\, d\beta^2 \int_{-1}^{1} dz\, \rho_q(\lambda_1)\,\rho_q(\lambda_2)\,\rho_\pi(\beta,z) \\ \Big\{\theta(z-2x+1) I_\phi^q(\lambda_1,\lambda_2,\beta,z;x) - \theta(2x-1-z) I_\phi^{\bar{q}}(\lambda_1,\lambda_2,\beta,z;x)\Big\}\,, \end{aligned} \tag{5.38}$$

where the superscripts ^{q} and $^{\bar{q}}$ refer to the respective poles r_q and $r_{\bar{q}}$ and the relative minus sign comes from the winding number of the chosen contour. For further details on the frequency integration and in particular the full expressions for $I_\phi^{q/\bar{q}}$, see Appendix A.5. Note that also the integration over the transverse momentum is easily carried out analytically, and leaves us with the spectral integrals, which carry the non-perturbative information of the quark propagator and the pion BSA.

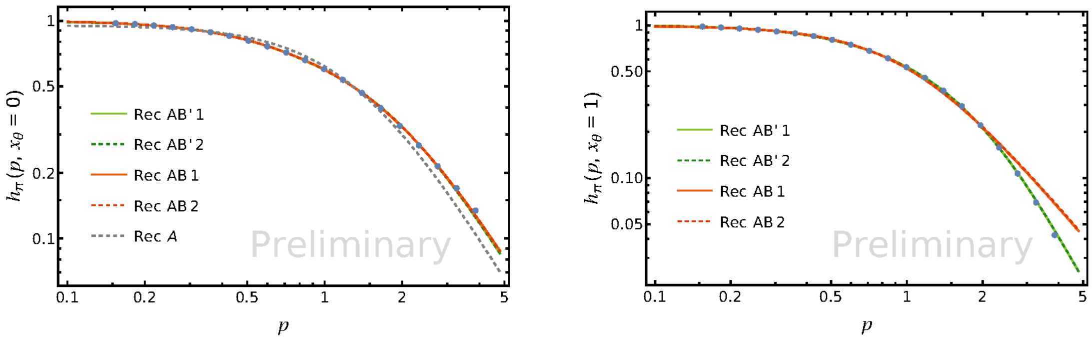

(a) Orthogonal angular configuration. The data is poorly described by a single term for ρ_π, the best form of the second term is ambiguous.

(b) Parallel angular configuration. The δ'-term is necessary to describe the decay at intermediate to large relative momenta.

Figure 5.8.: Comparison of the Pion BSA to different reconstructions in a double logarithmic plot over the relative momenta in GeV. The BSA was normalised to one at vanishing relative momentum. The blue dots stem from [36] and were extrapolated at different angular configurations $x_\theta = p \cdot P/\sqrt{p^2 P^2}$, leading to different decays. The solid and dashed line of the same colours correspond to two different sets of fit parameters, and the different fit-functions are given in (5.40). The fit-parameters are displayed in Table 5.1.

5.2.3. Reconstructing the BSA

For the BSA, we use the data from [36], where the authors use the fRG in Landau gauge QCD to compute fully momentum dependent propagators and four-quark interactions on the Euclidean axis. The (squared) BSA was extracted from the four quark interaction as the Residue of the pion pole, at different angular configurations $x_\theta = p \cdot P/\sqrt{p^2 P^2}$, with p being the relative momentum between the quarks and P the pions total momentum. The resulting BSA for $x_\theta = 0$ and $x_\theta = 1$ are shown in Figure 5.8 as blue dots. The data was normalised to one at vanishing relative momentum. The different angular configuration show a surprisingly different behaviour. In fact, they even show a decay with a different power law for the upper end of our momentum data. The strong angular dependence hints at artefacts of the analytic continuation, which might be related to the fact that angles between four-momenta are not invariant under a Wick rotation. The resolution of this problem, and whether it is to be attributed to a reconstruction artefact, is still under investigation. However, we will proceed with the data as it is, and emphasize that the extrapolation procedure in [36] is common in the field, see also [40, 174, 179] and references therein. We will use separate reconstructions on two different angular configurations, as the strong angular dependence cannot be accommodated for by our integral representation. While this strongly restrains the predictive power of our computation, it elucidates the ambiguities of reconstructions for functions of multiple momenta. Furthermore, our computation serves as a proof of principle, and we will discuss how to constrain the results with additional data in Section 5.2.6.

For the reconstruction of the weight function, we choose a simple ansatz similar to [275]. We consider a sum $\rho_\pi(z, \beta) = \sum_i \rho_\pi^{(i)}(\beta, z)$, where the β and z dependence is

Reconstruction	A	B	β_A	β_B	α_A	α_b
$AB1\,(x_\theta = 0)$	0.120	1.99	0.615	1.829	1.782	1.907
$AB2\,(x_\theta = 0)$	0.073	0.999	0.611	1.824	0.211	−0.119
$AB'1\,(x_\theta = 0)$	0.958	-1.892	0.929	1.262	−0.196	−0.060
$AB'2\,(x_\theta = 0)$	1.352	-2.608	−2.608	1.261	0.414	0.611
$AB1\,(x_\theta = 1)$	-0.447	1.397	0.907	0.985	0.546	1.180
$AB2\,(x_\theta = 1)$	0.339	0.204	1.043	1.073	-0.131	0.240
$AB'1\,(x_\theta = 1)$	0.121	2.798	0.695	2.130	0.397	-0.683
$AB'2\,(x_\theta = 1)$	0.150	3.582	0.695	2.130	1.058	-0.556

Table 5.1.: Fit parameters for the reconstructions of the weightfunctions (5.40a) (AB) and (5.40b) (ABprime). We chose two different sets of locally optimal parameter for each reconstruction ansatz and datasets ($x_\theta = 0$ and $x_\theta = 1$).

factorised in each term, what allows for a simple reconstruction of the data. Note that a parameter free reconstruction of the weight function is in principle possible, e.g. with Gaussian process regression, which has been used successfully for gluon and ghost spectral functions in [45, 185]. However, due to the dependence of the weight function on two different variables, this goes far beyond the scope of this work.

For large relative momenta, the BSA of the pion in QCD falls of as $1/p^2$. A convenient ansatz is therefore to approximate the weight function in β direction by a delta-peak at the average scale of decay,

$$\rho_\pi^A(\beta, z) = A\delta(\beta^2 - \beta_1^2)\left(1 - z^2\right)^{\alpha_1} \tag{5.39}$$

where A is a global factor and α_1 is a parameter which determines the z-dependence of the weight function. The resulting fit with a single term is shown in Figure 5.8a as gray dashed line. We find that BSA is not captured by a single term of the form (5.39). To model the data, we add a second term to the weight function. We devise two different fit functions, which differ by the momentum scaling of the second term. The first model, which we denote with AB is a simple sum of two delta functions, with different prefactors and exponents

$$\rho_\pi^{AB}(\beta, z) = A\delta(\beta^2 - \beta_A^2)\left(1 - z^2\right)^{\alpha_A} + B\delta(\beta^2 - \beta_B^2)\left(1 - z^2\right)^{\alpha_B} \ . \tag{5.40a}$$

The reconstructions of the BSA with (5.40a) are indicated in Figure 5.8 as solid and dashed red lines. The ansatz AB describes the data for $x_\theta = 0$ reasonably well, but fails to describe the tail for $x_\theta = 1$. The latter can be captured by a different momentum scaling, which can be accounted for in the second model AB':

$$\rho_\pi^{AB'}(\beta, z) = A\delta(\beta^2 - \beta_A^2)\left(1 - z^2\right)^{\alpha_A} - B\delta'(\beta^2 - \beta_B^2)\left(1 - z^2\right)^{\alpha_B} \ , \tag{5.40b}$$

where the prime denotes the weak derivative of the delta function. Green lines indicate the respective reconstructions. Inserting the δ' term in (5.34) effectively squares the kernel of the integral representation and leads to a decay of the form $1/p^4$ for intermediate to

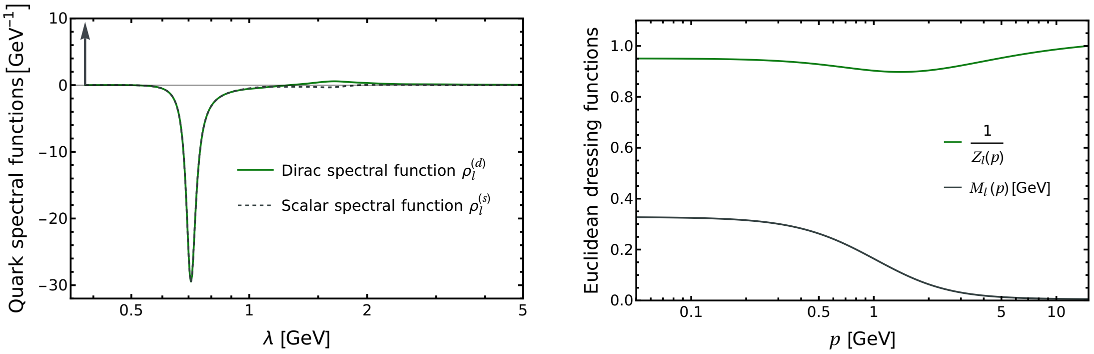

(a) Light quark spectral function. The real pole at $m_{l,\mathrm{pole}} = 0.381\,\mathrm{GeV}$ is marked by an arrow.

(b) Euclidean light quark dressing functions, for their definition see (5.1). The constituent mass is $M_l(0) = 0.328\,\mathrm{GeV}$.

Figure 5.9.: Light quark input for the PDA computation. For details see Section 5.1.3 and Section 5.1.4.

large momenta. At very large momenta, the first term, which decays as $1/p^2$, dominates as required.

Due to the one-dimensional fit data, both models for the reconstruction, (5.40a) and (5.40b), contain ambiguities in the fit parameters. Specifically, a change in the prefactors A and B can be compensated by the exponents α_A and α_B. The latter determine the distribution of the weight function in z direction. Note that the different parameter selection lead to practically indistinguishable results for the BSAs, as shown in Figure 5.8, even though the respective exponents have in parts different signs, shifting the weight of the distribution to the edges of the $z-$interval or the centre. This is partly explained by the fact that the integration variable z in the kernel of (5.34) appears only as the prefactor of the total momentum P. Hence, the ambiguity in the z-dependence is further strengthened by the smallness of the pion mass. We emphasize that this reconstruction problem does not only affect our work, but any attempt to reconstruct the BSA without prior constraints on its analytic structure. While the resulting PDAs are not too sensitive to the exponents in the mid x region, the details of the z-dependence matter for the small and large x region, as we will see in the next section.

5.2.4. Light quark input

Having the weight functions ρ_π determined, the last ingredient in (5.38) is the quark spectral function computed in the previous Section 5.1. This is not a self-consistent choice, as the quark propagator was computed in a far simpler approximation than the functional set-up of [36], which is a state-of-the-art computation of full QCD on the Euclidean axis. At the current stage, this level of truncation cannot be achieved with real-time methods. Instead, we resort to the quark spectral function computed with the causal vertex model in [4] as it contains a realistic model of the quark-gluon interaction. See also Section 5.1, and in particular Section 5.1.3 and Section 5.1.4. The quark spectral function is parametrised by a pole-cut split, i.e.,

$$\rho_l^{(s/d)}(\lambda > 0) = R_l^{(s/d)}\delta(\lambda - m_{l,\mathrm{pole}}) + \tilde{\rho}_l^{(s/d)}(\lambda)\,, \tag{5.41}$$

with $\rho_l^{(s/d)}(\lambda) = \mp\rho_l^{(s/d)}(-\lambda)$. See also the discussion in Section 5.1.4. The first term is associated with a real first singularity of the quark propagator, while the second term is associated with the cut, which is induced by the quark-gluon scattering.

In the following paragraph, we will discuss the choice of the tuning parameter for the quark-gluon vertex. Our vertex approximation is structurally comparable to common models in the literature for hadron-spectroscopy, like the Marris-Tandy interaction, see [148, 149], the review [40], and references therein. In truncations which only employ the classical tensor structure in the quark gluon vertex, the quark pole mass is typically larger than the constituent mass by a considerable amount of 50 MeV or more. On the other hand, as discussed in [181], this hierarchy is inverted for quark propagators that carry the dynamics of a full quark gluon vertex, as is the case in the computation of [36]. We deal with this inconsistency by choosing an infrared enhancement of the vertex $\alpha_\eta/\alpha_{\text{phys}} \approx 1.37$, which measures the magnitude of the peak of α_s relative to the physical coupling, see also the discussion below (5.18). This leads to a light quark pole-mass of $m_{l,\text{pole}} = 0.381\,\text{GeV}$, and a constituent mass of $M_l(0) = 0.325\,\text{GeV}$. The full spectral functions and the corresponding Euclidean dressing functions are shown in Figure 5.9a and Figure 5.9b, respectively. Evidently, the constituent quark mass is slightly below the error band of the constituent masses of the light quark in [36] (Fig. 7), but we consider this a reasonable compromise, given that the position of the pole in the quark propagator has a more direct impact on the BSA than the value of the constituent mass. The systematic error of this choice is difficult to estimate due to the inverted hierarchy of the quark masses. However, we expect it to be small compared to the reconstruction ambiguities.

There are two possibilities to reduce this systematic error in the future. The first one is to perform an optimised reconstruction on the high-precision Euclidean data of the quark dressing function. This includes utilizing the information on the form of the quark spectral function gained by the real-time computation, to reduce reconstruction ambiguities considerably. The second one is the systematic improvement of the real-time computation, by adding further tensor structures of the quark gluon vertex and solve the system of equations self-consistently. While we hope to report on respective results in the near future, the full real-time computation requires a substantial amount of technical development.

5.2.5. Pion distribution amplitudes

With the light quark spectral function Figure 5.9 we can compute the PDAs for the different reconstructions and data sets, by numerically integrating (5.38) with the spectral input. The results are shown in Figure 5.10. The upper two panels show the PDAs and the corresponding small x behaviour for the data set, distinguished by $x_\theta = 0$. The lower two panels correspond to the dataset with $x_\theta = 1$. For the latter, we only used the form $\rho_\pi^{AB'}$ for the reconstruction, as the $1/p^4$ decay was found to be necessary to describe the data. We also included the "asymptotic" form of the PDA $\phi_\pi^{(0)}(x) = 6x(1-x)$ as a gray, dashed line. This corresponds to the approximation, where the pion mass is neglected, and the quark mass is treated as constant. Even though this form is often referred to as "asymptotic" for large energies, it is never realised or approached in any sense, as the PDA is dominated by the chiral IR-dynamics.

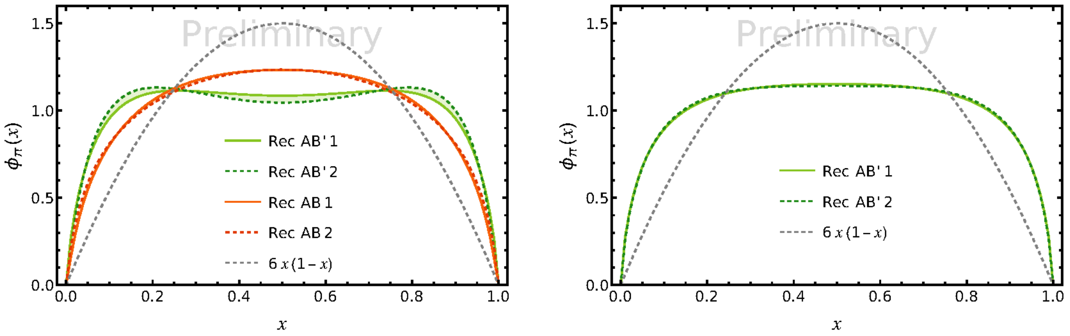

(a) PDAs for the dataset $x_\theta = 0$. The red and green curves corresponds to reconstructions with ρ_π^{AB} and $\rho_\pi^{AB'}$ respectivly.

(b) PDAs for the dataset $x_\theta = 1$. On this BSA data, only the reconstruction $\rho_\pi^{AB'}$ fits the data, see Figure 5.8b.

Figure 5.10.: Pion Distribution amplitudes for $x_\theta = 0$ in the left and $x_\theta = 1$ in the right panel. The fillings between the curves should only guide the eye. The fit-parameter are collected in Table 5.1. The gray dashed line marks the asymptotic PDA.

We start our discussion with the general shape of the PDAs in Figure 5.10. While both, ρ_π^{AB} and $\rho_\pi^{AB'}$ describe the $x_\theta = 0$ data reasonably well, see Figure 5.8a, the resulting PDAs are qualitatively different in the mid-x region, see Figure 5.10a. The red curves, corresponding to ρ_π^{AB} have a concave shape, centred around $x = 0.5$, while the green curves carry more weight towards the edges of the x-interval. The difference is explained by the different decay scales of the reconstructions, i.e.. $(\beta_A, \beta_B) \approx (0.61, 1.26)$GeV for ρ_π^{AB} in contrast to $(\beta_A, \beta_B) \approx (0.929, 1.82)$GeV for $\rho_\pi^{AB'}$. For the latter, the first decay scale is substantially larger than twice the pole mass. This already leads to a non-concave shape in the mid x region, which is further enhanced by the predominantly negative peaked structure of the quark spectral function, see Figure 5.9. The peak is closely related to DχSB and is located at the sum of the quark pole mass and the peak-position of the quark gluon coupling. This is precisely the characteristic decay scale of the quark mass function in Figure 5.9b. For a more detailed discussion, see also Section 5.1.4.

To strengthen this last point, we refer to Figure 5.11. There we show the different contributions of the different parts of the quark spectral function (5.41) to the PDA at the example of the data set $x_\theta = 0$. For the integration over the two quark spectral function in (5.38), we can distinguish three different contributions, namely the product of δ-functions, the product of one pole and one cut $\propto \delta(\lambda_1)\tilde{\rho}(\lambda_2) + \delta(\lambda_2)\tilde{\rho}(\lambda_1)$ and the product of the two cuts $\propto \tilde{\rho}(\lambda_1)\tilde{\rho}(\lambda_2)$. The first contribution is simply positive and the largest in magnitude. The absolute value of the second contribution is only slightly smaller than the first one. However, the “pole/cut”-part is negative and more centred around $x = 0.5$, what leads to a further shift of the PDA-weight towards the edges. Such a flattening is much less pronounced for the red-curves, i.e. the PDAs corresponding to ρ_π^{AB}.

For the data set with $x_\theta = 1$, we find a flat but concave PDA with $(\beta_A, \beta_B) \approx (0.695, 2.13)$GeV for $\rho_\pi^{AB'}$. This is displayed in Figure 5.10b. Here, the variation of the shape due to a reconstruction ambiguity is not as large compared to the dataset $x_\theta = 0$. This can be explained by the clearly separated decay scales, which are visible by eye in Figure 5.8b.

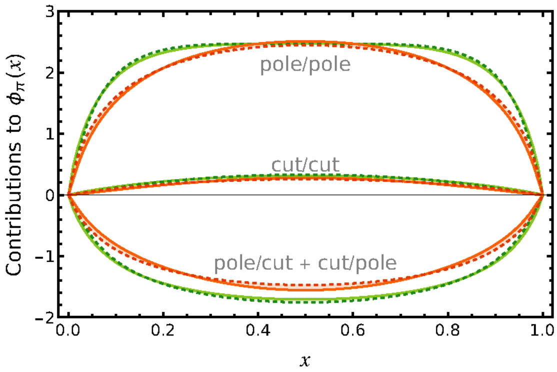

Figure 5.11.: Different contributions from the discontinuities of the quark propagator to the PDA for the data set $x_\theta = 0$, see also (5.41) for the split in the spectral function. The colour coding is the same as in Figure 5.10.

While the mid-x region is fairly well constrained by extrapolations from the Euclidean axis, the small and large x region have large extrapolation errors. Our approach on the other hand allows for the direct computation of the PDA at arbitrary momentum fraction x. The results for the present reconstructions are shown on a double logarithmic scale in Figure 5.12. The left panel, Figure 5.12a, shows the small x behaviour of the PDA for the dataset $x_\theta = 0$. The right panel shows the same for the dataset $x_\theta = 1$. For the data-set $x_\theta = 0$, we find a small x power law that is rather close to that of the asymptotic form. As we have seen in the previous paragraph, the shape of the PDA was dominated by the decay scales of the respective reconstruction. These were stable under the variation of the exponents α_A and α_B, if the respective prefactors compensated the change. This changes in particular for $x < 10^{-2}$, where the cones enclosed by the respective solid and dashed lines open up. This region probes the $z-$dependence of the weight function, which is not constrained by the data. The same is true for the dataset $x_\theta = 1$, visible in Figure 5.12b. There, the PDA approaches zero with a much smaller power in x, starting effectively below $x < 10^{-3}$. The change of slope is most likely related to the δ'-term in the reconstruction, which dominates the BSA for large relative momenta, see the discussion around (5.40b).

5.2.6. Conclusion

In this section, we have shown the first computation of the pion distribution amplitude with a fully selfconsistent quark spectral function. The latter was computed with a causal quark-gluon vertex, which resembles the physical dynamics of the quark-gluon interaction. As a first step, we used the available data from [36] for the Pion BSA, computed with a state of the art truncation of the functional renormalisation group, to reconstruct the weight function of the corresponding Nakanishi integral representation (5.34). We have seen that the naive reconstruction of the BSA contains large ambiguities, see Figure 4.16 which do not allow for reliable prediction of the PDA at the current stage. The general shape is highly dependent on the ansatz for the reconstruction, see Figure 5.10. We expect to overcome this problem by combining the spectral approach of this work with the quasi-pda approach of [36], which does not rely on a reconstructed integral representation. This approach has been proven to be reliable in the mid x region, and we plan to use it to constrain the reconstruction of the BSA.

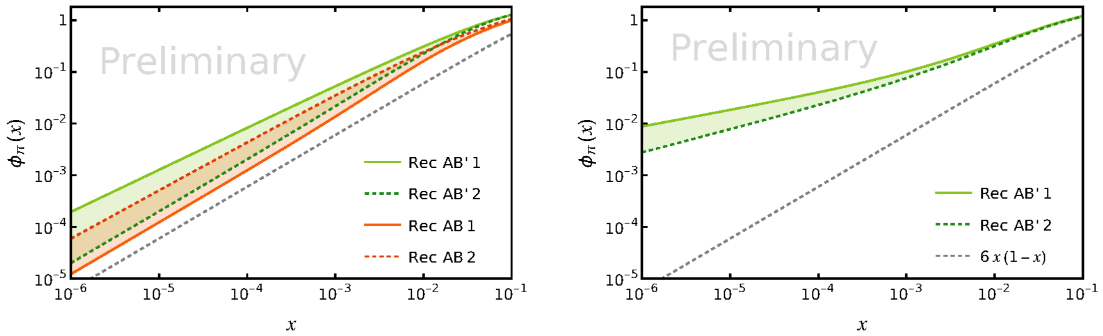

(a) PDAs for the dataset $x_\theta = 1$.

(b) PDAs for the dataset $x_\theta = 1$.

Figure 5.12.: Small x behaviour of the PDAs in a double logarithmic plot for the datasets $x_\theta = 0$ (left) and $x_\theta = 1$ (right). The relative numerical error is of order 10^{-2}.

Our findings suggest that the small and large x behaviour of the PDA is largely determined by the z-dependence of the Nakanishi weight function, see Figure 5.12. In this region, we cannot rely on extrapolations of the PDA from the quasi PDA approach or low order cumulants. Hence, the improvement of the systematic error in the small and large x region requires a direct computation of the Pion BSA on the real frequency axis. On the one hand, this would eliminate the need for a reconstruction of the BSA in the first place, with the sacrifice of having to rely on simple approximation. On the other hand, the real-time computation will reveal the qualitative structure of the Nakanishi weight function. This information can then be used to constrain the remaining ambiguities of the reconstruction. The combination of these two approaches is subject of ongoin work and we hope to report on respective results soon.

6. Summary & Conclusion

In this work, we developed a framework for the computation of real-time correlation functions and demonstrated its use for calculating dynamical observables such as bound state masses (Section 4.2) and the Pion Distribution Amplitude at the light front (Section 5.2). From a phenomenological perspective, this marks an important step towards direct and quantitative predictions of non-perturbative real-time observables in QCD.

With the upcoming Electron-Ion Collider (EIC) experiments, we aim to gain new insights into the fundamental structure of hadrons and the binding mechanisms of quarks and gluons. While the statistical phenomenology of infrared QCD is already well constrained through Euclidean lattice and functional methods, experimental observables such as cross sections are measured in the real-time domain. The same applies to the interpretation of heavy-ion collisions: although the phase structure of QCD can be accessed through static, Euclidean correlation functions, the actual dynamics—particle production, the hydrodynamic evolution of the quark-gluon plasma (QGP), and freeze-out—are governed by non-equilibrium physics. Especially the latter stages require non-perturbative information about the spectral properties of the underlying theory, crucial for describing transport phenomena and bound-state formation. To interpret and understand the phenomenology of these experiments, it is essential to develop theoretical tools for reliable real-time computations.

We outlined the spectral functional framework in Chapter 3. It builds on the spectral representations of correlation functions, such as the Källén-Lehmann and Nakanishi integral representations (Section 3.1), and exploits the analytic structure of full correlation functions to compute non-perturbative correlators across the complex frequency plane. In doing so, we employed functional identities of fundamental correlation functions, namely Dyson-Schwinger equations (Section 3.2.1) and the functional renormalisation group (Section 3.2.2). The spectral approach to functional diagrammatic relations allows the use of dimensional regularisation and enables a renormalisation procedure that preserves both symmetries and causality (Section 3.4). Specifically, for the functional renormalisation group, we derived the renormalised flow equation with a Callan-Symanzik cutoff, i.e., a simple momentum-independent mass term, in Section 4.1.2. The CS-cutoff preserves both causality and Lorentz invariance during the flow, at the expense of UV-finiteness. We demonstrated that the finite, functional CS equation emerges as the limit of finite Wetterich-type flows. The corresponding counterterm action can be fixed conveniently through a flowing renormalisation condition, allowing for the elimination of fine-tuning.

In Chapter 4, we complemented the conceptual developments with several applications. In Section 4.1, we set up the functional CS-flow for a three-dimensional scalar theory and computed the corresponding propagator spectral function fully self-consistently. The CS-flow, combined with a flowing (on-shell) renormalisation, constitutes a physical flow, where each cutoff scale corresponds to a unique point in the space of physical theories. This allowed us to connect the heavy mass limit deep in the broken phase to the non-perturbative regime of small pole masses. In Section 4.1.7, we approached the critical point of the Ising universality class from the symmetric phase and showed how the scaling form of the spectral function, with critical exponent η, emerges dynamically.

We then turned to the computation of bound-state masses in Section 4.2, combining the spectral DSE with the homogeneous Bethe-Salpeter equation for a scalar two-body bound state. The spectral framework allowed us to compute the bound-state mass directly on the real frequency axis. We presented the first direct computation of a bound-state mass in the scaling limit, providing a proof of principle for the capabilities of the spectral functional framework in hadron physics.

We concluded Chapter 4 with the first fully self-consistent computation of the graviton spectral function using the renormalised CS-flow (Section 4.3). We focused on the traceless-transverse mode of the graviton propagator. The flowing on-shell renormalisation not only facilitated the numerical implementation but also yielded a UV-normalised spectral function. This corresponds to momentum- and scale-dependent field redefinitions that absorb the anomalous running of the propagator in the UV and, in principle, allow for canonical commutation relations. The consequences of these redefinitions and their physical implications remain to be fully understood and will be the subject of future work.

In Chapter 5, we applied the spectral framework to QCD. We formulated the spectral gap equation for the quark propagator (Section 5.1.1) and constructed a causal model for the quark-gluon vertex based on its Slavnov-Taylor identities (Section 5.1.3). This enabled us to compute the light quark spectral function and analyse the causal structure of the quark propagator. Although the absence of a dynamically computed quark-gluon vertex prohibits definitive conclusions, we found strong evidence that the quark propagator exhibits a real and isolated first singularity in the complex plane (Section 5.1.4). As is common in approximations that retain only the classical Dirac structure, the quark-gluon coupling must be enhanced to reproduce the physical amount of dynamical chiral symmetry breaking. We observed that for physical coupling strengths, the quark propagator maintains an intact Källén-Lehmann representation, while an overenhanced coupling leads to its violation through the emergence of complex conjugate poles. However, the spectral functions remain effectively physical and suitable for phenomenological applications.

The quark spectral function forms a fundamental ingredient for functional hadron physics and further phenomenological studies. One of the most prominent hadrons is the pion—the lightest bound state in QCD. In Section 5.2, we employed the quark spectral functions to compute the Pion Distribution Amplitude (PDA) directly at the light front. The dominant systematic uncertainty stems from the reconstruction ambiguities of the pion's Bethe-Salpeter amplitude, particularly affecting the small-x region. Our results suggest that a direct computation of the Bethe-Salpeter amplitude at real frequencies is necessary to constrain the asymptotic behaviour of the PDA reliably. Nevertheless, we demonstrated the potential of the spectral functional framework, particularly in regions where lattice extrapolations become unreliable.

Finally, having outlined the progress achieved, we conclude this thesis with an outlook on future challenges and prospects. A crucial next step is the incorporation of higher-order scattering processes and vertex corrections to achieve apparent convergence of fundamental correlators. This will require conceptual advancements in the direction of vertex spectral functions and mixed expansion schemes including full effective potentials. Moreover, a full application of the framework to QCD necessitates a deeper understanding of the complex structure of the Yang-Mills sector. To date, a direct and self-consistent real-time computation of the gluon spectral function remains an open challenge.

While a complete real-time implementation of QCD remains a long-term objective, every advance in this direction provides valuable insights into the analytic structure of correlation functions. Beyond the conceptual understanding of real-time quantum field theories, these developments also constrain the reconstruction of dynamical observables from Euclidean or experimental data. Ultimately, they will contribute to physics-informed solutions to the challenging inverse problems in QCD phenomenology and help to unravel the real-time structure of strongly interacting matter from first principles.

Appendices

A. Additional material

A.1. Additional material for the scalar spectral flows

A.1.1. Spectral diagrams

The general spectral form of the diagrams in Figure 4.2 and Figure 4.4 is given by

$$\begin{aligned}
D_{\text{tad}}(p^2) &= \left(\prod_{i=1}^{2}\int_{\lambda_i}\rho(\lambda_i)\right)\mathcal{L}_{\text{tad}}(\vec{\lambda},p^2)\,,\\
D_{\text{pol}}(p^2) &= \left(\prod_{i=1}^{3}\int_{\lambda_i}\rho(\lambda_i)\right)\mathcal{L}_{\text{pol}}(\vec{\lambda},p^2)\,,\\
D_{\text{fish}}(p^2) &= \left(\prod_{i=1}^{2}\int_{\lambda_i}\rho(\lambda_i)\right)\mathcal{L}_{\text{fish}}(\vec{\lambda},p^2)\,,
\end{aligned}\tag{A.1}$$

with $\vec{\lambda}=(\lambda_1,..,\lambda_n)$ denoting the ordered vector of spectral masses. The loop structure reads

$$\begin{aligned}
\mathcal{L}_{\text{tad}}(\vec{\lambda},p^2) &= \int_q \frac{\Gamma^{(4)}[p,q,-p]}{(q^2+\lambda_1^2)(q^2+\lambda_2^2)}\,,\\
\mathcal{L}_{\text{pol}}(\vec{\lambda},p^2) &= \int_q \frac{\left(\Gamma^{(3)}[p,q]\right)^2}{(q^2+\lambda_1^2)(q^2+\lambda_2^2)\left((p-q)^2+\lambda_3^2\right)}\,,\\
\mathcal{L}_{\text{fish}}(\vec{\lambda},p^2) &= \int_q \frac{\Gamma^{(3)}[p,q]\,\Gamma^{(4)}[p,q,0]}{\left(q^2+\lambda_1^2\right)\left((p-q)^2+\lambda_2^2\right)}\,,
\end{aligned}\tag{A.2}$$

where the vertex functions are not specified yet, and we have dropped the field argument for readability. With the approximations discussed in Section 4.1.5, we have fixed all correlation functions and we can compute the final expressions for the diagrams. For the fish diagram, the four-point function is connected to the constant scale derivative of the field. With (4.33) and (4.31), the polarisation- and fish diagram of the flow equation in the broken phase read

$$\begin{aligned}
D_{\text{pol}}[p^2] &= \left(\Gamma^{(3)}\right)^2\int_{\vec{\lambda}}\rho(\lambda_1)\rho(\lambda_2)\rho(\lambda_3)\,I_{\text{pol}}(\vec{\lambda},p^2)\,,\\
D_{\text{fish}}[p^2] &= \frac{\left(\Gamma^{(3)}\right)^2}{\phi_0}\int_{\vec{\lambda}}\rho(\lambda_1)\rho(\lambda_2)\,\tilde{I}_{\text{pol}}(\vec{\lambda},p^2)\,,
\end{aligned}\tag{A.3a}$$

where

$$\begin{aligned}
I_{\text{pol}}(\vec{\lambda},p^2) &= \int_q \frac{1}{(q^2+\lambda_1^2)(q^2+\lambda_2^2)((q-p)^2+\lambda_3^2)}\,,\\
\tilde{I}_{\text{pol}}(\vec{\lambda},p^2) &= \int_q \frac{1}{(q^2+\lambda_1^2)((q-p)^2+\lambda_2^2)}\,,
\end{aligned}\tag{A.3b}$$

and $\vec{\lambda}$ is the ordered vector of spectral parameters, one for each internal propagator in the diagram. We denoted the loop structure of the fish diagram as $\tilde{I}_{\text{pol}}$, since it carries the momentum structure of a DSE polarisation diagram. The loop integrals I and $\tilde{I}$ are evaluated analytically and given in terms of real and imaginary frequencies in Appendix A.1.5.

Substituting the four-vertex in (4.9) with the respective spectral representation (4.5), the constant classical part of the tadpole is absorbed by renormalisation. The remaining dynamical part of the tadpole diagram reads

$$D_{\text{tad}}^{\text{dyn}}(p) = \int_{\vec{\lambda}} \rho(\lambda_1)\rho(\lambda_2)\rho_4(\lambda_3)\, I_{\text{pol}}(\vec{\lambda}, p^2)\,. \tag{A.4}$$

The four-point spectral function ρ_4 (A.4) is obtained from (4.21) in both phases. As discussed below (4.21), there are further diagrams with two or four three-point functions contributing to ρ_4. These diagrams are suppressed by roughly an order of magnitude.

A.1.2. Renormalised flow of the two-point function on the physical minimum

In this appendix, we provide details on the derivation of the flow equation in the broken phase (4.19a). In particular, we explain the crucial role of the three-point function in (4.16) for obtaining one-loop perturbation theory as leading order behaviour. We show that the flow of the two-point function has the expected sign, see (4.17), if we include the flow of the minimum correctly and that the on-shell renormalisation condition (4.13) can be imposed consistently.

The flow equation in the broken phase reads

$$\begin{aligned}\frac{d}{dt}\Gamma^{(2)}[\phi_0](p) =\ & (\partial_t\phi_0)\, S^{(3)}[\phi_0] - (2-\eta_\phi)\, Z_\phi k^2 \\ & + \dot{\mathcal{R}}\left[-\frac{1}{2}D_{\text{tad}} + D_{\text{pol}}\right] - \partial_t\phi_0 D_{\text{fish}} - \partial_t S_{\text{ct}}[\phi_0]\,,\end{aligned} \tag{A.5a}$$

where

$$\dot{\mathcal{R}} = \left(\partial_t\phi_0\Gamma^{(3)}[\phi_0] - (2-\eta_\phi)\, Z_\phi k^2\right)\,, \tag{A.5b}$$

as derived in Section 4.1.4.

To renormalise the flow of the two-point function and show how the correct sign of the flow is recovered by the inclusion of $\partial_t\phi_0$, we first separate the tree-level and loop-induced running of the prefactors of the diagrams in (A.5a). To that end, we start with the full three-point function in (A.5b). The separation into trivial and loop-induced RG running can be made apparent by introducing a corresponding split of the curvature mass (4.24) via $\Delta m^2_{\text{curv}} = m^2_{\text{curv}} - 2Z_\phi k^2$

$$\partial_t\phi_0\Gamma^{(3)} = \frac{1}{2}\left(\partial_t\phi_0^2\right)\Gamma^{(4)} = \frac{3}{2}\left(\partial_t\Delta m^2_{\text{curv}} + 2Z_\phi(2-\eta_\phi)k^2 - m^2_{\text{curv}}\frac{\partial_t\Gamma^{(4)}}{\Gamma^{(4)}}\right)\,. \tag{A.6a}$$

In the first line, we related the three- and four-point function by (4.31), and we used (4.32) in the second step.

For the classical three-vertex in (A.5a), we analogously obtain

$$\partial_t\phi_0 S^{(3)} = \frac{\lambda_\phi}{\Gamma^{(4)}}\left(\partial_t\phi_0\Gamma^{(3)}\right)\,. \tag{A.6b}$$

With (A.3a), the fish diagram in (A.5a) carries a prefactor proportional to

$$\frac{\partial_t\phi_0}{\phi_0} = \frac{\partial_t m^2_{\text{curv}}}{m^2_{\text{curv}}} - \frac{\partial_t\Gamma^{(4)}}{\Gamma^{(4)}}\,. \tag{A.7}$$

Inserting (A.6) and (A.7) in (A.5a), we can write down the final flow equation for the two-point function in the broken phase,

$$\frac{d}{dt}\Gamma^{(2)}[\phi_0](p) = \dot{\mathcal{R}}\left(-\frac{1}{2}D_{\text{tad}} + D_{\text{pol}}\right) + A\, D_{\text{fish}} + B\,(2-\eta_\phi)Z_\phi k^2 + C - \partial_t S^{(2)}_{\text{ct}}\,, \tag{A.8a}$$

with

$$\begin{aligned}
\dot{\mathcal{R}} &= 2Z_\phi\,(2-\eta_\phi)\;k^2 + \frac{3}{2}m^2_{\text{curv}}\left(\frac{\partial_t \Delta m^2_{\text{curv}}}{m^2_{\text{curv}}} - \frac{\partial_t\Gamma^{(4)}}{\Gamma^{(4)}}\right)\,,\\
A &= -\frac{\phi_0}{2}\left(\frac{\partial_t m^2_{\text{curv}}}{m^2_{\text{curv}}} - \frac{\partial_t\Gamma^{(4)}}{\Gamma^{(4)}}\right)\,,\\
B &= \left(\frac{3\lambda_\phi}{\Gamma^{(4)}} - 1\right)\,,\\
C &= \frac{3}{2}m^2_{\text{curv}}\frac{\lambda_\phi}{\Gamma^{(4)}}\left(\frac{\partial_t \Delta m^2_{\text{curv}}}{m^2_{\text{curv}}} - \frac{\partial_t\Gamma^{(4)}}{\Gamma^{(4)}}\right)\,.
\end{aligned} \tag{A.8b}$$

The diagrams D_{pol}, D_{fish} and $D^{\text{dyn}}_{\text{tad}}$ are given in (A.3) and (A.4), respectively.

The prefactor of the first term in (A.8b), $\dot{\mathcal{R}}$, carries the scale dependence of the internal propagators on the physical minimum. It takes the role of the regulator derivative in usual fRG applications. The first term of $\dot{\mathcal{R}}$ and the third term of the flow (A.8a) are explicitly proportional to k^2, and have the same structure as the respective contributions in (4.9), where the flow equation is evaluated at arbitrary values of the field. However, it carries an additional relative factor -2, stemming from the three-point function, which is proportional to $\partial_t\phi_0\Gamma^{(3)}$. In total, the tree-level term of $\dot{\mathcal{R}}$ is positive and can be written as the t-derivative of $2Z_\phi k^2$. This reflects the positivity of the physical pole mass. At one-loop order, it reduces to $4k^2$, resembling the k-dependence of a classical propagator with $m_\phi = 2k^2$, see (4.17).

The same holds true for the constant part of the flow, given by the third and fourth term of (A.8a). Complementary to $\dot{\mathcal{R}}$, these encode the explicit running of the mass. At tree-level, this running reduces to $4k^2$, which is nothing but the flow of the classical (squared) mass on the physical minimum. Hence, the deviation of the constant part of the flow from the classical running is, as expected, of one-loop order and beyond and can be absorbed in the renormalisation constant. With that, we can consistently impose our renormalisation condition.

The second term of (A.8a) is proportional to the fish diagram. Note that D_{fish} carries a factor $1/\phi_0$, which cancels the respective factor in A. At one-loop order, it carries the running of the classical three-point function. Together, D_{fish} and D_{pol} can be written as the total derivative of the (one-loop) vacuum polarisation.

We now apply our renormalisation condition (4.13) to the flow (A.8a), for which it translates into the condition

$$\partial_t m^2_{\text{pole}} = 4k^2\,. \tag{A.9}$$

This specifies our counterterm flow and leads us to the final renormalised flow equation in the broken phase:

$$\frac{d}{dt}\Gamma^{(2)}(p) = \dot{\mathcal{R}}\left(D_{\text{pol}}(p) - \frac{1}{2}D^{\text{dyn}}_{\text{tad}}(p)\right) + A\, D_{\text{fish}}(p) + 4k^2 - \partial_t \hat{S}^{(2)}_{\text{ct}}\,, \tag{A.10}$$

where we have split the tadpole in a constant and dynamical p-dependent part defined by (A.4), via the spectral representation (4.5) of the four-vertex. Furthermore, we have dropped all constants in p of order $(\lambda_\phi k)$, including the constant part of the tadpole, as they are subtracted by the renormalisation constant implicitly specified by (A.9). The remaining $\partial_t \hat{S}^{(2)}_{\text{ct}}[\phi_0]$ now comprises only the counterterms of the diagrammatic contributions, where the renormalisation scale is the pole mass.

A.1.3. Flow of ϕ_0 and critical exponents

In this appendix, we discuss the evolution of the solution of the EoM, ϕ_0, in the broken phase. It is given by (4.32). This exact relation depends on λ_2, which we have identified with $\Gamma^{(4)}$, dropping higher order terms proportional to λ_3, λ_4 and ϕ_0 itself. Implicitly, these terms can be included by solving the flow of ϕ_0. It is derived from the EoM for constant fields, which is solved for a k-dependent ϕ_0. Acting with a total t-derivative on the EoM (4.10) leads us to

$$\partial_t \phi_0 = -\frac{\partial_t V^{(1)}_{\text{eff}}(\phi_0)}{V^{(2)}_{\text{eff}}(\phi_0)} = -\frac{\partial_t V^{(1)}_{\text{eff}}(\phi_0)}{m^2_{\text{curv}}}\,. \tag{A.11}$$

The denominator is nothing but the curvature mass squared, while the numerator is given by the first field derivative of the CS equation (4.8), evaluated at ϕ_0. At each flow step, the latter generates higher order terms beyond the approximation (4.20). In summary, if using the flow equation in (A.11), we implicitly take into account terms dropped in (4.32). In the present approximation the numerator of (A.11) reads

$$\begin{aligned}\partial_t V^{(1)}[\phi_0] = \phi_0\ (2-\eta_\phi)\, Z_\phi k^2 &\left[\frac{1}{2}D_{\text{tad}}(0) - 1\right] \\ &- \phi_0\left(\partial_t \Delta m^2\right)\,. \end{aligned}\tag{A.12}$$

The last term stems from the flow of the counterterm action

$$\partial_t S_{\text{ct}}[\phi] = \text{Tr}\,\frac{1}{2}\left(\partial_t \Delta m^2\right)\phi^2\,. \tag{A.13}$$

Collecting the terms proportional to ϕ_0 and $\partial_t\phi_0$, we arrive at

$$\partial_t \log(\phi_0) = \frac{(2-\eta_\phi)\, Z_\phi k^2}{m^2_{\text{curv}}}\ (1+\mathcal{T})\,, \tag{A.14}$$

where $\mathcal{T}$ comprises the corrections from the tadpole diagram and the counterterm

$$\mathcal{T} = -\frac{1}{2}D_{\text{tad}}(0) + \frac{\partial_t \Delta m^2}{(2-\eta_\phi)\, Z_\phi k^2}\,. \tag{A.15}$$

Equation (A.14) is easily integrated, leading to

$$\phi_0 = \phi_{0,\Lambda} \exp\left\{ \int_\Lambda^k \frac{dk}{k} \frac{(2-\eta_\phi)\, Z_\phi k^2}{m^2_{\text{curv}}} \, (1+\mathcal{T}) \right\} , \tag{A.16}$$

where $\phi_{0,\Lambda}$ is the classical ultraviolet value of the condensate in the initial UV effective potential, (4.34), at the initial large mass Λ. For smaller pole masses the condensate gets progressively smaller and vanishes for $k = 0$. We can simplify (A.16) further by noting that the squared curvature mass, see (4.32), is conveniently written in terms of the spectral representation

$$m^2_{\text{curv}} = \frac{2 Z_\phi k^2}{1 + \int_2^\infty \frac{d\lambda}{\lambda} \bar{\rho}(\lambda)} , \tag{A.17}$$

where we defined the RG-invariant spectral function as

$$\bar{\rho}\,(\lambda) = \frac{2 Z_\phi k^2}{\pi} \rho\left(\sqrt{2k^2}\, \lambda \right) . \tag{A.18}$$

With (A.17), the exponent of (A.16) reads

$$\int_\Lambda^k \frac{dk}{k} \left[\left(1 - \frac{\eta_\phi}{2} \right) \left(1 + \int_2^\infty \frac{d\lambda}{\lambda} \bar{\rho}(\lambda) \right) (1+\mathcal{T}) \right] . \tag{A.19}$$

For large k, i.e. $\lambda_\phi \ll k$ we can approximate $m^2_{\text{curv}} \approx 2k^2$, and $\lambda_2 = \Gamma^{(4)}(0) \approx \lambda_\phi$. The flow of the renormalisation constants is dominated by the tadpole contribution for large cutoff scales. It is of mass dimension 2 and at leading order in k it is proportional to $(\lambda_\phi k)$. Consequently, $\frac{\partial_t \Delta m^2}{k^2} \approx 0$ as well as the tadpole contribution,

$$D_{\text{tad}} = \lambda_\phi \int \frac{d^3 q}{(2\pi)^3} \frac{1}{(q^2 + 2k^2)^2} = \frac{\lambda_\phi}{\sqrt{2}k\, 8\pi} . \tag{A.20}$$

The propagator is then well approximated by the free one, $Z_\phi = 1$ and $\tilde{\rho} = 0$ and (A.19) reduces to $1 + \mathcal{T} \approx 1 + \bar{\lambda}_\phi c$, with the effective coupling $\bar{\lambda}_\phi = \lambda_\phi / k$ and a dimensionless constant c. In the limit of large masses, (A.21) flows to the classical solution as expected:

$$\phi_{0,k} = \phi_{0,\Lambda} \text{exp} \left\{ \int_\Lambda^k \frac{dk}{k} + c \int_\Lambda^k \frac{dk}{k} \bar{\lambda} \right\} \longrightarrow \phi_{0,\Lambda} \left(\frac{k}{\Lambda} \right) . \tag{A.21}$$

Similar equations could be formulated in terms of $\rho = \phi^2$, reflecting the symmetry of the theory. In O(N)-theories and in the real scalar case such a representation is typically used, as derivatives in ρ project directly on λ_n in both phases. While all different formulations are equivalent if the full effective potential is used, they deal differently with the approximation (4.20).

A.1.4. Phase transition and critical scaling

Here we provide a qualitative discussion on the scaling limit and use the integrated flow of the physical minimum, ϕ_0, and the (hyper-)scaling relation (A.22) to derive explicit equations for the scaling exponent η_ϕ. The phase transition between the symmetric and broken phase is reached with $k \to 0$ in both phases. In the limit of a vanishing pole mass, $m^2_{\text{pole}} = 2k^2 = 2|\mu| \to 0$ we are interested in the running of the 'magnetisation' $\bar{\phi}_0 = \phi_0/\sqrt{Z_\phi}$. The division by $1/\sqrt{Z_\phi}$ eliminates the RG-scaling of the expectation value and leads to the physical observable. In the scaling limit, the magnetisation acquires a scaling form

$$\bar{\phi}_0 \propto \tau^\beta \,, \qquad \beta = \frac{1}{2}\nu\,(1+\eta_\phi) \approx 0.3264 \,, \tag{A.22}$$

where $\nu \approx 0.6300$ and $\eta_\phi \approx 0.03630$ are the scaling exponents of the three dimensional Ising universality class. The tuning parameter τ is, in contrast to usual critical theory, not directly proportional to the mass-parameter μ or k^2 as consequence of the flowing on-shell renormalisation. To see that, we consider the scaling form of the correlation length

$$\xi \propto \tau^{-\nu} \,, \tag{A.23}$$

with the mean-field scaling $\nu = \frac{1}{2}$. In general, the correlation length is inverse proportional to the lowest lying pole of the propagator. Beyond the mean field theory, the correlation length acquires an anomalous scaling in dimensions below $d = 4$. With the on-shell renormalisation procedure, this anomalous scaling is hidden and we have

$$\xi \propto k^{-1} \,, \tag{A.24}$$

for all cutoff scales. This entails that the tuning parameter τ is related to the pole-mass $m_{\text{pole}} \propto k$ as

$$\tau \propto k^{\frac{1}{\nu}} \,. \tag{A.25}$$

In every flow step, the diagrams of the flow introduce an anomalous scaling to the pole mass, which is subtracted by the counter-term and expresses the renormalisation of the full scaling of the pole mass to the classical one. Hence, the scaling exponent ν is encoded in the flow of the counter-term in the scaling limit. With (A.25), the magnetisation (A.22) can be rewritten as

$$\bar{\phi}_0 \propto k^{\frac{\beta}{\nu}} \,, \qquad \frac{\beta}{\nu} = \frac{1}{2}(1+\eta_\phi) \,. \tag{A.26}$$

The k-scaling of the magnetisation is encoded in the $k \to 0$ limit of (A.16). Resolving the brackets, we notice that the first two terms of the exponent (A.19) can be integrated immediately, leading to

$$\phi_0 = \phi_{0,\Lambda}\, \sqrt{Z_\phi} \left(\frac{k}{\Lambda}\right) \, \exp\left\{\int_\Lambda^k \frac{dk'}{k'}\mathcal{D}(k')\right\} \,, \tag{A.27a}$$

where we used the definition of η_ϕ. The residual integrand is abbreviated as

$$\mathcal{D}(k) = \left(1 - \frac{\eta_\phi}{2}\right) \left[(1+\mathcal{T}) \int_2^\infty \frac{d\lambda}{\lambda} \bar{\rho}(\lambda) \; + \mathcal{T}\left(1 + \int_2^\infty \frac{d\lambda}{\lambda}\bar{\rho}(\lambda)\right)\right] \,, \tag{A.27b}$$

with $\mathcal{T}$ given in (A.15). In the scaling regime we have $k \to 0$ and

$$\bar{\phi}_0 \propto \lim_{k\to 0} k \exp\left\{\int_\Lambda^k \frac{dk'}{k'}\mathcal{D}(k')\right\} \,. \tag{A.28}$$

In the limit $k \to 0$ the integral in (A.28) diverges logarithmically with the prefactor $\mathcal{D}_0 = \mathcal{D}(0)$. Then we can read of β/ν and solve (A.26) for η_ϕ,

$$\eta_\phi = 1 + 2\mathcal{D}_0 \,. \tag{A.29}$$

The prefactor $\mathcal{D}_0$ is either computed for $k \to 0$ or is extrapolated when the scaling regime is reached. Alternatively, η_ϕ can be computed directly from the flow in the scaling limit via it's definition, see (A.121c). The size of the scaling regime can be estimated from the running of the four-point function: For large values of the dimensionless coupling $\lambda_\phi/m_{\text{pole}} >> 1$, the loop correction in the denominator of (4.21) outgrows the constant part,

$$\Gamma^{(4)}(p) = \frac{\lambda_\phi}{1 + \frac{\lambda_\phi}{2}\int_q G(p+q)G(q)} \to \frac{2}{\int_q G(p+q)G(q)} \,, \tag{A.30}$$

and the flow becomes independent of the coupling. Our computational set-up did not allow for a direct computation in this limit. Hence, we refrain from giving an estimate for the scaling exponents and defer quantitative results to future publications.

Let us close this investigation with a discussion of the spectral function in the critical regime. To begin with, for $k \to 0$ the pole contribution of the propagator vanishes as $Z_\phi \propto k^{-\eta_\phi} \to \infty$. In turn, for $k = 0$, the scattering tail carries all the weight, and the solution for $k = 0$ is given by

$$\tilde\rho(\lambda) \propto \frac{1}{\lambda^{2-\eta_\phi}} \quad \to \quad G_k(p) \propto \frac{1}{(p)^{2-\eta_\phi}} \,. \tag{A.31}$$

Note that the scaling (A.31) is naturally cut off in the infrared at $\lambda = 2m_{\text{pole}}$ according to (4.14). In the ultraviolet, for $\lambda \to \infty$, the spectral function also has to decay faster than (A.31). As has been discussed in [79, 80], the propagators of *physical* states or fields have to decay as $1/p^2$ for large momenta. This is at odds with (A.31) and indeed the spectral function $\tilde\rho$ in (A.31) is not (UV) normalisable. For a finite k, $\tilde\rho$ decays faster than $1/\lambda^2$, as is manifest in our explicit solutions in the broken and symmetric phase, Figures 4.7a and 4.7b respectively.

A.1.5. Calculation of diagrams

In this section, all diagrammatic expressions appearing in the main text are given in analytic form. The spectral approach we use, allows us to calculate diagrams with full propagators in terms of integrals known from perturbation theory. The insertion of a mass-derivative in Figure 4.2 leads to a squared propagator on one line in comparison with the usual vacuum polarisation or tadpole diagram. Using the spectral representation, the momentum structure of the regulator line can be rewritten via a partial fraction decomposition

$$\frac{1}{(\lambda_1^2+q^2)(\lambda_2^2+q^2)} = \frac{-1}{(\lambda_1^2-\lambda_2^2)}\left(\frac{1}{\lambda_1^2+q^2} - \frac{1}{\lambda_2^2+q^2}\right) . \tag{A.32}$$

A given (spectral) flow-diagram can therefore be reduced to the computation of the momentum integral, where the regulator line is replaced by a single propagator, which we will denote with a tilde. Denoting the spectral parameter of the divided line as λ_1 and λ_2, we write schematically

$$\mathrm{D}(\lambda_1, \lambda_2, ..., p^2) = \frac{-1}{(\lambda_1^2 - \lambda_2^2)} \left[\tilde{D}(\lambda_1..., p^2) - \tilde{D}(\lambda_2..., p^2)\right], \tag{A.33}$$

and accordingly

$$\mathrm{D}(\lambda, \lambda, ..., p^2) = \frac{-1}{2\lambda}\partial_\lambda \, \tilde{D}(\lambda..., p^2). \tag{A.34}$$

This reduces the calculation of I_{pol}, as defined in (A.3b) to the calculation of $\tilde{I}_{\text{pol}}$ as given below

$$I_{\text{pol}}(\lambda_1, \lambda_2, \lambda_3, p^2) = \frac{-1}{(\lambda_1^2 - \lambda_2^2)} \left[\tilde{I}_{\text{pol}}(\lambda_1, \lambda_3, p^2) - \tilde{I}_{\text{pol}}(\lambda_2, \lambda_3, p^2)\right], \tag{A.35}$$

Denoting the Euclidean and Minkowskian frequencies by p and ω respectively, the momentum structure of the spectral polarisation diagram reads

$$\begin{aligned}\tilde{I}_{\text{pol}}(p, \lambda_1, \lambda_2) =& \frac{1}{4\pi p} \text{Arctan}\left[\frac{p}{\lambda_1 + \lambda_2}\right], \\ \tilde{I}_{\text{pol}}(\omega, \lambda_1, \lambda_2) =& \frac{1}{4\pi\omega} \left\{ \text{Arctanh}\left[\frac{w}{\lambda_1 + \lambda_2}\right] + \mathrm{i}\,\theta\big(\omega - (\lambda_1 + \lambda_2)\big)\right\},\end{aligned} \tag{A.36}$$

see [54, 277]. We find the integrand I_{pol} of the polarisation diagram to have a branch cut with compact support, i.e., for $\omega \in [\lambda_1 + \lambda_3, \lambda_2 + \lambda_3]$ for $\lambda_1 \leq \lambda_2$. This peculiarity is a dimension dependent property of the polarisation diagram which does not hold in four dimensions. There, the imaginary part of I_{pol} has support for $\omega \in [\lambda_1 + \lambda_3, \infty)$ for $\lambda_1 \leq \lambda_2$.

The onset position of these structures allow us to discuss the scattering continua. To this end we note that the diagrams with a polarisation topology have two or three lines that can carry either a mass-pole or a scattering contribution, see Figure 4.5. If all lines carry a pole contribution, which is the leading order for all couplings in the considered coupling range, we find the flow of a discontinuity seeded at $2m_{\text{pole}}$, representing a 1 → 2 scattering.

A.1.6. Flow equation of the effective potential

In this section we briefly discuss the flow equation of the effective potential in the local potential approximation for the sake of completeness and for the illustration of consistency of the approach. Its derivation including the determination of the counter term has been discussed in detail in Appendix A of [1]. The flow of the first field derivative of the effective potential in three dimensions is given by

$$\partial_\mu V_{\text{eff}}^{(1)}(\phi) = -\frac{1}{2}\int \frac{\mathrm{d}^3 p}{(2\pi)^3} \frac{V_{\text{eff}}^{(3)}(\phi)}{\left[p^2 + V_{\text{eff}}^{(2)}(\phi)\right]^2} + \phi - \partial_\mu S_{\text{ct}}^{(1)}[\phi], \tag{A.37}$$

where we have dropped the multiplication with μ present in (4.8). We have already used that the momentum integral in (A.37) is finite, and hence we can remove additional regularisations such as dimensional regularisation relevant in the $d = 4$ case, see again

Appendix A of [1]. The momentum integral in (A.37) is readily performed and we arrive at

$$\partial_\mu V_{\text{eff}}^{(1)}(\phi) = -\frac{1}{4\pi^2} \frac{V_{\text{eff}}^{(3)}(\phi)}{\sqrt{V_{\text{eff}}^{(2)}(\phi)}} + \phi - \partial_\mu S_{\text{ct}}^{(1)}[\phi]\,, \tag{A.38}$$

and upon ϕ-integration we are led to

$$\partial_\mu V_{\text{eff}}(\phi) = -\frac{1}{8\pi^2} \sqrt{V_{\text{eff}}^{(2)}(\phi)} + \frac{1}{2}\phi^2 - \partial_\mu S_{\text{ct}}[\phi]\,, \tag{A.39}$$

where we have set the integration constant to zero. Note that (A.39) has a peculiar form: the loop contribution is negative, while its diagrammatic form is seemingly positive but not well-defined without regularisation. We emphasise that the the first field derivative of the flow (A.39) is negative (times $V_{\text{eff}}^{(3)}$), see (A.38), as holds true for all momentum-cutoff flows.

It is illustrative to consider the large field limit with $\phi^2/|\mu| \to \infty$. For these field values the effective potential (or rather its interaction part) reduces to the classical one, and the flow reduces to

$$\partial_\mu V_{\text{eff}}(\phi) \to -\frac{1}{8\pi^2} \sqrt{\frac{\lambda_\phi}{2}\phi^2} + \frac{1}{2}\phi^2 - \partial_\mu S_{\text{ct}}[\phi]\,, \tag{A.40}$$

up to sub-leading terms. We note in passing that (A.40) shows the self-consistency of the assumption that the interaction part reduces to the classical one. The right hand side is proportional to $|\phi| = \sqrt{2\rho}$. This reflects the infrared cut in three dimensional momentum cutoff flows for $\mu \to 0$. For the CS flow it is present for all μ in the large field limit in contradistinction to momentum cutoff flows that decay with $1/V_{\text{eff}}^{(2)}(\phi)$ for large fields.

A.1.7. Anomalous dimension η_ϕ

In this Appendix, we provide the relation used for the determination of the anomalous dimension η_ϕ defined in (4.8b). We start with the parametrisation of $\Gamma^{(2)}(p)$

$$\Gamma^{(2)}(p) = Z_\phi(p)\left(p^2 + m_{\text{pole}}^2\right)\,, \tag{A.41}$$

where we use Euclidean momenta p^2. Throughout the derivation we use the on-shell renormalisation condition (4.12), leading to $m_{\text{pole}}^2 = k^2$. The on-shell wave function is given by $Z_\phi = Z_\phi(p^2 = -k^2)$, which can be computed from the p^2-derivative of $\Gamma^{(2)}(p)$,

$$Z_\phi = \left.\frac{\partial \Gamma^{(2)}(p)}{\partial p^2}\right|_{p^2=-k^2}\,, \tag{A.42}$$

where we have used $m_{\text{pole}}^2 = k^2$. The t-derivative of (A.42), which hits both the explicit k-dependence of $\Gamma^{(2)}$ and the k-dependence of the momentum argument, leads us to an explicit expression for η_ϕ,

$$\eta_\phi = \frac{1}{Z_\phi}\left[\frac{\partial}{\partial p^2}\partial_t \Gamma^{(2)}(p) - 2k^2 \frac{\partial^2 \Gamma^{(2)}(p)}{(\partial p^2)^2}\right]_{p^2=-k^2}\,. \tag{A.43}$$

The second term in (A.43) can be expressed in terms of the spectral representation (4.3) of the propagator. To that end we use that

$$\partial^2_{p^2}\Gamma^2(p) = (p^2+k^2)\partial^2_{p^2}Z_\phi(p) + 2\,\partial_{p^2}Z_\phi(p) \tag{A.44}$$

The first term vanishes on-shell with $p^2=-k^2$. For the second term we use that

$$\frac{\partial Z_\phi(p)}{\partial p^2} = -Z^2_\phi(p)\frac{\partial}{\partial p^2}\left[\frac{1}{Z_\phi(p)}\right] = -Z^2_\phi(p)\frac{\partial}{\partial p^2}\Big[(p^2+k^2)\,G(p)\Big]\,. \tag{A.45}$$

Now we use the spectral representation (4.3) of the propagator and use (4.4) to split the propagator in its pole and tail contributions,

$$\frac{\partial Z_\phi(p)}{\partial p^2} = -Z^2_\phi(p)\frac{\partial}{\partial p^2}\left[\frac{1}{Z_\phi} + (p^2+k^2)\int\limits_\lambda \frac{\tilde\rho(\lambda)}{\lambda^2+p^2}\right]. \tag{A.46}$$

The on-shell residue $1/Z_\phi$ is momentum-independent. Hence, the one-particle pole of the propagator does not contribute to $\partial_{p^2}Z(p)$. Going also on-shell, we arrive at

$$\left.\frac{\partial Z_\phi(p)}{\partial p^2}\right|_{p^2=-k^2} = -Z^2_\phi\int_\lambda \frac{\tilde\rho(\lambda)}{\lambda^2-k^2}\,. \tag{A.47}$$

Note that the on-shell pole of the integrand lies outside of the support of $\tilde\rho(\lambda)$. Putting these results together, we arrive at

$$\eta_\phi = \left.\frac{1}{Z_\phi}\frac{\partial}{\partial p^2}\partial_t\Gamma^{(2)}(p)\right|_{p^2=-k^2} + 4k^2 Z_\phi\int_\lambda \frac{\tilde\rho(\lambda)}{\lambda^2-k^2}\,. \tag{A.48}$$

The first term in (A.48) is readily derived from the spectral form of $\partial_t\Gamma^{(2)}(p)$ provided in (4.27), as it admits analytic p^2-derivatives. However, (4.27) also depends on η_ϕ, and a respective resummation leads us to the final relation,

$$\eta_\phi = \left.\frac{-k^2\frac{\partial D^{\text{tad}}_{\text{dyn}}(\omega)}{\partial\omega^2} + 4k^2 Z^2_\phi\int_\lambda\frac{\tilde\rho(\lambda)}{\lambda^2-m^2_{\text{pole}}}}{1-\frac{k^2}{2}\frac{\partial D^{\text{tad}}_{\text{dyn}}(\omega)}{\partial\omega^2}}\right|_{\omega^2=m^2_{\text{pole}}}\,. \tag{A.49}$$

Note, that the derivatives can be taken fully analytically due to the analytic momentum dependence of the diagrams as discussed in Appendix A.1.5. This avoids any numerical instabilities introduced by numerical derivatives.

A.1.8. Scaling of $\rho_4(\lambda)$

In this Appendix, we discuss the scaling limits of the s-channel spectral function of the four-point scattering vertex. The respective numerical results are shown in Figure 4.10b and Figure 4.11b. The lowest possible scattering is 2 → 2 scattering, the spectral function has its onset at $m_{\text{scat}} = 2m_{\text{pole}}$, as can be seen in Figure 4.10b. For small momenta or spectral values, both $\Gamma^{(4)}$ and ρ_4 approach a power law, the latter one is given by (4.39b). Notably, both the prefactor and the exponent of these power laws are independent of λ_ϕ. For very

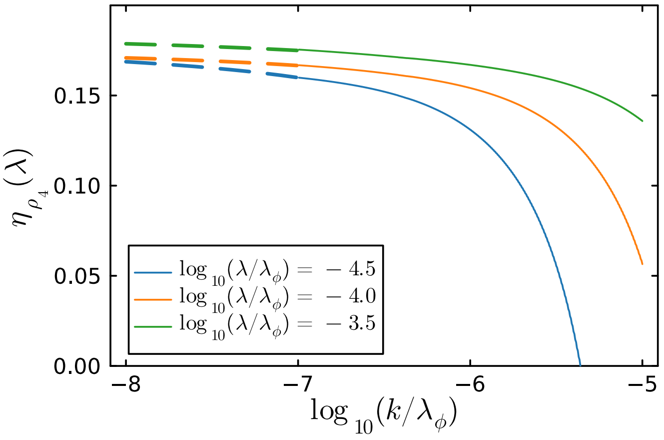

Figure A.1.: Anomalous dimension $\eta_{\rho_4}(\lambda, k)$, (4.40b), for different spectral parameters, at different spectral parameters, $\lambda/\lambda_\phi = 10^{-3.5}, 10^{-4.0}, 10^{-4.5}$, as functions of the cutoff scale k. The critical exponent $\eta_{\rho_4} = \eta_{\rho_4}(\lambda \to 0, 0)$ can be determined by an extrapolation: $\eta_{\rho_4} = 0.093(5)$, see (4.41b).

large momenta, the four point function goes into the classical limit $\Gamma^{(4)}(\omega \to \infty) = \lambda_\phi$. In turn, the spectral function decays with ω^{-1}, see Figure 4.10b. This reflects the subleading one-loop behaviour of $\Gamma^{(4)}$, and $\rho_4(\lambda)$ approaches the respective one-loop spectral function: this one-loop result is readily computed with classical spectral functions in D_{fish} in (4.21) with a vanishing mass, $\rho(\lambda) \to 2\pi\delta(\lambda^2)$. In this limit, $\Gamma^{(4)}$ reduces to

$$\Gamma^{(4)}(\omega) = \frac{\lambda_\phi}{1 + \mathrm{i}\frac{\lambda_\phi}{16\omega}} \tag{A.50}$$

and the s-channel spectral function function ρ_4 reads

$$\rho_4(\omega) = \frac{\lambda_\phi}{\frac{16\omega}{\lambda_\phi} + \frac{\lambda_\phi}{16\omega}}\,. \tag{A.51}$$

In the scaling limit, the propagator has the form $G(p) \propto (p^2)^{-(1-\eta/2)}$, (4.39a). Inserting (4.39a) into the denominator of (4.21), leads us to

$$\Gamma^{(4)}(\omega) \propto (\omega)^{1-2\eta}\,, \tag{A.52}$$

and the scaling law (4.39b) for ρ_4 with the exponent $1 - 2\eta$.

In Figure 4.11b we show $\eta_{\rho_4}(\lambda)$ for different pole masses $m_{\text{pole}} = k$ together with the one-loop result from (A.51). The convergence of the plateau towards the scaling exponent η_{ρ_4} is shown in Figure A.1. There, the anomalous dimension $\eta_{\rho_4}(\lambda, k)$ is shown for three different spectral parameters in the plateau, $\lambda/\lambda_\phi = 10^{-3.5}, 10^{-4.0}, 10^{-4.5}$, as functions of the cutoff scale k. The $\eta_{\rho_4}(\lambda, k)$ converge towards a unique value η for $k \to 0$, but at $k/\lambda_\phi = 10^{-7}$, this limit is not reached yet. We extract the limit η from an extrapolation towards $k = 0$, as indicated by the dashed lines. The respective uncertainty informs our error estimate.

A.1.9. Computation of the LPA′ benchmark

In this Appendix we provide some details on the fixed point analysis in LPA′ used as a benchmark in Section 4.1.7.3. This result links the CS-regulator results to other ones obtained with different regulators and also higher orders of the derivative expansion. The flow of the dimensionless effective potential in the three-dimensional scalar theory is given as

$$\big[\partial_t - (1+\eta_\phi)\bar\rho\,\partial_{\bar\rho}\big]\,u(\bar\rho) + 3\,u(\bar\rho) = \frac{2-\eta_\phi}{8\pi}\,\sqrt{1+\mu(\bar\rho)} - \dot\mu_{\rm ct}\,\bar\rho\,, \tag{A.53}$$

where the t-derivative in (A.53) is performed at fixed $\bar\rho$. The field-dependent dimensionless mass function $\mu(\bar\rho)$ in (A.53) reads,

$$\mu(\bar\rho) = u'(\bar\rho) + 2\bar\rho\, u''(\bar\rho)\,. \tag{A.54}$$

The dimensionless potential u and and field $\bar\rho$ are defined by rescaling the dimensionful quantities by appropriate powers of the cutoff scale k,

$$u(\bar\rho) = \frac{V_{\rm eff}(\rho)}{k^3} - \bar\rho\,, \qquad \bar\rho = Z_\phi\,\frac{\rho}{k}\,, \tag{A.55}$$

and hence $s_\pm$ drops out of the square root in the flow equation (A.53), but stays as a global prefactor in the second line. We have only introduced it as (A.55) incorporates the standard fRG convention, in which the cutoff term is subtracted from the effective action. Keeping this standard convention allows for a straightforward comparison.

The term $-\dot\mu_{\rm ct}\,\bar\rho$ is a part of the flow $\partial_t S_{\rm ct}$ of the counter term action in the renormalised CS-equation (4.9). Note, that despite the fixed point potential being in the broken phase, the standard fixed point analysis uses the CS-regulator $R_{\rm CS} = +Z_\phi k^2$ and finiteness in the three-dimensional theory is achieved by studying the flow of the $\bar\rho$-derivative of u, that is $\partial_t u'$. This translates into a flowing counter term action with $\dot\mu_{\rm ct} = 0$ in (A.53). This setup is used for the benchmark computation of the standard LPA′ fixed point analysis. We note in passing, that $\dot\mu_{\rm ct}$ also accommodates flowing renormalisation conditions for momentum-dependent regulators, see [1] which can be used for an optimisation of the convergence properties of a given expansion. Equation (A.53) is complemented by the algebraic relation for η_ϕ,

$$\eta_\phi = \frac{2\lambda_2\mu_0}{\lambda_2\mu_0 + 8\pi\left(4+4\sqrt{1+\mu_0}+\mu_0\left(5+\mu_0+3\sqrt{1+\mu_0}\right)\right)}\,, \tag{A.56}$$

with $\mu_0 = \mu(\kappa)$ in (A.54), evaluated on the solution κ of the equation of motionThe fixed point equation for the effective potential follows from (A.53) with $\partial_t u \equiv 0$. For its iterative solution we use the Taylor series representation of u within an expansion about the t-dependent minimum κ,

$$u(\bar\rho) = \sum_{n\geq 2}\frac{\lambda_n}{n!}(\bar\rho-\kappa)^n\,, \tag{A.57}$$

valid for $\kappa > 0$ with

$$\left.\frac{\partial u(\bar\rho)}{\partial\bar\rho}\right|_{\bar\rho=\kappa} = 0\,. \tag{A.58}$$

The λ_n are the dimensionless and RG-invariant scattering couplings of the ϕ^4-theory. The critical scaling on the phase transition is obtained by evaluating (A.53) on the fixed point u^* with $\partial_t u^*(\bar\rho) = 0$. This leads us to the fixed point equation

$$3\,u^*(\bar\rho) - (1+\eta_\phi)\bar\rho\, u^{*\prime}(\bar\rho) = \frac{2-\eta_\phi}{8\pi}\,\sqrt{1+\mu^*(\bar\rho)\bar\rho}\,. \tag{A.59}$$

Equation (A.59) can be solved iteratively order by order in the Taylor expansion (A.55) upon convergence.

We have computed the anomalous dimensions η on the fixed point for different truncations of the effective potential. The truncation best suited for comparison with the spectral flow is one where we only used the terms up to $\bar\rho^2$ in the effective potential. To analyse the improvement of the results with higher orders, we went up to $\bar\rho^9$. The results are discussed in Section 4.1.7.3.

A.1.10. Possible improvements and further work

In Appendix A.1.8 we discussed the computation of the four-point function via s-channel resummation. As described, this method does not allow for uniform scaling behaviour because it has an intrinsic scale, set by the value of the classical vertex in the UV. In this section, we discuss different options of addressing this issue.

To achieve quantitative precision for scaling exponents, the resolution of higher order scatterings appears to be crucial. This can be achieved by coupling the flow of the propagator to that of the effective potential. The latter can be treated either by a Taylor expansion around the minimum or by solving the full partial differential equation for the effective potential. In the symmetric phase, the full solution does not suffer from numerical difficulties due to symmetry restoration, and we hope to report on results in the near future.

To solve the issue of the UV-scale in the four-point function, see Appendix A.1.8, one option is the inclusion of different momentum channels. As the four-point function only appears in the tadpole-diagram it is enough to consider $\Gamma^{(4)}(p,l,-l,-p)$ where p is the external momentum and l the loop momentum which is integrated over. This specific momentum configuration means, that the s and u channel contribute equally. The t channel however does not carry any momentum ($t=0$) and can therefore only contribute an additive constant in such a configuration. The inclusion of these channels does two things. First, it includes more momentum dependency, what evidently leads to better approximation. Second, the constant contribution of the channels shifts the intrinsic scale of the four-point function to higher momenta. To illustrate this, we consider our s-channel approximation. Its UV-limit is given by the classical coupling, as the loop integral decays. To accommodate for the t-channel contribution in the resummation, we have to replace the classical coupling in (4.21) by an effective coupling $\lambda_{\text{eff}} = \lambda_\phi + \int \frac{dk}{k} flow_{\text{const}}$. The second term is comprised by the diagrams of the flow of the 4-point function, which do not depend on the s-channel momentum. Note, that these terms in the flow are proportional to λ_ϕ^2. The dimensionality of the four-point function hence requires that they are roughly proportional to $1/k$ what is the only other scale around. This shifts the UV-boundary of the scaling region to higher momenta, if the flow of the four-point function is taken into account. We aim to implement this in future works.

A.2. Additional material for the spectral DSE-BSE system

In this appendix, we provide additional information on the spectral DSE-BSE system we use to compute the mass of the scalar bound-state in Section 4.2. We first discuss detail on the spectral DSE in Appendix A.2.1 and then proceed to discuss the BSE system in Appendix A.2.4.

A.2.1. Spectral DSE

In this appendix we provide details on the spectral DSE solution. Our starting point is the spectral representation (4.49), which allows one to compute the full propagator from the spectral function. This relation can be inverted by analytic continuation to real frequencies,

$$\rho(\omega, |\vec{p}|) = 2\,\mathrm{Im}\, G(-i(\omega + i0^{+}), |\vec{p}|)\,. \tag{A.60}$$

The spectral representation allows one to determine the complete analytic structure of Feynman diagrams containing full propagators $G_i(p)$, since one only needs to perform the Euclidean loop integrals $I_j(p, \lambda_i)$ with classical propagators but different spectral masses λ_i. These integrals absorb the full momentum dependence so that one can perform an analytic continuation into real time.

The self-energy integrals with full propagators are then given by

$$\Pi_j(p) = g_j \prod_{i=1}^{N_j} \left(\int_0^\infty \frac{\mathrm{d}\lambda_i}{\pi} \lambda_i \rho(\lambda_i) \right) I_j(p, \lambda_i)\,, \tag{A.61}$$

where $\int_0^\infty \mathrm{d}\lambda_i\, \lambda_i/\pi = \int_{\lambda_i}$ is the spectral integral and g_j the prefactor of the particular diagram. In practice, these integrals are performed numerically since also the spectral function is usually computed numerically. Because the complex structure of the integrand is fully contained within the known functions $I_j(p, \lambda_i)$ and only enters in the complex structure of the full diagram $\Pi_j(p)$ via its spectral weight $\rho(\lambda_i)$, these computations are numerically stable.

The computation of real-time Feynman diagrams with full vertices also requires a spectral representation of the latter and possesses is own technical limitations [77, 237, 278]. In this work we ignore the momentum structure of the vertices by approximating them at zero momentum. The DSE can then be put in the general form

$$\Gamma^{(2)}(p) = p^2 + m^2 + \sum_j \Pi_j(p)\,, \tag{A.62}$$

where m is the bare mass in the classical action and $\Pi_j(p)$ are the spectral integrals (A.61) corresponding to the diagrams $I_j(p, \lambda_i)$ with $j = \{\mathrm{tad}, \mathrm{pol}, \mathrm{squint}, \mathrm{sun}\}$, whose prefactors g_j come from the combinatorial prefactors in the DSE and the vertices in the diagrams. We importantly remark that these constants are not trivial, as they include the action of the full vertices in the diagrams and thus may also depend on the spectral function itself by means of the corresponding DSE of each vertex.

As the full analytical structure of the diagrams $I_j(p, \lambda_i)$ can be computed, the equation can also be represented in real time as

$$\Gamma^{(2)}(\omega) = -\omega^2 + m^2 + \sum_j \Pi_j(\omega)\,, \tag{A.63}$$

where $\Pi_j(\omega)$ is computed over the analytically continued diagram $I_j(\omega, \lambda_i)$ according to (A.60) and carries its own real and imaginary component.

The explicit form of the diagrams is known [277]. We collect them below alongside their analytical continuation

$$p \to -i(\omega + i0^+)\,, \tag{A.64}$$

where the generated branch cuts are in accordance with `Mathematica` conventions. We abbreviate $\lambda_{12} = \lambda_1 + \lambda_2$, $\lambda_{123} = \lambda_1 + \lambda_2 + \lambda_3$, etc., and we also list the limits at zero momentum, if they are used in the computations:

Polarisation:

The polarisation diagram I_{pol} is given by

$$I_{\text{pol}}(p, \lambda_1, \lambda_2) = \frac{1}{4\pi p} \arctan \frac{p}{\lambda_{12}}\,, \quad I_{\text{pol}}(0, \lambda_1, \lambda_2) = \frac{1}{4\pi\lambda_{12}}\,. \tag{A.65}$$

With (A.64) we are led to

$$I_{\text{pol}}(\omega, \lambda_1, \lambda_2) = \frac{1}{4\pi\omega}\left[\text{arctanh}\frac{\omega}{\lambda_{12}} + i \arg\left(1 - \frac{\omega}{\lambda_{12}}\right)\right].$$

Sunset:

The sunset diagram I_{sun} is given by

$$I_{\text{sun}}(p, \lambda_1, \lambda_2, \lambda_3) = \frac{1}{(4\pi)^2} \qquad \times \left[\frac{1}{2} \ln \frac{1}{\lambda_{123}^2 + p^2} - \frac{\lambda_{123}}{p} \arctan \frac{p}{\lambda_{123}}\right], \tag{A.66}$$

With (A.64) we are led to

$$I_{\text{sun}}(\omega, \lambda_1, \lambda_2, \lambda_3) = \frac{1}{(4\pi)^2}\left[\frac{1}{2} \ln \frac{1}{\lambda_{123}^2 - \omega^2} - \frac{\lambda_{123}}{\omega}\left[\text{arctanh}\frac{\omega}{\lambda_{123}} + i \arg\left(1 - \frac{\omega}{\lambda_{123}}\right)\right]\right], \tag{A.67}$$

Squint:

The squint diagram I_{squint} is given by

$$I_{\text{squint}}(p, \lambda_1, \lambda_2, \lambda_3, \lambda_4) = \frac{1}{(8\pi)^2 \lambda_4\, p} \times \Bigg\{ 2 \ln\left(\frac{\lambda_{234}}{\lambda_{23} - \lambda_4}\right) \arctan \frac{p}{\lambda_{14}} + \\ i\left[\text{Li}_2\left(\frac{ip - \lambda_{14}}{\lambda_{23} - \lambda_4}\right) - \text{Li}_2\left(\frac{-ip - \lambda_{14}}{\lambda_{23} - \lambda_4}\right) + \text{Li}_2\left(\frac{-ip - \lambda_1 + \lambda_4}{\lambda_{234}}\right) - \text{Li}_2\left(\frac{ip - \lambda_1 + \lambda_4}{\lambda_{234}}\right)\right]\Bigg\}, \tag{A.68}$$

With (A.64) we are led to

$$I_{\text{squint}}(\omega, \lambda_1, \lambda_2, \lambda_3, \lambda_4) = \frac{\text{Re}\, F - i\theta\big(\omega - |\lambda_{14}|\big)\text{Im}\, F}{(8\pi)^2 \lambda_4\, \omega}\,, \tag{A.69}$$

with

$$F = 2\ln\left(\frac{\lambda_{234}}{\lambda_{23}-\lambda_4}\right)\operatorname{arctanh}\frac{\omega}{\lambda_{14}} - \mathrm{Li}_2\left(\frac{\omega-\lambda_{14}}{\lambda_{23}-\lambda_4}\right) + \mathrm{Li}_2\left(\frac{-\omega-\lambda_{14}}{\lambda_{23}-\lambda_4}\right)$$
$$- \mathrm{Li}_2\left(\frac{-\omega-\lambda_1+\lambda_4}{\lambda_{234}}\right) + \mathrm{Li}_2\left(\frac{\omega-\lambda_1+\lambda_4}{\lambda_{234}}\right). \tag{A.70}$$

Finally, the triangle at zero momentum is given by

$$I_{\mathrm{tr}}(P = p_1 = p_2 = 0, \lambda_1, \lambda_2, \lambda_3) = \frac{1}{4\pi}\frac{1}{\lambda_{12}\,\lambda_{23}\,\lambda_{31}}. \tag{A.71}$$

The tadpole and sunset diagram in the propagator DSE are divergent and need a subtraction. We choose an on-shell renormalisation condition $\Gamma^{(2)}(\omega = m_{\mathrm{pole}}) = 0$ such that the renormalised mass is the pole mass m_{pole}. The renormalised DSE thus acquires the form

$$\Gamma^{(2)}(\omega) = -\omega^2 + m_{\mathrm{pole}}^2 + \sum_j \Big[\Pi_j(\omega) - \Pi_j(m_{\mathrm{pole}})\Big]. \tag{A.72}$$

We note that no renormalisation of the coupling λ_ϕ is necessary due to the super-renormalisability of ϕ^4-theory in three dimensions. Furthermore, the DSE can easily be made dimensionless when dividing by m_{pole}^2, thus explicitly recovering the fact that the theory is determined by the dimensionless ratio $\lambda_\phi/m_{\mathrm{pole}}$ only. From now on we denote the pole mass by m for simplicity, as also done in the main text.

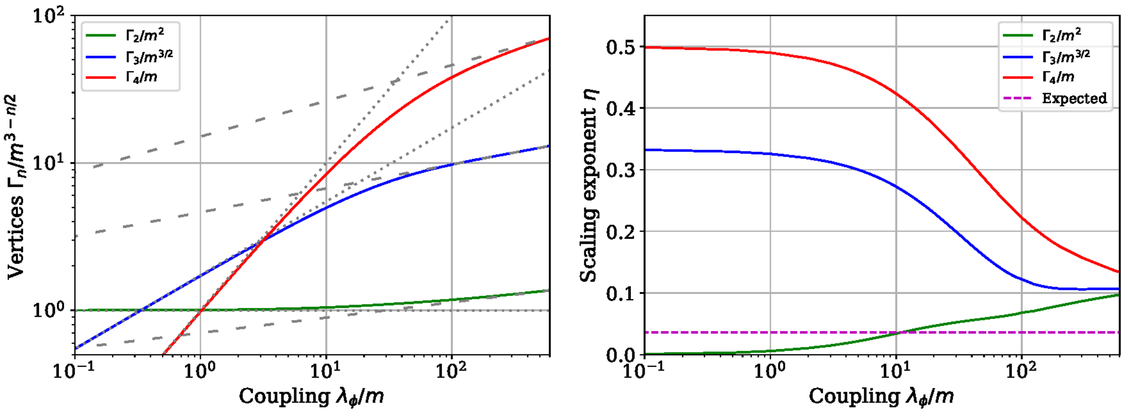

Figure A.2.: *Left:* Dimensionless zero momentum vertices $\Gamma_n/m^{3-n/2}$ as a function of the coupling λ_ϕ/m. The dotted gray lines are the tree-level values from (4.77), whereas the dashed gray lines are the asymptotic curves which follow the scaling limit (A.74). *Right:* Scaling exponent of each vertex, extrapolated from (A.74) for each value of the coupling. All vertices approach the same scaling exponent $\eta \approx 0.11$. The best theoretical prediction of the scaling exponent $\eta = 0.0360$ is represented with the dashed line for comparison.

The spectral DSE (A.72) constitutes a non-linear coupled system of integral equations for the spectral function $\rho(\lambda)$. The spectral integrals on the r.h.s. contain the full vertices, which implicitly also depend on $\rho(\lambda)$ through their own DSEs. In practice we solve the spectral DSE by iteration: We first introduce a reasonable guess for $\rho(\lambda)$ and compute the prefactors and diagrams according to our truncation scheme. We then compute the full propagator via the DSE of the two point function and extract $\rho(\lambda)$ from the l.h.s. of (A.60), which we introduce again in the spectral DSE. The three- and four-point vertices along with the condensate ϕ_0 are computed in parallel. We repeat the process until convergence is achieved.

One obtains the mass m_i of each stable one-particle state by computing the zeroes of the two-point function and determine their residue as

$$Z_i = -\frac{2m_i}{\partial_\omega \Gamma^{(2)}(\omega)}\bigg|_{\omega=m_i} . \tag{A.73}$$

In our case we only find one root coming from the original one-particle state. The corresponding residue is bounded by 1, being exactly 1 for the non-interacting theory and expected to decrease as dispersive states become more relevant in the interacting theory. The continuous tail from these dispersive states can be computed from (A.60). This tail starts at the two-particle threshold $2m$ and goes to zero in the UV, although it also has successive tails at every subsequent n-particle threshold which are suppressed by their corresponding mass.

A.2.2. Scaling limit

For the (dimensionless) zero-momentum vertices, the scaling relations suggest

$$\frac{\Gamma_2}{m^2} \sim \left[\frac{\lambda_\phi}{m}\right]^{\eta} , \quad \frac{\Gamma_3}{m^{3/2}} \sim \left[\frac{\lambda_\phi}{m}\right]^{\frac{3\eta}{2}} , \quad \frac{\Gamma_4}{m} \sim \left[\frac{\lambda_\phi}{m}\right]^{2\eta} , \tag{A.74}$$

where η is the anomalous dimension and λ_ϕ/m takes the role of the momentum in (4.58) in Section 4.2.1.3. With (A.74) we can infer a scaling exponent η from converging results of the RG-variant correlation functions displayed in Figure A.2. The left panel shows the set of zero-momentum vertices Γ_2, Γ_3 and Γ_4 as functions of the coupling λ_ϕ/m. These approach their tree level values (dotted lines) for small couplings, whereas for larger couplings they asymptotically approach a scaling behaviour which matches (A.74). By applying a logarithmic derivative, we obtain the associated scaling exponent η. This is shown in the right panel of Figure A.2, where it is visible how all three vertices approach a common scaling exponent $\eta \approx 0.11$, which is in agreement with fRG calculations on the Keldysh contour in the broken phase [142]. The authors find a deviation between the broken and symmetric phase which might point towards an interplay of η and ν in the broken phase. However, fRG results in the symmetric phase in a similar truncation point towards a very small scaling region, where momentum scaling of the vertices and in particular the two-point function emerge [5], which is by no means reached in the present work. See also Section 4.1.7, for the respective results.

A.2.3. Modified skeleton expansion

To estimate the relevance of the resummed 4-point function, we devise another approximation scheme, where we drop the full vertex in the tadpole. The diagrammatic depiction of the gap equation is provided in Figure A.3. The re-adjusted prefactor of the sunset

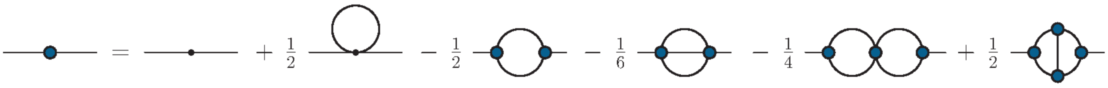

Figure A.3.: The modified skeleton expansion.

diagram guarantees two-loop consistency, and hence both approximations agree at two loop, but not beyond.

The respective DSE results are presented in Figure A.4. In comparison to the full results, the modified skeleton approximation does not exhibit scaling. All quantities approach a finite large coupling value, including the residue of the mass pole of the spectral function. The reason for this is that the zero momentum approximation of all of the vertices in this expansion fails to correctly represent the approaching quadratic divergence which is supposed to be present in the scaling limit. This nevertheless means that this DSE system is numerically stable, allowing us to solve for arbitrary values of the coupling.

We see that the full momentum dependence of the tadpole in the skeleton expansion of the main text is the reason for successfully achieving a scaling behaviour. Furthermore, this scaling behaviour is also what produces the numerical instabilities that prohibit us from obtaining solutions for $\lambda_\phi/m \gtrsim 10^3$.

We show the corresponding bound state mass in Figure A.5 for which we also made use of the scaling Kernel (4.70). This was devised in order to compare the differences coming solely from the changes in the self energy of each approximation. We see that, just as with the RG invariant vertices, the bound state mass of both approximations is in very good agreement even when close to the phase transition. This allows us to confidently extrapolate the limiting bound state mass of the skeleton expansion at the given value $M/m \approx 1.85$.

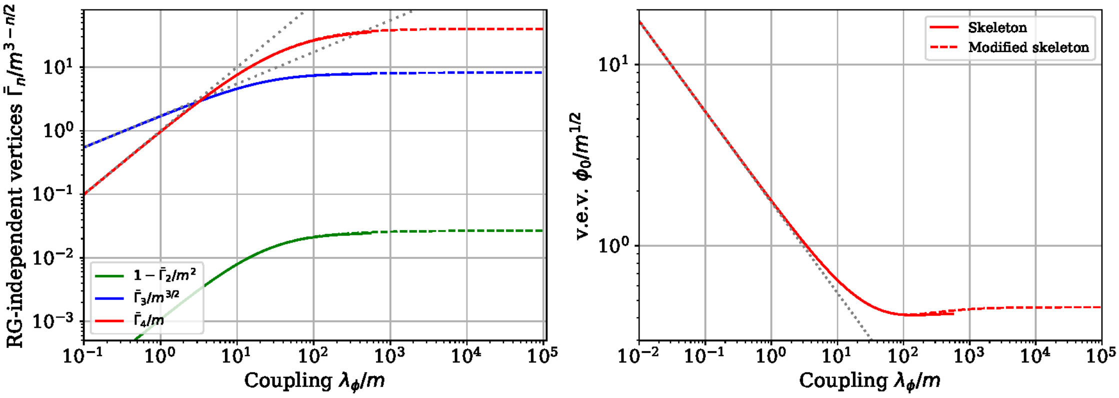

Figure A.4.: Evolution of the dimensionless zero momentum RG-independent vertices (4.76) and of the vacuum expectation value $\phi_0/m^{1/2}$ with the coupling λ_ϕ/m compared for the two DSE truncations: Solid curves come from the skeleton expansion of the main text, and the dashed lines correspond to the modified skeleton expansion of this appendix. The dotted gray lines are the tree-level values from (4.77). All quantities saturate for large couplings.

A.2.4. Bethe-Salpeter equation

Here we give details on the BSE solution discussed in Section 4.2.1.4. According to the spectral decomposition (4.49), the BSE kernel reads

$$
\begin{aligned}
K(q,k,P) &= \Gamma_3^2 \int_0^\infty \frac{d\lambda_3}{\pi}\, \lambda_3\, \rho(\lambda_3)\, \mathcal{K} - \frac{\Gamma_4}{2}\,, \\
\mathcal{K} &= \frac{1}{2}\left[\frac{1}{(q-k)^2+\lambda_3^2} + \frac{1}{(q+k)^2+\lambda_3^2}\right]\,,
\end{aligned}
\tag{A.75}
$$

where $\mathcal{K}$ comes from the t- and u-channel contributions in the kernel.

For the explicit coordinate representation we follow the conventions of [48] and express the momenta in three-dimensional Euclidean spherical coordinates,

$$
\frac{q}{m} = \sqrt{X}\begin{pmatrix} 0 \\ \sqrt{1-Z^2} \\ Z \end{pmatrix}\,, \qquad \frac{k}{m} = \sqrt{x}\begin{pmatrix} \sqrt{1-z^2}\,\sin\varphi \\ \sqrt{1-z^2}\,\cos\varphi \\ z \end{pmatrix}\,,
\tag{A.76}
$$

with $P = 2m\sqrt{t}\,(0,0,1)$, where at the end of the calculations we take $\sqrt{t} = iM/(2m)$. This implies

$$
\begin{aligned}
q^2 &= m^2 X\,, & q\cdot P &= 2m^2\sqrt{Xt}\,Z\,, \\
k^2 &= m^2 x\,, & k\cdot P &= 2m^2\sqrt{xt}\,z\,, \\
P^2 &= 4m^2 t = -M^2\,, & q\cdot k &= m^2\sqrt{xX}\,\Omega,
\end{aligned}
\tag{A.77}
$$

with $\Omega = zZ + \sqrt{1-z^2}\sqrt{1-Z^2}\cos\varphi$. The integral measure then takes the form

$$
\int d^3k = \frac{m^3}{2}\int_0^\infty dx\sqrt{x}\int_{-1}^{1} dz\sqrt{1-z^2}\int_0^{2\pi} d\varphi\,.
\tag{A.78}
$$

Equation (4.71) turns into

$$
\frac{1}{k_+^2+\lambda_1^2}\,\frac{1}{k_-^2+\lambda_2^2} = \frac{1}{m^4}\,\frac{1}{\tilde{Q}_1^4-\tilde{Q}_2^4}\,,
\tag{A.79}
$$

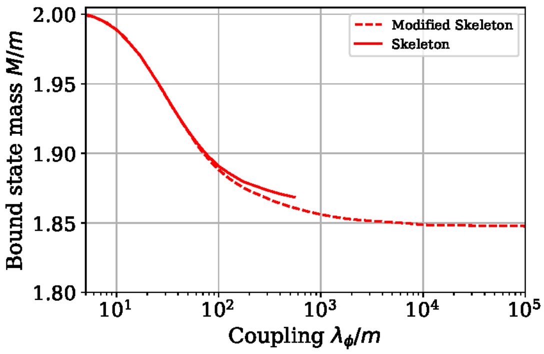

Figure A.5.: Evolution of the bound state mass M/m as a function of λ_ϕ/m calculated from the BSE, with propagators and vertices determined from their DSEs.

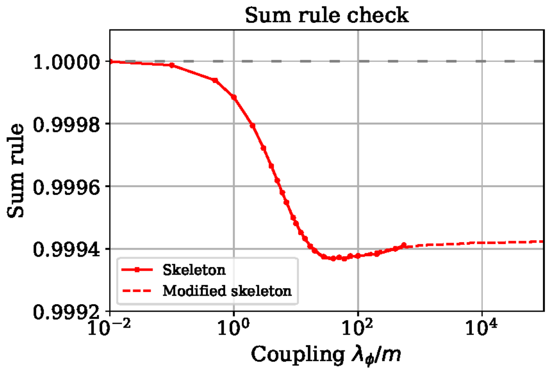

Figure A.6.: Results for the sum rule (the integral of the spectral function) from each DSE truncation.The deviations from unity are well within our conservative estimate 10^{-2} for the relative numerical error.

with

$$\tilde{Q}_1^2 = x + t + \frac{\lambda_1^2 + \lambda_2^2}{2m^2}\,, \qquad \tilde{Q}_2^2 = 2\sqrt{xt}z + \frac{\lambda_1^2 - \lambda_2^2}{2m^2}\,, \tag{A.80}$$

and the t- and u-channel exchange kernel $\mathcal{K}$ reads

$$\mathcal{K} = \frac{1}{m^2}\frac{X + x + \lambda_3^2/m^2}{\left(X + x + \lambda_3^2/m^2\right)^2 - 4Xx\,\Omega^2}\,. \tag{A.81}$$

The total bound state momentum P is evaluated in the timelike region, but this analytic continuation is trivial within our spectral decomposition. Despite the imaginary term $\sim \sqrt{t}$ in the denominator of (A.79), the product of the dressed propagators is real because its imaginary part is odd in (λ_1, λ_2) and integrates to zero in the spectral integrals. Furthermore, because the spectral variables λ_1 and λ_2 only take values at m and above $2m$, (A.79) is finite for all masses $M < 2m$ below the two-particle threshold. Finally, the integration over φ in (A.81) can also be done analytically using

$$\int_0^{2\pi} \frac{\mathrm{d}\varphi}{1 - (a + b\cos\varphi)^2} = \sum_{\chi=\pm 1} \frac{\pi}{\sqrt{(1+\chi a)^2 - b^2}}\,. \tag{A.82}$$

A.3. Additional material for the graviton spectral function

In this appendix, we present the additional informations that is referred to in Section 4.3. This concernes the expression of the diagrams and the analytic expressions of the spectral integration kernels in Appendix A.3.1. We further provide the details for generalised spectral kernels for the regulator line in Section A.6.4.1 and derive the UV behaviour of the on-shell renormalised graviton spectral function analytically in Appendix A.3.2.

A.3.1. Analytic expressions of the diagrams

The diagrams read schematically

$$\begin{aligned}
\partial_t \Gamma^{(hh)}_{\mathrm{TT}}\Big|_{\text{tadpole}} &= \prod_{i=1}^{2}\int_0^\infty \frac{d\lambda_i}{\pi}\lambda_i\,\rho_h(\lambda_i)\int\frac{d^dq}{(2\pi)^d}\frac{V_{\text{tadpole}}(p,q)}{(q^2+\lambda_1^2)(q^2+\lambda_2^2)}\,,\\
\partial_t \Gamma^{(hh)}_{\mathrm{TT}}\Big|_{\text{3-point}} &= \prod_{i=1}^{3}\int_0^\infty \frac{d\lambda_i}{\pi}\lambda_i\,\rho_h(\lambda_i)\int\frac{\mathrm{d}^dq}{(2\pi)^d}\frac{V_{\text{3-point}}(p,q)}{(q^2+\lambda_1^2)(q^2+\lambda_2^2)\big((p+q)^2+\lambda_3^2\big)}\,,\\
\partial_t \Gamma^{(hh)}_{\mathrm{TT}}\Big|_{\text{ghost}} &= \prod_{i=1}^{3}\int_0^\infty \frac{d\lambda_i}{\pi}\lambda_i\,\rho_c(\lambda_i)\int\frac{\mathrm{d}^dq}{(2\pi)^d}\frac{V_{\text{ghost}}(p,q)}{(q^2+\lambda_1^2)(q^2+\lambda_2^2)\big((p+q)^2+\lambda_3^2\big)}\,. \qquad \text{(A.83)}
\end{aligned}$$

Where the vertex functions V_i combine the contractions of the vertices with the regulator derivative $\partial_t R_k(q) = (2-\eta_h)Z_h k^2$. Up to a factor of Z_h they can be found in the additional material of [81].

While the full expressions of the diagrams are far too long to be displayed here, the respective imaginary parts can be reduced to a few terms. For the ghost diagram, we use the treelevel spectral function instead of the full spectral function, which leads to a simple expression:

$$\mathrm{Im}D_{ghost}(k,\omega) = -2g\frac{20k^4-8k^2\lambda^2+\lambda^4}{\lambda\sqrt{\lambda^2-4k^2}}\,\theta\big(\lambda^2-4k^2\big)\,. \qquad \text{(A.84)}$$

The imaginary part of the tadpole diagram vanishes and the imaginary part of the graviton polarisation diagram can be reduced to

$$\mathrm{Im}D_{3-point}(\lambda_1,\lambda_2,\omega) = \frac{g\,N(\lambda_1,\lambda_2,\omega)\theta(\omega-\lambda_1-\lambda_2)}{(12\omega^6\xi_{\text{cut}}(\lambda_1,\lambda_2,\omega)\left(-\lambda_1^4+2\lambda_1^2\lambda_2^2-\lambda_2^4+\omega^4\right))}\,, \qquad \text{(A.85a)}$$

whith the numerator function

$$\begin{aligned} N(\lambda_1,\lambda_2,\omega) = \Big\{ &- \lambda_1^{10} + \lambda_2^{10} + \lambda_2^8\omega^2 + 4\lambda_2^6\omega^4 + 8\lambda_2^4\omega^6 + 23\lambda_2^2\omega^8 + \lambda_1^8(5\lambda_2^2 - 3\omega^2) \\ &+ 11\omega^{10} - 2\lambda_1^6(5\lambda_2^4 - 4\lambda_2^2\omega^2 + 4\omega^4) + 2\lambda_1^4(5\lambda_2^6 - 3\lambda_2^4\omega^2) \\ &+ 14\lambda_2^2\omega^4 + 8\omega^6 - \lambda_1^2(5\lambda_2^8 + 24\lambda_2^4\omega^4 - 32\lambda_2^2\omega^6 + 15\omega^8)\Big\} \times \\ \times \Big\{ &(-\lambda_1^2 + \lambda_2^2)\left(\sqrt{(\lambda_1^2 - \lambda_2^2 + \omega^2)^2} - \sqrt{(-\lambda_1^2 + \lambda_2^2 + \omega^2)^2}\right) \\ &+ \omega^2\left(\sqrt{(\lambda_1^2 - \lambda_2^2 + \omega^2)^2} + \sqrt{(-\lambda_1^2 + \lambda_2^2 + \omega^2)^2}\right)\Big\}\,. \end{aligned} \tag{A.85b}$$

and the cut function

$$\xi_{\text{cut}}(\lambda_1,\lambda_2,w) = \sqrt{(\lambda_1 - \lambda_2 - \omega)(\lambda_1 + \lambda_2 - \omega)(\lambda_1 - \lambda_2 + \omega)(\lambda_1 + \lambda_2 + \omega)}\,. \tag{A.85c}$$

A.3.2. UV-limit of the spectral tail

The UV-limit of the spectral tail is fully determined by the UV-limit of the imaginary part of the flow and in particular of the flow induced by the graviton mass-pole. While the feedback of the spectral tail is strongly suppressed in the IR, the respective terms in the flow have the same UV-scaling as the leading one, and are suppressed only by an overall factor. Furthermore, the ghostloop has the same structure and differs only in the prefactors and signs. Hence, we can extract the UV-scaling of the spectral tail from the UV-dominant term of the flow arising from Graviton peak only. It reads

$$\text{Im}\dot{\Gamma}_k^{(2)}(\omega \to \infty) \propto g(k)\frac{\omega^3}{\sqrt{\omega^2 - 4k}}\theta(\omega - 2k)\,. \tag{A.86}$$

As already discussed in the main text, the flow is localised at the onset, ie. it diverges at the onset as $1/\sqrt{\omega^2 - 4k}$, which is integrable and leads to a finite contribution when integrated with respect to k. Evidently, this structure gives only a sizable contribution to the integral, wenn k is close to $\omega/2$. For $\omega > k$ the flow simply goes as w^2, where the only k-dependence is given by the prefactor $g(k)$, which goes exactly as k^2 in the IR and approaches a constant beyond the Planckscale. Hence, the integral is strongly dominated by the scales between M_{pl} and $w/2$. This allows to approximate the dimensionless newton coupling by its fixed point value and we we can integrate the UV-limit of the flow analytically:

$$\text{Im}\Gamma_k^{(2)}(\omega \to \infty) \propto \int_k^{\omega/2} \frac{dk'}{k'}\, g^* \frac{\omega^3}{\sqrt{\omega^2 - 4k'}} = g^*\omega^2 \log\left(\frac{\omega + \sqrt{w^2 - 4k^2}}{2k}\right)\,. \tag{A.87}$$

For the real part, we can use the subtracted Kramers-Kronig relation eq. (A.138), where we can set $x_0 = 0$, $f(x_0) = 0$ and even $(\partial_{x^2} f)(x_0) = 0$, as we are interested only in the leading behaviour which we anticipate to be larger than w^2. Furthermore, we assume $w \ll k$ and k to be arbitrarily small but larger than zero, such that we find for the leading UV-behaviour of the real part:

$$\text{Re}\Gamma_k^{(2)}(\omega \to \infty) \propto \omega^4\, \text{PV}\int_{2k}^{\infty} \frac{dt}{\pi}\frac{2\log(t)}{t(t^2 - \omega^2)} \propto \omega^2\log(\omega)^2 + O(\omega^2\log(\omega))\,. \tag{A.88}$$

This result allows us to determine the UV-scaling of the spectral tail, by noting that the real part grows faster in the UV than the imaginary part and the classical ω^2 behaviour. Hence the UV scaling of the spectral tail is given by

$$\rho_h(\lambda \to \infty) \propto \frac{\mathrm{Im}\,\Gamma_k^{(2)}(\lambda \to \infty)}{\mathrm{Re}\,\Gamma_k^{(2)}(\lambda \to \infty)^2} \propto \frac{\lambda^2\,\log(\lambda^2)}{(\lambda^2\,\log(\lambda^2)^2)^2} = \frac{1}{\lambda^2\,\log(\lambda^2)^3}\,. \tag{A.89}$$

which falls off slightly faster than $1/(\lambda^2 \log(\lambda))$ and hence leads to a normalisable spectral function.

A.4. Additional material for the quark gap equation

In this appendix, we present additional material for Section 5.1. We discuss a the spectral STI-vertex and its renormalisation in Appendix A.4.1 and present the details of the spectral self energy calculation in Appendix A.4.2.

A.4.1. The spectral STI-vertex

The Slavnov-Taylor identity (STI) of the Quark-Gluon vertex reads

$$k_\mu \Gamma^\mu_{\bar{q}qA}(k,p) = g \frac{1}{Z_c(k)} t^a \Big[G_q^{-1}(p+k)\mathcal{H}(k,q) - G_q^{-1}(p)\bar{\mathcal{H}}(-k,p+q) \Big]\,, \tag{A.90}$$

for a derivation, see, e.g., [33]. The inclusion of non-trivial scattering kernels goes beyond the scope of the present work. We drop it in an Abelian approximation of the STI, $\mathcal{H}(k,q) = 1$, and only keep the prefactor gt^a on the right-hand side together with the overall ghost dressing function $1/Z_c(k)$. The latter leads to an enhancement of the vertex in the IR. For a non-abelian computation see [256]. The inverse quark propagators are cancelled by multiplying (A.90) from both sides with the respective quark propagator, also using their spectral representation,

$$k_\mu G_q(p+k)\, \Gamma^\mu_{\bar{q}qA}(k,p)\, G_q(p) = g_s \frac{1}{Z_c(k)} t^a \Big[G_q(p+k) - G_q(p) \Big] \tag{A.91}$$

$$= -\mathrm{i} g_s \frac{1}{Z_c(k)} t^a \int_\lambda \rho_q(\lambda) \frac{1}{\mathrm{i}(\not{p} + \not{k}) + \lambda}\, \not{k}\, \frac{1}{\mathrm{i}\not{p} + \lambda}\,. \tag{A.92}$$

Equation (A.92) admits the simple solution,

$$G_q(p+k)\Gamma^\mu_{\bar{q}qA}(k,p)G_q(p) \approx -\mathrm{i} g_s \frac{1}{Z_c(k)} t^a \mathcal{K}^\mu(k,p)(p)\,,$$

with

$$\mathcal{K}^\mu(k,p) = \int_\lambda \rho_q(\lambda) \frac{1}{\mathrm{i}(\not{p} + \not{k}) + \lambda} (\gamma^\mu) \frac{1}{\mathrm{i}\not{p} + \lambda}\,. \tag{A.93}$$

Equation (A.93) is unique up to general transverse functions. For a QED version of this vertex, see [53, 237].

In contrast to the usual Ball-Chiu construction for the quark gluon vertex, (A.93) allow a consistent renormalisation of the gap equation, without the addition of further terms. To see this, we start by multiplying the gap equation with the quark propagator from the right hand side, what allows us to insert (A.93) into the loop integral:

$$1 = (\mathrm{i}\, Z_2 \not{p} + Z_q m_q) G(p) + g_s^2 C_f Z_1 \int_{\lambda_q,\lambda_A} \lambda_A \rho_q \bar{\rho}_A I_1(\lambda_q, \lambda_A, p) \frac{1}{\mathrm{i}\not{p} + \lambda_q} \tag{A.94}$$

The momentum integral is linearly divergent and requires renormalisation. This can be implemented via a BPHZ scheme on the level of the DSE. To see this, we start by bringing the renormalised DSE in a form, where we can apply the STI-vertex formulation. we note that the divergent terms of both the scalar and dirac parts of I_Σ is constant in p and spectral parameter (up to the basiselement $\not{p}$), as can be seen in appendix A.4.2. This allows us to write

$$\begin{aligned}
&(\Sigma(p) - \Sigma(\mu))G(p) = \Sigma(p)G(p) - \Sigma(\mu)G(\mu)G^{-1}(\mu)G(p) \\
&= \left(\frac{c}{\epsilon}\right) \int_{\lambda_q,\lambda_A} \lambda_A \rho_q \rho_A \frac{1}{\mathrm{i}\not{p} + \lambda_q} - \left(\frac{c}{\epsilon}\right) \int_{\lambda_q,\lambda_A} \lambda_A \rho_q \rho_A \frac{1}{\mathrm{i}\not{\mu} + \lambda_q} G^{-1}(\mu)G(p) \\
&+ \int_{\lambda_q,\lambda_A} \lambda_A \rho_q \rho_A f(\lambda_q, \lambda_A, p) \frac{1}{\mathrm{i}\not{p} + \lambda_q} - \int_{\lambda_q,\lambda_A} \lambda_A \rho_q \rho_A f(\lambda_q, \lambda_A, \mu) \frac{1}{\mathrm{i}\not{\mu} + \lambda_q} G^{-1}(\mu)G(p) \\
&= \int_{\lambda_A} \rho_A \left(\frac{c}{\epsilon}\right) \left\{ G(p) - G(\mu)G^{-1}(\mu)G(p) \right\} \\
&+ \int_{\lambda_q,\lambda_A} \lambda_A \rho_q \rho_A f(\lambda_q, \lambda_A, p) \frac{1}{\mathrm{i}\not{p} + \lambda_q} - \int_{\lambda_q,\lambda_A} \lambda_A \rho_q \rho_A f(\lambda_q, \lambda_A, \mu) \frac{1}{\mathrm{i}\not{\mu} + \lambda_q} G^{-1}(\mu)G(p)\,,
\end{aligned} \tag{A.95}$$

Where the finite part of the loop ingegral indicated by $f(p, \lambda_q, \lambda_A)$ comprises all terms that are not constant in p or the spectral parameter. Evidently, the divergent part of the loop integral is eliminiated by the subtraction and we are left with a finite self energy. Equation (A.94), with the STI-vertex has an appealing form as it is in principle equivalent to a linear equation for the quark spectral functions. However, the distributional nature of the spectral function complicates the implementation substantially. Ideally, a weak formulation of the equation would be beneficial. Alternatively, we can insert a representation of unity in the self-energy $1 = G_q(p)\Gamma^{(\bar{q}q)}(p)$. We can then cast the renormalised self energy as

$$\begin{aligned}
\Sigma^{\mathrm{ren}}(p) =& \mathrm{i}\not{p}\,(\Sigma_d(p) - \Sigma_d(\mu)) + (\Sigma_s(p) - \Sigma_s(\mu)) \\
=& g_s^2 C_f \int_{\lambda_q,\lambda_A} \rho_q(\lambda_q)\bar{\rho}_A(\lambda_A) I_1^{\mathrm{ren}}(\lambda_q, \lambda_A, p) \frac{1}{\mathrm{i}\not{p} + \lambda_q} \Gamma^{\bar{q}q}(p) - \left(\mathrm{i}\not{p}\,\delta Z + \delta m\right)
\end{aligned} \tag{A.96}$$

where I_1^{ren} consists of the finite and regularisation scale independent part of the momentum integral. The dependence on the latter is absorbed in the renormalisation constants δZ and δm, which are determined by the renormalisation conditions.

In the following, we would like to lay out a possible solution strategy for (A.96). The actual implementation with the reconstructedn ghost and gluon spectral functions turned out to be numerically instable, due to oscillations which we deem most likely to be a consequence of reconstruction artefacts. Nevertheless, we would like to discuss the resulting equations for the imaginary part of the self energy and defer a numerical solution to a future work.

With the STI vertex, we can use the decomposition (A.100a) to project onto the scalar and dirac parts of the self energy and take the imaginary part. The dirac part is given by

$$\begin{aligned}
&\mathrm{Im}\ \Sigma_d^{ren}(-\mathrm{i}\omega^+) = \mathrm{Im}\,\mathrm{Tr}\,\frac{-\mathrm{i}\not{p}}{4p^2}\ \Sigma^{ren}(p) \\
&\quad = C_f g_s^2 \int d\mu[\bar{\rho}_A, \{\lambda_i\}]\mathrm{Im}\ \frac{I_s^{\mathrm{ren}}(-\mathrm{i}\omega_+)C_d^s(\lambda_q, -\mathrm{i}\omega_+) + I_d^{\mathrm{ren}}(-\mathrm{i}\omega_+)C_d^d(\lambda_q, -\mathrm{i}\omega_+)}{\lambda_q^2 - w^2 - \mathrm{sign}(\omega)0^+}
\end{aligned} \tag{A.97a}$$

and the scalar part reads

$$\operatorname{Im}\,\Sigma_s^{ren}(-\mathrm{i}\omega^+) = \operatorname{Im}\operatorname{Tr}\frac{1}{4}\,\Sigma^{ren}(p)$$
$$= C_f g_s^2 \int d\mu[\bar\rho_A,\{\lambda_i\}]\operatorname{Im}\,\frac{I_s^{\rm ren}(-\mathrm{i}\omega_+)C_s^s(\lambda_q,-\mathrm{i}\omega_+) + I_d^{\rm ren}(-\mathrm{i}\omega_+)\,C_s^d(\lambda_q,-\mathrm{i}\omega_+)}{\lambda_q^2 - w^2 - \operatorname{sign}(\omega)0^+} \tag{A.97b}$$

with the coefficients

$$C_d^s(\lambda_q,p) = Z(p)\lambda_q - B(p)\,, \qquad C_d^d(\lambda_q,p) = B(p)\lambda_q + Z(p)p^2\,,$$
$$C_s^s(\lambda_q,p) = C_d^d(\lambda_q,p)\,, \qquad C_s^d(\lambda_q,p) = -p^2 C_d^s(\lambda_q,p)\,, \tag{A.97c}$$

and $B(p) = M(p)Z(p)$. Note that these imaginary parts contain potential deltafunctions also after integration if the quark spectral function contains a deltafunction at the quark pole mass. This is indeed the case, but the deltafunction is then multiplied by the real part of the coefficients or the imaginary part of the loop integrals, which both vanish on the quark pole mass. The same holds true for the potential branch cut singularity arising from the $\lambda_q^2 - w^2$ in the denominator for the pole contribution to the quark spectral function. Here, the value of the cut goes to zero when approaching the pole as it is multiplied with either the imaginary part of the loop function and the realpart of the coefficient or the imaginary part of the latter. Hence the imaginary parts of the self energy consist only of a cut, starting from a value of zero at the quark pole mass, what supports the scenario of a real first singularity. Suppressing the arguments, we arrive at the final results for the imaginary parts of the self energy:

$$\operatorname{Im}\,\Sigma_d^{ren}(-\mathrm{i}\omega^+) = C_f g_s^2 \int d\mu[\bar\rho_A,\{\lambda_i\}]\Bigg\{\frac{\operatorname{Im}\left(\lambda_q I_s^{\rm ren} C_d^s + I_d^{\rm ren} C_d^d\right)}{\lambda_q^2 - w^2}$$
$$+ \frac{w}{|w|}\pi\delta(\lambda_q^2 - w^2)\operatorname{Re}\left(I_s^{\rm ren} C_d^s + I_d^{\rm ren} C_d^d\right)\Bigg\} \tag{A.98}$$

and the scalar part reads

$$\operatorname{Im}\,\Sigma_s^{ren}(-\mathrm{i}\omega^+) = C_f g_s^2 \int d\mu[\bar\rho_A,\{\lambda_i\}]\Bigg\{\frac{\operatorname{Im}\left(\lambda_q I_s^{\rm ren} C_s^s + I_d^{\rm ren} C_s^d\right)}{\lambda_q^2 - w^2}$$
$$+ \frac{w}{|w|}\pi\delta(\lambda_q^2 - w^2)\operatorname{Re}\left(I_s^{\rm ren} C_s^s + I_d^{\rm ren} C_s^d\right)\Bigg\} \tag{A.99}$$

The integrands can be further reduced, and we first note, that the coefficient functions $C_{s/d}^{s/d}$ contain different powers of λ_q, what mixes the scalar and dirac parts of the spectral functions and hence the vertex construction (in presence of a non-vanishing mass function) has overlap with chiral symmetry breaking tensor structures. However, if one sets $B(p) = 0$ (and accordingly the anti-symmetric/mass part of the quark spectral function), this mixing is absent and we deduce that the vertex construction does not break chiral symmetrie explicitly. The deltafunction is integrated out immidiately and we are left with the products of the real parts of loopintegrals and coefficient functions and the spectral functions, evaluated at $\lambda_q = \omega$, as the imaginary parts of $I^{\text{ren}}_{s/d}(w, \lambda_q)$ vanish for $w \leqslant \lambda_q$. The remaining spectral integral is carried out numerically. While it is in principle possible to reduce first integral furter by using Kramers-Kronig relations, it is computationally more efficient to refrain from doing so and solve the integral in two steps, where the numerical integral over the gluon spectral parameter can be precomputed and reused as it does not change in this truncation with the itteration.

A.4.2. Self-energy calculations

Here, we collect the results of the momentum integrals for the quark self energy contributions. The momentum integral (5.20) has been computed in [191] within dimensional regularisation, and we arrive at

$$I_1(p, \lambda_A, \lambda_q) = \int_q \gamma^\mu \frac{\Pi_{\mu\nu}(q)(-\mathrm{i}(\not{p} + \not{q}) + \lambda_q)}{(q^2 + \lambda_A^2)((p+q)^2 + \lambda_q^2)} \gamma^\nu = \lambda_q I_1^{(s)}(p, \lambda_A, \lambda_q) + \mathrm{i}\not{p}\, I_1^{(d)}(p, \lambda_A, \lambda_q)\,, \tag{A.100a}$$

with the scalar and Dirac parts of the integrals

$$I_1^{(s)}(p, \lambda_A, \lambda_q) = \frac{3\lambda_q}{(4\pi)^2} \left(\frac{1}{\epsilon} + \log \mu_r^2 - f_0 \right),$$

$$I_1^{(d)}(p, \lambda_A, \lambda_q) = \frac{-1}{(4\pi)^2} \left[\left(\frac{1}{\epsilon} + \log \mu_r^2 \right) \sum_{i=0}^{3} \frac{\alpha_i^1 + \beta_i^1}{i+1} \sum_{i=0}^{3} \Big(\alpha_1^i f_i + \beta_1^i g_i \Big) \right].$$

The functions f_i and g_i are given by the weighted Feynman integrals over the logarithms of the cut function $\Delta(\lambda_1, \lambda_2, x, p^2) = x\,(1-x)\,p^2 + x\left(\lambda_2^2 - \lambda_1^2\right) + \lambda_1^2$,

$$f_i = \int_0^1 dx\, x^i \,\log\Big(\Delta(\lambda_A, \lambda_q, x, p^2) \Big),$$

$$g_i = \int_0^1 dx\, x^i \,\log\Big(\Delta(0, \lambda_q, x, p^2) \Big) \tag{A.101}$$

and the respective prefactors a_1^i and b_1^i read in the Landau gauge

$$\alpha_1^0 = -2\,, \qquad \alpha_1^1 = 4 - \frac{p^2 + \lambda_q^2}{\lambda_A^2}\,, \qquad \alpha_1^2 = \frac{3p^2}{\lambda_A^2}\,,$$

$$\beta_1^0 = 0\,, \qquad \beta_1^1 = \frac{p^2 + \lambda_q^2}{\lambda_A^2}\,, \qquad \beta_1^2 = \frac{-3p^2}{\lambda_A^2}\,. \tag{A.102}$$

The Dirac part of the momentum integral is finite, which reflects the fact that the one-loop anomalous dimension vanishes in the Landau gauge,

$$\sum_{i=0}^{3} \frac{\alpha_i^1 + \beta_i^1}{i+1} = 0\,. \tag{A.103}$$

Note that the loop integral is not finite beyond the one-loop approximation, and the respective divergence is carried by the spectral integral. This divergence and the one of the scalar part are cancelled by the BPHZ-subtraction in eq. (5.21), using the spectral BPHZ-scheme introduced in [54]. Within this scheme, the renormalised self energy follows as

$$\begin{aligned}\Sigma_q^{\mathrm{ren}}(p) =& g_s^2\, C_f Z_1 \int\limits_{\lambda_q,\lambda_A} \lambda_A\, \bar{\rho}_A(\lambda_A)\rho_q(\lambda_q)\\ &\times \left\{ \mathrm{i}\not{p}\Big(I_1^{(d)}(p,\lambda_A,\lambda_q) - I_1^{(d)}(\mu_r,\lambda_A,\lambda_q)\Big) + \lambda_q \Big(I_1^{(s)}(p,\lambda_A,\lambda_q) - I_1^{(s)}(\mu_r,\lambda_A,\lambda_q)\Big)\right\},\end{aligned} \tag{A.104}$$

with

$$I_1^{(s)}(p,\lambda_A,\lambda_q) = -\frac{3}{(4\pi)^2} f_0\,, \qquad I_1^{(d)}(p,\lambda_A,\lambda_q) = \frac{1}{(4\pi)^2}\sum_{i=0}^{3}(\alpha_1^i f_i + \beta_1^i g_i)\,. \tag{A.105}$$

The inverse Wick rotation is done analytically and the imaginary parts of the self energy read

$$\begin{aligned}\mathrm{Im}\, I_1^{(s)}(-\mathrm{i}\omega^+,\lambda_A,\lambda_q) &= \frac{\mathrm{sign}(w) 3\lambda_q}{16\pi}\theta(\omega-\lambda_A-\lambda_q)\frac{\xi_{\mathrm{cut}}}{\omega^2}\,,\\ \mathrm{Im}\, I_1^{(d)}(-\mathrm{i}\omega^+,\lambda_A,\lambda_q) &= \frac{\mathrm{sign}(w)}{16\pi}\left[\theta(\omega-\lambda_q)\frac{\left(\lambda_q^2-\omega^2\right)^3}{2\lambda_A^2\omega^4} + \theta(\omega-\lambda_A-\lambda_q)\frac{\xi_{\mathrm{cut}} l_1}{2\lambda_A^2\omega^4}\right],\end{aligned} \tag{A.106}$$

with

$$\begin{aligned}\xi_{\mathrm{cut}} &= \sqrt{(\omega^2-(\lambda_q+\lambda_A)^2)(\omega^2-(\lambda_q-\lambda_A)^2)}\,,\\ l_1 &= \Big(\lambda_q^4 - 2\lambda_A^4 + \lambda_A^2\omega^2 + \omega^4 + \lambda_q^2(\lambda_A^2 - 2\omega^2)\Big)\,.\end{aligned}$$

A.5. Spectral integrands for the pions DA and LFWF

In this appendix, we give some more details on the analytic computation of the spectral integrand in (5.38). As discussed in the main text, for $0 < x < 1$ one can allways close the contour either in the upper half plane around r_q or in the lower one around $r_{\bar{q}}$. Which half-plane to choose is determined by the location of the third pole

$$r_\pi = \mathrm{i}\, \frac{m_\pi^2(4x - (z-1)^2) + 4(q_\perp^2 + \beta'^2)}{4m_\pi(z - 1 + 2x)}\,, \tag{A.107}$$

where one simply chooses the half-plane that excludes it. For $\beta' > m_\pi$, which is certainly the case for the Pion BSA, the numerator is allways positive and $\mathrm{Im}\, r_\pi \gtrless 0$ if $z-1+2x \gtrless 0$. With the residue theorem, the frequency integral evaluates to

$$\begin{aligned}\frac{1}{16\pi^3} I_\psi &= \int_{-\infty}^{\infty} dp_0\, \frac{\mathrm{i}\,(\lambda_1(x-1) - \lambda_2 x)}{4m_\pi^2 x(x-1)(2x-1+z)(q_0 - r_q)(q_0 - r_{\bar{q}})(q_0 - r_\pi)} \\ &= \theta(1-2x-z) I_\psi^q - \theta(z-1+2x)\theta(1-2x-z) I_\psi^{\bar{q}}\,,\end{aligned} \tag{A.108}$$

and the residues (including the winding number and a factor $2\pi\mathrm{i}$) take the simple form

$$I_\psi^{q/\bar{q}} = \frac{a_{q/\bar{q}}}{(q_\perp^2 + b_{q/\bar{q}})(q_\perp^2 + c_{q/\bar{q}})}\,, \tag{A.109}$$

with the coefficients

$$a_q = \frac{(4x(\lambda_1(-1+x) - \lambda_2 x))}{(-1+z)}\,, \qquad a_{\bar{q}} = \frac{4(1-x)(\lambda_1(-1+x) - \lambda_2 x)}{1+z}\,,$$

$$b_q = -\lambda_1^2(-1+x) + (\lambda_2^2 + m_\pi^2(-1+x))x\,, \qquad b_{\bar{q}} = b_q\,,$$

$$c_q = \frac{2\lambda_1^2(-1+2x+z) - x(4\beta^2 - m_\pi^2(-1+z)(-1+2x+z))}{2(-1+z)}\,, \quad c_{\bar{q}} = c_q\,.$$

The remaining $p_\perp$-integral over (A.109) can be carried out analytically and yields

$$\mathcal{I}_\phi^{q/\bar{q}} = \frac{1}{16\pi^3} \int d^2 p_\perp I_\psi^{q/\bar{q}} = \pi \frac{a_{q/\bar{q}} \left(\log b_{q/\bar{q}}^2 - \log c_{q/\bar{q}}^2\right)}{b_{q/\bar{q}}^2 - c_{q/\bar{q}}^2}\,. \tag{A.110}$$

We close this Appendix by checking the asymptotic limit of the PDA. If we consider a vanishing pion mass, classical quarks with mass M and the corresponding minimal weight function to satisfy the axial-vector WTI $\rho_\pi(\beta, z) \propto \delta(\beta - M)(1 - z^2)$, see also the model in [275], the integrand simplifies significantly, $b_{q/\bar{q}} = c_{q/\bar{q}} = M^2$ and the LFWF reads

$$\begin{aligned}\psi(x) &\propto \frac{4M\tilde{\mathcal{N}}}{(p_\perp^2 + M^2)^2} \int_{-1}^{1} dz \left(\frac{\theta(1-2x-z)x(1-z^2)}{1-z} + \frac{\theta(z-1+2x)(1-x)(1-z^2)}{1+z} \right) \\ &= \frac{8M\tilde{\mathcal{N}} x(1-x)}{(p_\perp^2 + M^2)^2}\,.\end{aligned} \tag{A.111}$$

The integration over the transverse momentum factorises from the x-dependence and normalisation to one leads to the asymptotic form of the PDA, $\phi_\pi(x) = 6x(1-x)$.

A.6. Technical details and numerics

In this appendix, we provide addtional information on the numerical implementation of each project. This includes individually the numerical implementation of the spectral fRG for the scalar field theory in Appendix A.1 and Appendix A.6.2, were we distinguish the flows far away and close to the phase transition. The details on the implementation of the spectral DSE-BSE system are discussed in Appendix A.6.3. We then proceed with the spectral flows in asymptotic gravity Appendix A.6.4, and provide the details on the solution of the quark gap equation in Appendix A.6.5.

A.6.1. Scalar spectral flows

This section is dedicated to the numerical solution of the flow equation. First, we rewrite the leading contributions as scale derivatives and integrate by parts in k-direction. This allows to flow the non-analyticities at the respective onset positions analytically, see (A.113). We will make use of this relation to define consistent initial conditions in the UV. The second part explains the numerical algorithm we used to obtain the results given in Section 4.1.6.

A.6.1.1. Leading order and initial conditions

Inserting (4.14) in (A.1), we find all combinations of poles and tails we have to integrate over. The leading order is given by the contribution of δ-functions only and is already present on the classical level. To study the structure of the flow and the dependency of the result of the initial condition, we first note that certain contributions of the Callan-Symanzik flow can be rewritten in terms of a scale derivative. This is possible for every contribution to the Callan-Symanzik flow that carries only pole contributions on the two lines surrounding the (modified) regulator insertion in Figure 4.5. This allows us to integrate the flow by parts, which reduces the degree of divergence of potential integrable singularities and simplifies the numerical treatment. To this end, we rewrite the (modified) fRG polarisation diagram at leading order as

$$I_{\text{pol}}(m_{\text{pole}}, m_{\text{pole}}, m_{\text{pole}}, p^2) = -\frac{1}{8k}\partial_k \tilde{I}_{\text{pol}}(m_{\text{pole}}, m_{\text{pole}}, p^2)\,, \tag{A.112}$$

where the factor $1/4k$ follows from the k-derivative of the spectral kernel with $\partial_k m_{\text{pole}}^2 = 4k$ and another factor 1/2 accounts for the double counting from hitting both arguments in k with the derivative. This connects both polarisation type momentum structures, I_{pol} and $\tilde{I}_{\text{pol}}$, given in (A.3b). Evaluating every spectral parameter on the mass pole we can integrate the combined contribution of the polarisation and fish diagram to arrive at

$$\begin{aligned}\left[\Gamma^{(2)}(p^2)\right]_\Lambda^k &= \int_\Lambda^k \frac{dk}{k}\,\frac{(\Gamma_k^{(3)})^2}{Z_\phi^2}\left(-\frac{\dot{\mathcal{R}}}{8Z_\phi k}\partial_k + \frac{A}{\phi_0}\right)\tilde{I}_{\text{pol}}(p^2)\\ &= \left[-\mathcal{F}(k)\tilde{I}_{\text{pol}}(p^2)\right]_\Lambda^k + \int_\Lambda^k \frac{dk}{k}\mathcal{L}(k)\tilde{I}_{\text{pol}}(p^2)\,,\end{aligned} \tag{A.113}$$

where we summarised the prefactors of the fRG polarisation diagram and the prefactors from the t-integral as

$$\mathcal{F}(k) = \frac{\dot{\mathcal{R}}\,(\Gamma_k^{(3)})^2}{8\,Z_\phi^3\,k^2}\left[\frac{(2-\eta_\phi)}{4} + \frac{\mathcal{S}}{Z_\phi}\right]\frac{(\Gamma_k^{(3)})^2}{Z_\phi^2}\,, \tag{A.114}$$

with

$$\mathcal{S} = \frac{3}{16}\,\frac{m_{\text{curv}}^2}{k^2}\left(\frac{\partial_t \Delta m_{\text{curv}}^2}{m_{\text{curv}}^2} + \frac{\partial_t \Gamma^{(4)}}{\Gamma^{(4)}}\right)\,. \tag{A.115}$$

The boundary term will be the leading contribution. At one-loop order, i.e. $Z_\phi = 1$ and $\Gamma^{(4} = \lambda_\phi$, $\mathcal{S}$ vanishes identically and $\mathcal{F}$ reduces to $\frac{1}{2}(S^{(3)})^2$, which is the prefactor of the one-loop polarisation diagram times the squared classical three-vertex. The factor in the remaining integral reads

$$\begin{aligned}
\mathcal{L}(k) &= \left(\partial_t \mathcal{F}(k) + \frac{A}{\phi_0}\frac{(\Gamma_k^{(3)})^2}{Z_\phi^2}\right)\\
&= \left\{\frac{(2-\eta_\phi)}{4}\frac{\partial_t\Gamma^{(4)}}{\Gamma^{(4)}} - \frac{(2-\eta_\phi)}{2}\eta_\phi + \frac{\dot{\eta}_\phi}{4} - \frac{\eta_\phi\,\partial_t m_{\text{curv}}^2}{4m_{\text{curv}}^2}\right.\\
&\quad \left. + \frac{1}{Z_\phi}\left[\partial_t\mathcal{S} + \mathcal{S}\left(3\eta_\phi + \frac{\partial_t m_{\text{curv}}^2}{m_{\text{curv}}^2} + \frac{\partial_t\Gamma^{(4)}}{\Gamma^{(4)}}\right)\right]\right\}\frac{(\Gamma_k^{(3)})^2}{Z_\phi^3}\,,
\end{aligned} \tag{A.116}$$

where the tree-level terms stemming from $\mathcal{F}(k)$ and A cancel exactly. With that, we recover one-loop perturbation theory. Without the additional one-loop structure of the three-point function in (4.19a), i.e. $A = 0$, the remaining tree-level term would spoil the one-loop result.

To discuss the necessity of a consistent initial condition, it is instructive to work out the one-loop result from a spectral fRG perspective. In the large k limit, we can neglect the non-trivial flow of $\Gamma^{(2)}(p=0)$ and Z_ϕ, leading to $Z_\phi = 1$ and $(\Gamma_k^{(3)})^2 = 3\lambda m_{\text{pole}}^2$ with $m_{\text{pole}}^2 = 2k^2$. Equation (A.113) is then readily integrated and reduces to

$$\Gamma_{\text{1-loop}}^{(2)}(p^2)\big|_k = \Gamma^{(2)}(p^2)\big|_\Lambda + 3\lambda_\phi\left[k^2\tilde{I}_{\text{pol}}(\sqrt{2}k, \sqrt{2}k, p^2)\right]_k^\Lambda\,. \tag{A.117}$$

With a classical initial condition, (A.117) leads to

$$\Gamma_{\text{1-loop}}^{(2)}(p^2)\big|_k = p^2 + \frac{3\lambda_\phi}{2}\left[2k^2\tilde{I}_{\text{pol}}(\sqrt{2}k, \sqrt{2}k, p^2)\right]_k^\Lambda\,. \tag{A.118}$$

Performing the Wick rotation of (A.118) and extracting the spectral function with (3.7), we find that the one-loop scattering contribution to the spectral function is discontinuous at $\omega = 2\sqrt{2\Lambda^2} = 2m_{\text{pole}}^\Lambda$ and turns negative for larger spectral values. Clearly, leading order information is lost above the initial onset scale and can not be recovered by the flow. Even worse, for higher frequencies than $2m_{\text{pole}}^\Lambda$, the positivity of the spectral function is violated. This is cured by using RG-consistent initial conditions, which appears to be crucial to obtain a physical spectral function from the flow. To that end, we require the solution to be independent of the initial scale Λ. This can be achieved, by sending the

Λ/λ_ϕ	$\Gamma^{(3)}$ $[\lambda_\phi^{\frac{3}{2}}]$	Z_ϕ
10	17.3084	1.0007

Table A.1.: Initial conditions obtained from (A.119). We measure the initial RG-scale Λ in units of the coupling and every other quantity in units of the mass.

initial scale to infinity, corresponding to an initial condition that cancels the Λ dependence trivially. This is done by choosing the initial condition to be an iterative solution of

$$\Gamma^{(2)}[p^2, Z_\phi, \Gamma^{(3)}, m_{\text{pole}}] = m_{\text{pole}}^2 + p^2 - \frac{1}{2}\frac{(\Gamma^{(3)})^2}{Z_\phi^3} \times \left[\tilde{I}_{\text{pol}}(m_{\text{pole}}, m_{\text{pole}}, p^2) - \tilde{I}_{\text{pol}}(m_{\text{pole}}, m_{\text{pole}}, -m_{\text{pole}}^2)\right], \tag{A.119}$$

where the last term accounts for the on-shell renormalisation. As initial guess we use the parameter of the classical effective potential (4.33) and (4.34) with $Z_\phi = 1$ and $m_{\text{pole}}^2 = 2\Lambda^2$. In other words, we choose our initial condition to be compatible with (A.113). Note that with this choice of initial conditions, the loss of leading order information is circumvented at all momentum scales, as all contributions of order $O(\lambda/k)$ are taken into account. The flow is initialised at large cutoff scales, where higher terms in $\lambda_{\text{eff}} = \lambda_\phi/k$ are strongly suppressed. To determine the three-point function dynamically, (A.119) was coupled to the resummed four-point function via (4.33). The initial values for Z_ϕ and $\Gamma^{(3)}$ are presented in Table A.1.

It is left to determine the flow of the vertices and η. These have exact diagrammatic expressions which are in parts necessary to consider. It is convenient to approximate $\partial_t\Gamma^{(4)}$ by the t-derivative of (4.21), where we only consider the contributions of the mass-pole for simplicity. It leads to

$$\begin{aligned}\partial_t\Gamma^{(4)} &\approx \frac{(1-2\eta_\phi)}{Z_\phi^2}\frac{(\Gamma^{(4)})^2}{16\pi\sqrt{2}k}\,,\\ (\partial_t)^2\,\Gamma^{(4)} &\approx \frac{2(\partial_t\Gamma^{(4)})^2}{\Gamma^{(4)}} - \partial_t\Gamma^{(4)} + \frac{(\eta_\phi(1-2\eta_\phi) - \dot{\eta}_\phi)}{Z_\phi^2}\frac{(\Gamma^{(4)})^2}{8\pi\sqrt{2}k}\,.\end{aligned} \tag{A.120}$$

The explicit k-dependences of (A.120) can now be taken into account analytically in (A.113). For η_ϕ we use the definition of Z_ϕ as the residue on the mass-pole

$$Z_\phi = -\partial_{\omega^2}\Gamma^2(\omega^2)\big|_{\omega^2 = m_{\text{pole}}^2}\,. \tag{A.121a}$$

With the parametrisation of the real part of the inverse propagator as

$$\Gamma^{(2)}(\omega^2) = Z(\omega)\left(m_{\text{pole}}^2 - \omega^2\right)\,, \tag{A.121b}$$

the anomalous dimension η_ϕ is computed conveniently from the momentum derivative of the flow on the mass-pole,

$$\eta_\phi = \frac{1}{Z_\phi}\partial_{\omega^2}\frac{d}{dt}\Gamma^2(\omega^2)\big|_{m_{\text{pole}}^2} - \frac{1}{Z_\phi}4k^2\partial_{\omega^2}Z(\omega)\big|_{m_{\text{pole}}^2}\,. \tag{A.121c}$$

Only the diagrams of (A.10) contribute due to the momentum derivative. The second term is given in terms of the spectral function:

$$\partial_{\omega^2} Z(\omega)\big|_{\omega^2=m^2_{\text{pole}}} = \frac{1}{Z_\phi}\int_\lambda \frac{\rho(\lambda)}{\lambda^2 - m^2_{\text{pole}}} \,. \tag{A.122}$$

The other parameters such as $\dot{\eta}_\phi$ and $\partial_t \Delta m^2_{\text{curv}}$ where approximated by a numerical right-derivative.

A.6.1.2. Numerical implementation

The numerical implementation uses Mathematica [279]. The leading order contribution to the flow was integrated by means of (A.113), where we split the explicit k-dependencies of each term from the sub-leading running of the respective parameter. This was facilitated by the split of the tree-level curvature mass: $m^2_{\text{curv}} = Z_\phi(2k^2) + \Delta m^2_{\text{curv}}$, as it allowed us to incorporate the tree-level running of the integrand in (A.113) analytically. The sub-leading corrections to the flow-parameter were approximated as constants in each step, while the combined k-dependence of $\tilde{I}_{\text{pol}}$ and the tree-level k-dependence of m^2_{curv} and $\partial_t \Gamma^{(4)}$ was integrated analytically.

For the one-cut contributions, including the tadpole, we approximated the k-integral by an explicit Euler scheme. For the sake of computation time, higher dimensional spectral integrals where dropped as they were numerically negligible in the considered coupling range in comparison to the leading order and next to leading order contributions. For an investigation of the scaling limit, their incorporation is crucial. The numerical integrations of spectral integrals were carried out using a global adaptive integration strategy. All contributions to diagrams were calculated and interpolated separately, where we used finer grids around sharp structures and more coarse grids where the functions are smooth. We implemented a local feedback of the spectral function with a step size $dk = 0.005$, using the spectral function ρ to calculate $\partial_t \Gamma^{(2)}$. The correct renormalisation was enforced conveniently in every step by subtracting the value of the inverse propagator on the mass pole. The residue on the pole was extracted from $\Gamma^{(2)}(p)$ in each step via (A.121a).

A.6.2. Scaling-Limit of scalar spectral flows

This section is dedicated to the numerical solution of the flow equation toward the scaling limit.

In this Appendix, we provide some technical details on the numerical solution of the spectral flow equation.

A.6.2.1. Numerical implementation

The numerical implementation uses Julia [280]. The two-point function (and therefore the spectral function) was calculated on a logarithmic momentum grid, which over the course of the flow was expanded to include lower momenta. To interpolate the values, we used a third order spline for the double-logarithmic values above the onset. The integrals over these functions were solved using Gaussian quadrature with a logarithmic substitution, because the prominent features of the spectral functions were several orders of magnitude smaller than the integration region. Wherever possible, singularities were subtracted and solved analytically.

We solved the flow equation (4.27) using a Runge-Kutta method of third order with a step size $\Delta \log_{10}(k/\lambda_\phi) = 0.005$. Flowing in $\log_{10}(k)$ allowed us to keep a constant step size over the whole flow.

A.6.2.2. Initial condition

To solve the flow of $\Gamma^{(2)}$, we need a starting condition. At a sufficiently high mass scale Λ, we can approximate $\Gamma^{(2)}$ using (RG-improved) perturbation theory, where we only consider the leading order corrections. The first relevant diagram is the sunset diagram with classical propagators and vertices at two-loop-level, since the constant tadpole is absorbed in the renormalisation condition. Therefore, the initial value for the two-point function $\Gamma^{(2)}_\Lambda$ is

$$\Gamma^{(2)}_\Lambda(\omega) = m^2_{\text{pole}} - \omega^2 - \frac{1}{6}\left[D_{\text{sun}}(\omega) - D_{\text{sun}}(m_{\text{pole}})\right] , \tag{A.123}$$

with the sunset diagram on two-loop level

$$D_{\text{sun}}(\omega) = \frac{1}{Z^3_{\phi,\Lambda}} \frac{1}{(4\pi)^2} \left[\frac{1}{2}\log\left(\frac{1}{(3m_{\text{pole}})^2 - \omega^2}\right) - \frac{3m_{\text{pole}}}{\omega}\text{artanh}\left(\frac{\omega}{3m_{\text{pole}}}\right)\right] \tag{A.124}$$

This formula is taken from [54]. The initial residue $\frac{1}{Z_{\phi,\Lambda}}$ was computed iteratively from the sumrule. This leads to an RG-improved two-loop form for the initial condition, which fixes the initial values for the spectral tail and Z_ϕ.

A.6.2.3. Sum rule

At each step of the flow we calculate the flow of the non-trivial part of the two-point function $\partial_t \Pi_k(\omega)$ as well as $\partial_t Z_\phi$ to calculate the corresponding values at the next step. The former is defined as

$$\Gamma^{(2)}(\omega) \equiv k^2 - \omega^2 + \Pi_k(\omega) \tag{A.125}$$

In the deep IR, the finite numerical precision leads to small, numerical deviations from the sum rule, which, if not corrected, can build up to destabilize the flow. To ensure that the sum rule is always fulfilled, we rescale the spectral tail of the propagator by a factor

$$r = \frac{1 - \frac{1}{Z_\phi}}{\int_\lambda \tilde{\rho}(\lambda)} \,. \tag{A.126}$$

This leads to a change in Π_k by

$$\Pi_k(\omega) \to \left(\frac{1}{r} - 1\right)(k^2 - \omega^2) + \frac{1}{r}\Pi_k(\omega). \tag{A.127}$$

A.6.3. Scalar bound state

In this appendix, we discuss the numerical implementation of the DSE-BSE system in Section 4.2.

A.6.3.1. Spectral convolution

Here we describe a method used to effectively compute spectral integrals even in the large coupling limit where one has an increased weight of the spectral tail.

Suppose one has a 2-dimensional spectral integral over two spectral functions which are not necessarily the same,

$$\Pi_j(\omega) = \int_0^\infty \int_0^\infty \frac{\mathrm{d}\lambda_1 \mathrm{d}\lambda_2}{\pi^2} \lambda_1 \lambda_2 \rho_1(\lambda_1) \rho_2(\lambda_2) I_j(\omega, \lambda_1, \lambda_2) \,, \tag{A.128}$$

but with a diagram (such as the polarisation diagram) which solely depends on the sum of the spectral weights: $I_j(\omega, \lambda_1, \lambda_2) = I_j(\omega, \lambda_1 + \lambda_2)$. Then, a change of variables $\eta = \lambda_1 + \lambda_2$ and a reparametrisation of the region of integration transforms this into a one-dimensional spectral integral

$$\Pi_j(\omega) = \int_0^\infty \frac{\mathrm{d}\eta}{\pi} \eta \rho_{12}(\eta) I_j(\omega, \eta) \,, \tag{A.129}$$

over a new spectral function, which is given by the convolution of the two initial spectral functions,

$$\rho_{12}(\eta) = \frac{\pi}{\eta} \int_0^\eta \frac{\mathrm{d}\lambda_2}{\pi^2} (\eta - \lambda_2) \lambda_2 \rho_1(\eta - \lambda_2) \rho_2(\lambda_2). \tag{A.130}$$

This transforms a two-dimensional spectral integral into a one-dimensional integral over a convolution of the spectral function constituents, which we call spectral convolution. The convolution of spectral functions inherits all of the basic properties of the convolution. For a basic decomposition of the form

$$\rho_i(\lambda_i) = \frac{\pi}{\lambda_i} Z_i \delta(\lambda_i - m_i) + \tilde{\rho}_i(\lambda_i) \,, \tag{A.131}$$

the spectral convolution results in

$$\begin{aligned} \rho_{12}(\eta) = {} & \frac{\pi}{\eta} Z_1 Z_2 \delta(\eta - m_1 - m_2) + \frac{\eta - m_1}{\eta} Z_1 \tilde{\rho}_2(\eta - m_1) \\ & + \frac{\eta - m_2}{\eta} Z_2 \tilde{\rho}_1(\eta - m_2) + \tilde{\rho}_{12}(\eta) \,, \end{aligned} \tag{A.132}$$

where $\tilde{\rho}_{12}(\eta)$ is the convolution of the tails following from (A.130). Thus, the spectral convolution has the same decomposition of the initial spectral functions in a way which compactifies all of the information of contributing to the spectral integral of its constituents.

The spectral convolution can be easily generalised for three-dimensional spectral integrals of diagrams which depend on the sum of the three spectral weights (such as the sunset) by the repeated convolution of spectral functions, or partially implemented in a diagram which depends on the sum of only some of the spectral weights (such as the squint).

The advantage of this method is that the convolution of the spectral functions does not depend on the diagrams. Thus, it is an integral over smooth functions which can be precomputed and reutilised for any diagram whose components also depend on the sum of two spectral weights. But most importantly, it considerably optimises the numerical implementation of the spectral integrals, because the resolution of the curve of poles in two dimensions, usually given by the equation $\omega = \lambda_1 + \lambda_2$, simplifies to the resolution of a pole at a point $\omega = \eta$.

A.6.3.2. Numerical implementation

In every computation, the spectral integrals were performed with an adaptive quadrature routine with error equal to 1×10^{-8} via the spectral convolution method. The diagrams and spectral functions were computed for a finite sampling of points on two intervals: One small interval $(0, b)$ for a medium sbehaviourd b which gave us the momentum features in detail, and another bigger interval (b, c) which gave us the correct weight of the corresponding UV tail. The sampling on the first interval was performed with an adaptive parallel function evaluation algorithm, whereas the sampling of the UV tail was performed on a logarithmic grid. We generally chose the values $b = 20m$ and $c = 10\lambda_\phi + 1000m$, for which an accurate interpolation of the momentum features and the UV tail was obtained. The only exception was the spectral function of the 4-point function, for which $b = \max(20m, \lambda_\phi/2)$ needed to be taken while still leaving the same value for c. For the first interval we chose a sampling of 200 points for both spectral functions, 120 for the polarization and 100 for the sunset and tadpole diagrams. For the second interval we used 100 points for all of the objects. With the aforementioned sampling, all of the objects were interpolated with a piecewise cubic Hermite interpolating polynomial which both ensures smoothness and a monotonous tail for monotonous data, which is important in the UV with a logarithmic spacing.

The process of iterating the spectral function and vertices back into the DSE was made until all of the parameters Z, m_{cur}/m, Γ_4/m, $\Gamma_3/m^{3/2}$ and $\phi_0/\sqrt{m}$ had a relative change no greater than 0.2×10^{-3} between iterations. This leads to our conservative estimate for the numerical error of the order of 10^{-2} for our results.

The computation of the BSE matrix was performed on a discretised momentum grid of $(N_X, N_Z, N_x, N_z) = (40, 40, 40, 40)$ points. The root finding algorithm for solving (4.75) was implemented with an accuracy of 1×10^{-3} for M/m. The use of finer grids for the BSE matrix did not change the value of the resulting mass within this level of accuracy. Nevertheless, coming from the estimated numerical error of our DSE computations, we expect our final results to have an error of 10^{-2}.

As a consistency check we computed the sum rule (integral of the spectral function) for each value of the coupling and each DSE truncation; this is shown in Figure A.6. We obtain deviations no bigger than 3×10^{-3} from the theoretical result, which means that the spectral sum rule is satisfied within the estimated numerical error of 10^{-2}.

A.6.4. Spectral Gravity

This section contains the technical details for the graviton spectral function in Section 4.3.

A.6.4.1. Higher order spectral kernels

Flow diagrams for correlation functions always contains a regulator line of the form

$$G(q)\dot{R}_k(q)G(q) = 2k^2 G(q)^2 \,. \tag{A.133}$$

where we already inserted the CS-regulator used throughout this work. While the usual KL-representation of the propagator would lead to two spectral integrals, we can simplify the flow equation and reduce the dimensionality of the spectral integration by expressing the regulator line in terms of one spectral integral. One can show that if the propagator fullfill a spectral representation, this holds for it's square as well and we can write

$$G^2(q) = \int_0^\infty \frac{d\lambda\,\lambda}{\pi} \frac{\rho(\lambda)}{q^2+\lambda^2} \,. \tag{A.134}$$

While this is in principal possible, it complicates the spectral renormalisation as it increases the superficial degree of divergence of the momentum integrals after changing the order of integration. Instead, we resort to a higher order kernel:

$$G^2(q) = \int_0^\infty \frac{d\lambda\,\lambda}{\pi} \frac{\rho^{(2)}(\lambda)}{(q^2+\lambda^2)^2} \,, \qquad \partial_{w^2}\rho^{(2)}(w) = 2\,\mathrm{Im}\, G^2\left(-\mathrm{i}(w+\mathrm{i}0^+)\right) \,. \tag{A.135}$$

Note that the Cauchy-Principal value of this integral for $q^2 < -\lambda_{\min}$ does not exist if the pole of the integrand is inside the integral domain, instead it is defined by the corresponding Hadamart finite part, or equivalently via an integration by parts which transforms the integral back to the usual spectral representation. By inserting the spectral representation of the propagator of the form eq. (4.94), we can decompose the imaginary part of G^2 as follows:

$$\begin{aligned}\mathrm{Im}\, G^2(q) =& \frac{1}{Z_h^2}\Bigg(\pi\partial_{w^2}\delta(m_h^2-w^2) - \frac{f_h(w)\Theta(w-2m_h)}{w^2-m_h^2} \\ & + \delta(m_h^2-w^2)\int_{2m_h}^\infty d\lambda^2 \frac{f_h(\lambda)}{(\lambda^2-m_k^2)} - \int_{2m_k}^\infty \frac{d\lambda^2}{2\pi}\frac{f_h(\lambda)f_h(w)}{w^2-\lambda^2}\Bigg) \,. \end{aligned} \tag{A.136}$$

The first and the third term can be integrated analytically to obtain $\rho^{(2)}(w)$, while the second and the fourth are taken care of numerically. This leads to a delta peak at $w = m_h$ and a constant but non-zero term for $m_h < w$, which carries the nonsingular real part of the propagator on the pole as a prefactor. This constant contribution gets subtracted for $w > 2m_h$ by the integrated second term. Both terms cancel exactly in the weight function as w approaches infinity.

A.6.4.2. Numerical implementation

To solve the flow-equation of the graviton spectral function, we employ a fix point itteration. The flow-equation is hence, interpreted as a integral equation, where the spectral function, ie the propagator on the right hand side is fully known as a function of ω and k. This allows to compute and integrate the diagrams with this input and readout the new fully k-dependent spectral function. One then itterates this procedure untill convergence. We start with an initial guess for the spectral function, which we chose to be the tree-level one, $\rho^{(0)}(w,k) = 2\pi\delta(\omega^2 - k^2)$. The chosen on-shell renormalisation condition eq. (4.96) entails that the delta part of the graviton spectral function remains the same uppon itteration. All numerical routines are implemented in Julia.

The flow of the spectral diagrams is then computed by evaluating the imaginary parts of the diagrams only, which leads to significant simplification of the spectral integrals and avoids precision bounds in the numerical integration. Schematically, we can write

$$\mathrm{Im}\Gamma^{(2)}_{k,i+1}(w) = \int_k^{k_{max}} \frac{dk}{k}\,\mathrm{Im}\,\mathrm{flow}_k[\rho_h^{(i)}](\omega,k)\,. \tag{A.137}$$

The real-part of the integrated diagrams is then obtained by a subtracted Kramers-Kronig relation,

$$\mathrm{Re}\left[f(x) - f(x_0) - (x^2 - x_0^2)\partial_{x^2} f(x_0)\right] = \frac{2}{\pi}\,PV\int_0^\infty d\omega\,\frac{(x^2-x_0^2)^2}{(w^2-x_0^2)^2}\,\frac{\omega\,\mathrm{Im}\,f(\omega)}{\omega^2 - x^2}\,, \tag{A.138}$$

where the subtracted taylor expansion serves two purposes: it renders the Kramers-Kronig integral finite and it allows for an convenient implementation of the on-shell renormalisation condition. The numerical implementation of the Principal Value integral is based on an h-adaptive gauss-kronrod quadrature rule implemented in the quadgk routine of the Julia package QuadGK.jl. The tail of the spectral function is then obtained via

$$\rho_h^{(i+1)}(w,k) = -2\,\frac{\mathrm{Im}\Gamma^{(2)}_{k,i+1}(w)}{\Big(\mathrm{Im}\Gamma^{(2)}_{k,i+1}(w)\Big)^2 + \Big(\mathrm{Re}\Gamma^{(2)}_{i+1}(w,k)\Big)^2}\,. \tag{A.139}$$

where $\mathrm{Re}\Gamma^{(2)}_{i+1}(w,k)$ also contains the term $k^2 - w^2$, where $-w^2$ is the frequency dependence of the (classical) initial condition and k^2 is the regulator. This procedure is then itterated until we reach $\rho_h^{(i+1)} = \rho_h^{(i)}$ withhin the numerical precision. For the feedback of the spectral tail, we use the same adaptive quadrature rule as for the Kramers-Kronig integral for the one dimensional spectral integrals and the "hcubature" routine of the Cubature.jl package for the respective two dimensional spectral integrals, where a simple change of variables is neccecary to avoid the evaluation of the integrands at the singular points given by $\lambda_1 + \lambda_2 = \omega$. For the one dimensional integrals, we specify a relative tolerance of 10^{-10} with a fixed integration order of 20, while the two dimensional integrals are computed with a relative tolerance of 10^{-4} as their contributions are typically subleading. The absolute tolerance is set to 0 in all cases.

A.6.5. Numerical implementation of the quark gap equation

In this Appendix, we discuss the numerical solution of the spectral gap equation. All numerical calculations have been carried out in Julia 1.10.4 [281]. Numerical integrations are based on q-adaptive quadrature (QuadGK.jl) and cubature rules (HCubature.jl) for one and two-dimensional integrals, respectively. The computation of the self-energy simplifies by using its analytic properties and causal structure. In particular, the Kramers-Kronig relations entail that the real part of the self-energy is up to a constant given by a principal value integral over its imaginary part and vice versa. Hence, we only compute the finite imaginary parts of the self-energy, see (A.104) and (A.106), and use the subtracted Kramers-Kronig relations,

$$\mathrm{Re}\,\Sigma_{d/s}(\omega) - \mathrm{Re}\,\Sigma_{d/s}(\mathrm{i}\mu_r) = \ \mathrm{PV} \int_0^\infty dt \frac{2t}{\pi} \frac{(\mu_r^2+\omega^2)\mathrm{Im}\,\Sigma_{d/s}(t)}{(t^2+\mu_r^2)(t^2-\omega^2)}\,. \tag{A.140}$$

In (A.140) we imposed the Euclidean renormalisation condition at $\mathrm{i}\mu_r$. For the numerical integration, we use a fixed but non-linear grid in the variable $\log_{10}[(w - m_{\mathrm{pole}})/\mathrm{GeV}]$ in the range $[-3, 2]$. It is constructed by choosing a grid-spacing of polynomial form with a cubic and linear term to achieve a higher resolution around the peaked structure of the self energies induced by the peak of the effective coupling. The non-linear transformation of the grid is easily inverted for applying standard cubic interpolation methods on a linearly spaced grid, and we use 400 points in frequency direction for the imaginary part of the self energy. The numerical implementation of the Kramers-Kronig relations require an extrapolation of the imaginary parts beyond the grid points. A discontinuity of the integrand at the boundaries of the integration domain leads to a logarithmic divergence of the Principal Value integral at the same scale. For the extrapolation, we use a power-law form. To solve the gap equation, we have employed a fix-point iteration procedure. For an initial enhancement factors $\eta_0 = 0.601$ with a small size of chiral symmetry breaking we initialise the iteration with a classical spectral function

$$\rho_q(\lambda > 0) = \pi\delta(\lambda - m_q)\,, \tag{A.141}$$

and iterate until convergence. For successively larger values of η_{const}, we use the converged solution obtained for the next smaller value of η_{const} as the input. This leads to a rapid convergence of the iteration scheme and starts the iteration in the basin of attraction of the chirally broken solution. Using (A.141) in the presence of a large dynamical chiral symmetry breaking may destabilise the iteration, and we may not start in the basin of attraction of the chirally broken solution.

The onset of the scattering continuum starts exactly at the pole mass. Therefore, a mismatch of pole mass and onset is always present for iteration steps which shift the latter to higher values. This mismatch is regularised by introducing a small shift of the imaginary parts of the self energies at spectral values above the new pole mass. This shift is implemented by cutting off the remnants of the pole at $m_{\mathrm{pole}} + \gamma$, where the width γ is given by the absolute value of the imaginary part of the mass function on the pole. The final spectral function is then approached in the limit $\gamma \to 0$.

Acknowledgments

First and foremost, I would like to thank Jan M. Pawlowski for the supervision of my PhD, his advice, and collaboration. I have learned a lot during countless discussions and have benefited from the scientific and professional insights he is always open to share. I have greatly appreciated his open-door policy and the amount of time and effort he was willing to spend to support me, while giving me the freedom to pursue my research interests.

Furthermore, I would like to thank Joerg Jaeckel for agreeing to be my second referee.

Many thanks go to my collaborators, whom I have enjoyed working with over the past years and who have contributed to my scientific knowledge.

I would like to thank all my colleagues at the ITP in Heidelberg, with whom I had a lot of fun discussing physics and all kinds of arbitrary topics during my time in the basement office. Special mention should go to Álvaro Pastor-Gutiérrez, Chuang Huang, Victoria Noel, Marc Bauer, Renzo Kapust, Konrad Kockler, and of course my officemates Franz Sattler, Friederike Ihssen, and Jan Horak.

Special thanks also go to my former math and physics teacher, Matthias Hauck, without whom I would most likely not have studied physics.

Lastly, I would like to thank my friends and family — in particular my parents, who have always supported me in pursuing my interests, and my girlfriend Laura for her constant emotional support, throughout my PhD and, most importantly, during its final stage.

Bibliography

[1] J. Braun *et al.*, "Renormalised spectral flows," SciPost Phys. Core 6, 061 (2023), arXiv:2206.10232 [hep-th].

[2] G. Eichmann, A. Gómez, J. Horak, J. M. Pawlowski, J. Wessely, and N. Wink, "Bound states from the spectral Bethe-Salpeter equation," Phys. Rev. D 109, 096024 (2024), arXiv:2310.16353 [hep-ph].

[3] J. Horak, F. Ihssen, J. M. Pawlowski, J. Wessely, and N. Wink, "Scalar spectral functions from the spectral functional renormalization group," Phys. Rev. D 110, 056009 (2024), arXiv:2303.16719 [hep-th].

[4] J. M. Pawlowski and J. Wessely, "The causal structure of the quark propagator," (2024), arXiv:2412.12033 [hep-ph].

[5] K. Kockler, J. M. Pawlowski, and J. Wessely, "Critical scaling for spectral functions," unpublished (2025), in preparation.

[6] J. M. Pawlowski, M. Reichert, and J. Wessely, "Self-consistent graviton spectral functions," unpublished (2025), in preparation.

[7] C. Huang, J. M. Pawlowski, and J. Wessely, "Light-front PDAs from (spectral) functional methods," unpublished (2025), in preparation.

[8] J. Braun, Y.-r. Chen, W.-j. Fu, F. Gao, A. Geissel, C. Huang, F. Ihssen, J. M. Pawlowski, F. Rennecke, F. Sattler, B. Schallmo, Y.-y. Tan, S. Töpfel, R. Wen, J. Wessely, S. Yin, N. Zorbach, and K. Jamaly, fQCD collaboration (2024).

[9] F. Gross *et al.*, "50 Years of Quantum Chromodynamics," Eur. Phys. J. C 83, 1125 (2023), arXiv:2212.11107 [hep-ph].

[10] Y. Akiba *et al.*, "The Hot QCD White Paper: Exploring the Phases of QCD at RHIC and the LHC," (2015), arXiv:1502.02730 [nucl-ex].

[11] A. Andronic, P. Braun-Munzinger, K. Redlich, and J. Stachel, "Decoding the phase structure of QCD via particle production at high energy," Nature 561, 321 (2018), arXiv:1710.09425 [nucl-th].

[12] X. Luo and N. Xu, "Search for the QCD Critical Point with Fluctuations of Conserved Quantities in Relativistic Heavy-Ion Collisions at RHIC : An Overview," Nucl. Sci. Tech. 28, 112 (2017), arXiv:1701.02105 [nucl-ex].

[13] L. Adamczyk *et al.* (STAR), "Bulk Properties of the Medium Produced in Relativistic Heavy-Ion Collisions from the Beam Energy Scan Program," Phys. Rev. C 96, 044904 (2017), arXiv:1701.07065 [nucl-ex].

[14] C. Höhne (CBM), “Status of the CBM experiment at FAIR,” EPJ Web Conf. 296, 08004 (2024).

[15] R. Baier and P. Romatschke, “Causal viscous hydrodynamics for central heavy-ion collisions,” Eur. Phys. J. C 51, 677 (2007), arXiv:nucl-th/0610108.

[16] B. Schenke, S. Jeon, and C. Gale, “(3+1)D hydrodynamic simulation of relativistic heavy-ion collisions,” Phys. Rev. C 82, 014903 (2010), arXiv:1004.1408 [hep-ph].

[17] E. D. Bloom *et al.*, “High-Energy Inelastic e p Scattering at 6-Degrees and 10-Degrees,” Phys. Rev. Lett. 23, 930 (1969).

[18] M. Breidenbach, J. I. Friedman, H. W. Kendall, E. D. Bloom, D. H. Coward, H. C. DeStaebler, J. Drees, L. W. Mo, and R. E. Taylor, “Observed behavior of highly inelastic electron-proton scattering,” Phys. Rev. Lett. 23, 935 (1969).

[19] J. S. Poucher *et al.*, “High-Energy Single-Arm Inelastic e - p and e - d Scattering at 6-Degrees and 10-Degrees,” Phys. Rev. Lett. 32, 118 (1974).

[20] A. Accardi *et al.*, “Electron Ion Collider: The Next QCD Frontier: Understanding the glue that binds us all,” Eur. Phys. J. A 52, 268 (2016), arXiv:1212.1701 [nucl-ex].

[21] A. C. Aguilar *et al.*, “Pion and Kaon Structure at the Electron-Ion Collider,” Eur. Phys. J. A 55, 190 (2019), arXiv:1907.08218 [nucl-ex].

[22] R. Abir *et al.*, “The case for an EIC Theory Alliance: Theoretical Challenges of the EIC,” (2023), arXiv:2305.14572 [hep-ph].

[23] D. P. Anderle *et al.*, “Electron-ion collider in China,” Front. Phys. (Beijing) 16, 64701 (2021), arXiv:2102.09222 [nucl-ex].

[24] S. D. Drell and T.-M. Yan, “Partons and their Applications at High-Energies,” Annals Phys. 66, 578 (1971).

[25] J. D. Bjorken, “Asymptotic Sum Rules at Infinite Momentum,” Phys. Rev. 179, 1547 (1969).

[26] J. Blumlein, “The Theory of Deeply Inelastic Scattering,” Prog. Part. Nucl. Phys. 69, 28 (2013), arXiv:1208.6087 [hep-ph].

[27] Y. Aoki, G. Endrodi, Z. Fodor, S. Katz, and K. Szabo, “The Order of the quantum chromodynamics transition predicted by the standard model of particle physics,” Nature 443, 675 (2006), arXiv:hep-lat/0611014 [hep-lat].

[28] S. Aoki *et al.* (PACS-CS), “Physical Point Simulation in 2+1 Flavor Lattice QCD,” Phys. Rev. D81, 074503 (2010), arXiv:0911.2561 [hep-lat].

[29] S. Borsanyi *et al.* (Wuppertal-Budapest Collaboration), “Is there still any T_c mystery in lattice QCD? Results with physical masses in the continuum limit III,” JHEP 1009, 073 (2010), arXiv:1005.3508 [hep-lat].

[30] Z. Fodor and C. Hoelbling, “Light Hadron Masses from Lattice QCD,” Rev.Mod.Phys. 84, 449 (2012), arXiv:1203.4789 [hep-lat].

[31] S. Borsanyi *et al.*, “Calculation of the axion mass based on high-temperature lattice quantum chromodynamics,” Nature 539, 69 (2016), arXiv:1606.07494 [hep-lat].

[32] S. Aoki *et al.*, “Review of lattice results concerning low-energy particle physics,” Eur. Phys. J. C77, 112 (2017), arXiv:1607.00299 [hep-lat].

[33] A. K. Cyrol, M. Mitter, J. M. Pawlowski, and N. Strodthoff, “Nonperturbative quark, gluon, and meson correlators of unquenched QCD,” Phys. Rev. D 97, 054006 (2018), arXiv:1706.06326 [hep-ph].

[34] W.-j. Fu, J. M. Pawlowski, and F. Rennecke, “QCD phase structure at finite temperature and density,” Phys. Rev. D 101, 054032 (2020), arXiv:1909.02991 [hep-ph].

[35] F. Ihssen, J. M. Pawlowski, F. R. Sattler, and N. Wink, “Towards quantitative precision in functional QCD I,” (2024), arXiv:2408.08413 [hep-ph].

[36] W.-j. Fu, C. Huang, J. M. Pawlowski, Y.-y. Tan, and L.-j. Zhou, “Four-quark scatterings in QCD III,” (2025), arXiv:2502.14388 [hep-ph].

[37] C. S. Fischer, “QCD at finite temperature and chemical potential from Dyson–Schwinger equations,” Prog. Part. Nucl. Phys. 105, 1 (2019), arXiv:1810.12938 [hep-ph].

[38] F. Gao and J. M. Pawlowski, “QCD phase structure from functional methods,” Phys. Rev. D 102, 034027 (2020), arXiv:2002.07500 [hep-ph].

[39] F. Gao, J. Papavassiliou, and J. M. Pawlowski, “Fully coupled functional equations for the quark sector of QCD,” Phys. Rev. D 103, 094013 (2021), arXiv:2102.13053 [hep-ph].

[40] G. Eichmann, H. Sanchis-Alepuz, R. Williams, R. Alkofer, and C. S. Fischer, “Baryons as relativistic three-quark bound states,” Prog. Part. Nucl. Phys. 91, 1 (2016), arXiv:1606.09602 [hep-ph].

[41] L. Schlessinger, “Use of Analyticity in the Calculation of Nonrelativistic Scattering Amplitudes,” Phys. Rev. 167, 1411 (1968).

[42] R.-A. Tripolt, I. Haritan, J. Wambach, and N. Moiseyev, “Threshold energies and poles for hadron physical problems by a model-independent universal algorithm,” Phys. Lett. B 774, 411 (2017), arXiv:1610.03252 [hep-ph].

[43] A. K. Cyrol, J. M. Pawlowski, A. Rothkopf, and N. Wink, “Reconstructing the gluon,” SciPost Phys. 5, 065 (2018), arXiv:1804.00945 [hep-ph].

[44] D. Binosi and R.-A. Tripolt, “Spectral functions of confined particles,” Phys. Lett. B 801, 135171 (2020), arXiv:1904.08172 [hep-ph].

[45] J. Horak, J. M. Pawlowski, J. Rodríguez-Quintero, J. Turnwald, J. M. Urban, N. Wink, and S. Zafeiropoulos, “Reconstructing QCD spectral functions with Gaussian processes,” Phys. Rev. D 105, 036014 (2022), arXiv:2107.13464 [hep-ph].

[46] J. M. Pawlowski, C. S. Schneider, J. Turnwald, J. M. Urban, and N. Wink, "Yang-Mills glueball masses from spectral reconstruction," Phys. Rev. D 108, 076018 (2023), arXiv:2212.01113 [hep-ph].

[47] S. Ali, D. Bala, A. Francis, G. Jackson, O. Kaczmarek, J. Turnwald, T. Ueding, and N. Wink (HotQCD), "Lattice QCD estimates of thermal photon production from the QGP," Phys. Rev. D 110, 054518 (2024), arXiv:2403.11647 [hep-lat].

[48] G. Eichmann, P. Duarte, M. T. Peña, and A. Stadler, "Scattering amplitudes and contour deformations," Phys. Rev. D100, 094001 (2019), arXiv:1907.05402 [hep-ph].

[49] G. Eichmann, E. Ferreira, and A. Stadler, "Going to the light front with contour deformations," Phys. Rev. D 105, 034009 (2022), arXiv:2112.04858 [hep-ph].

[50] M. Q. Huber, W. J. Kern, and R. Alkofer, "Analytic structure of three-point functions from contour deformations," Phys. Rev. D 107, 074026 (2023), arXiv:2212.02515 [hep-ph].

[51] L. V. Keldysh, "Diagram technique for nonequilibrium processes," Zh. Eksp. Teor. Fiz. 47, 1515 (1964).

[52] N. Nakanishi, "A General survey of the theory of the Bethe-Salpeter equation," Prog.Theor.Phys.Suppl. 43, 1 (1969).

[53] R. Delbourgo and P. C. West, "A Gauge Covariant Approximation to Quantum Electrodynamics," J. Phys. A 10, 1049 (1977).

[54] J. Horak, J. M. Pawlowski, and N. Wink, "Spectral functions in the ϕ^4-theory from the spectral DSE," Phys. Rev. D 102, 125016 (2020), arXiv:2006.09778 [hep-th].

[55] G. Kallen, "On the definition of the Renormalization Constants in Quantum Electrodynamics," Helv. Phys. Acta 25, 417 (1952).

[56] H. Lehmann, "On the Properties of propagation functions and renormalization contants of quantized fields," Nuovo Cim. 11, 342 (1954).

[57] M. Gell-Mann, "A Schematic Model of Baryons and Mesons," Phys. Lett. 8, 214 (1964).

[58] G. Zweig, "An SU(3) model for strong interaction symmetry and its breaking. Version 1," (1964), 10.17181/CERN-TH-401.

[59] J. D. Bjorken and S. L. Glashow, "Elementary Particles and SU(4)," Phys. Lett. 11, 255 (1964).

[60] S. L. Glashow, J. Iliopoulos, and L. Maiani, "Weak Interactions with Lepton-Hadron Symmetry," Phys. Rev. D 2, 1285 (1970).

[61] M. Kobayashi and T. Maskawa, "CP Violation in the Renormalizable Theory of Weak Interaction," Prog. Theor. Phys. 49, 652 (1973).

[62] O. W. Greenberg, "Spin and Unitary Spin Independence in a Paraquark Model of Baryons and Mesons," Phys. Rev. Lett. 13, 598 (1964).

[63] M. Y. Han and Y. Nambu, “Three Triplet Model with Double SU(3) Symmetry,” Phys. Rev. 139, B1006 (1965).

[64] H. Fritzsch, M. Gell-Mann, and H. Leutwyler, “Advantages of the Color Octet Gluon Picture,” Phys. Lett. B 47, 365 (1973).

[65] C.-N. Yang and R. L. Mills, “Conservation of Isotopic Spin and Isotopic Gauge Invariance,” Phys. Rev. 96, 191 (1954).

[66] D. J. Gross and F. Wilczek, “Asymptotically Free Gauge Theories - I,” Phys. Rev. D 8, 3633 (1973).

[67] H. D. Politzer, “Reliable Perturbative Results for Strong Interactions?” Phys. Rev. Lett. 30, 1346 (1973).

[68] S. Navas *et al.* (Particle Data Group), “Review of particle physics,” Phys. Rev. D 110, 030001 (2024).

[69] A. C. Aguilar, D. Ibanez, V. Mathieu, and J. Papavassiliou, “Massless bound-state excitations and the Schwinger mechanism in QCD,” Phys. Rev. D 85, 014018 (2012), arXiv:1110.2633 [hep-ph].

[70] A. C. Aguilar, M. N. Ferreira, and J. Papavassiliou, “Exploring smoking-gun signals of the Schwinger mechanism in QCD,” Phys. Rev. D 105, 014030 (2022), arXiv:2111.09431 [hep-ph].

[71] M. N. Ferreira and J. Papavassiliou, “Gauge Sector Dynamics in QCD,” Particles 6, 312 (2023), arXiv:2301.02314 [hep-ph].

[72] A. C. Aguilar, F. De Soto, M. N. Ferreira, J. Papavassiliou, F. Pinto-Gómez, C. D. Roberts, and J. Rodríguez-Quintero, “Schwinger mechanism for gluons from lattice QCD,” Phys. Lett. B 841, 137906 (2023), arXiv:2211.12594 [hep-ph].

[73] N. Alkofer and R. Alkofer, “Features of ghost-gluon and ghost-quark bound states related to BRST quartets,” Phys. Lett. B 702, 158 (2011), arXiv:1102.2753 [hep-th].

[74] V. N. Gribov, “Quantization of non-Abelian gauge theories,” Nucl. Phys. B139, 1 (1978).

[75] M. E. Peskin and D. V. Schroeder, *An Introduction to quantum field theory* (Addison-Wesley, Reading, 1995) p. 842.

[76] S. Weinberg, *The quantum theory of fields. Vol. 2: Modern applications* (Cambridge University Press, Cambridge, 1996) cambridge, UK: Univ. Pr. (1996) 489 p.

[77] T. S. Evans, “N point finite temperature expectation values at real times,” Nucl. Phys. B 374, 340 (1992).

[78] J. Bros and D. Buchholz, “Axiomatic analyticity properties and representations of particles in thermal quantum field theory,” Ann. Inst. H. Poincare Phys. Theor. 64, 495 (1996), arXiv:hep-th/9606046 [hep-th].

[79] A. Bonanno, T. Denz, J. M. Pawlowski, and M. Reichert, "Reconstructing the graviton," (2021), arXiv:2102.02217 [hep-th].

[80] J. Horak, J. Papavassiliou, J. M. Pawlowski, and N. Wink, "Ghost spectral function from the spectral Dyson-Schwinger equation," Phys. Rev. D 104 (2021), 10.1103/PhysRevD.104.074017, arXiv:2103.16175 [hep-th].

[81] J. Fehre, D. F. Litim, J. M. Pawlowski, and M. Reichert, "Lorentzian Quantum Gravity and the Graviton Spectral Function," Phys. Rev. Lett. 130, 081501 (2023), arXiv:2111.13232 [hep-th].

[82] R. Oehme and W. Zimmermann, "QUARK AND GLUON PROPAGATORS IN QUANTUM CHROMODYNAMICS," Phys. Rev. D21, 471 (1980).

[83] R. Oehme, "On superconvergence relations in quantum chromodynamics," Phys. Lett. B 252, 641 (1990).

[84] T. Denz, J. M. Pawlowski, and M. Reichert, "Towards apparent convergence in asymptotically safe quantum gravity," (2016), arXiv:1612.07315 [hep-th].

[85] R. Alkofer and L. von Smekal, "The infrared behavior of QCD Green's functions: Confinement, dynamical symmetry breaking, and hadrons as relativistic bound states," Phys. Rept. 353, 281 (2001), arXiv:hep-ph/0007355.

[86] K. G. Wilson, "Renormalization group and critical phenomena. 1. Renormalization group and the Kadanoff scaling picture," Phys.Rev. B4, 3174 (1971).

[87] K. G. Wilson, "Renormalization group and critical phenomena. 2. Phase space cell analysis of critical behavior," Phys.Rev. B4, 3184 (1971).

[88] C. Wetterich, "Exact evolution equation for the effective potential," Phys.Lett. B301, 90 (1993).

[89] J. M. Pawlowski, "Aspects of the functional renormalisation group," Annals Phys. 322, 2831 (2007), arXiv:hep-th/0512261 [hep-th].

[90] S. Floerchinger, "Analytic Continuation of Functional Renormalization Group Equations," JHEP 05, 021 (2012), arXiv:1112.4374 [hep-th].

[91] J. M. Pawlowski and N. Strodthoff, "Real time correlation functions and the functional renormalization group," Phys. Rev. D92, 094009 (2015), arXiv:1508.01160 [hep-ph].

[92] J. M. Pawlowski, N. Strodthoff, and N. Wink, "Finite temperature spectral functions in the O(N)-model," Phys. Rev. D98, 074008 (2018), arXiv:1711.07444 [hep-th].

[93] R.-A. Tripolt, L. von Smekal, and J. Wambach, "Flow equations for spectral functions at finite external momenta," Phys.Rev. D90, 074031 (2014), arXiv:1408.3512 [hep-ph].

[94] K. Symanzik, "Small distance behavior in field theory and power counting," Commun. Math. Phys. 18, 227 (1970).

[95] M. Simionato, "Gauge consistent Wilson renormalization group: Abelian case," Int. J. Mod. Phys. A 15, 2121 (2000), arXiv:hep-th/9809004.

[96] M. Simionato, "Gauge consistent Wilson renormalization group.2. NonAbelian case," Int. J. Mod. Phys. A 15, 2153 (2000), arXiv:hep-th/9810117.

[97] J. Alexandre and J. Polonyi, "Functional Callan-Symanzik equation," Annals Phys. 288, 37 (2001), arXiv:hep-th/0010128.

[98] S. Correia, J. Polonyi, and J. Richert, "Functional Callan-Symanzik equation for the Coulomb gas," Annals Phys. 296, 214 (2002), arXiv:cond-mat/0108048.

[99] J. Alexandre, J. Polonyi, and K. Sailer, "Functional Callan-Symanzik equation for QED," Phys. Lett. B 531, 316 (2002), arXiv:hep-th/0111152.

[100] K. Otto, C. Busch, and B.-J. Schaefer, "Regulator scheme dependence of the chiral phase transition at high densities," Phys. Rev. D 106, 094018 (2022), arXiv:2206.13067 [hep-ph].

[101] J. V. Roth, D. Schweitzer, L. J. Sieke, and L. von Smekal, "Real-time methods for spectral functions," Phys. Rev. D 105, 116017 (2022), arXiv:2112.12568 [hep-ph].

[102] J. M. Pawlowski, M. M. Scherer, R. Schmidt, and S. J. Wetzel, "Physics and the choice of regulators in functional renormalisation group flows," (2015), arXiv:1512.03598 [hep-th].

[103] J. Braun, M. Leonhardt, and J. M. Pawlowski, "Renormalization group consistency and low-energy effective theories," SciPost Phys. 6, 056 (2019), arXiv:1806.04432 [hep-ph].

[104] O. J. Rosten, "Fundamentals of the Exact Renormalization Group," Phys. Rept. 511, 177 (2012), arXiv:1003.1366 [hep-th].

[105] L. Fister, *On the Phase Diagram of QCD with Dynamical Quarks*, Ph.D. thesis, Heidelberg U. (2012).

[106] U. Ellwanger, "Flow equations and BRS invariance for Yang-Mills theories," Phys. Lett. B335, 364 (1994), arXiv:hep-th/9402077.

[107] U. Ellwanger, M. Hirsch, and A. Weber, "Flow equations for the relevant part of the pure Yang-Mills action," Z.Phys. C69, 687 (1996), arXiv:hep-th/9506019 [hep-th].

[108] J. M. Pawlowski, D. F. Litim, S. Nedelko, and L. von Smekal, "Infrared behavior and fixed points in Landau gauge QCD," Phys.Rev.Lett. 93, 152002 (2004), arXiv:hep-th/0312324 [hep-th].

[109] C. S. Fischer and H. Gies, "Renormalization flow of Yang-Mills propagators," JHEP 10, 048 (2004), arXiv:hep-ph/0408089.

[110] J. Braun, H. Gies, and J. M. Pawlowski, "Quark Confinement from Color Confinement," Phys.Lett. B684, 262 (2010), arXiv:0708.2413 [hep-th].

[111] A. K. Cyrol, L. Fister, M. Mitter, J. M. Pawlowski, and N. Strodthoff, "Landau gauge Yang-Mills correlation functions," Phys. Rev. D94, 054005 (2016), arXiv:1605.01856 [hep-ph].

[112] A. K. Cyrol, M. Mitter, J. M. Pawlowski, and N. Strodthoff, "Non-perturbative finite-temperature Yang-Mills theory," (2017), arXiv:1708.03482 [hep-ph].

[113] L. Corell, A. K. Cyrol, M. Mitter, J. M. Pawlowski, and N. Strodthoff, "Correlation functions of three-dimensional Yang-Mills theory from the FRG," SciPost Phys. 5, 066 (2018), arXiv:1803.10092 [hep-ph].

[114] N. Dupuis, L. Canet, A. Eichhorn, W. Metzner, J. M. Pawlowski, M. Tissier, and N. Wschebor, "The nonperturbative functional renormalization group and its applications," Phys. Rept. 910, 1 (2021), arXiv:2006.04853 [cond-mat.stat-mech].

[115] J. Horak, J. M. Pawlowski, and N. Wink, "On the complex structure of Yang-Mills theory," (2022), arXiv:2202.09333 [hep-th].

[116] N. N. Bogolyubov, A. A. Logunov, A. I. Oksak, and I. T. Todorov, *General principles of quantum field theory* (1990).

[117] P. Lowdon, "Non-perturbative constraints on the quark and ghost propagators," Nucl. Phys. B 935, 242 (2018), arXiv:1711.07569 [hep-th].

[118] D. Dudal, O. Oliveira, M. Roelfs, and P. Silva, "Spectral representation of lattice gluon and ghost propagators at zero temperature," Nucl. Phys. B 952, 114912 (2020), arXiv:1901.05348 [hep-lat].

[119] P. Lowdon, "Nonperturbative structure of the photon and gluon propagators," Phys. Rev. D 96, 065013 (2017), arXiv:1702.02954 [hep-th].

[120] P. Lowdon, "Dyson–Schwinger equation constraints on the gluon propagator in BRST quantised QCD," Phys. Lett. B 786, 399 (2018), arXiv:1801.09337 [hep-th].

[121] P. Lowdon, "On the analytic structure of QCD propagators," PoS Confinement2018, 050 (2018), arXiv:1811.03037 [hep-th].

[122] M. Haas, L. Fister, and J. M. Pawlowski, "Gluon spectral functions and transport coefficients in Yang–Mills theory," Phys.Rev. D90, 091501 (2014), arXiv:1308.4960 [hep-ph].

[123] E.-M. Ilgenfritz, J. M. Pawlowski, A. Rothkopf, and A. Trunin, "Finite temperature gluon spectral functions from $N_f = 2 + 1 + 1$ lattice QCD," Eur. Phys. J. C 78, 127 (2018), arXiv:1701.08610 [hep-lat].

[124] D. Dudal, J. A. Gracey, S. P. Sorella, N. Vandersickel, and H. Verschelde, "A Refinement of the Gribov-Zwanziger approach in the Landau gauge: Infrared propagators in harmony with the lattice results," Phys.Rev. D78, 065047 (2008), arXiv:0806.4348 [hep-th].

[125] S. P. Sorella, "Gluon confinement, i-particles and BRST soft breaking," J.Phys.A A44, 135403 (2011), arXiv:1006.4500 [hep-th].

[126] Y. Hayashi and K.-I. Kondo, "Complex poles and spectral function of Yang-Mills theory," Phys. Rev. D 99, 074001 (2019), arXiv:1812.03116 [hep-th].

[127] S. W. Li, P. Lowdon, O. Oliveira, and P. J. Silva, "The generalised infrared structure of the gluon propagator," Phys. Lett. B 803, 135329 (2020), arXiv:1907.10073 [hep-th].

[128] C. S. Fischer and M. Q. Huber, "Landau gauge Yang-Mills propagators in the complex momentum plane," Phys. Rev. D 102, 094005 (2020), arXiv:2007.11505 [hep-ph].

[129] Y. Hayashi and K.-I. Kondo, "Reconstructing confined particles with complex singularities," Phys. Rev. D 103, L111504 (2021), arXiv:2103.14322 [hep-th].

[130] Y. Hayashi and K.-I. Kondo, "Complex poles and spectral functions of Landau gauge QCD and QCD-like theories," Phys. Rev. D 101, 074044 (2020), arXiv:2001.05987 [hep-th].

[131] K.-I. Kondo, Y. Hayashi, R. Matsudo, Y. Suda, and M. Watanabe, "Complex poles, spectral function and reflection positivity violation of Yang-Mills theory," PoS LC2019, 053 (2019), arXiv:1912.06261 [hep-th].

[132] K.-I. Kondo, M. Watanabe, Y. Hayashi, R. Matsudo, and Y. Suda, "Reflection positivity and complex analysis of the Yang-Mills theory from a viewpoint of gluon confinement," Eur. Phys. J. C 80, 84 (2020), arXiv:1902.08894 [hep-th].

[133] M. Q. Huber, "Correlation functions of Landau gauge Yang-Mills theory," Phys. Rev. D 101, 114009 (2020), arXiv:2003.13703 [hep-ph].

[134] G. Eichmann, J. M. Pawlowski, and J. a. M. Silva, "On mass generation in Landau-gauge Yang-Mills theory," (2021), arXiv:2107.05352 [hep-ph].

[135] M. Caselle, M. Hasenbusch, P. Provero, and K. Zarembo, "Bound states and glueballs in three-dimensional Ising systems," Nucl. Phys. B 623, 474 (2002), arXiv:hep-th/0103130.

[136] V. Agostini, G. Carlino, M. Caselle, and M. Hasenbusch, "The Spectrum of the (2+1)-dimensional gauge Ising model," Nucl. Phys. B484, 331 (1997), arXiv:hep-lat/9607029 [hep-lat].

[137] M. Caselle, M. Hasenbusch, and P. Provero, "Nonperturbative states in the 3-D phi**4 theory," Nucl. Phys. B556, 575 (1999), arXiv:hep-lat/9903011 [hep-lat].

[138] F. Rose, F. Benitez, F. Léonard, and B. Delamotte, "Bound states of the Φ^4 model via the nonperturbative renormalization group," Phys. Rev. D93, 125018 (2016), arXiv:1604.05285 [cond-mat.stat-mech].

[139] S. El-Showk, M. F. Paulos, D. Poland, S. Rychkov, D. Simmons-Duffin, and A. Vichi, "Solving the 3d Ising Model with the Conformal Bootstrap II. c-Minimization and Precise Critical Exponents," J. Stat. Phys. 157, 869 (2014), arXiv:1403.4545 [hep-th].

[140] I. Balog, H. Chaté, B. Delamotte, M. Marohnic, and N. Wschebor, "Convergence of Nonperturbative Approximations to the Renormalization Group," Phys. Rev. Lett. 123, 240604 (2019), arXiv:1907.01829 [cond-mat.stat-mech].

[141] A. J. Helmboldt, J. M. Pawlowski, and N. Strodthoff, "Towards quantitative precision in the chiral crossover: masses and fluctuation scales," Phys. Rev. D91, 054010 (2015), arXiv:1409.8414 [hep-ph].

[142] J. Roth and L. Von Smekal, "Critical dynamics in a real-time formulation of the functional renormalization group," Journal of High Energy Physics 2023, 1 (2023).

[143] D. F. Litim, "Optimization of the exact renormalization group," Phys.Lett. B486, 92 (2000), arXiv:hep-th/0005245 [hep-th].

[144] D. F. Litim, "Derivative expansion and renormalization group flows," JHEP 0111, 059 (2001), arXiv:hep-th/0111159 [hep-th].

[145] D. F. Litim, "Critical exponents from optimized renormalization group flows," Nucl.Phys. B631, 128 (2002), arXiv:hep-th/0203006 [hep-th].

[146] E. E. Salpeter, "Wave Functions in Momentum Space," Phys. Rev. 84, 1226 (1951).

[147] E. Salpeter and H. Bethe, "A Relativistic equation for bound state problems," Phys.Rev. 84, 1232 (1951).

[148] P. Maris and C. D. Roberts, "pi and K meson Bethe-Salpeter amplitudes," Phys. Rev. C56, 3369 (1997), arXiv:nucl-th/9708029.

[149] P. Maris and P. C. Tandy, "Bethe-Salpeter study of vector meson masses and decay constants," Phys. Rev. C60, 055214 (1999), arXiv:nucl-th/9905056.

[150] R. Alkofer, P. Watson, and H. Weigel, "Mesons in a Poincare covariant Bethe-Salpeter approach," Phys. Rev. D65, 094026 (2002), bethe-Salpeter, arXiv:hep-ph/0202053.

[151] A. Windisch, "Analytic properties of the quark propagator from an effective infrared interaction model," Phys. Rev. C 95, 045204 (2017), arXiv:1612.06002 [hep-ph].

[152] C. S. Fischer, P. Watson, and W. Cassing, "Probing unquenching effects in the gluon polarisation in light mesons," Phys. Rev. D72, 094025 (2005), arXiv:hep-ph/0509213.

[153] A. Krassnigg, "Excited mesons in a Bethe-Salpeter approach," PoS CONFINEMENT8, 075 (2008), arXiv:0812.3073 [nucl-th].

[154] S. M. Dorkin, L. P. Kaptari, T. Hilger, and B. Kampfer, "Analytical properties of the quark propagator from a truncated Dyson-Schwinger equation in complex Euclidean space," Phys. Rev. C89, 034005 (2014), arXiv:1312.2721 [hep-ph].

[155] S. M. Dorkin, L. P. Kaptari, and B. Kampfer, "Accounting for the analytical properties of the quark propagator from the Dyson-Schwinger equation," Phys. Rev. C91, 055201 (2015), arXiv:1412.3345 [hep-ph].

[156] E. Rojas, B. El-Bennich, and J. P. B. C. de Melo, “Exciting flavored bound states,” Phys. Rev. D 90, 074025 (2014), arXiv:1407.3598 [nucl-th].

[157] T. Hilger, M. Gómez-Rocha, A. Krassnigg, and W. Lucha, “Aspects of open-flavour mesons in a comprehensive DSBSE study,” Eur. Phys. J. A 53, 213 (2017), arXiv:1702.06262 [hep-ph].

[158] P. Maris, “Confinement and complex singularities in QED in three-dimensions,” Phys. Rev. D 52, 6087 (1995), arXiv:hep-ph/9508323.

[159] G. Eichmann, *Hadron properties from QCD bound-state equations*, Ph.D. thesis, Karl-Franzens-University Graz (2009), arXiv:0909.0703 [hep-ph].

[160] S. Strauss, C. S. Fischer, and C. Kellermann, “Analytic structure of the Landau gauge gluon propagator,” Phys. Rev. Lett. 109, 252001 (2012), arXiv:1208.6239 [hep-ph].

[161] A. Windisch, M. Q. Huber, and R. Alkofer, “On the analytic structure of scalar glueball operators at the Born level,” Phys.Rev. D87, 065005 (2013), arXiv:1212.2175 [hep-ph].

[162] A. Windisch, R. Alkofer, G. Haase, and M. Liebmann, “Examining the Analytic Structure of Green’s Functions: Massive Parallel Complex Integration using GPUs,” Comput. Phys. Commun. 184, 109 (2013), arXiv:1205.0752 [hep-ph].

[163] E. Weil, G. Eichmann, C. S. Fischer, and R. Williams, “Electromagnetic decays of the neutral pion,” Phys. Rev. D 96, 014021 (2017), arXiv:1704.06046 [hep-ph].

[164] M. Bluhm, Y. Jiang, M. Nahrgang, J. M. Pawlowski, F. Rennecke, and N. Wink, “Time-evolution of fluctuations as signal of the phase transition dynamics in a QCD-assisted transport approach,” *Proceedings, 27th International Conference on Ultrarelativistic Nucleus-Nucleus Collisions (Quark Matter 2018): Venice, Italy, May 14-19, 2018*, Nucl. Phys. A982, 871 (2019), arXiv:1808.01377 [hep-ph].

[165] R. Williams, “Vector mesons as dynamical resonances in the Bethe–Salpeter framework,” Phys. Lett. B 798, 134943 (2019), arXiv:1804.11161 [hep-ph].

[166] A. S. Miramontes and H. Sanchis-Alepuz, “On the effect of resonances in the quark-photon vertex,” Eur. Phys. J. A 55, 170 (2019), arXiv:1906.06227 [hep-ph].

[167] T. Frederico, D. C. Duarte, W. de Paula, E. Ydrefors, S. Jia, and P. Maris, “Towards Minkowski space solutions of Dyson-Schwinger Equations through un-Wick rotation,” (2019), arXiv:1905.00703 [hep-ph].

[168] N. Santowsky, G. Eichmann, C. S. Fischer, P. C. Wallbott, and R. Williams, “σ-meson: Four-quark versus two-quark components and decay width in a Bethe-Salpeter approach,” Phys. Rev. D 102, 056014 (2020), arXiv:2007.06495 [hep-ph].

[169] K. Kusaka and A. G. Williams, “Solving the Bethe-Salpeter equation for scalar theories in Minkowski space,” Phys. Rev. D 51, 7026 (1995), arXiv:hep-ph/9501262.

[170] V. Sauli and J. Adam, Jr., “Study of relativistic bound states for scalar theories in the Bethe-Salpeter and Dyson-Schwinger formalism,” Phys. Rev. D 67, 085007 (2003), arXiv:hep-ph/0111433.

[171] V. A. Karmanov and J. Carbonell, “Solving Bethe-Salpeter equation in Minkowski space,” Eur. Phys. J. A 27, 1 (2006), arXiv:hep-th/0505261.

[172] T. Frederico, G. Salme’, and M. Viviani, “Quantitative studies of the homogeneous Bethe-Salpeter Equation in Minkowski space,” Phys. Rev. D 89, 016010 (2014), arXiv:1312.0521 [hep-ph].

[173] W. de Paula, T. Frederico, G. Salmè, and M. Viviani, “Advances in solving the two-fermion homogeneous Bethe-Salpeter equation in Minkowski space,” Phys. Rev. D 94, 071901 (2016), arXiv:1609.00868 [hep-th].

[174] L. Schlessinger, “Use of analyticity in the calculation of nonrelativistic scattering amplitudes,” Phys. Rev. 167, 1411 (1968).

[175] R.-A. Tripolt, I. Haritan, J. Wambach, and N. Moiseyev, “Threshold energies and poles for hadron physical problems by a model-independent universal algorithm,” Phys. Lett. B774, 411 (2017), arXiv:1610.03252 [hep-ph].

[176] I. Haritan and N. Moiseyev, “On the calculation of resonances by analytic continuation of eigenvalues from the stabilization graph,” J. Chem. Phys. 147, 014101 (2017).

[177] R.-A. Tripolt, P. Gubler, M. Ulybyshev, and L. Von Smekal, “Numerical analytic continuation of Euclidean data,” Comput. Phys. Commun. 237, 129 (2019), arXiv:1801.10348 [hep-ph].

[178] R. Alkofer, A. Maas, W. A. Mian, M. Mitter, J. París-López, J. M. Pawlowski, and N. Wink, “Bound state properties from the functional renormalization group,” Phys. Rev. D 99, 054029 (2019), arXiv:1810.07955 [hep-ph].

[179] M. Q. Huber, C. S. Fischer, and H. Sanchis-Alepuz, “Spectrum of scalar and pseudoscalar glueballs from functional methods,” Eur. Phys. J. C 80, 1077 (2020), arXiv:2004.00415 [hep-ph].

[180] Z.-F. Cui, D. Binosi, C. D. Roberts, and S. M. Schmidt, “Fresh Extraction of the Proton Charge Radius from Electron Scattering,” Phys. Rev. Lett. 127, 092001 (2021), arXiv:2102.01180 [hep-ph].

[181] K. Fukushima, J. Horak, J. M. Pawlowski, N. Wink, and C. P. Zelle, “Nuclear liquid-gas transition in QCD,” Phys. Rev. D 110, 076022 (2024), arXiv:2308.16594 [nucl-th].

[182] L. Kades, J. M. Pawlowski, A. Rothkopf, M. Scherzer, J. M. Urban, S. J. Wetzel, N. Wink, and F. P. G. Ziegler, “Spectral Reconstruction with Deep Neural Networks,” Phys. Rev. D 102, 096001 (2020), arXiv:1905.04305 [physics.comp-ph].

[183] A. Windisch, T. Gallien, and C. Schwarzlmüller, “Deep reinforcement learning for complex evaluation of one-loop diagrams in quantum field theory,” Phys. Rev. E 101, 033305 (2020), arXiv:1912.12322 [hep-ph].

[184] A. Windisch, T. Gallien, and C. Schwarzlmueller, "A machine learning pipeline for autonomous numerical analytic continuation of Dyson-Schwinger equations," EPJ Web Conf. 258, 09003 (2022), arXiv:2112.13011 [hep-ph].

[185] J. Horak, J. M. Pawlowski, J. Turnwald, J. M. Urban, N. Wink, and S. Zafeiropoulos, "Nonperturbative strong coupling at timelike momenta," Phys. Rev. D 107, 076019 (2023), arXiv:2301.07785 [hep-ph].

[186] A. Rothkopf, "Bayesian inference of real-time dynamics from lattice QCD," Front. Phys. 10, 1028995 (2022), arXiv:2208.13590 [hep-lat].

[187] A. Rothkopf, "Inverse problems, real-time dynamics and lattice simulations," EPJ Web Conf. 274, 01004 (2022), arXiv:2211.10680 [hep-lat].

[188] T. Lechien and D. Dudal, "Neural network approach to reconstructing spectral functions and complex poles of confined particles," SciPost Phys. 13, 097 (2022), arXiv:2203.03293 [hep-lat].

[189] A. Lupo, L. Del Debbio, M. Panero, and N. Tantalo, "Fits of finite-volume smeared spectral densities," PoS LATTICE2022, 215 (2023), arXiv:2212.08019 [hep-lat].

[190] E. L. Solis, C. S. R. Costa, V. V. Luiz, and G. Krein, "Quark propagator in Minkowski space," Few Body Syst. 60, 49 (2019), arXiv:1905.08710 [hep-ph].

[191] J. Horak, J. M. Pawlowski, and N. Wink, "On the quark spectral function in QCD," SciPost Phys. 15, 149 (2023), arXiv:2210.07597 [hep-ph].

[192] K. Kusaka, K. Simpson, and A. G. Williams, "Solving the bethe-salpeter equation for bound states of scalar theories in minkowski space," Phys. Rev. D 56, 5071 (1997).

[193] J. Carbonell and V. A. Karmanov, "Solving Bethe-Salpeter equation for two fermions in Minkowski space," Eur. Phys. J. A 46, 387 (2010), arXiv:1010.4640 [hep-ph].

[194] J. Carbonell and V. A. Karmanov, "Solving bethe-salpeter scattering state equation in minkowski space," Phys. Rev. D 90, 056002 (2014).

[195] S. Leitão, Y. Li, P. Maris, M. T. Peña, A. Stadler, J. P. Vary, and E. P. Biernat, "Comparison of two Minkowski-space approaches to heavy quarkonia," Eur. Phys. J. C 77, 696 (2017), arXiv:1705.06178 [hep-ph].

[196] S. Leitão, A. Stadler, M. T. Peña, and E. P. Biernat, "Covariant spectator theory of quark-antiquark bound states: Mass spectra and vertex functions of heavy and heavy-light mesons," Phys. Rev. D 96, 074007 (2017).

[197] W. de Paula, T. Frederico, G. Salmè, M. Viviani, and R. Pimentel, "Fermionic bound states in Minkowski-space: Light-cone singularities and structure," Eur. Phys. J. C 77, 764 (2017), arXiv:1707.06946 [hep-ph].

[198] E. P. Biernat, F. Gross, M. T. Peña, A. Stadler, and S. Leitão, "Quark mass function from a one-gluon-exchange-type interaction in minkowski space," Phys. Rev. D 98, 114033 (2018).

[199] E. Ydrefors, J. H. Alvarenga Nogueira, V. A. Karmanov, and T. Frederico, "Solving the three-body bound-state Bethe-Salpeter equation in Minkowski space," Phys. Lett. B 791, 276 (2019), arXiv:1903.01741 [hep-ph].

[200] M. Caselle, M. Hasenbusch, and P. Provero, "Nonperturbative states in the three-dimensional phi**4 theory," Nucl. Phys. B Proc. Suppl. 83, 715 (2000), arXiv:hep-lat/9907018.

[201] Y. Nishiyama, "Universal critical behavior of the two-magnon-bound-state mass gap for the (2+1) -dimensional Ising model," Physica A: Statistical Mechanics and its Applications 413, 577 (2014), arXiv:1407.8243 [cond-mat.stat-mech].

[202] Y. Nishiyama, "Bound-state energy of the three-dimensional ising model in the broken-symmetry phase: Suppressed finite-size corrections," Phys. Rev. E 77, 051112 (2008).

[203] D. Lee, N. Salwen, and M. Windoloski, "Introduction to stochastic error correction methods," Phys. Lett. B502, 329 (2001), arXiv:hep-lat/0010039 [hep-lat].

[204] J. Zinn-Justin, *Quantum field theory and critical phenomena*, Vol. 171 (Oxford university press, 2021).

[205] J. Zinn-Justin, "Precise determination of critical exponents and equation of state by field theory methods," Phys. Rept. 344, 159 (2001), arXiv:hep-th/0002136.

[206] F. Gliozzi and A. Rago, "Critical exponents of the 3d ising and related models from conformal bootstrap," Journal of High Energy Physics 2014 (2014), 10.1007/JHEP10(2014)042.

[207] F. Benitez, J.-P. Blaizot, H. Chaté, B. Delamotte, R. Méndez-Galain, *et al.*, "Non-perturbative renormalization group preserving full-momentum dependence: implementation and quantitative evaluation," Phys.Rev. E85, 026707 (2012), arXiv:1110.2665 [cond-mat.stat-mech].

[208] M. E. Carrington, "The 4PI effective action for phi**4 theory," Eur. Phys. J. C35, 383 (2004), arXiv:hep-ph/0401123.

[209] M. Carrington, W. Fu, T. Fugleberg, D. Pickering, and I. Russell, "Bethe-Salpeter Equations from the 4PI effective action," Phys.Rev. D88, 085024 (2013), arXiv:1310.3295 [hep-ph].

[210] M. Carrington, W.-J. Fu, P. Mikula, and D. Pickering, "Four-point vertices from the 2PI and 4PI effective actions," Phys.Rev. D89, 025013 (2014), arXiv:1310.4352 [hep-ph].

[211] H. Sanchis-Alepuz and R. Williams, "Recent developments in bound-state calculations using the Dyson–Schwinger and Bethe–Salpeter equations," Comput. Phys. Commun. 232, 1 (2018), arXiv:1710.04903 [hep-ph].

[212] G. C. Wick, "Properties of Bethe-Salpeter Wave Functions," Phys. Rev. 96, 1124 (1954).

[213] R. E. Cutkosky, "Solutions of a Bethe-Salpeter equations," Phys. Rev. 96, 1135 (1954).

[214] S. Ahlig and R. Alkofer, "(In)consistencies in the relativistic description of excited states in the Bethe-Salpeter equation," Annals Phys. 275, 113 (1999), arXiv:hep-th/9810241.

[215] S. Weinberg, "ULTRAVIOLET DIVERGENCES IN QUANTUM THEORIES OF GRAVITATION," General Relativity: An Einstein centenary survey, Eds. Hawking, S.W., Israel, W; Cambridge University Press , 790 (1979).

[216] M. Reuter, "Nonperturbative Evolution Equation for Quantum Gravity," Phys. Rev. D57, 971 (1998), arXiv:hep-th/9605030.

[217] J. M. Pawlowski and M. Reichert, "Quantum gravity: a fluctuating point of view," Front. in Phys. 8, 527 (2020), arXiv:2007.10353 [hep-th].

[218] S. Weinberg, "Critical Phenomena for Field Theorists," in *14th International School of Subnuclear Physics: Understanding the Fundamental Constitutents of Matter* (1976) p. 1.

[219] A. Bonanno, A. Eichhorn, H. Gies, J. M. Pawlowski, R. Percacci, M. Reuter, F. Saueressig, and G. P. Vacca, "Critical reflections on asymptotically safe gravity," Front. in Phys. 8, 269 (2020), arXiv:2004.06810 [gr-qc].

[220] M. Mitter, J. M. Pawlowski, and N. Strodthoff, "Chiral symmetry breaking in continuum QCD," Phys.Rev. D91, 054035 (2015), arXiv:1411.7978 [hep-ph].

[221] R. Williams, "The quark-gluon vertex in Landau gauge bound-state studies," Eur. Phys. J. A51, 57 (2015), arXiv:1404.2545 [hep-ph].

[222] R. Williams, C. S. Fischer, and W. Heupel, "Light mesons in QCD and unquenching effects from the 3PI effective action," Phys. Rev. D93, 034026 (2016), arXiv:1512.00455 [hep-ph].

[223] T. Gasenzer and J. M. Pawlowski, "Towards far-from-equilibrium quantum field dynamics: A functional renormalisation-group approach," Phys. Lett. B 670, 135 (2008), arXiv:0710.4627 [cond-mat.other].

[224] T. Gasenzer, S. Kessler, and J. M. Pawlowski, "Far-from-equilibrium quantum many-body dynamics," Eur.Phys.J. C70, 423 (2010), arXiv:1003.4163 [cond-mat.quant-gas].

[225] K. Kamikado, N. Strodthoff, L. von Smekal, and J. Wambach, "Real-Time Correlation Functions in the O(N) Model from the Functional Renormalization Group," Eur.Phys.J. C74, 2806 (2014), arXiv:1302.6199 [hep-ph].

[226] R.-A. Tripolt, N. Strodthoff, L. von Smekal, and J. Wambach, "Spectral Functions for the Quark-Meson Model Phase Diagram from the Functional Renormalization Group," Phys. Rev. D89, 034010 (2014), arXiv:1311.0630 [hep-ph].

[227] K. Kamikado, T. Kanazawa, and S. Uchino, "Mobile impurity in a Fermi sea from the functional renormalization group analytically continued to real time," Phys. Rev. A95, 013612 (2017), arXiv:1606.03721 [cond-mat.quant-gas].

[228] C. Jung, F. Rennecke, R.-A. Tripolt, L. von Smekal, and J. Wambach, "In-Medium Spectral Functions of Vector- and Axial-Vector Mesons from the Functional Renormalization Group," Phys. Rev. D95, 036020 (2017), arXiv:1610.08754 [hep-ph].

[229] Z. Wang and P. Zhuang, "Meson spectral functions at finite temperature and isospin density with the functional renormalization group," Phys. Rev. D96, 014006 (2017), arXiv:1703.01035 [hep-ph].

[230] R.-A. Tripolt, C. Jung, N. Tanji, L. von Smekal, and J. Wambach, "In-medium spectral functions and dilepton rates with the Functional Renormalization Group," *Proceedings, 27th International Conference on Ultrarelativistic Nucleus-Nucleus Collisions (Quark Matter 2018): Venice, Italy, May 14-19, 2018*, Nucl. Phys. A982, 775 (2019), arXiv:1807.04952 [hep-ph].

[231] R.-A. Tripolt, J. Weyrich, L. von Smekal, and J. Wambach, "Fermionic spectral functions with the Functional Renormalization Group," Phys. Rev. D98, 094002 (2018), arXiv:1807.11708 [hep-ph].

[232] L. Corell, A. K. Cyrol, M. Heller, and J. M. Pawlowski, "Flowing with the temporal renormalization group," Phys. Rev. D 104, 025005 (2021), arXiv:1910.09369 [hep-th].

[233] S. Huelsmann, S. Schlichting, and P. Scior, "Spectral functions from the real-time functional renormalization group," Phys. Rev. D 102, 096004 (2020), arXiv:2009.04194 [hep-ph].

[234] C. Jung, J.-H. Otto, R.-A. Tripolt, and L. von Smekal, "Self-consistent O(4) model spectral functions from analytically continued functional renormalization group flows," Phys. Rev. D 104, 094011 (2021), arXiv:2107.10748 [hep-ph].

[235] Y.-y. Tan, Y.-r. Chen, and W.-j. Fu, "Real-time dynamics of the $O(4)$ scalar theory within the fRG approach," SciPost Phys. 12, 026 (2022), arXiv:2107.06482 [hep-ph].

[236] M. Heller and J. M. Pawlowski, "Causal Temporal Renormalisation Group Flow of the Energy-Momentum Tensor," (2021), arXiv:2112.12652 [hep-th].

[237] S. Jia and M. R. Pennington, "Exact Solutions to the Fermion Propagator Schwinger-Dyson Equation in Minkowski space with on-shell Renormalization for Quenched QED," Phys. Rev. D96, 036021 (2017), arXiv:1705.04523 [nucl-th].

[238] V. Sauli, "The quark spectral functions and the Hadron Vacuum Polarization from application of DSEs in Minkowski space," Few Body Syst. 61, 23 (2020), arXiv:1809.07644 [hep-ph].

[239] C. Mezrag and G. Salmè, "Fermion and Photon gap-equations in Minkowski space within the Nakanishi Integral Representation method," Eur. Phys. J. C 81, 34 (2021), arXiv:2006.15947 [hep-ph].

[240] S. J. Stainsby and R. T. Cahill, "IS SPACE-TIME EUCLIDEAN 'INSIDE' HADRONS?" Phys. Lett. A 146, 467 (1990).

[241] P. Maris and H. A. Holties, "Determination of the singularities of the Dyson-Schwinger equation for the quark propagator," Int. J. Mod. Phys. A 7, 5369 (1992).

[242] R. Oehme, "Analytic structure of amplitudes in gauge theories with confinement," Int. J. Mod. Phys. A 10, 1995 (1995), arXiv:hep-th/9412040.

[243] A. F. Falcão, O. Oliveira, and P. J. Silva, "Analytic structure of the lattice Landau gauge gluon and ghost propagators," Phys. Rev. D 102, 114518 (2020), arXiv:2008.02614 [hep-lat].

[244] F. Siringo, "Analytic structure of QCD propagators in Minkowski space," Phys. Rev. D 94, 114036 (2016), arXiv:1605.07357 [hep-ph].

[245] A. C. Aguilar, M. N. Ferreira, B. M. Oliveira, J. Papavassiliou, and G. T. Linhares, "Infrared properties of the quark-gluon vertex in general kinematics," Eur. Phys. J. C 84, 1231 (2024), arXiv:2408.15370 [hep-ph].

[246] J. S. Ball and T.-W. Chiu, "Analytic Properties of the Vertex Function in Gauge Theories. 1." Phys.Rev. D22, 2542 (1980).

[247] A. Bender, W. Detmold, C. Roberts, and A. W. Thomas, "Bethe-Salpeter equation and a nonperturbative quark gluon vertex," Phys.Rev. C65, 065203 (2002), arXiv:nucl-th/0202082 [nucl-th].

[248] C. S. Fischer and R. Alkofer, "Non-perturbative Propagators, Running Coupling and Dynamical Quark Mass of Landau gauge QCD," Phys. Rev. D67, 094020 (2003), arXiv:hep-ph/0301094.

[249] M. Bhagwat, A. Holl, A. Krassnigg, C. Roberts, and P. Tandy, "Aspects and consequences of a dressed quark gluon vertex," Phys.Rev. C70, 035205 (2004), arXiv:nucl-th/0403012 [nucl-th].

[250] C. S. Fischer, "Infrared properties of QCD from Dyson-Schwinger equations," J.Phys.G G32, R253 (2006), arXiv:hep-ph/0605173 [hep-ph].

[251] C. S. Fischer, D. Nickel, and J. Wambach, "Hadronic unquenching effects in the quark propagator," Phys. Rev. D76, 094009 (2007), arXiv:0705.4407 [hep-ph].

[252] C. S. Fischer and R. Williams, "Beyond the rainbow: effects from pion back-coupling," Phys. Rev. D78, 074006 (2008), arXiv:0808.3372 [hep-ph].

[253] L. Chang and C. D. Roberts, "Sketching the Bethe-Salpeter kernel," Phys.Rev.Lett. 103, 081601 (2009), arXiv:0903.5461 [nucl-th].

[254] L. Chang and C. D. Roberts, "Tracing masses of ground-state light-quark mesons," Phys.Rev. C85, 052201 (2012), arXiv:1104.4821 [nucl-th].

[255] C. S. Fischer and J. Luecker, "Propagators and phase structure of Nf=2 and Nf=2+1 QCD," Phys.Lett. B718, 1036 (2013), arXiv:1206.5191 [hep-ph].

[256] A. C. Aguilar, J. C. Cardona, M. N. Ferreira, and J. Papavassiliou, "Quark gap equation with non-abelian Ball-Chiu vertex," Phys. Rev. D 98, 014002 (2018), arXiv:1804.04229 [hep-ph].

[257] F. Gao, A. S. Miramontes, J. Papavassiliou, and J. M. Pawlowski, "Heavy-light mesons from a flavour-dependent interaction," (2024), arXiv:2411.19680 [hep-ph].

[258] C. S. Fischer, D. Nickel, and R. Williams, "On Gribov's supercriticality picture of quark confinement," Eur. Phys. J. C60, 1434 (2008), arXiv:0807.3486 [hep-ph].

[259] M. S. Bhagwat, M. A. Pichowsky, C. D. Roberts, and P. C. Tandy, "Analysis of a quenched lattice QCD dressed quark propagator," Phys. Rev. C 68, 015203 (2003), arXiv:nucl-th/0304003.

[260] R. Alkofer, C. S. Fischer, F. J. Llanes-Estrada, and K. Schwenzer, "The quark-gluon vertex in Landau gauge QCD: Its role in dynamical chiral symmetry breaking and quark confinement," Annals Phys. 324, 106 (2009), arXiv:0804.3042 [hep-ph].

[261] R. Alkofer, W. Detmold, C. S. Fischer, and P. Maris, "Analytic properties of the Landau gauge gluon and quark propagators," Phys. Rev. D70, 014014 (2004), arXiv:hep-ph/0309077.

[262] A. F. Falcão and O. Oliveira, "The analytic structure of the Landau gauge quark propagator from Padé analysis," (2022), arXiv:2209.14815 [hep-lat].

[263] A. V. Belitsky and A. V. Radyushkin, "Unraveling hadron structure with generalized parton distributions," Phys. Rept. 418, 1 (2005), arXiv:hep-ph/0504030.

[264] C. Lorce, B. Pasquini, and M. Vanderhaeghen, "Unified framework for generalized and transverse-momentum dependent parton distributions within a 3Q light-cone picture of the nucleon," JHEP 05, 041 (2011), arXiv:1102.4704 [hep-ph].

[265] X. Ji, "Parton Physics on a Euclidean Lattice," Phys. Rev. Lett. 110, 262002 (2013), arXiv:1305.1539 [hep-ph].

[266] X. Ji, "Parton Physics from Large-Momentum Effective Field Theory," Sci. China Phys. Mech. Astron. 57, 1407 (2014), arXiv:1404.6680 [hep-ph].

[267] X. Ji, Y.-S. Liu, Y. Liu, J.-H. Zhang, and Y. Zhao, "Large-momentum effective theory," Rev. Mod. Phys. 93, 035005 (2021), arXiv:2004.03543 [hep-ph].

[268] J.-H. Zhang, J.-W. Chen, X. Ji, L. Jin, and H.-W. Lin, "Pion Distribution Amplitude from Lattice QCD," Phys. Rev. D 95, 094514 (2017), arXiv:1702.00008 [hep-lat].

[269] J. Hua *et al.* (Lattice Parton), "Pion and Kaon Distribution Amplitudes from Lattice QCD," Phys. Rev. Lett. 129, 132001 (2022), arXiv:2201.09173 [hep-lat].

[270] J. Holligan, X. Ji, H.-W. Lin, Y. Su, and R. Zhang, "Precision control in lattice calculation of x-dependent pion distribution amplitude," Nucl. Phys. B 993, 116282 (2023), arXiv:2301.10372 [hep-lat].

[271] H. Dutrieux, J. Karpie, C. J. Monahan, K. Orginos, A. Radyushkin, D. Richards, and S. Zafeiropoulos, "Inverse problem in the LaMET framework," (2025), arXiv:2504.17706 [hep-lat].

[272] D.-y. Zhang, C. Huang, and W.-j. Fu, "Quasi parton distributions of pions at large longitudinal momentum," (2025), arXiv:2502.15384 [hep-ph].

[273] R. Arthur, P. A. Boyle, D. Brommel, M. A. Donnellan, J. M. Flynn, A. Juttner, T. D. Rae, and C. T. C. Sachrajda, "Lattice Results for Low Moments of Light Meson Distribution Amplitudes," Phys. Rev. D 83, 074505 (2011), arXiv:1011.5906 [hep-lat].

[274] G. S. Bali, V. M. Braun, S. Bürger, M. Göckeler, M. Gruber, F. Hutzler, P. Korcyl, A. Schäfer, A. Sternbeck, and P. Wein (RQCD), "Light-cone distribution amplitudes of pseudoscalar mesons from lattice QCD," JHEP 08, 065 (2019), [Addendum: JHEP 11, 037 (2020)], arXiv:1903.08038 [hep-lat].

[275] L. Chang, I. C. Cloet, J. J. Cobos-Martinez, C. D. Roberts, S. M. Schmidt, and P. C. Tandy, "Imaging dynamical chiral symmetry breaking: pion wave function on the light front," Phys. Rev. Lett. 110, 132001 (2013), arXiv:1301.0324 [nucl-th].

[276] N. Nakanishi, "Partial-Wave Bethe-Salpeter Equation," Phys. Rev. 130, 1230 (1963).

[277] A. K. Rajantie, "Feynman diagrams to three loops in three-dimensional field theory," Nucl. Phys. B480, 729 (1996), [Erratum: Nucl. Phys.B513,761(1998)], arXiv:hep-ph/9606216 [hep-ph].

[278] N. Wink, *Towards the spectral properties and phase structure of QCD.*, Ph.D. thesis, U. Heidelberg, ITP (2020).

[279] W. R. Inc., "Mathematica, Version 13.1," Champaign, IL, 2022.

[280] J. Bezanson, A. Edelman, S. Karpinski, and V. B. Shah, "Julia: A fresh approach to numerical computing," SIAM Review 59, 65 (2017).

[281] J. Bezanson, A. Edelman, S. Karpinski, and V. B. Shah, "Julia: A fresh approach to numerical computing," SIAM review 59, 65 (2017).